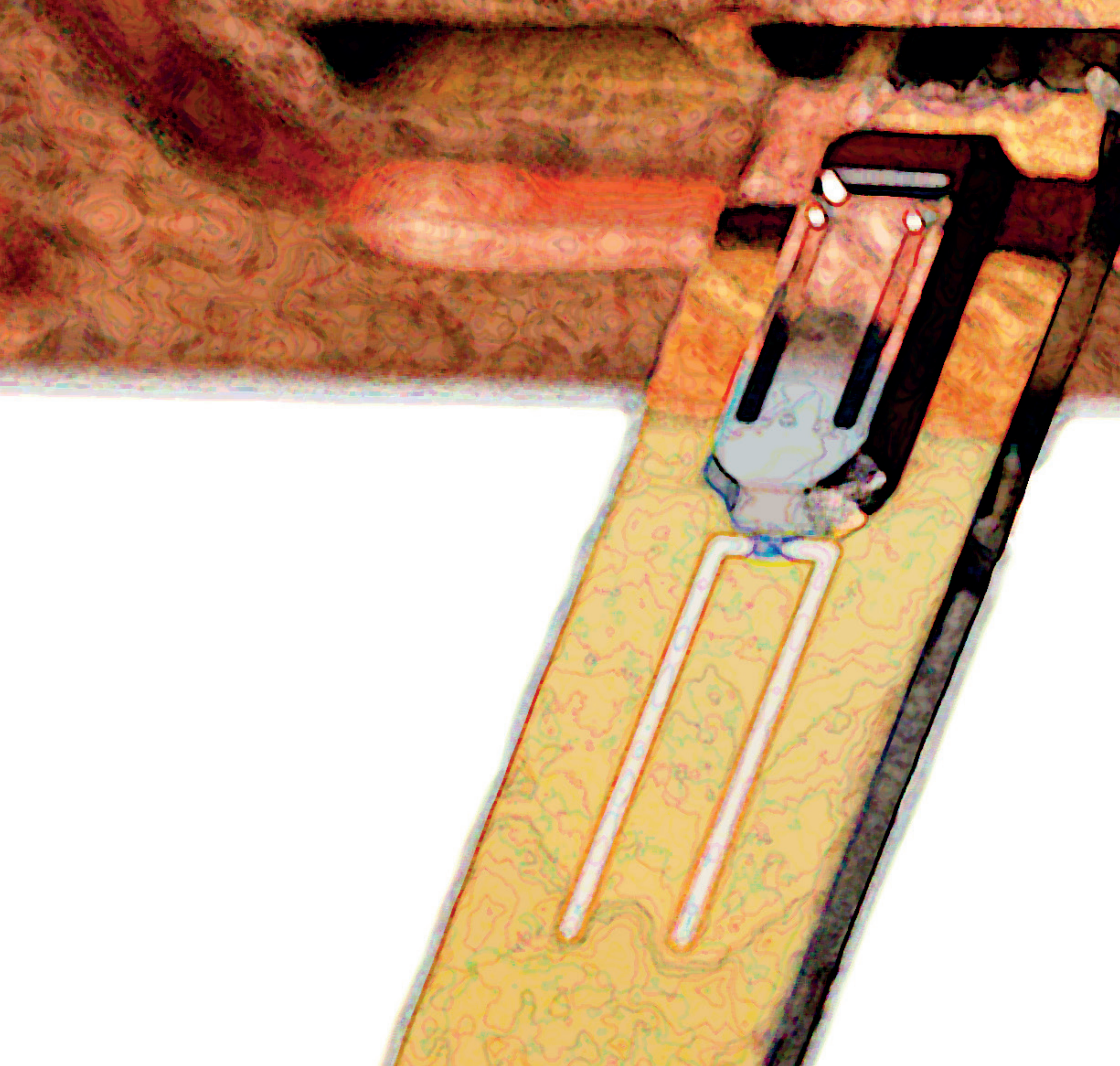

Demonstration of nonlinear enhanced backaction cooling in microwave magnetomechanics

David Zöpfl

Demonstration of nonlinear enhanced backaction cooling in microwave magnetomechanics

by

David Zöpfl

Thesis submitted to the

Faculty of Mathematics, Computer Science and Physics of the

Leopold-Franzens University of Innsbruck

in partial fulfillment for the degree of Doctor of Philosophy (PhD).

Carried out at the Institute of Experimental Physics under the supervision of

Univ.-Prof. Dr. Gerhard Kirchmair.

September 2022

Abstract

This thesis presents a novel optomechanical setup, where a mechanical cantilever is inductively coupled to a nonlinear cavity. This approach is based on a theoretical proposal [1] with the aim of increasing the coupling strengths compared to other - more traditional - optomechanical setups, using capacitive coupling. Indeed this was achieved by measuring single-photon coupling strengths of up to nearly 10 kHz, which is on par with other very recent inductive coupling experiments [2, 3]. The main result of this work is however that the intrinsic nonlinearity of the cavity can be used for more efficient backaction cooling. This is especially true in the sideband unresolved regime (cavity linewidth exceeding mechanical frequency). In this regime, measurements show the increase of the the cooling backaction by more than an order of magnitude compared to an otherwise identical linear system. The best cooling currently achieved is cooling to around 14 quanta of mechanical occupation - an around 300 fold compression from the thermal equilibrium. While in the experiment, the limitation for cooling is magnetic/mechanical noise, the fundamental theoretical limit is around 3 phonons for the setup parameters. This is the first demonstration of the benefits of nonlinear cooling, proposed by theory more than a decade ago [4, 5]. This effect might be highly relevant for optomechanical systems with massive mechanical resonators, which are typically at low frequency, allowing much more efficient cooling compared to the conventional approach involving a linear cavity.

Kurzfassung

In dieser Arbeit wird ein neuartiges optomechanisches Setup vorgestellt. Dabei wird ein mechanischer Cantilever induktiv an einen nichtlinearen Mikrowellenresonator gekoppelt. Dieser Aufbau basiert auf einem theoretischen Vorschlag [1], mit dem Ziel die Kopplungsstärke gegenüber anderen, traditionelleren Zugängen mit kapazitiver Kopplung zu erhöhen. Dieses Ziel konnte auch erreicht werden und es wurden einzelphoton Kopplungsstärken von beinahe 10 kHz gemessen. Ähnliche Kopplungsstärken wurden kürzlich auch von anderen Experiementen erreicht, die auch auf induktiver Kopplung basieren [2, 3].

Das Hauptergebnis dieser Arbeit ist jedoch nicht die hohen Kopplungsstärke an sich, sondern dass die intrinsische Nichtlinearität des Resonators für effizienteres Kühlen der mechanischen Mode verwendet werden kann. Insbesonders gilt das im unaufgelösten Seitenbandregime, in dem die Linienbreite des Resonators über der mechanischen Frequenz liegt. In diesem Regime konnte ein verbessertes Kühlen um mehr als den Faktor von 10 im Vergleich zu einem herkömmlichen linearen System mit gleichen Parameteren gezeigt werden. Im besten Fall kann die mechanische Mode momentan auf etwa 14 Anregungsquanten gekühlt werden, was einer mehr als 300-fachen Verringerung der Anregungen gegenüber dem thermischen Gleichgewicht entspricht. Während das experimentelle Setup derzeit durch mechanisches/magnetisches Rauschen limitiert ist, liegt das theoretische Limit bei etwa 3 Anregungszuständen. In dieser Arbeit werden erstmals die Vorteile des nichtlinearen Kühlen experimentell gezeigt, die theoretisch schon vor mehr als 10 Jahren vorhergesagt wurden [4, 5]. Dieser Kühlungsmechanismus ist möglicherweise für optomechanische Systeme, die massive mechanische Oszillatoren verweden, sehr relevant. Denn massive Oszillatoren schwingen zumeist mit geringer Frequenz, wodurch mithilfe einem nichtlinearien Resonator viel effizienter gekühlt werden kann.

List of Publications

D. Zoepfl, P. R. Muppalla, C. M. F. Schneider, S. Kasemann, S. Partel, and G. Kirchmair. Characterization of low loss microstrip resonators as a building block for circuit QED in a 3D waveguide. *AIP Advances*, 7(8):085118, August 2017.

D. Zoepfl, M. L. Juan, C. M. F. Schneider, and G. Kirchmair. Single-Photon Cooling in Microwave Magnetomechanics. *Physical Review Letters*, 125(2):023601, July 2020.

D. Zoepfl, M. L. Juan, N. Diaz-Naufal, C. M. F. Schneider, L. F. Deeg, A. Sharafiev, A. Metelmann, and G. Kirchmair. Kerr enhanced backaction cooling in magnetomechanics. *arXiv:2202.13228 [quant-ph]*, February 2022.

Contents

1 | Introduction

1.1 Why to do quantum state control

In the late 19^{th} century physicists distinguished between processes involving matter and ones based on radiation, either described by Newton's laws or by Maxwell's equations. With the beginning of the 20^{th} century physics changed fundamentally, with the formulation of the theory of relativity and quantum mechanics [6]. Classical physics lost its validity if the object moved at a speed comparable to the speed of light and on lengths scales of atomic sizes.

In quantum theory the properties of a particle - for instance its position - are described by a wave function, given by the Schrödinger equation. This wave function is usually interpreted as a probability for finding the particle in a given state, in case of the example, at a given position [7]. Oddly enough, only the measurement forces the particle to take a certain state, which is not precise before conducting the measurement. Thus, the measurement is known as 'collapsing the wave function' into a particular state. Furthermore, the uncertainty principle says, that there exists an uncertainty between certain pairs of quantities, i.e. position and momentum or energy and time. This means, that fundamentally those quantities cannot be measured with absolute precision at the same time [7]. Additionally, despite being in the state of lowest energy - the ground state - a particle still exhibits some motion, known as the zero point motion [8]. This can be seen as a consequence of the uncertainty principle, as the particle can never be completely at rest.

It is also possible to create a superposition of different states. There, a particle is in multiple quantum states simultaneously and only the measurement forces the particle to take one of the possible states. Notably, before conducting the measurement the particle is physically in different states at the same time. Another peculiar effect of the quantum world is entanglement. It describes, that two particles can be correlated and still interact instantaneously, even though they can be separated over wide distances.

These phenomena are counter-intuitive and sometimes even strange. Still quantum theory seems to give an accurate prediction of nature at small scales and so far passed every test. It is highly successful and widely accepted today, an increasing number of companies even use the powerful effects of quantum theory for quantum computation.

There is no reason to assume that quantum mechanics does not apply beyond a certain mass or size. However, while quantum mechanics is well tested for small objects, it is very challenging to prepare bigger (massive) objects in a quantum state. Among the reasons is, that those states typically decohere faster and additionally the zero point motion typically decreases with mass. As a consequence, quantum phenomena have less influence for massive objects, but this also makes it more challenging to control such objects near their ground state. Further, quantum states are typically fragile and have to be protected from the environment, as the interaction leads to decay. Also this gets increasingly challenging with size.

Still, despite the challenges, there are several reasons for testing quantum physics on larger scales. For instance, so-called collapse models predict the collapse of the quantum mechanical wave function if the quantum state of an object above a certain mass is delocalised beyond a critical distance [9, 10]. Those models assume that the Schrödinger equation is only an approximation. Also gravity is not included in the Schrödinger equation and thus it is highly interesting to test the influence of gravity on quantum states, e.g. proposed in [11, 12]. Such experiments could also pave the way for unifying quantum theory and (general) relativity, which are currently incompatible, leading to a more profound understanding of nature. With increasing mass, objects in quantum states could even act as source masses in gravitational experiments.

With this, it becomes clear that the ability to operate massive mechanical objects in or near quantum states is highly relevant for experimental physics. This requires exceptional control over such an object. A prime candidate for achieving this is optomechanics, where photons are coupled to quanta of mechanical motion (phonons).

While optomechanics is very well suited for testing fundamental physics, it is also has many additional cases of applications. As optomechanical devices can couple to different photonic systems, another field of application is as a building block in a 'quantum internet' (quantum transducer), converting e.g. microwave to optical photons and vice versa. For those networks, the quantum computation could be done with superconducting qubits at microwave frequencies. Transporting signals at such frequencies is highly susceptible to loss and optical frequencies are much better suited for this [13]. Thus one would do the transport over larger distances in the optical domain, and quantum transducers are required for converting the signal to and from microwave frequencies. Optomechanical devices are among the prime candidates for this task [13, 14, 15, 16].

Another highly interesting field is (quantum) sensing. Due to the high controllability of the mechanical mode it is also possible to detect small changes in position, leading to unprecedented sensing capabilities [17, 18]. Preparing the mechanical mode in a superposition or an entangled state could even boost the sensing capabilities further by operating at the fundamental limits of quantum physics [19]. Depending on the mass, different systems are either better suited for acceleration sensing (heavier is better) or force sensing (lighter is better) [20].

1.2 A brief introduction to optomechanics

As we have seen, optomechanics is a very versatile platform. Within optomechanics objects as small as single atoms up to kilogram heavy objects have been coupled to different photonic systems [21]. While many different implementations exist and will be discussed below, from a theoretical description, all of those systems are described by the same set of equations. The main parameter, next to the decay rates of the photonic and the mechanical mode is g_0, the single-photon coupling rate between the mechanical object and the photonic mode. As a pre-requisite, for doing experiments in the quantum regime, the mechanical mode has to be cooled into or close to its quantum-mechanical ground state. As typically - even in cryogenic environments - the mechanical mode is in a highly excited thermal state. Fortunately different schemes for cooling exist and ground state cooling has been shown in many different systems, e.g. [22, 23, 24]. This is already a landmark feature of the very high controllability over the mechanical system in optomechanics.

The next step after cooling, would be to prepare the mechanical mode in a quantum state, where it gets usually more delicate [25]. With tools available today, it is possible to prepare a quantum state in the photonic mode, which has to be transferred to the mechanical mode. This brings us to the type of quantum state, where we typically distinguish between Gaussian and non-Gaussian states. While Gaussian states have a classical analogous, non-Gaussian states do not and are therefore often considered as fundamentally quantum. Examples of non-Gaussian states would be Fock or cat states, whereas coherent or squeezed states follow Gaussian statistics. For transferring such a state then, it is usually required, that the coupling rate g_0 exceeds the decay rate of the photonic mode, κ, as well as of the mechanical mode Γ_m, which is highly demanding. To my knowledge there exists no experiment to date, which comes even close of having the required coupling with a massive mechanical mode.

To give an overview of the field of optomechanics, a few examples of different systems are named in the following without any claim of completeness (Fig. 1.1). Single atoms or an ensemble of cold atoms can be coupled to an optical cavity, Fig. 1.1a. Light can be either sent through the input cavity mirror or directly into the atomic ensemble, to study for instance cooling, trapping or also diffusion [26]. Increasing in size, photonic crystals are another platform, where the vibrational mode can couple to the optical mode [27]. Further, one can simply place a membrane in an optical cavity, which changes, depending on the position of the membrane, the optical properties [28], Fig. 1.1c. Among the most massive optomechanical systems is LIGO with a movable mirror, having more than 1 kg, in an optical interferometer [29, 17].

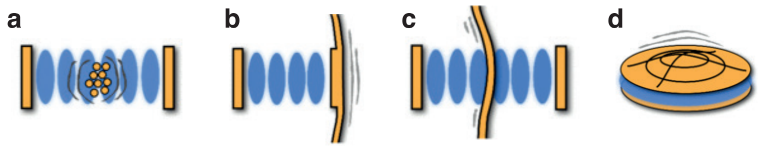

Figure 1.1: Sketch of different optomechanical system implementation. Indicated are the photonic modes (blue) and the mechanical modes (gray lines). **a.** Ensemble of atoms in an optical cavity. **b.** Movable back mirror of an optical cavity. **c.** Membrane in the middle of an optical cavity. **d.** Movable capacitor plate being part of a microwave resonator. Graphic adapted from [21].

The above schemes are all about coupling an optical cavity to a mechanical mode. Another possibility is to couple a microwave signal to a mechanical mode, as for example coupling a string [30], or different types of drums, which serve as position dependent capacitors [23, 31], Fig. 1.1d.

In the next part, a more detailed summary of experiments in the field of microwave optomechanics is given, for putting the work discussed in this thesis, also a microwave cavity coupled to a mechanical mode, into context. One of the first works was [30] in 2008, where the authors coupled a beam capacitively to an LC circuit, and even showed optomechanical cooling of the mechanical mode. In [23] cooling a mechanical mode to the ground state was shown. Several articles [32, 33, 34] also reported measuring a squeezed state in a mechanical resonator. Also entanglement between two massive mechanical resonators [35] or the mechanical resonator and the electric field [36] could be demonstrated. Other experiments even coupled a superconducting qubit directly to the mechanical mode [37, 38]. While great accomplishment have been achieved, so far all experiments with massive mechanical modes lack coupling strength to bring the mechanical mode in a true non-Gaussian quantum state. For doing so, the single-photon coupling strength has to exceed the cavity as well as the mechanical decay rate, which is a highly demanding challenge. In all of those experiments the coupling is realised capacitively, which limits the coupling strengths to several hundred Hertz, fundamentally limited by the minimal distance between the capacitor plates and their area.

Recently, the rather new field of quantum acoustodynamics was established, where bulk or surface acoustic waves couple to microwave resonators [31, 39, 40]. One way to realise the coupling is by utilising the pieze-electro effect, to influence for instance the electrical field of a qubit, placed in the vicinity of the acoustic mode [41]. Indeed this approach shows very promising coupling rates and in [41] the authors could demonstrate the control of non-Gaussian Fock states in a bulk acoustic mode. In another very recent experiment the parity of a non-classical mechanical state could be measured using a superconducting qubit [42].

In an effort to boost the single-photon coupling strength in more conventional optomechanical devices, recently another type of experiments was developed, where the mechanical mode couples inductively to the microwave circuit [2, 3, 43]. Indeed this approach seems to allow for coupling strengths deep in the kHz regime. Naturally other problems arise for this type of experiment. The setup, which I developed together with my colleagues is also an approach relying on inductive coupling, based on a proposal [1]. My PhD work covered most of the steps from designing the microwave cavity, over putting the optomechanical setup together and characterising it to doing detailed measurements of the cooling backaction. This also resulted in three journal articles [44, 45, 46].

To summarise, the goal of my work was to develop an optomechanical system, where the coupling is realised magnetically. At the start of the thesis, such an experimental system did not exist. As discussed in the previous paragraphs, the motivation was to exceed coupling strengths possible with capacitively coupled systems, to eventually even exceed the linewidth of the cavity. On a time scale, of a Phd work, the goal was to show cooling of the system and in best case cooling the mechanical mode to the ground state.

1.3 Organisation of the thesis

The thesis is organised as follows. First I will give the theoretical background. I will start with introducing the theory describing an optomechanical systems and discuss backaction cooling. In the next chapter, I will discuss nonlinear cavities, as the cavity used in the thesis will be nonlinear. Bringing both fields together, we arrive at nonlinear optomechanics. The introduced theory was specifically developed for our system by Nicolas Diaz-Naufal (FU Berlin) and Anja Metelmann (KIT) and is required later on for describing the measurement results. In a final theory chapter, I will discuss and introduce superconducting resonators (cavities), their loss mechanisms and how to make them magnetic flux tunable. This is required to couple a magnetic mechanical mode to our cavity, and is realised by embedding a SQUID in the cavity.

In a next part, I will focus on the experimental platform. First, I will describe the rectangular waveguide, which is used as the environment for our cavities. Then I will describe the different cavities I measured, the mechanical system, as well as putting both main constitutes together. Briefly I will also discuss the cryostat, which houses the experiment.

In the Chapter 7, I will discuss the major measurement result. I will start with the characterisation of the cavities, first simple designs and later on the second generation of cavities, which are sensitive to magnetic fields. Subsequent I will discuss the characterisation of the full optomechanical setup. Afterwards I will describe the (cooling) backaction measurements done on the mechanical mode. First the proof of principle measurements and then measurements at single photon powers, which are possible due to our large coupling strength. Finally, I will focus on the main results of this work, which are backaction cooling measurements boosted by the intrinsic nonlinearity of the cavity. To my knowledge this is the first demonstration of this effect, which was predicted by theory more than a decade ago.

2 | Cavity optomechanics

This chapter gives a basic introduction to (linear) optomechanics, describing the interaction between a photonic cavity and a mechanical resonator. We will derive and discuss the Hamiltonian for such a system and investigate the optomechanical backaction from the cavity on the mechanical resonator, used for cooling the mechanical mode. Most considerations within this chapter are based on [21], other sources are explicitly noted.

2.1 Optomechanical system

2.1.1 Full Hamiltonian

A typical optomechanical system consists of a cavity mode coupled with a mechanical mode. The Hamiltonian of the uncoupled system is given by

$$\hat{H}_0 = \hbar\omega_c \hat{a}^\dagger \hat{a} + \hbar\omega_m \hat{b}^\dagger \hat{b} \tag{2.1}$$

with $\hbar$ being the reduced Planck constant, ω_c and ω_m the cavity and mechanical resonance frequency, $\hat{a}^\dagger$ ($\hat{a}$) and $\hat{b}^\dagger$ ($\hat{b}$) the creation (annihilation) operators for the cavity and mechanical mode.

Fig. 2.1a shows a sketch of a generic optomechanical system. One mirror of an optical cavity is supported on a spring and as it oscillates, it periodically changes the length of the optical cavity, leading to a periodic modulation of its resonance frequency. The cavity frequency thus depends on the position x of the mirror, which can be approximated to first order by

$$\omega_c(x) \approx \omega_c + x\frac{\partial \omega_c}{\partial x}. \tag{2.2}$$

Here, a positive x means that the cavity length increases. We can define $G := \frac{\partial \omega_c}{\partial x}$ [1] as the frequency shift per mechanical displacement.

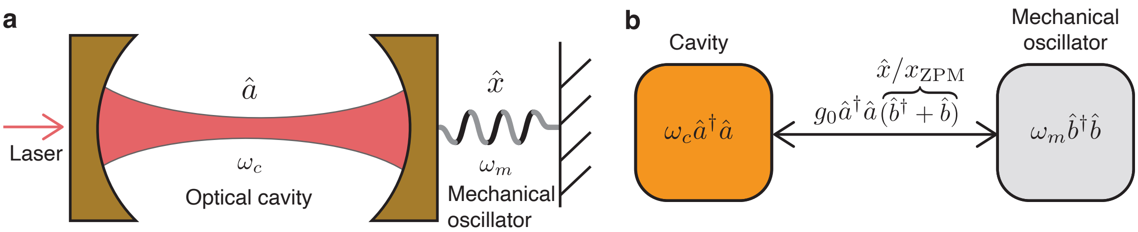

Figure 2.1: Optomechanical setup. **a.** Canonical optomechanical setup. The second mirror of an optical cavity can oscillate, which changes the length of the cavity, leading to a change of its resonance frequency. **b.** Symbolic representation of the setup. A mechanical oscillator is coupled with a coupling strength g_0 to a cavity.

[1] Note that in [21], $G := -\frac{\partial \omega_c}{\partial x}$ is used. To be consistent with Chapter 4, we will use a positive sign for this definition, which is also the case in [8, 4, 47], but does not change any of the conclusions.

To obtain the effect of a variable cavity frequency on the system, we can expand ω_c in the Hamiltonian, Eq. 2.1, which yields for the part describing the cavity

$$\hbar\omega_c\hat{a}^\dagger\hat{a} \approx \hbar(\omega_c + \hat{x}G)\hat{a}^\dagger\hat{a}. \tag{2.3}$$

Further, we can replace $\hat{x} = x_{\mathsf{ZPM}}(\hat{b} + \hat{b}^\dagger)$ with x_{ZPM} being the zero point motion of the mechanical mode given by

$$x_{\mathsf{ZPM}} = \sqrt{\frac{\hbar}{2m_{\mathsf{eff}}\omega_m}}, \tag{2.4}$$

where m_{eff} is the effective mass of the mechanical mode. The mechanical occupation can be given by the phonon occupation number, where the amplitude of the displacement relates as

$$\langle x_{\mathsf{amp}}\rangle = 2x_{\mathsf{ZPM}}\sqrt{n_m} \tag{2.5}$$

and n_m is the number of phonons in the mechanical mode. Doing this replacement leads to an interaction part of the Hamiltonian

$$\hat{H}_{\mathsf{int}} = \hbar g_0\hat{a}^\dagger\hat{a}(\hat{b} + \hat{b}^\dagger), \tag{2.6}$$

where we used that $g_0 := Gx_{\mathsf{ZPM}}$, expressing the coupling strength in terms of the zero point motion amplitude of the mechanical system. The full Hamiltonian is then given as $\hat{H} = \hat{H}_0 + \hat{H}_{\mathsf{int}}$. A symbolic representation of the system is shown in Fig. 2.1b.

2.1.2 Simplified interaction Hamiltonian

In the next step we simplify the system by doing two approximations. First, we assume to probe the system with a single tone at frequency ω_p, where it makes sense to switch into the rotating frame of this probe tone, introducing the detuning $\Delta = \omega_p - \omega_c$. Second, we can do a linearised approximation, where the field amplitude is separated in a coherent average amplitude $\langle\hat{a}\rangle = \bar{\alpha}$ and a fluctuation term, such that $\hat{a} = \bar{\alpha} + \delta\hat{a}$. This leads to a Hamiltonian of the following form, where we omitted constant terms

$$\hat{H} = -\hbar\Delta\delta\hat{a}^\dagger\delta\hat{a} + \hbar\omega_m\hat{b}^\dagger\hat{b} + \hat{H}_{\mathsf{int}}. \tag{2.7}$$

Terms of the order $\bar{\alpha}\delta\hat{a}$ are absorbed in the drive. The interaction part, $\hat{H}_{\mathsf{int}}$, is then given by

$$\hat{H}_{\mathsf{int}} = \hbar g_0(\bar{\alpha} + \delta\hat{a})^\dagger(\bar{\alpha} + \delta\hat{a})(\hat{b} + \hat{b}^\dagger). \tag{2.8}$$

This leads to three terms, where the $\bar{\alpha}^2$ term can be absorbed in a constant shift of the displacement x. The term containing $\delta\hat{a}^\dagger\delta\hat{a}$ can be neglected as it is comparably small, which leaves

$$\hat{H}_{\mathsf{int}} \approx \hbar g_0(\bar{\alpha}^*\delta\hat{a} + \bar{\alpha}\delta\hat{a}^\dagger)(\hat{b} + \hat{b}^\dagger). \tag{2.9}$$

Further, we can introduce the photon number of the cavity, n_c, using that $|\bar{\alpha}| = \sqrt{\bar{n}_c}$ and arrive at a linearised interaction term

$$\hat{H}^{\mathsf{lin}}_{\mathsf{int}} = \hbar g_0\sqrt{\bar{n}_c}(\delta\hat{a} + \delta\hat{a}^\dagger)(\hat{b} + \hat{b}^\dagger). \tag{2.10}$$

Here, we identify, that the coupling strength is enhanced by the photon number and introduce the photon enhanced coupling g as

$$g \equiv g_0\sqrt{\bar{n}_c}. \tag{2.11}$$

2.1.3 Special cases of the interaction Hamiltonian

To get an intuitive understanding of the Hamiltonian, it makes sense to consider $\hat{H}_{\text{int}}^{\text{lin}}$ for three different detunings. Here, we will only consider terms which are resonant due to energy conservation reasons, where this distinction makes most sense in the resolved sideband regime, where $\kappa \ll \omega_m$, with κ being the decay rate of the cavity. In contrast to that, we speak of the unresolved sideband regime in case $\omega_m \ll \kappa$.

- $\Delta \approx -\omega_m$: As we are in the rotating frame, there are two harmonic oscillators with nearly degenerate frequency and we obtain

$$\hat{H}_{\text{int}}(\Delta \approx -\omega_m) \approx \hbar g(\delta\hat{a}^\dagger \hat{b} + \delta\hat{a}\hat{b}^\dagger). \tag{2.12}$$

  There are no terms where two quanta are created/destroyed, as they are nonresonant. This is the relevant interaction for cooling/damping, which is also known as beam-splitter interaction. As the probe frequency is below the cavity frequency, this case is considered as being red detuned.

- $\Delta \approx +\omega_m$:

$$\hat{H}_{\text{int}}(\Delta \approx +\omega_m) \approx \hbar g(\delta\hat{a}^\dagger \hat{b}^\dagger + \delta\hat{a}\hat{b}) \tag{2.13}$$

  Considering resonant terms, there are only processes, where two quanta are created/destroyed. This interaction is the so-called two-mode squeezer. Amplification occurs in both modes, which are also highly correlated, and we expect to observe a growth of the population in the mechanical, due to the fact that it is coherently driven. As the probe frequency is above the cavity frequency, this is considered as of being blue detuned.

- $\Delta \approx 0$:

$$\hat{H}_{\text{int}}(\Delta \approx 0) \approx \hbar g(\delta\hat{a} + \delta\hat{a}^\dagger)(\hat{b} + \hat{b}^\dagger) \tag{2.14}$$

  This can be interpreted as the position of the mechanical model ($(\hat{b}+\hat{b}^\dagger) \propto \hat{x}$) shifting the cavity phase. Such a detuning can be used for detecting the mechanical mode without cooling or amplification (heating) backaction.

2.2 Optomechanical backaction cooling

The thermal occupation of a resonator following bosonic occupation statistics is given by the Bose-Einstein distribution

$$\bar{n}_m^{\text{th}} = \frac{1}{e^{\hbar\omega_m/k_b T} - 1} \simeq \frac{k_b T}{\hbar\omega_m}. \tag{2.15}$$

Here, k_b is Boltzmann constant and T bath temperature. As mechanical frequencies are usually a few 100 kHz to MHz and working temperatures are typically from around 100 mK for microwave setups up to room temperature for optical setups, the mechanical mode is in a highly excited thermal state and requires further cooling to investigate quantum phenomena [23, 48, 49]. There are different ways for cooling mechanical objects. They can be cooled, by detecting the position of the mechanical resonator and directly cool them by applying feedback. This was for instance proposed in [50], and shown several years ago [51], but also more recently e.g. [52] and even cooling to the ground state has been shown [22]. Another way of cooling the mechanical mode is to directly utilise the cavity as briefly introduced in Section 2.1.3 and theoretically investigated in [53, 54]. There are many realisations of this cooling scheme, where ground state cooling was shown several years ago, e.g. in [23, 24]. In the experiment, we will also use the cavity to cool the mechanical resonator and in the following, we will review why and how this works. Afterwards we will also discuss the limits of this scheme.

2.2.1 Optomechanical damping and frequency shift

First, we will investigate backaction of the cavity on the mechanical system (mode) in terms of mechanical frequency shift and change of linewidth, which will lead to cooling and amplification (heating), discussed afterwards. To see the dynamics, we use the equations of motion for our system, where it is sufficient to treat the classical versions. To do so, we use $\alpha(t) = \langle \hat{a}(t) \rangle$, where we do not consider the time average at first in contrast to Sec. 2.1.2, and $x(t) = \langle \hat{x}(t) \rangle$, where we neglect fluctuations. We treat the mechanical system in terms of its position, written as $x(t) = 2x_{\mathsf{ZPM}}\mathsf{Re}(\langle \hat{b}(t) \rangle)$. With this, the following equations of motions are obtained

$$\dot{\alpha} = -\frac{\kappa}{2}\alpha + i(\Delta - Gx)\alpha - \sqrt{\kappa}\alpha_{\mathsf{in}} \tag{2.16}$$

and

$$m_{\mathsf{eff}}\ddot{x} = -m_{\mathsf{eff}}\omega_m^2 x - m_{\mathsf{eff}}\Gamma_m \dot{x} + \hbar G|\alpha|^2, \tag{2.17}$$

where Γ_m is the decay rate of the mechanical resonator. Similar to what was done for the derivation of the interaction Hamiltonian in Section 2.1.2, we now do a linearised approximation for the classical equations, with $\alpha(t) = \bar{\alpha} + \delta\alpha$ and only keep linear terms to obtain

$$\delta\dot{\alpha} = (i\Delta - \frac{\kappa}{2})\delta\alpha - iG\bar{\alpha}x \tag{2.18}$$

and

$$m_{\mathsf{eff}}\ddot{x} = -m_{\mathsf{eff}}\omega_m^2 x - m_{\mathsf{eff}}\Gamma_m \dot{x} - \hbar G(\bar{\alpha}^*\delta\alpha + \bar{\alpha}\delta\alpha^*). \tag{2.19}$$

Here, we again neglected terms of the order $(\delta\alpha)^2$, as they are comparably small.

In the next step, we do a Fourier transformation, with $\hat{a}[\omega] = \int_{-\infty}^{\infty} dt e^{i\omega t}\hat{a}(t)$, to get the above equations in frequency space

$$-i\omega\delta\alpha[\omega] = \left(i\Delta - \frac{\kappa}{2}\right)\delta\alpha[\omega] - iG\bar{\alpha}x[\omega] \tag{2.20}$$

and

$$-m_{\mathsf{eff}}\omega^2 x[\omega] = -m_{\mathsf{eff}}\omega_m^2 x[\omega] + i\omega m_{\mathsf{eff}}\Gamma_m x[\omega] - \hbar G(\bar{\alpha}^*\delta\alpha[\omega] + \bar{\alpha}\delta\alpha^*[\omega]). \tag{2.21}$$

With Eqs. 2.20 and 2.21 describing the system, we can investigate the effect from the cavity on the mechanical resonator. This is done by considering the influence on the susceptibility of the mechanical resonator with its bare susceptibility given by

$$\chi_m^{-1}(\omega) = m_{\mathsf{eff}}[(\omega_m^2 - \omega^2) - i\Gamma_m\omega]. \tag{2.22}$$

The interaction with the cavity can be seen as an additional force and it is convenient to consider this using a modified susceptibility

$$\chi_{m,\mathsf{eff}}^{-1}(\omega) = \chi_m^{-1}(\omega) + \Sigma(\omega). \tag{2.23}$$

In order to find the effect of backaction from the cavity on the mechanical resonator, we use the equations of motion 2.20 and 2.21, where we substitute $\delta\alpha[\omega]$ in Eq. 2.21. With this we find

$$\Sigma(\omega) = 2m_{\mathsf{eff}}\omega_m g^2 \left[\frac{1}{(\Delta + \omega) + i\kappa/2} + \frac{1}{(\Delta - \omega) - i\kappa/2}\right], \tag{2.24}$$

which appears as an additional force term in the equation of motion, where we used that $|\alpha|^2 = \bar{n}_c$. Now we can impose that the susceptibility should have the form of $\Sigma(\omega) := m_{\mathsf{eff}}\omega[2\delta\omega_m(\omega) - i\Gamma_{\mathsf{OM}}(\omega)]$, which is valid in the high-Q approximation ($\omega_m \gg \Gamma_m$). Extracting the real and imaginary part from Eq. 2.24 we obtain the expressions for the optical frequency shift and change of linewidth due to backaction from the cavity on the mechanics

$$\delta\omega_m(\omega) = g^2 \frac{\omega_m}{\omega} \left[\frac{\Delta + \omega}{(\Delta + \omega)^2 + \kappa^2/4} + \frac{\Delta - \omega}{(\Delta - \omega)^2 + \kappa^2/4} \right] \tag{2.25}$$

and

$$\Gamma_{\mathsf{OM}}(\omega) = g^2 \frac{\omega_m}{\omega} \left[\frac{\kappa}{(\Delta + \omega)^2 + \kappa^2/4} - \frac{\kappa}{(\Delta - \omega)^2 + \kappa^2/4} \right]. \tag{2.26}$$

If we further assume a weak enough drive, such that $\kappa \gg g$, it is sufficient to evaluate Eqs. 2.25 and 2.26 at ω_m and obtain explicit solutions for the optical spring effect and damping.

- Optical spring effect:

$$\delta\omega(\omega_m) = g^2 \left[\frac{\Delta + \omega_m}{(\Delta + \omega_m)^2 + \kappa^2/4} + \frac{\Delta - \omega_m}{(\Delta - \omega_m)^2 + \kappa^2/4} \right] \tag{2.27}$$

  For a red detuned probe tone we expect a lowering of the mechanical frequency, thus a spring softening and for a blue detuned a spring hardening, leading to an increase of the mechanical frequency. This is the origin of the spring effect. Remarkably, the response is very different whether being in the sideband resolved or unresolved regime (Fig. 2.3b). Working in the resolved sideband regime, the frequency shift completely vanishes for a detuning of $\Delta = \pm\omega_m$.

- Optomechanical damping rate:

$$\Gamma_{\mathsf{OM}}(\omega_m) = g^2 \left[\frac{\kappa}{(\Delta + \omega_m)^2 + \kappa^2/4} - \frac{\kappa}{(\Delta - \omega_m)^2 + \kappa^2/4} \right] \tag{2.28}$$

  with the full damping rate being

$$\Gamma_{\mathsf{eff}} = \Gamma_m + \Gamma_{\mathsf{OM}}. \tag{2.29}$$

  The change of damping leads to cooling or amplification (heating) of the mechanical mode, as it can be negative or positive. For a red detuned probe tone we expect a broadening of the linewidth, thus additional damping (cooling) and for a blue detuned probe tone less damping (amplification). If Γ_{eff} is below zero, the mechanical mode enters the regime of dynamical instability. This can be also understood as mechanical lasing, as an exponential growth of the oscillation occurs until a steady state is reached [21, 55, 56].

Fig. 2.2 shows the optomechanical induced damping and frequency shift for a system in the unresolved sideband regime with increasing photon number. As the backaction increases, the damping and frequency shift increase, but the detuning for highest backaction remains the same. In Fig. 2.3 the same is plotted, but for a changing sideband resolution, by decreasing the cavity linewidth κ for a fixed photon number. As the system advances towards the sideband resolved regime, not only does the strength of the backaction increase, but also the detuning of most backaction changes from $\Delta = \pm\kappa/2$ in the unresolved to $\Delta = \pm\omega_m$ in the resolved regime. In the frequency shift, Fig. 2.3b, there is also a significant change of the behaviour, as in the unresolved sideband regime the highest frequency shift occurs at highest (anti)damping. In contrast to this, in the resolved regime, there is zero frequency shift at highest (anti)damping, with the highest frequency shift occurring in the vicinity of those zero crossings. In the next part we will derive the direct impact of the cavity on the occupation number of the mechanical system.

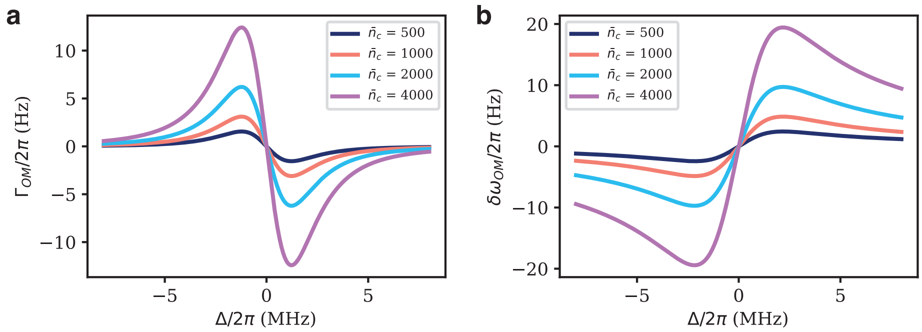

Figure 2.2: Change of **a.** mechanical linewidth and **b.** frequency due to optomechanical backaction for different cavity population. The other parameters considered here are: $g_0/2\pi = 100\,\text{Hz}, \omega_m/2\pi = 500\,\text{kHz}, \kappa/2\pi = 4\,\text{MHz}$, putting the setup in the unresolved sideband regime ($\kappa \gg \omega_m$).

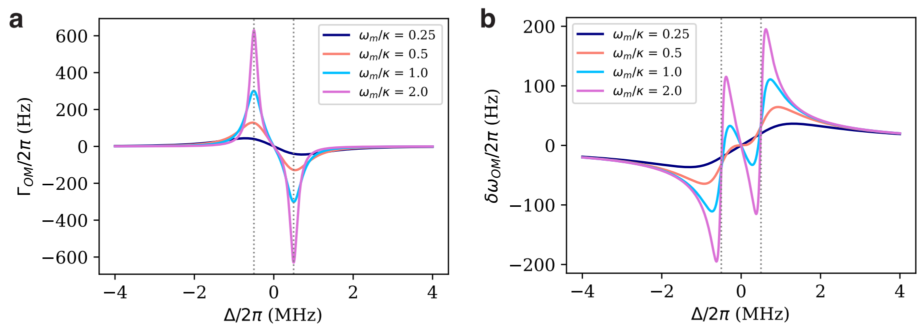

Figure 2.3: Changing sideband resolution by decreasing κ and using a cavity photon number of $\bar{n}_c = 4000$, with otherwise identical parameters as Fig. 2.2. **a.** Change of mechanical linewidth versus detuning for different cavity photon numbers. Entering the resolved sideband regime we see distinct features at $\Delta = \pm\omega_m$ (dotted lines), where the highest (anti)damping backaction happens. For the unresolved sideband regime this happens at $\Delta = \pm\kappa/2$. **b.** Mechanical frequency shift against detunings. At the detuning of most (anti)damping the frequency shift is exactly zero for the resolved sideband case, which is clearly different from the unresolved regime.

2.2.2 Phonon occupation number under backaction

The effect of cooling can be understood in two different ways. On one hand, photons in the cavity exert a force on the mechanical resonator, however with a time lag due to a finite cavity lifetime. The resulting force is non conservative and can lead to cooling or heating depending on the detuning [57], Fig. 2.4a. This illustrative picture gives an idea about the origin of the backaction, however it is only applicable in the sideband unresolved regime. On the other hand, the effect of backaction can be also considered within the scattering picture, Fig. 2.4b. If we use a red detuned probe tone, photons can be scattered to the cavity frequency. For this they need additional energy, which is taken from a mechanical phonon, thus the energy of one phonon is removed from the mechanical mode (= cooling). Using a blue detuned probe tone, the opposite effect (adding a phonon to the mechanical mode) may happen and amplification (heating) of the mechanical mode occurs. The rate of this processes depends on the scattering rates, known as the Stokes (heating, Γ^+) and anti-Stokes (cooling, Γ^-) rates [54, 58].

Now we want to quantitatively investigate the influence on the phonon number. Going to strong cooling and thus low occupation numbers, quantum noise (photon shot noise) will limit the cooling strength [21, 56]. In fact, the rate lowering the phonon occupation by one ($\Gamma_{n_m \to n_m - 1} = n_m \Gamma^-$) and the one increasing the occupation ($\Gamma_{n_m \to n_m + 1} = (n_m + 1)\Gamma^+$) are competing, giving the cooling rate

$$\Gamma_{\text{OM}} = \Gamma^- - \Gamma^+. \tag{2.30}$$

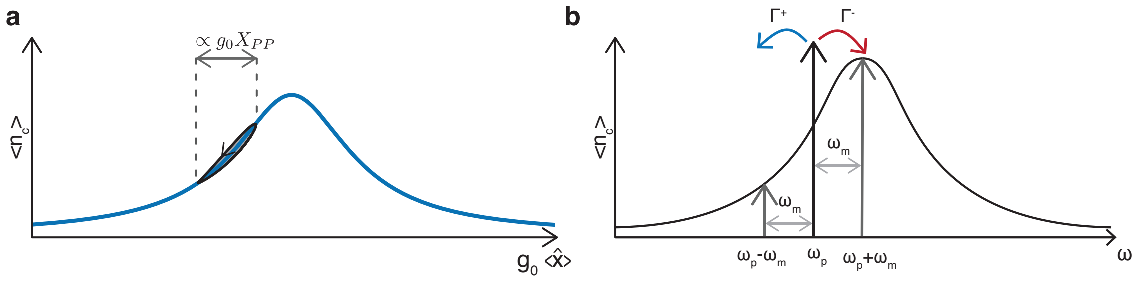

Figure 2.4: Sketch of optomechanical cooling. **a.** Time-lag picture, where the cavity photons exert a non-conservative force on the mechanical mode leading to cooling. Here, we consider the response of the cavity to a fixed frequency probe tone, while the cavity frequency itself is changed due to the optomechanical interaction ($g_0\hat{x}$). The enclosed area depicts the cooling work done being ideally red detuned, with X_{pp} being the peak-to-peak amplitude of the mechanical resonator. This figure is based on realistic system parameters. The data for this figure was provided by a colleague of mine, Christian Schneider. More information on the calculation can be found in [46]. **b.** Scattering picture. Photons are scattered from the pump at ω_p to higher (lower) frequency due to the optomechanical interaction leading to cooling (heating) of the mechanical mode. The rates Γ^- (Γ^+) determine if the mechanical mode is cooled or heated, see text for details.

This has to be taken into account for the final occupation number, given by

$$\bar{n}_m = \frac{\Gamma^+ + \bar{n}_m^{\mathsf{th}}\Gamma_m}{\Gamma_m + \Gamma_{\mathsf{OM}}}, \tag{2.31}$$

where $\bar{n}_m^{\mathsf{th}}$ is the occupation in the thermal equilibrium.

To investigate the limits, we can set $\Gamma_m = 0$ in Eq. 2.31, which is reasonable, if the other rates are dominating and can be achieved by using very high photon number or coupling. Using this, we obtain

$$\bar{n}_m^{\mathsf{min}} = \frac{\Gamma^+}{\Gamma^- - \Gamma^+}, \tag{2.32}$$

which leads to a nonzero occupation.

In order to get a quantitative result, the rates, $\Gamma^\pm$, have to be determined. This derivation can be done using Fermi's golden rule. The idea is, to consider the fluctuations of the force from the cavity photons an the mechanical resonator, where additional details are given in [21, 54]. To obtain the rates, it is sufficient to calculate the photon number noise spectrum

$$S_{\mathsf{NN}}(\omega) = \int_{-\infty}^{\infty} dt e^{i\omega t}\langle(\hat{a}^\dagger\hat{a})(t)(\hat{a}^\dagger\hat{a})(0)\rangle = \bar{n}_c\frac{\kappa}{\kappa^2/4 + (\Delta+\omega)^2}. \tag{2.33}$$

The cooling/amplification rates arise from differences in this spectrum at the mechanical frequencies and are given by

$$\Gamma^\pm = g_0^2 S_{\mathsf{NN}}(\omega = \mp\omega_m) = \frac{g^2\kappa}{\kappa^2/4 + (\Delta \mp \omega_m)^2}. \tag{2.34}$$

Fig. 2.5 shows the mechanical occupation for different cavity photon numbers (a) and sideband resolution (b) against detuning. As already seen for the damping and frequency change (Figs. 2.2, 2.3), the backaction increases when either increasing photon number or sideband resolution, where in the latter case also the line shape changes.

To determine the limit on the occupation number, we can simply use Eq. 2.32, which yields

$$\bar{n}_m^{\mathsf{min}}(\Delta) = \left(\frac{\Gamma^-}{\Gamma^+} - 1\right)^{-1} = \left(\frac{\kappa^2/4 + (\Delta+\omega_m)^2}{\kappa^2/4 + (\Delta-\omega_m)^2} - 1\right)^{-1}. \tag{2.35}$$

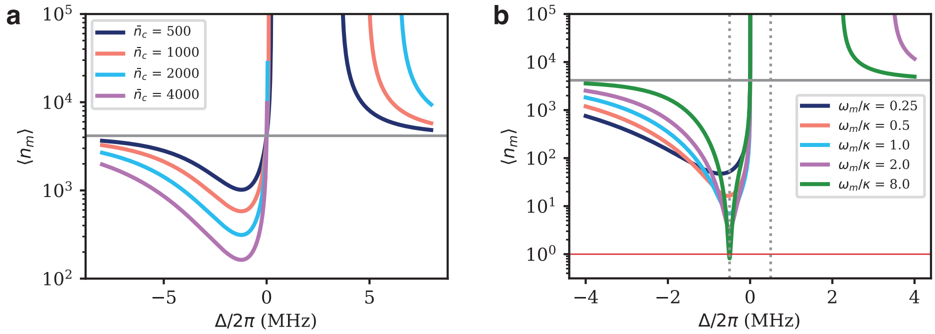

Figure 2.5: Change of mechanical phonon number against detuning, using the following parameters: $g_0/2\pi = 100\,\text{Hz}, \omega_m/2\pi = 500\,\text{kHz}, \Gamma_m/2\pi = 0.5\,\text{Hz}, T = 0.1\,\text{K}$. **a.** Phonon number against detuning for different cavity photon number. We use $\kappa/2\pi = 4\,\text{MHz}$ as in Fig. 2.2. We see the decreasing phonon number for increasing drive strength, where the minimum is always found at the same detuning. We omit phonon numbers in the mechanical instability, where $\Gamma_{\text{eff}} < 0$. The grey solid line is the thermal phonon population. **b.** Phonon number for a fixed cavity photon number of $\bar{n}_c = 4000$ photons, but with a changing sideband resolution by decreasing κ. We see that the cooling strengths increases with increasing sideband resolution and also the detuning for best cooling shifts to $\Delta = -\omega_m$, as already discussed in Fig. 2.3. The grey dotted lines are at $\Delta = \pm\omega_m$, the red line marks the single photon line.

The optimal detuning for lowest phonon occupation is given by [30]

$$\Delta_{\text{opt}} = -\frac{1}{2}\sqrt{\kappa^2 + 4\omega_m^2}. \tag{2.36}$$

To investigate the limits for optimal detuning, it makes sense to distinguish between the resolved and unresolved sideband regime. In the sideband resolved regime ($\omega_m \gg \kappa$), we obtain a minimum phonon occupation of

$$\bar{n}_m^{\text{min}} = \left(\frac{\kappa}{4\omega_m}\right)^2 \ll 1 \tag{2.37}$$

at an optimal detuning of $\Delta = -\omega_m$. This allows cooling to the ground state. In contrast to this, in the sideband unresolved regime, ($\kappa \gg \omega_m$), we obtain

$$\bar{n}_m^{\text{min}} = \frac{\kappa}{4\omega_m} \gg 1, \tag{2.38}$$

which does not allow cooling to the ground state. Also the point of optimal detuning for best cooling changes to $\Delta = -\kappa/2$. We do not discuss further limiting effects, like a residual cavity occupation on the final phonon occupation. The best cooling also occurs at a certain enhanced coupling strength ($g = g_0\bar{n}_c$) [59], where the anti-Stokes and Stokes rates are balanced, such that the lowest phonon occupation is reached. However, depending on the experimental constraints, it might be not possible to reach a high enough coupling, due to a limit in pump strength.

2.3 Cooperativity

Further, we should briefly discuss cooperativity, which is an important quantity in cavity optomechanics. It is defined as

$$C := \frac{4\sqrt{\bar{n}_c}g_0^2}{\kappa\Gamma_m} \tag{2.39}$$

and compares the photon enhanced coupling rate to the decay rates of the cavity and the mechanical resonator. If it exceeds unity, backaction is sufficient to heat/cool the mechanical mode.

The single photon cooperativity is then given by

$$C_0 = \frac{4g_0^2}{\kappa\Gamma_m} \tag{2.40}$$

and gives a measure for the interaction strength with only a single photon populating the cavity. If it exceeds one it allows to cool with only a single photon and also quantifies the strength of optomechanical induced transparency [60].

Further, the quantum cooperativity is given by

$$C_{\mathsf{qu}} = C/\bar{n}_m^{\mathsf{th}}. \tag{2.41}$$

It compares the cooperativity with the thermal population. If it exceeds unity, the state transfer between the cavity and the mechanical mode exceeds the mechanical decoherence rate.

3 Nonlinear cavities

In this part we will focus on nonlinear cavities. First, we will consider a Hamiltonian formulation, discuss strategies for solving the system and develop expressions for the gain, as nonlinear cavities are used as parametric amplifiers. As an alternative, we will analyse the Duffing model, which is a completely different, yet equivalent, approach for solving a nonlinear system. This part closely follows [61, 62], other sources are explicitly mentioned.

3.1 Nonlinear cavity in the Hamiltonian formulation

The Hamiltonian describing a Kerr nonlinear system is given by

$$H = \hbar\omega_c \hat{a}^\dagger \hat{a} + \hbar\frac{\mathcal{K}}{12}(\hat{a} + \hat{a}^\dagger)^4 \simeq \hbar\omega_c \hat{a}^\dagger \hat{a} + \hbar\frac{\mathcal{K}}{2}\hat{a}^\dagger \hat{a}^\dagger \hat{a}\hat{a}. \tag{3.1}$$

Here, $\mathcal{K}$ is the so-called Kerr constant, quantifying the strength of the nonlinearity, which is typically negative in systems we are discussing. Further, $\hat{a}^\dagger$ and $\hat{a}$ are the creation and annihilation operators acting on a cavity having a resonance frequency ω_c. In this simplification, we ignore fast rotating terms after the rotating wave equation. We will see in Chapter 5.5, that this is the Hamiltonian describing a microwave cavity like ours.

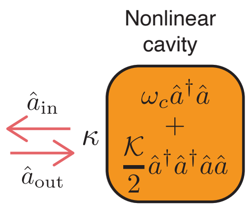

Figure 3.1: Symbolic representation of the considered setup, a nonlinear cavity coupled to a port with a rate κ.

Using input output theory [63] we find the following equation of motion

$$\frac{d\hat{a}}{dt} = -i(\omega_c + \frac{\kappa}{2})\hat{a} - i\mathcal{K}\hat{a}^\dagger \hat{a}\hat{a} - \sqrt{\kappa}\hat{a}_{\mathrm{in}}, \tag{3.2}$$

where κ is the coupling rate to an external port. First we want to solve this for a single pump tone, to understand the dynamics of a such a nonlinear system. Thereafter, we will linearise around an additional weak probe tone, to develop expressions for the gain.

3.1.1 Response to a single pump tone

For now, we will solve the system for a strong classical pump tone, where we proceed as in the previous chapter by using $\alpha(t) = \langle \hat{a}(t) \rangle$. In this chapter it is useful to also consider the ansatz, as this will become very relevant when deriving expressions for the gain in Chapter 3.1.2. We use an ansatz of the following form

$$\begin{aligned} \alpha_{\mathrm{in}} &= \bar{\alpha}_{\mathrm{in}} e^{-i(\omega_p t + \psi)} \\ \alpha &= \bar{\alpha} e^{-i(\omega_p t + \phi)}, \end{aligned} \tag{3.3}$$

where ψ and ϕ are the respective phases of the input and the internal cavity field and $\bar{\alpha}_{\text{in}}$ and $\bar{\alpha}$ are their amplitudes. Before solving the system itself, it is useful to move into the rotating frame, with $\Delta = \omega_p - \omega_c$ being the detuning between pump and cavity frequency. With this Eq. 3.2 becomes

$$\dot{\alpha} = (i\Delta - \frac{\kappa}{2})\alpha - i\mathcal{K}|\alpha|^2\alpha - \sqrt{\kappa}\alpha_{\text{in}}. \tag{3.4}$$

It is then straight forward to obtain a steady state solution using our ansatz

$$-(i\Delta + \frac{\kappa}{2})\bar{\alpha} + i\mathcal{K}\bar{\alpha}^3 = -\sqrt{\kappa}\bar{\alpha}_{\text{in}}e^{i(\phi-\psi)}. \tag{3.5}$$

To extract the magnitude of the response, we multiply this solution with its complex conjugate. Further we can identify $\bar{n}_c = |\bar{\alpha}|^2$ as the cavity photon number, already known from Chapter 2, and $\bar{n}_{\text{in}} = |\bar{\alpha}_{\text{in}}|^2$, to be the input photon rate. With this we arrive at

$$\bar{n}_c\left[(\mathcal{K}\bar{n}_c - \Delta)^2 + \left(\frac{\kappa}{2}\right)^2\right] = \kappa\bar{n}_{\text{in}}. \tag{3.6}$$

In addition, the phase between the pump and the cavity field is given by

$$\tan(\phi - \psi) = -\frac{\kappa/2}{-\Delta + \mathcal{K}\bar{n}_c}. \tag{3.7}$$

Now, we can plot the response of the system for different values of the input photon number, Fig. 3.2. We see that the response shifts to lower frequencies, as we choose a negative value for $\mathcal{K}$, which will be also the case for the experiment. Further, we see that the response gets increasingly steep on the lower frequency side. Beyond a certain (critical) input drive strength, two metastable solutions appear in a certain range of frequencies (bistability).

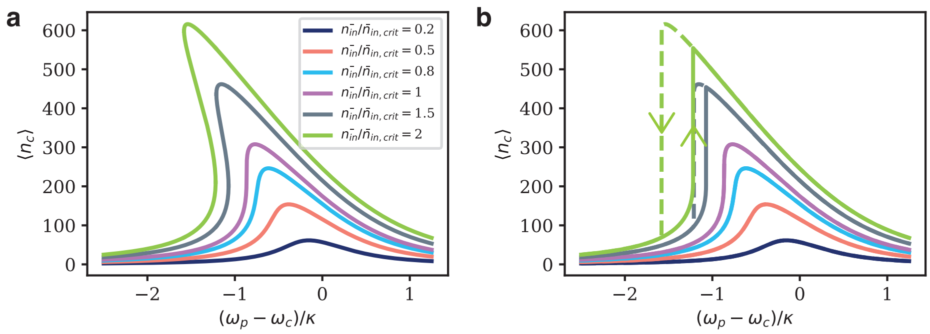

Figure 3.2: Response of a nonlinear cavity for increasing drive strength compared to the critical drive. **a.** Response of the nonlinear system. The maximum response shifts to lower frequencies and gets increasingly steep, until three solutions appear in a certain range of detunings. The lowest and highest solutions are metastable, while the intermediate one cannot be reached experimentally, as it is unstable. **b.** Only the low and the high photon number state can be measured in the experiment, where it depends on the sweep direction (arrows), whether the low or the high photon number state is reached. Same drive strength as in (a).

Further, we can evaluate the parameters for the critical point, where the cavity response is infinitely steep, just before bistability. When we arrive at this point, the cavity photon number diverges with respect to the input photon number or, which can be differently written as $d\bar{n}_{\text{in}}/d\bar{n}_c = 0$. Additionally, to make sure that we are exactly at bistability and not above, the cavity response must be continuous, meaning that $d\bar{n}_{\text{in}}^2/d\bar{n}_c^2 = 0$. Following Eq. 3.6 this results in

$$\begin{aligned} (-\Delta + \mathcal{K}\bar{n}_c)^2 + \left(\frac{\kappa}{2}\right)^2 - 2\mathcal{K}(-\Delta + \mathcal{K}\bar{n}_c)\bar{n}_c = 0 \\ 2\mathcal{K}^2\bar{n}_c - 4\mathcal{K}(-\Delta + \mathcal{K}\bar{n}_c) = 0. \end{aligned} \tag{3.8}$$

With those conditions, we can calculate the critical parameters to reach the onset of bistability

$$\begin{aligned} \omega_{p,crit} - \omega_c = \Delta_{crit} &= \frac{\sqrt{3}}{2}\frac{\mathcal{K}}{|\mathcal{K}|}\kappa \\ \bar{n}_{c,crit} &= \frac{\sqrt{3}\kappa}{3|\mathcal{K}|} \\ \bar{n}_{\text{in,crit}} &= \frac{1}{3\sqrt{3}}\frac{\kappa^2}{|\mathcal{K}|}. \end{aligned} \tag{3.9}$$

When pumping our cavity close to bistability, amplification occurs when adding a weak probe tone. We will investigate this in the following section.

3.1.2 Adding a weak probe tone to measure gain

Here, we will discuss how the response changes when adding a weak probe tone to our cavity, which will be amplified under certain driving conditions. As this probe tone is weak, we can linearise the solution derived for a single strong pump given by α, (Chapter 3.1.1) and add an additional signal $\hat{c}$. With this our previous ansatz, Eq. 3.3, becomes

$$\begin{aligned} \hat{a}_{\text{in,out}} &= \bar{\alpha}_{\text{in,out}} e^{-i(\omega_p t + \psi)} + \hat{c}_{\text{in,out}}(t) e^{-i\omega_p t} \\ \hat{a} &= \bar{\alpha} e^{-i(\omega_p t + \phi)} + \hat{c}(t) e^{-i\omega_p t}. \end{aligned} \tag{3.10}$$

It is also useful to include the output field already here, as it will be relevant for deriving expressions for the gain.

It is sufficient to keep linear terms in $\hat{c}$ and $\hat{c}_{\text{in,out}}$ as the signal is much weaker than the pump. Moving again in the rotating frame of the pump and using the photon number $\bar{n}_c$ known from the classical solution, Eq. 3.6, we obtain from Eq. 3.2

$$\frac{d}{dt}\hat{c} = \left(i\Delta - \frac{\kappa}{2}\right)\hat{c} - 2i\mathcal{K}\bar{n}_c\hat{c} - i\mathcal{K}\bar{n}_c e^{i2\phi}\hat{c}^\dagger - \sqrt{\kappa}\hat{c}_{\text{in}}. \tag{3.11}$$

For deriving expressions for the gain, it is useful to make a Fourier transformation and move into frequency space

$$\left(-\Delta - \Delta_s - i\frac{\kappa}{2} + 2\mathcal{K}\bar{n}_c\right)\hat{c}[\Delta_s] + \mathcal{K}\bar{n}_c e^{i2\phi}\hat{c}^\dagger[-\Delta_s] = \sqrt{\kappa}\hat{c}_{\text{in}}. \tag{3.12}$$

Here, it makes sense to introduce a second detuning between the signal and the pump $\Delta_s = \omega_s - \omega_p$ where ω_s is the frequency of the signal tone.

At this point, it is further convenient to introduce the following abbreviations

$$\begin{aligned} \tilde{\Delta} &= \Delta - 2\mathcal{K}\bar{n}_c \\ \Lambda &= \mathcal{K}\bar{n}_c e^{i2\phi} = \mathcal{K}\bar{n}_c e^{i\phi_\Lambda} \\ \lambda_\pm &= \frac{\kappa}{2} \pm \sqrt{\mathcal{K}^2\bar{n}_c^2 - (-\Delta + 2\mathcal{K}\bar{n}_c)^2}, \end{aligned} \tag{3.13}$$

where $\tilde{\Delta}$ can be seen as a modified detuning and Λ as the single-mode squeezing strength. Also ϕ_Λ is introduced as $\phi_\Lambda = 2\phi$. With those simplifications, Eq. 3.12 becomes

$$-i\Delta_s\hat{c}[\Delta_s] + (-i\tilde{\Delta} + \frac{\kappa}{2})\hat{c}[\Delta_s] + i\Lambda\hat{c}^\dagger[\Delta_s] = \sqrt{\kappa}\hat{c}_{\text{in}}. \tag{3.14}$$

Now we can solve for the internal fields in terms of the input fields, details on this calculation are given in [62], and obtain

$$\hat{c}[\Delta_s] = \frac{i\sqrt{\kappa}\left(\hat{c}_{\text{in}}[\Delta_s]((i\tilde{\Delta} + \frac{\kappa}{2}) - i\Delta_s) - i\Lambda\hat{c}_{\text{in}}^\dagger[-\Delta_s]\right)}{(-i\Delta_s + \lambda_-)(-i\Delta_s + \lambda_+)}. \tag{3.15}$$

We then use that $\hat{c}_{\text{out}}(t) + \hat{c}_{\text{in}}(t) = -i\sqrt{\kappa}\hat{c}$ to obtain the output field

$$\begin{aligned}\hat{c}_{\text{out}}[\Delta_s] = &\left(-1 + \frac{\kappa(-i\Delta_s + (i\tilde{\Delta} + \frac{\kappa}{2}))}{(-i\Delta_s + \lambda_-)(-i\Delta_s + \lambda_+)}\right)\hat{c}_{\text{in}}[\Delta_s] \\ &+ \frac{i\kappa\Lambda}{(-i\Delta_s + \lambda_-)(-i\Delta_s + \lambda_+)}\hat{c}^\dagger_{\text{in}}[-\Delta_s] \\ &= g_s(\Delta_s)\hat{a}_{\text{in}}[\Delta_s] + g_i(\Delta_s)\hat{a}^\dagger_{\text{in}}[-\Delta_s].\end{aligned} \tag{3.16}$$

where g_s and g_i were introduced, which will lead to expressions for the gain. Eq. 3.16 describes the output field $\hat{c}_{\text{out}}$ at a signal detuning, Δ_s, which is a combination from the input fields at $\pm\Delta_s$. Components at Δ_s will lead to the signal gain and components at $-\Delta_s$ to the idler gain. Further, g_s and g_i satisfy the following relations, which is also a consequence from commutator relations [64]

$$\begin{aligned}|g_s(\Delta_s)|^2 - |g_i(\Delta_s)|^2 = 1 \\ g_s(\Delta_s)g_i(-\Delta_s) = g_s(-\Delta_s)g_i(\Delta_s).\end{aligned} \tag{3.17}$$

From this relations we see several remarkable aspects. In case we have no gain, $|g_s(\Delta_s)|^2 = 1$. There is no influence from the idler as $|g_i(\Delta_s)|^2 = 0$. In case of large gain, $|g_s(\Delta_s)|^2 \ll 1$, it follows that $|g_s(\Delta_s)|^2 \simeq |g_i(\Delta_s)|^2$. We can further see that for a signal tone at Δ_s, also an idler is created at $-\Delta_s$.

The gain itself is then calculated from Eq. 3.16 by comparing the output to the input field. For doing so, we use $\hat{c}_{\text{in,out}}$ representing classical signals at Δ_s and arrive at

$$\begin{aligned}G_s(\Delta_s) :=&\frac{|\delta a_{\text{out}}[\Delta_s]|^2}{|\delta a_{\text{in}}[\Delta_s]|^2} = |g_s(\Delta_s)|^2 \\ =&\frac{|-(-i\Delta_s + \lambda_-)(-i\Delta_s + \lambda_+) + \kappa(-i\Delta_s + (i\tilde{\Delta}^* + \frac{\kappa}{2}))|^2}{|(-i\Delta_s + \lambda_-)(-i\Delta_s + \lambda_+)|^2}\end{aligned} \tag{3.18}$$

for the signal. For the idler we find

$$\begin{aligned}G_i(\Delta_s) :=&\frac{|\delta a_{\text{out}}[\Delta_s]|^2}{|\delta a_{\text{in}}[-\Delta_s]|^2} = |g_i(\Delta_s)|^2 \\ =&\frac{|\kappa\Lambda|^2}{|(-i\Delta_s + \lambda_-)(-i\Delta_s + \lambda_+)|^2}.\end{aligned} \tag{3.19}$$

Fig. 3.3 shows several different (signal) gain profiles, where we see that the gain profiles are symmetric around zero detuning. This is another aspect which can be derived using Eq. 3.17 where we find

$$\begin{aligned}g_s(\Delta_s) = g_s(-\Delta_s) \\ g_i(\Delta_s) = g_i(-\Delta_s).\end{aligned} \tag{3.20}$$

Further, we see that the gain increases operating closer to bistability, while the amplification bandwidth decreases, leading to the constant gain bandwidth product (see following section). Fig. 3.4 shows a 2D plot of changing the pump and the probe frequency for two different powers (while in Fig. 3.3 the pump was set to the frequency which maximised the gain). We clearly see that the region of highest gain shifts to lower values with increasing power.

Now, we want to consider several aspects of parametric amplification.

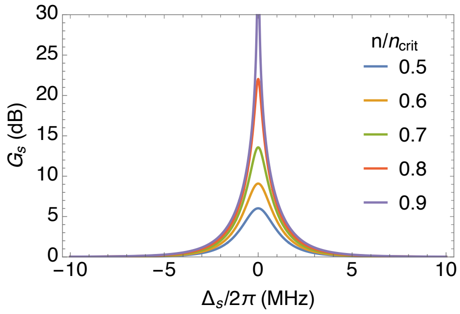

Figure 3.3: Gain profiles for the signal gain for different photon number compared to the critical one for a cavity with $\kappa/2\pi = 4\,\mathrm{MHz}$. Shown is the signal gain which increases approaching bistability, always adjusting the pump frequency to achieve highest gain. The gain is symmetric around zero and we can also see that while the overall gain increases, the linewidth 3 dB below maximal gain decreases, leading to the constant gain bandwidth product.

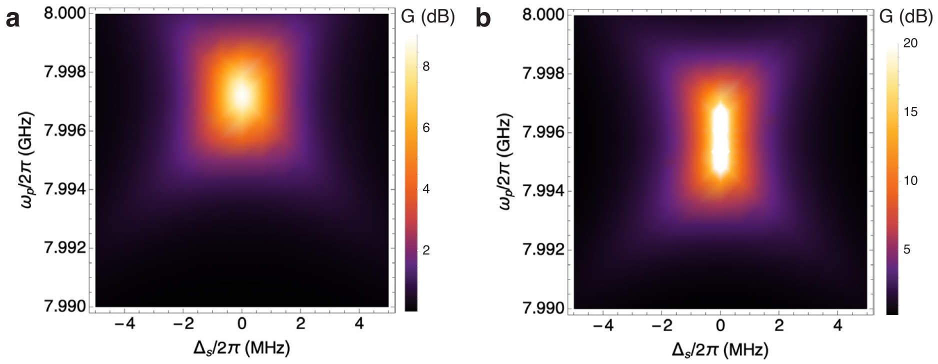

Figure 3.4: Gain profiles at **a** 50% and **b** 90% of the critical drive. Here, the 2D maps show a change of signal and pump frequency. We see that the highest gain shifts to lower frequencies when increasing the power.

Gain bandwidth product

As already seen in Fig. 3.3, the gain bandwidth product is limited. In the large gain limit, we find that $G_s \approx G_i = G$, which can be seen from Eq. 3.17 and was discussed previously. Thus it is sufficient to calculate G_i (Eq. 3.19), where we find

$$G(\Delta_s) = \frac{|\kappa\Lambda|^2}{|(-i\Delta_s + \lambda_-)(-i\Delta_s + \lambda_+)|^2} \approx \frac{G(0)}{1 + \left(\frac{2\Delta_s}{B_{\Delta_s}}\right)^2}. \tag{3.21}$$

Here, we introduced the 3 dB bandwidth, $B_{\Delta_s} = 2\lambda_-$. For the approximation, we use that λ_- is always smaller than λ_+, and thus the $1/\lambda_-$ leads to the dominant contribution. Further the contribution from the Δ_s^2 is neglected.

Now, using parameters for the critical point (Eq. 3.9), B_{Δ_s} can be re-written as

$$B_{\Delta_s} = 2\lambda_- = \frac{2}{\sqrt{3}} \frac{\kappa}{\sqrt{G(0)}}. \tag{3.22}$$

To obtain this equation we use that $\lambda_\pm$ reduces to $\kappa/2$, when taking parameters for the critical point. Using this and inserting for $G(0)$ (Eq. 3.19), the above equation can be shown. Thus, we find that the bandwidth reduces with increasing gain, which is the gain-bandwidth limit.

Squeezing and its influence on gain

The amplifier squeezes the input state and in this section, we want to discuss the influence of squeezing on the gain. One quadrature of the internal fields gets squeezed, while the other one gets amplified. At best, the phase of the signal lies along the amplified quadrature to get maximum amplification. The intracavity quadratures can be written as

$$\begin{aligned} X_1(t) &= \frac{1}{2}(\hat{a}(t) + \hat{a}^\dagger(t)) \\ X_2(t) &= \frac{1}{2i}(\hat{a}(t) - \hat{a}^\dagger(t)). \end{aligned} \tag{3.23}$$

However, those are not necessarily the amplified quadratures, which can be a linear combination of X_1 and X_2. Thus, it is useful to define a rotated quadrature

$$X_\theta(t) = \frac{1}{2}\left(e^{-i\theta}\hat{a}(t) + e^{i\theta}\hat{a}^\dagger(t)\right). \tag{3.24}$$

Evaluating the signal gain for this quadrature, where details on the calculation are given in [61], we find

$$G_\theta(\Delta_s) = 2G_s(\Delta_s) - 1 + 2\sqrt{G_s(\Delta_s)(G_s(\Delta_s) - 1)}\cos(2\theta - \phi_\Lambda). \tag{3.25}$$

Here, ϕ_Λ is the angle between the complex gains $g_s(\Delta_s)$ and $g_i(\Delta_s)$

$$g_s(\Delta_s)g_i(-\Delta_s) = \sqrt{G_s(\Delta_s)}\sqrt{G_s(\Delta_s) - 1}e^{i\phi_\Lambda} \tag{3.26}$$

The angle with the highest gain $G_\theta(\Delta_s)$ defines the amplified quadrature, while the one with the lowest the squeezed quadrature. With changing the phase of the pump field, we can go from maximum amplification to maximum squeezing. Considering large gain, $G_s \gg 1$, we find for the amplified and squeezed quadratures, $X_{1,2}$ (Eq. 3.23)

$$\begin{aligned} G_1 &= 4G_s \\ G_2 &= \frac{1}{4G_s} \end{aligned} \tag{3.27}$$

The gain in the amplified quadrature is 6 dB higher than the signal gain (Eq. 3.18). However, the gain bandwidth product only increases by a factor of two as the effective bandwidth halves.

With this, we see the importance of matching the phase of the pump, such that the signal lies ideally along the amplified quadrature.

Added noise

Both signal and idler can be used for amplification. Noiseless amplification is only possible, if the signal consists of symmetric components at $\pm\Delta_s$. If the signal only consists of a single component, at least half a quanta of noise is added. This is true for the here discussed pump scheme, having a single pump tone in the vicinity (but detuned) from the signal frequency. As the pump and the signal are at different frequencies, the relative phase between them constantly evolves and there is no fixed phase relation. This can be different using other schemes, for example using two pumps [65] or parametrically modifying the flux bias point (flux pumping) [66, 67].

3.2 Duffing model

Here, we will investigate a nonlinear system directly using the equation of motion, which is another, but equivalent, way for describing such a system. To be specific, we base our considerations on the equation of motion of a damped, driven oscillator in a nonlinear potential, which is the so-called Duffing equation and reads

$$\ddot{x} + \kappa\dot{x} + \omega_c^2 x + \eta x^3 = F\cos(\omega_p t). \tag{3.28}$$

Here, x is the amplitude of motion of the system. As before, κ relates to the damping of the cavity. The strength of the nonlinearity is given by η, where we will assume $\eta < 0$, as this will be the case for our system. The system is driven with the drive strength F at a frequency ω_p.

For solving this system, we use an iterative approach. The idea is to have an initial guess for the solution, which is close to the actual solution. By solving the equation of motion using the initial guess, we can update the parameters, giving solutions closer to the actual solution. Here we assume a zeroth order solution of the form $x_0 = A\cos(\omega_p t)$, which is an exact solution only in case of a linear potential ($\eta = 0$) and ignore damping for now by setting $\kappa = 0$. Putting this ansatz into Eq. 3.28 we obtain after integration

$$x_1 = A_1 \cos(\omega_p t) + \frac{\eta A^3}{36\omega_p^2}\cos(3\omega_p t), \tag{3.29}$$

where we defined

$$A_1 := \frac{1}{\omega_p^2}\left(\omega_c^2 A + \frac{3}{4}\eta A^3 - F\right). \tag{3.30}$$

With this we have completed the first step of the iterative process and x_1 is the solution after the first iteration. With another iteration step, we could determine x_2, the solution after the second step, by plugging x_1 (Eq. 3.29) back into Eq. 3.28. However, assuming a small η, we can rather argue that A_1 is very similar to A. Thus we assume that after the first step we already have a solution sufficiently close to the actual solution. With this we can use $A = A_1$ and obtain from Eq. 3.30

$$\left(\omega_c^2 - \omega_p^2 + \frac{3\eta}{4}A^2\right) A = F. \tag{3.31}$$

The condition necessary such that it is sufficient to only solve until first order is

$$\frac{\eta A^2}{36\omega_p^2} \ll 1. \tag{3.32}$$

In a next step, we include the damping, which leads to a phase difference between the response of the cavity and the drive field. This phase can be simply included into the drive, by modelling the drive as $F\cos(\omega t + \phi)$. The system can be solved with the same iterative approach, where additional details are found in [61]. After the calculation one obtains

$$\begin{aligned} F^2 &= \left[(\omega_c^2 - \omega_p^2)A + \frac{3}{4}\eta A^3\right]^2 + (\kappa\omega_p A)^2 \\ \tan(\phi) &= \frac{\kappa\omega_c}{(\omega_c^2 - \omega_p^2) + \frac{3}{4}\eta A^2}, \end{aligned} \tag{3.33}$$

which includes losses. With this we solved the response of a Duffing-like oscillator. Now, we can simplify this solution by assuming a high quality factor ($\kappa \ll \omega_c$). This allows to approximate $\omega_c + \omega_p \approx 2\omega_c$ and $\omega_p/\omega_c \approx 1$, and Eq. 3.33 becomes

$$\begin{aligned} F^2 &= \left[\left(2\omega_c(\omega_c - \omega_p) + \frac{3}{4}\eta A^2\right)^2 + (\kappa\omega_c)^2\right] A^2 \\ \tan(\phi) &= \frac{\kappa\omega_c}{2\omega_c(\omega_c - \omega_p) + \frac{3}{4}\eta A^2}. \end{aligned} \tag{3.34}$$

Fig. 3.5 shows the amplitude response for different drive strengths against detuning. We see that those results are identical to what we obtained from the Hamiltonian formulation, plotted in Fig. 3.2, which shows the equivalence of those two approaches.

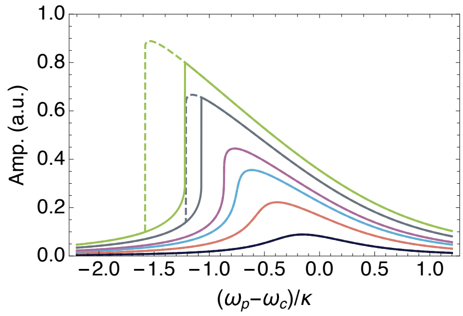

Figure 3.5: Results of the Duffing model for increasing drive strengths of $\{0.2, 0.5, 0.8, 1.0, 1.5, 2.0\} \times \bar{n}_{\text{crit}}$. Here plotted are the low (solid) and high solutions (dashed) as in Fig. 3.2b. We see that the results of the Duffing model are identical as those we get when solving the Hamiltonian formulation.

To make the expressions we get from solving the Duffing model in Eq. 3.34 identical to what we obtained using the Hamiltonian formulation, we can do the following replacements

$$\begin{aligned} A^2 &\mathrel{\widehat{=}} \frac{\bar{n}_c}{(2\omega_c)^2} \\ F^2 &\mathrel{\widehat{=}} \kappa\bar{n}_{\text{in}} \\ \eta &\mathrel{\widehat{=}} \frac{4}{3}\mathcal{K}(2\omega_c)^3. \end{aligned} \tag{3.35}$$

With this, Eq. 3.34 is identical to Eq. 3.6. Further, the frequency of the maximum response (shifted resonance frequency) is found at

$$\omega_c - \omega_p = \frac{3\eta}{4\omega_c}\frac{A^2}{2} \tag{3.36}$$

Re-writing this using the replacements, Eq. 3.35, we find

$$\omega_c - \omega_p = \mathcal{K}\bar{n}_c. \tag{3.37}$$

As already discussed in the Hamiltonian formulation, such a nonlinear resonator shows bistability above a critical drive strength in a certain range of probe frequencies. We can determine the critical parameters similar to before and find

$$\begin{aligned} \Delta_{crit} = \omega_c - \omega_{crit} &= \frac{\sqrt{3}}{2}\frac{\eta}{|\eta|}\kappa \\ F^2_{crit} &= \frac{32\kappa^3}{9\sqrt{3}}\frac{\omega_c^3}{|\eta|} \\ A^2_{crit} &= \frac{8\kappa}{3\sqrt{3}}\frac{\omega_c}{|\eta|}, \end{aligned} \tag{3.38}$$

which are identical to the conditions obtained for the critical point in the Hamiltonian formulation, Eq. 3.9.

With this we have shown that this very different approach leads to the same results. As the derivation of the gain is simpler in the Hamiltonian formulation, it was only shown there. With this, nonlinear cavities are introduced and their main aspects were discussed in this chapter. In a next step, we will discuss how to combine what has been introduced in the two previous chapters, cavity optomechanics and nonlinear cavities, to enter the field of nonlinear optomechanics.

4 | Nonlinear optomechanics

In this chapter, we will combine cavity optomechanics, introduced in Chapter 2, and nonlinear cavities, Chapter 3. We are foremost interested what effects the nonlinearity of the cavity has on the optomechanical backaction onto the mechanical resonator. This chapter is mainly based on [4, 47, 5] and the presented theory was developed by Nicolas Diaz-Naufal and Anja Metelmann from the FU Berlin and KIT specifically for our system.

4.1 Nonlinear optomechanical Hamiltonian

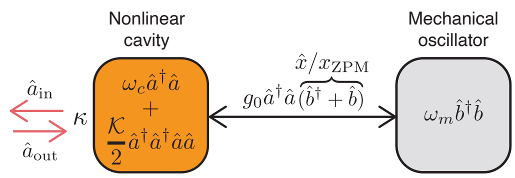

Figure 4.1: Symbolic representation of the considered setup, a nonlinear cavity coupled to a mechanical resonator. The cavity itself is also coupled to a port at a rate κ.

We can find the Hamiltonian describing a nonlinear optomechanical system, by combing the known Hamiltonian from linear optomechanics, Eq. 2.6, and the Hamiltonian describing a nonlinear system, Eq. 3.1,

$$\hat{H} = \hbar\omega_c \hat{a}^\dagger \hat{a} + \hbar\omega_m \hat{b}^\dagger \hat{b} + \frac{\mathcal{K}}{2}\hat{a}^\dagger\hat{a}^\dagger\hat{a}\hat{a} + \hbar g_0 \hat{a}^\dagger \hat{a}(\hat{b} + \hat{b}^\dagger). \tag{4.1}$$

At first we will consider the classical dynamics, by discussing the influence of the mechanical mode on the nonlinear cavity. In a second step, we will take the influence from quantum fluctuations into account to derive expressions for the optomechanical backaction on the mechanical system. To do so, we split the field amplitude into a classical part and a part carrying the fluctuations: $\hat{a} = \alpha + \delta\hat{a}$, where $\langle \hat{a}(t) \rangle = \alpha(t)$, similar to Chapter 2.1.2.

4.2 Classical dynamics

Now we will consider the classical part, $\hat{a} = \alpha$, using input output theory [63]. As already in the previous chapter, we move into a rotating frame around the pump frequency, ω_p, and find the following equation of motion

$$\dot{\alpha} = (i\Delta - \frac{\kappa}{2})\alpha - i\mathcal{K}|\alpha|^2\alpha - i\sqrt{2}g_0\langle\hat{q}\rangle\alpha - \sqrt{\kappa}\alpha_{\text{in}}, \tag{4.2}$$

where κ is the coupling rate to an external port with a drive amplitude α_{in}. $\langle\hat{q}\rangle = (\hat{b} + \hat{b}^\dagger)/\sqrt{2}$ is the position quadrature of the mechanical resonator. This equation is - up to the Kerr nonlinearity - equivalent to Eq. 2.16, and can be made identical by identifying $\sqrt{2}g_0\langle\hat{q}\rangle = g_0(\hat{b} + \hat{b}^\dagger) = G\hat{x}$.

Now we want to find a steady state solution for Eq. 4.2. For this we first analyse the mechanical mode, which is described by

$$\begin{aligned}\frac{d}{dt}\langle\hat{q}\rangle &= \omega_m\langle\hat{p}\rangle - \frac{\Gamma_m}{2}\langle\hat{q}\rangle,\\ \frac{d}{dt}\langle\hat{p}\rangle &= -\omega_m\langle\hat{q}\rangle - \frac{\Gamma_m}{2}\langle\hat{p}\rangle - \sqrt{2}g_0|\alpha|^2,\end{aligned} \tag{4.3}$$

where $\hat{p} = i(\hat{b}^\dagger - \hat{b})/\sqrt{2}$ is the momentum quadrature. As the mechanical resonator only weakly influences cavity field, it can be solved in the long time limit. The steady state solution for the mechanical position operator is then found to

$$\langle\hat{q}\rangle_s = -\frac{\sqrt{2}g_0\omega_m|\alpha|^2}{\omega_m^2 + \frac{\Gamma_m^2}{4}}. \tag{4.4}$$

This steady state solution implies that the amplitude of the displacement is constant over time. We can insert this back into Eq. 4.2 and find a $|\alpha|^2\alpha$ dependence. This dependence is the same as for a Kerr-term, meaning that the coupling results in an additional Kerr nonlinearity. This allows us to introduce an effective Kerr, modified by the mechanical interaction

$$\dot{\alpha} = \left(i\Delta - \frac{\kappa}{2}\right)\alpha - i\mathcal{K}_{\text{eff}}\alpha|\alpha|^2 - \sqrt{\kappa}\alpha_{\text{in}} \tag{4.5}$$

with

$$\mathcal{K}_{\text{eff}} := \mathcal{K} - \frac{2g_0^2\omega_m}{\omega_m^2 + \frac{\Gamma_m^2}{4}}. \tag{4.6}$$

As the Kerr constant is typically negative, the nonlinearity increases with increasing g_0. It should be pointed out, that $\mathcal{K}_{\text{eff}}$ does not depend on the enhanced coupling strength, as does the backaction, but the single-photon coupling strength. In the high-Q limit, where $\omega \gg \Gamma_m$, the mechanical impact on the Kerr is $\propto g_0^2/\omega_m$, which is usually only a small correction to the Kerr, when working with an intrinsically nonlinear cavity. However, for linear cavities, with $\mathcal{K} = 0$, or large coupling strengths, it can lead to a significant influence.

Finally, we want to find a solution for the classical cavity dynamics. Therefore, we multiply the steady state solution of Eq. 4.5 with its complex conjugate and find the steady state solution for the cavity response, which is up to the mechanical Kerr identical to Eq. 3.6,

$$\bar{n}_c\left[(-\Delta + \mathcal{K}_{\text{eff}}\bar{n}_c)^2 + \left(\frac{\kappa}{2}\right)^2\right] = \kappa\bar{n}_{\text{in}}. \tag{4.7}$$

With this we see that the dynamics of the nonlinear cavity is barely influenced by the presence of the mechanical resonator, only the Kerr constant changes for large couplings. Interestingly, a linear optomechanical system always has a Kerr nonlinearity arising from the coupling to the mechanical resonator, which is however for typical coupling strength too small to have an influence.

4.3 Dynamics and occupation of the mechanical mode

Now we want to investigate the influence of quantum fluctuations introduced by $\delta\hat{a}$, but already using the solutions of the classical dynamics. From Eq. 4.1 we can find a linearised Hamiltonian in the rotating frame

$$H = -\hbar\tilde{\Delta}\delta\hat{a}^\dagger\delta\hat{a} + \hbar\omega_m\hat{b}^\dagger\hat{b} + \hbar\frac{1}{2}\left(\Lambda\delta\hat{a}^\dagger\delta\hat{a}^\dagger + \Lambda^*\delta\hat{a}\delta\hat{a}\right) + (\widetilde{g}\delta\hat{a}^\dagger + \widetilde{g}^*\delta\hat{a})(\hat{b} + \hat{b}^\dagger). \tag{4.8}$$

Here, we already used the modified detuning, $\tilde{\Delta}$, and the single-mode squeezing strength, Λ, introduced in Eq. 3.13. Further, a modified coupling is introduced with $\widetilde{g} = |\alpha| g_0 e^{i\phi_{\widetilde{g}}}$ and the phase $\phi_{\widetilde{g}}$.

Again we derive the equations of motion using input-output theory to find

$$\frac{d}{dt}\delta\hat{a} = \left(i\tilde{\Delta} - \frac{\kappa}{2}\right)\delta\hat{a} - i\Lambda\delta\hat{a}^\dagger - i\widetilde{g}\left(\hat{b} + \hat{b}^\dagger\right) - \sqrt{\kappa}\delta\hat{a}_{\text{in}}. \tag{4.9}$$

for the cavity mode and

$$\frac{d}{dt}\hat{b} = -\left(i\omega_m + \frac{\Gamma_m}{2}\right)\hat{b} - i\left(\widetilde{g}^*\hat{d} + \widetilde{g}\hat{d}^\dagger\right) - \sqrt{\Gamma_m}\hat{b}_{\text{in}} \tag{4.10}$$

for the mechanical mode. Together with the input noise operators $\delta\hat{a}_{\text{in}}, \hat{b}_{\text{in}}$ associated with the generalised nonzero correlators $\langle \hat{f}_{\text{in}}(t)\hat{f}^\dagger_{\text{in}}(\tau)\rangle = (\bar{n}^{\text{th}}_m + 1)\delta(t-\tau)$ and $\langle \hat{f}^\dagger_{\text{in}}(\tau)\hat{f}_{\text{in}}(t)\rangle = \bar{n}^{\text{th}}_m\,\delta(t-\tau)$ and, $\bar{n}^{\text{th}}_m$, the thermal occupation[1].

In a next step, we want to decouple Eqs. 4.9 and 4.10 to find a description of the mechanical mode. For doing this, we transform the equations into Fourier space, similar to what we did in Chapter 2.2.1. For Eq. 4.9 we then find

$$\begin{bmatrix} \mathcal{X}_c^{-1}[\omega] & i\Lambda \\ -i\Lambda^* & \mathcal{X}_c^{*-1}[-\omega] \end{bmatrix} \begin{bmatrix} \delta\hat{a}[\omega] \\ \delta\hat{a}^\dagger[\omega] \end{bmatrix} = -i \begin{bmatrix} \widetilde{g} & \widetilde{g} \\ -\widetilde{g}^* & -\widetilde{g}^* \end{bmatrix} \begin{bmatrix} \hat{b}[\omega] \\ \hat{b}^\dagger[\omega] \end{bmatrix} - \sqrt{\kappa} \begin{bmatrix} \delta\hat{a}_{\text{in}}[\omega \\ \delta\hat{a}^\dagger_{\text{in}}[\omega] \end{bmatrix}, \tag{4.11}$$

where $\mathcal{X}_c^{-1}[\omega] = -i(\omega + \tilde{\Delta}) + \kappa/2$ is the cavity susceptibility. Analogously, we find for Eq. 4.10

$$\begin{bmatrix} -i(\omega - \omega_m) + \frac{\Gamma_m}{2} & 0 \\ 0 & -i(\omega + \omega_m) + \frac{\Gamma_m}{2} \end{bmatrix} \begin{bmatrix} \hat{b}[\omega] \\ \hat{b}^\dagger[\omega] \end{bmatrix} = -i \begin{bmatrix} \widetilde{g}^* & \widetilde{g} \\ -\widetilde{g}^* & -\widetilde{g} \end{bmatrix} \begin{bmatrix} \delta\hat{a}[\omega] \\ \delta\hat{a}^\dagger[\omega] \end{bmatrix} - \sqrt{\Gamma_m} \begin{bmatrix} \hat{b}_{\text{in}}[\omega] \\ \hat{b}^\dagger_{\text{in}}[\omega] \end{bmatrix}. \tag{4.12}$$

To decouple this system, we can solve Eq. 4.11 for $\delta\hat{a}$ and $\delta\hat{a}^\dagger$ and substitute the solutions into Eq. 4.12. We then find for the dynamics of the mechanical resonator

$$\begin{bmatrix} -i(\omega - \omega_m) + \frac{\Gamma_m}{2} - i\Sigma_c[\omega] & -i\Sigma_c[\omega] \\ i\Sigma_c[\omega] & -i(\omega + \omega_m) + \frac{\Gamma_m}{2} + i\Sigma_c[\omega] \end{bmatrix} \begin{bmatrix} \hat{b}[\omega] \\ \hat{b}^\dagger[\omega] \end{bmatrix} = -\sqrt{\Gamma_m} \begin{bmatrix} \hat{B}_{\text{in}}[\omega] \\ \hat{B}^\dagger_{\text{in}}[\omega], \end{bmatrix}. \tag{4.13}$$

Here, we introduced $\Sigma_c[\omega] = -2|\widetilde{g}|^2 \left\{\tilde{\Delta} + |\Lambda|\cos(\varphi)\right\} \tilde{\mathcal{X}}_c[\omega]$, which captures the backaction from the cavity on the mechanical mode[2], using the modified cavity susceptibility $\tilde{\mathcal{X}}_c^{-1}[\omega] = \mathcal{X}_c^{-1}[\omega]\mathcal{X}_c^{*-1}[-\omega] - |\Lambda|^2$ and the phase $\varphi = 2\phi_G - \phi_\Lambda$. From the classical cavity we find $\phi_G = \phi_\Lambda/2$, which implies that $\varphi = 0$ and thus that the phases are not independent.

The optomechanical induced frequency shift and damping are found from $\Sigma_c[\omega]$ as

$$\begin{aligned} \delta\omega_m &= \Re\{\Sigma_c[\omega]\} \\ \Gamma_{\text{OM}} &= \pm 2\Im\{\Sigma_c[\omega]\} \end{aligned} \tag{4.14}$$

The modified mechanical noise is given by

$$\hat{B}_{\text{in}}[\omega] = \hat{b}_{\text{in}}[\omega] - i|\widetilde{g}|\sqrt{\frac{\kappa}{\Gamma_m}}\tilde{\mathcal{X}}_c[\omega]\left\{e^{-i\phi_G}\left(\mathcal{X}_c^{*-1}[-\omega] + i|\Lambda|\right)\delta\hat{a}_{\text{in}}[\omega] + e^{+i\phi_G}\left(\mathcal{X}_c^{-1}[\omega] - i|\Lambda|\right)\delta\hat{a}^\dagger_{\text{in}}[\omega]\right\}, \tag{4.15}$$

[1] Those correlators are generalised, where $\hat{f}_{\text{in}}$ stands for the operators $\delta\hat{a}_{\text{in}}$ or $\hat{b}_{\text{in}}$. For instance, for $\hat{b}_{\text{in}}$ we obtain $\langle \hat{b}_{\text{in}}(t)\hat{b}^\dagger_{\text{in}}(\tau)\rangle = (\bar{n}^{\text{th}}_m + 1)\delta(t-\tau)$.

[2] In contrast to the derivation of the self energy in Chapter 2.2.1 (Eq. 2.24), we treat the mechanical system in terms of the operator $\hat{b}$ instead of the position operator $\hat{x}$. This leads to a factor of 2 difference, which is reflected when deriving the cavity induced damping and frequency shift.

which now includes the noise contribution from the cavity.

With this, we have analysed the influence from the cavity on the dynamics of the mechanical resonator. Finally, we want to directly find the phonon number of the mechanical mode under backaction, which is given by

$$\bar{n}_m = \int_{-\infty}^{\infty} \frac{d\omega}{2\pi} S_{bb}(\omega) d\omega = \int_{-\infty}^{\infty} \frac{d\omega}{2\pi} \int_{-\infty}^{\infty} \frac{d\Omega}{2\pi} \langle \hat{b}^\dagger[\Omega] \hat{b}[\omega] \rangle, \tag{4.16}$$

using the operators from Eq.4.13 together with the nonzero correlators, which read in frequency space for $\delta\hat{a}_{\text{in}}, \hat{b}_{\text{in}}$: $\langle \hat{f}_{\text{in}}[\omega] \hat{f}_{\text{in}}^\dagger[\Omega] \rangle = 2\pi(\bar{n}_m^{\text{th}} + 1)\,\delta[\omega + \Omega]$ and $\langle \hat{f}_{\text{in}}^\dagger[\Omega] \hat{f}_{\text{in}}[\omega] \rangle = 2\pi \bar{n}_m^{\text{th}}\,\delta[\omega + \Omega]$. What we do here, is integrating over the mechanical noise spectrum, $S_{bb}(\omega)$, yielding the area of the mechanical spectrum, being the phonon occupation.

With this, we have theoretically described, how a nonlinear cavity can be used for optomechanical backaction. Now, we want to qualitatively compare a linear to a nonlinear system.

4.4 Illustrative picture showing nonlinear cooling benefits and key features

While we did the theoretical description of the nonlinear cooling in the above chapters and found Eq. 4.16 describing the final occupation of the mechanical mode under backaction, it might not be obvious to see the benefits of the nonlinear cooling.

To get an intuitive picture, we consider the time lag picture, as discussed in Chapter 2.2.2. In Fig. 4.2 we compare a linear (a) to a nonlinear cavity (b), where the probe-cavity detuning is changed due to the optomechanical interaction. In case of a completely linear system, a symmetric response is recovered, identical to the response when sweeping a probe tone over a fixed frequency cavity. The shaded area depicts the cooling work done on the mechanical system within one cycle for an ideal red detuned probe tone, which we simulate with a simple model [46]. To see the enhancement of the nonlinear cavity, we consider a cavity with a

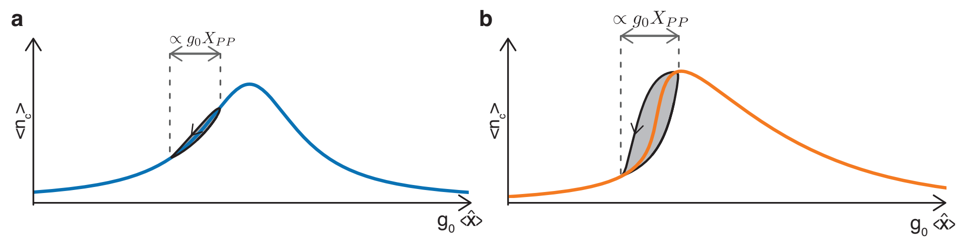

Figure 4.2: The cavity frequency changes due to the optomechanical interaction ($g_0\langle\hat{x}\rangle$), changing the probe-cavity detuning. **a.** For the linear case we recover a symmetric response while for the nonlinear case, **b.**, we recover the typical nonlinear response. This is identical to sweeping the probe tone itself through a fixed frequency cavity. The shaded area indicates the cooling work done on a mechanical system within a cycle by the cavity for realistic parameters. X_{PP} denotes the peak-to-peak amplitude of the mechanical resonator. The cooling enhancement provided by the nonlinearity is clearly visible. As already state before, the data for the work cycle figures was provided by a colleague of mine, Christian Schneider, more information on the calculation can be found in [46].

negative Kerr nonlinearity, such that the cavity is close to bistability, Eq. 3.9, using otherwise the same parameters as for the linear case discussed previously. Probing this system with a fixed frequency tone, we obtain the typical nonlinear response. For lower drive strengths the cavity would be effectively linear, while for higher drives bistability is reached. As the enclosed area within one cycle increases, it is evident that the cooling is enhanced compared to the linear case. This effect becomes increasingly relevant for driving the cavity close to bistability as the cavity response becomes effectively steeper, leading to an increased cooling. Due to the nonlinear line shape, small changes of the cavity frequency related to the mechanical motion, induce a large variation of the cavity photon number, which makes the cooling more efficient. Working on the blue side (i.e. frequency of the probe tone above the cavity frequency), the cavity slope is effectively more shallow compared to the linear case, leading a decrease of the heating backaction. For a positive Kerr, this effect would be entirely reversed.

Now, we want to compare simulated cooling traces to see what happens when approaching bistability and how nonlinear and linear cooling compare. Fig. 4.3a shows the phonon occupation of the mechanical mode under backaction for increasing photon number in the cavity up to bistability. It is evident, that the cooling gets much stronger operating close to bistability. We further see, that the region of most cooling shifts to lower frequencies, due to the Kerr shift of the cavity, and that the cooling happens over an increasingly narrow range of detunings due to the nonlinear lineshape. Also the cooling backaction gets stronger approaching bistability. Working blue detuned compared to the (shifted) cavity frequency, the amplification/heating backaction remains similar despite the increasing pump power. As for increasing power the cavity lineshape gets shallower on the blue side, which compensates the enhancement of backaction with photon number. Fig. 4.3b shows a comparison of the nonlinear cooling curve at 10% and 99 % of the bistable photon number to a linear cooling curve for - besides the nonlinearity - identical parameters, using the same number of photons[3]. For the low power case, the curves are very similar, as the nonlinear cavity is still in the linear regime. In the high power case, the nonlinear cooling is much enhanced compared to the linear case and we also note the nonlinear frequency shift, shifting the cooling backaction to lower detunings. Considering the amplifying regime, we see that this is much suppressed, which - for this parameters - prevents the mechanical system from entering the regime of dynamical instability, in contrast to the linear cooling.

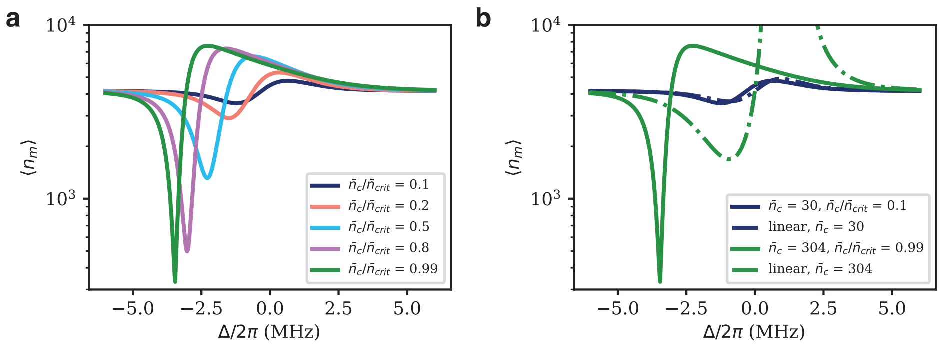

Figure 4.3: Simulated cooling traces for increasing power. **a.** Phonon occupation against probe-cavity detuning for increasing cavity photon number approaching bistability. It is clearly visible, that the cooling backaction shifts to lower frequencies due to the nonlinearity of the cavity response and also that the backaction happens over an increasingly narrow region of frequencies. **b.** Comparison between linear and nonlinear cooling for the same parameters and input power, operating the nonlinear cavity at 10% and 99% of the bistable power. For the low power case, where the nonlinear cavity is in the linear regime, both traces show very similar cooling. However, working closer to bistability, it is evident, that owing to the nonlinearity, the cooling is much enhanced compared to the linear case, having a nearly 10 fold increase for the parameters chosen here. Also, we see that the cooling happens further red detuned. The parameters used here are: $g_0/2\pi = 100\,\text{Hz}, \omega_m/2\pi = 500\,\text{kHz}, \Gamma_m/2\pi = 0.5\,\text{Hz}, \kappa/2\pi = 4\,\text{MHz}, \mathcal{K}/2\pi = 10\,\text{kHz}$.

Fig. 4.4 shows the optomechanical damping (a) and frequency shift (c) induced by a nonlinear cavity approaching bistability. Similar to Fig. 4.3a we see the increasing backaction for increasing power. The frequency shift shows a hump in the region of most cooling backaction

[3] When considering linear cooling in Chapter 2.2.2, I plotted the curve for a given number of photons in the cavity, regardless of the detuning, as it is typically done for plotting such cooling traces. Here, I take the lineshape into account, which leads to a decreasing photon number being detuned from the resonance frequency and it is done in the same way for the nonlinear cooling curves.

for higher powers, which (partly) cancels the induced frequency shift. Comparing to the linear theory (c,d), we clearly see the increased backaction working close to bistability. Looking at the blue detuned region, we notice that while for the linear cooling, the mechanical resonator would enter the regime of dynamical instability ($\Gamma_{\text{eff}} < 0$), this is not the case for the nonlinear theory due to the reduced backaction being blue detuned.

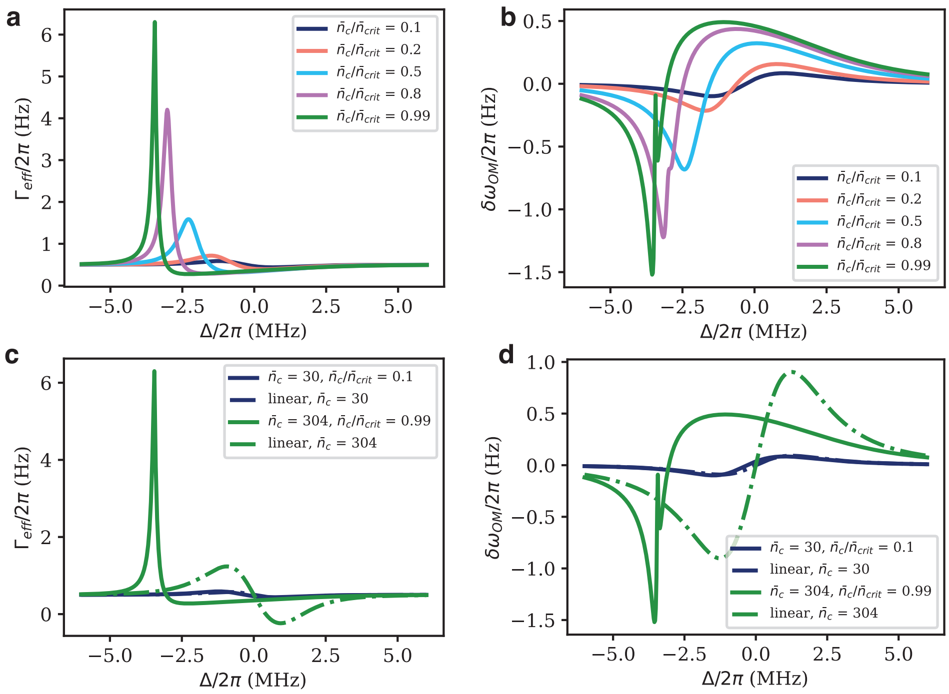

Figure 4.4: Optomechanical induced damping and frequency shift with increasing photon number approaching bistability and comparison to linear theory. **a.** Optomechanical induced damping against probe-cavity detuning approaching bistability. Similar to the phonon occupation, Fig. 4.3, the damping increases approaching bistability and highest damping happens at increasingly lower detunings. Here, we plot $\Gamma_{\text{eff}} = \Gamma_m + \Gamma_{\text{OM}}$. **b.** The optomechanical induced frequency shift of the mechanical mode develops an interesting feature approaching bistability, showing a narrow hump in the vicinity of highest cooling backaction. **c,d.** Comparing the damping and frequency shift to linear theory, we observe much enhanced damping, when working close to bistability. Again, we observe that this strong damping also happens in a narrow range of frequencies compared to the linear case. The parameters used here are the same as for Fig. 4.3

In this chapter we have discussed how we can combine a nonlinear cavity with a mechanical resonator, leading to nonlinear optomechanics. We developed strategies for solving this system, to see the influence of the mechanical resonator on the steady state response of the cavity, but also the modified backaction on the mechanical resonator due to the nonlinear cavity. Finally, we looked at qualitative results to see that operating the nonlinear cavity with a negative Kerr close to bistability the cooling backaction is much enhanced over a purely linear system with otherwise identical parameters, which is the key message of this chapter.

5 | Superconducting cavities for optomechanics

So far, we have discussed how nonlinear cavities (resonators) can be combined with mechanical resonators to enter the field of nonlinear optomechanics. In this chapter we will focus on superconducting cavities, as such cavities will be used in the experiment. We will discuss superconductivity in general and how nonlinear superconducting cavities can be built. Next to discussing their major loss mechanisms, we will also speak about using such cavities as magnetic field sensors. Finally, we will analyse, the equivalence of such cavities, to the Kerr and Duffing formulation introduced in Chapter 3.

5.1 Superconductivity and Josephson effect

This part is mainly based on [68], other sources will be explicitly mentioned.

5.1.1 Superconductivity

Superconducting materials can conduct electrical currents without any resistance, which is explained by electrons forming so-called Cooper pairs. Those form a coherent state across the superconductor and do not undergo scattering events within the metal anymore, which is typically associated with loss. To describe Cooper pairs we can use a macroscopic matter wave function across the superconductor, which makes it an inherit quantum phenomena

$$\Psi(\vec{r},t) = \psi_0(\vec{r},t)e^{i\Theta(\vec{r},t)}. \tag{5.1}$$

Next to $\vec{r}$ being the position, Θ is the phase of the wave function ψ_0. It is normalised, such that $|\Psi(\vec{r},t)|^2 = n_s(\vec{r},t)$ with n_s being the local density of superconducting electrons.

Superconductivity appears as an abrupt change below a certain, critical, temperature, which is only shown by some materials. In the experiment we usually use niobium having a critical temperature of $T_c = 9.25\,\mathrm{K}$ and aluminium with $T_c = 1.19\,\mathrm{K}$ [68]. While also other materials having much higher critical temperatures above 90 K exist.

Next to being perfect conductors, superconductors have a second fundamental property, as they are also perfect diamagnets, meaning that magnetic fields completely vanish inside them (Meisner-Ochsenfeld effect). To shield superconductors from magnetic fields, a superconducting current forms on their surface, expelling magnetic fields. As this is not possible for infinite fields, a critical field exists, B_{cth}, where superconductivity breaks down. This critical field also changes with temperature, having the following dependence

$$B_{\mathsf{cth}}(T) = B_{\mathsf{cth}}(0)\left(1 - \frac{T}{T_c}\right). \tag{5.2}$$

Furthermore, it also depends on the type of superconductor:

- Type I superconductors, like Al, expel the field until B_{cth} is reached and superconductivity breaks down for stronger fields.

- Type II superconductors, like Nb, expel the field until a first critical field is reached, which is below B_{cth} and behave as type I superconductors. For increasing fields, parts of the field are not expelled and go through the superconductor, which behaves like a normal conductor in those areas, but is superconducting besides. For even bigger fields, which can significantly exceed B_{cth}, superconductivity completely breaks down.

As seen in Eq. 5.2, also below T_c superconductivity depends on temperature. This can be explained with Cooper pairs breaking due to thermal activation, leading to so-called quasi particles. For temperatures below $T_c/2$, a two fluid model gives a valid description of the breakdown of superconductivity. The following temperature dependence of the resistance is found [69]

$$R_{TF} = \frac{A}{T} exp\left(-\frac{\Delta_0}{k_b T}\right). \tag{5.3}$$

Here T is the temperature, Δ_0 the superconducting gap at zero temperature, k_b the Boltzmann constant and A a constant.

5.1.2 Flux quantisation and Josephson effect

The magnetic field in a closed superconducting loop is quantized in integers of the flux quantum

$$\Phi_0 = h/2e, \tag{5.4}$$

where h is the the Planck constant and e is the electron charge. This can be derived integrating the current along a closed loop and using Stokes theorem. As the superconducting wave function is determined up to integer multiples of 2π only integer multiples of the flux quantum are allowed to thread a closed loop. We will see that this can be used to build a highly field sensitive detector.

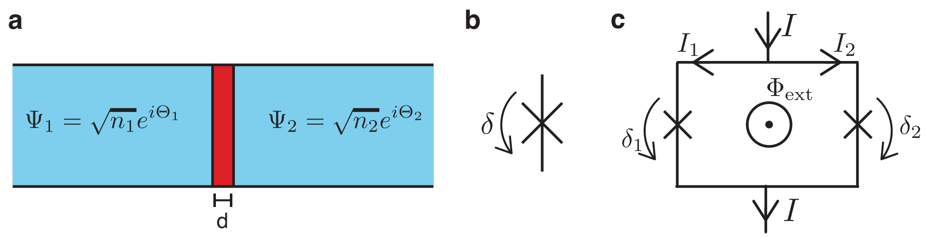

Figure 5.1: a. Schematic depiction of a Josphson junction. Two supercondcutors (blue, described by the macroscopic wave function $\Psi_{1,2}$) are separated by a thin layer of insulator (red) of thickness d. As this layer is thin, the superconducting wave function of both superconductors is still coupled. **b.** Symbolic representation of a Josephson junction by a cross. The phase difference between the wave function of the two superconductors over the junction is δ. **c.** Symbolic representation of a SQUID, where two Josephson junctions are put in parallel.

Brian David Josephson postulated that interrupting a superconductor by a thin layer of insulator - a so called Josephson junction - allows Cooper pairs to tunnel. The Josephson junction is described by the two Josephson equations, the first one is given by

$$I(\delta) = I_c \sin \delta. \tag{5.5}$$

with the critical current I_c. If a small current (below I_c) flows across the junction, it still remains superconducting and the superconducting wave functions to both sides of the junction are related by a phase drop δ. If the current exceeds I_c, superconductivity in the junction breaks, which then becomes normal conducting. The second Josephson equation is given by

$$\dot{\delta} = \frac{2\pi}{\Phi_0} U. \tag{5.6}$$

Here U is the voltage drop across the junction.

At this point, it makes sense to introduce the two most basic elements of circuitry, being the inductance and the capacitance:

- An inductance can be seen as the ability of a conductor to oppose a change of electrical current flowing through it and it stores its energy in the magnetic field. The change of current (I) to voltage (U) is related via the inductivity L
$$U(t) = L\dot{I}(t). \tag{5.7}$$
- The second basic element is the capacitor, which stores its energy in the electric field. The charge on a capacitor, Q, relates via its capacitance, C, to the voltage within the capacitor $Q = CU$. Taking the time derivative, we obtain
$$\dot{Q}(t) = I(t) = C\dot{U}(t). \tag{5.8}$$

Those basic elements are already sufficient to create a resonator, which will be discussed in more detail in Chapter 5.2.

Now we can use those equations together with the Josephson equations and show that the Josephson junction can be described as an inductor. We can see this by re-writing the time derivative of I as $dI/dt = dI/d\delta \cdot d\delta/dt$. Using the Josephson equations, Eqs. 5.5 and 5.6, and re-arranging, we obtain
$$U = \frac{L_{J0}}{\cos\delta}\dot{I}. \tag{5.9}$$
From this we see that the Josephson junction is a nonlinear element, where the inductance depends on $\cos\delta$ and thus the current passing through the junction. Here, we introduced the Josephson inductance L_{J0}, given by
$$L_{J0} = \frac{\Phi_0}{2\pi I_c}. \tag{5.10}$$
Thus, a Josephson junction can be seen as a nonlinear inductance, where its inductance depends on the phase drop δ across it. Furthermore, as an inductance stores energy, we can assign an energy to the junction [70]
$$E_J(\delta) = -\frac{I_c\Phi_0}{2\pi}\cos\delta = -E_{J0}\cos\delta, \tag{5.11}$$
where we used $E_{J0} = \frac{I_c\Phi_0}{2\pi}$.

5.1.3 The SQUID

Now, we combine two pieces introduced so far being, that the flux is quantized in a loop and the Josephson junction. Putting two junctions in parallel in a loop creates a so-called superconducting quantum interference device (SQUID). For describing the SQUID, we will assume that both junctions have an identical critical current, I_c, and have phase drops δ_1 and δ_2 across them. Using Kirchhoff's law together with trigonometric identities, we obtain
$$I_{\mathsf{SQ}} = I_{\mathsf{SQ1}} + I_{\mathsf{SQ2}} = 2I_c\cos\left(\frac{\delta_1-\delta_2}{2}\right)\sin\left(\frac{\delta_1+\delta_2}{2}\right). \tag{5.12}$$
Here, we assume that only an external flux Φ_{ext} penetrates the loop. As the flux through the loop has to be quantized (Eq. 5.4), the phase drop across the junctions has to match the external flux and we obtain
$$\delta_2 - \delta_1 = \frac{2\pi\Phi_{\mathsf{ext}}}{\Phi_0}. \tag{5.13}$$

Inserting this back into Eq. 5.12 we obtain the following maximum possible current through the SQUID

$$I_{\mathrm{SQ}}^{\mathrm{max}} = 2I_c \left|\cos\left(\frac{\pi\Phi_{\mathrm{ext}}}{\Phi_0}\right)\right|. \tag{5.14}$$

Thus, the critical current of a SQUID is tunable by an external magnetic field. Using Eq. 5.10, we see that the inductance depends on the critical current, and as the critical current of the SQUID depends on the external field, so does the inductance

$$L_{\mathrm{SQ}} = \frac{\Phi_0}{4\pi I_c \left|\cos\left(\frac{\pi\Phi_{\mathrm{ext}}}{\Phi_0}\right)\right|} = \frac{L_J}{2\left|\cos\left(\frac{\pi\Phi_{\mathrm{ext}}}{\Phi_0}\right)\right|}. \tag{5.15}$$

Thus, also the inductance on the SQUID can be tuned using an external field.

It should be noted, that here we assumed that the flux is solely of external nature. This condition does not necessarily hold in practice, as the loop itself usually has a geometric inductance. This creates an additional magnetic field penetrating the loop itself, as usually a current flows around the loop (and through the junctions) to fulfil condition Eq. 5.13. In the end this will counter act the external field and as a consequence reduce the effective amount of flux penetrating the loop and thus shield the SQUID. There it is useful to introduce the so-called screening parameter β_l [71]

$$\beta_l = \frac{2L_{\mathrm{geom}}I_c}{\Phi_0}. \tag{5.16}$$

Here, L_{geom} is the geometric inductance of the loop itself. As the flux is then not only the external flux anymore, condition 5.13 has to be modified, which however does not allow for an analytic solution anymore. Furthermore, the response to flux gets hysteric, if β_l exceeds $1/2\pi$. Additional information on this can be found in literature literature, e.g. [72, 61, 73]. In Chapter 5.3 we will discuss using SQUIDs as magnetic field sensors. Before that, we will discuss superconducting resonators.

5.2 Superconducting resonators

5.2.1 LC resonator

Combining an inductor and a capacitor in parallel already gives a simple resonator (cavity), Fig. 5.2a. To solve this resonator, we use Eqs. 5.7 and 5.8 together with Kichhoff's laws

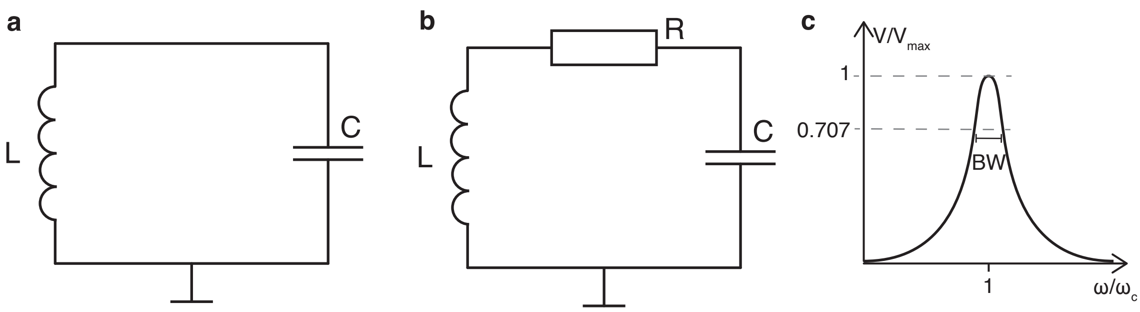

Figure 5.2: LC resonators. **a.** An inductor in parallel to a capacitor forms an LC resonator. **b.** Adding a resistor, does not change the resonance frequency, but leads to losses. **c.** This leads to a bandwidth of the resonance feature, when measuring the resonator.

$$C\ddot{U} = -\frac{1}{L}U. \tag{5.17}$$

Using an ansatz of the form $A = \sin(\omega_c t)$, we find

$$\omega_c = \sqrt{\frac{1}{LC}}. \tag{5.18}$$

Thus, simply putting a capacitance and inductance in parallel indeed gives us a resonator (cavity), and its frequency is directly given by the capacitance and inductance.

Such a circuit can be also quantized. A detailed description can be found in [74, 75] or [76], while here only key points will be mentioned. To quantize the circuit, it makes sense to introduce generalised flux and charge variables, defined as

$$\begin{aligned} \Phi_b(t) &= \int_{-\infty}^{t} U_b(t')dt' \\ Q_b(t) &= \int_{-\infty}^{t} I_b(t')dt', \end{aligned} \tag{5.19}$$

where the subindex b indicates a certain branch of the circuit. Using those variables, a Lagrangian can be defined and further a Hamiltonian can be derived for any given circuit. For an LC circuit, we find the following Hamiltonian

$$H_{\mathsf{LC}} = \frac{Q^2}{2C} + \frac{\Phi^2}{2L}. \tag{5.20}$$

Here, Q is the charge on the capacitor and Φ corresponds to the magnetic flux in the inductor. To quantize the circuit, we impose the commutator relation $[\hat{\Phi}, \hat{Q}] = i\hbar$ and express $\hat{\Phi}$ and $\hat{Q}$ using the creation and annihilation operators $\hat{a}^\dagger$ and $\hat{a}$ [74]

$$\begin{aligned} \hat{\Phi} &= \sqrt{\frac{\hbar Z_0}{2}}(\hat{a} + \hat{a}^\dagger) \\ \hat{Q} &= \sqrt{\frac{\hbar}{2Z_0}} i(\hat{a}^\dagger - \hat{a}). \end{aligned} \tag{5.21}$$

Here, we introduced the impedance of the circuit, $Z_0 = \sqrt{L/C}$. Further, we obtain the commutation relation $[\hat{a}, \hat{a}^\dagger] = 1$. Putting this back into the Hamiltonian, Eq. 5.20, we get

$$H_{\mathsf{LC}} = \hbar\omega_c \left(\hat{a}^\dagger \hat{a} + \frac{1}{2}\right). \tag{5.22}$$

This is the Hamiltonian describing a linear resonator, already used in chapters 2 and 3. Usually the factor $1/2$ is neglected as it only gives a constant offset. We want to note that a Josephson junction itself has next to its inductance a capacitance and also forms an LC resonator on its own, at the so-called plasma frequency.

5.2.2 Describing loss in resonators

Such an LC circuit also is susceptible to loss. At first we will consider the general idea for adding loss to such a circuit [77] and afterwards we will discuss the different kinds of loss mechanisms in more detail. To add loss, we can add a resistor in parallel to the LC circuit, , Fig. 5.2. While the resonance frequency of the circuit does not change, assuming for our devices typical large quality factor, the resonance feature gets a bandwidth, which depends on the loss. Here, it makes sense to introduce the so-called quality (Q) factor

$$Q = \omega_c \frac{\text{average energy stored}}{\text{energy loss/second}}, \tag{5.23}$$

which compares the stored energy to the energy lost per cycle. The quality factor can be calculated from the circuit parameters as follows

$$Q = \frac{R}{\omega_c L} = \omega_c RC. \tag{5.24}$$

The Q factor relates directly to the bandwidth, where the bandwidth in reduced frequency (normalised to ω_c) is given by

$$\mathsf{BW}[\omega/\omega_c] = \frac{1}{Q}. \tag{5.25}$$

By changing to direct frequency, we obtain the linewidth as $\kappa = \omega_c/Q$.

5.2.3 Loss mechanisms superconducting resonators

While supercondcuting resonators transport current without resistance, there are still mechanisms which lead to loss. Typically there are many loss mechanisms. To quantify them it is useful to introduce the participation ratio (p_n) and the loss tangent ($\tan\delta_n$) [78]. The first gives the amount of energy stored in a mechanism sensitive to loss, the latter how lossy a process is, which is an intrinsic property. With this we can express the Q factor as

$$\frac{1}{Q} = \sum_n \frac{1}{Q_n} = \sum_n \frac{1}{p_n \tan\delta_n}. \tag{5.26}$$

We distinguish between internal and external loss mechanisms. External (or coupling) loss is necessary in order to excite and read out a resonator and typically can be controlled by carefully engineering the setup, while internal loss mechanisms are typically intrinsic to a device. In the following we will focus on internal loss mechanisms, while a more sophisticated discussion on external coupling is done in [78].

A discussion on how different geometries will effect the participation ratio of internal loss mechanism can be found in [78] or also in [79]. Here, we will discuss two reasons for internal loss mechanisms which will become relevant for the measurements discussed later: Losses due to two level systems (TLS) and losses due to quasiparticles, which are especially relevant for increasing temperature.

A major loss mechanism of many superconducting resonators are TLS. The idea is that TLS exist around the resonator with a frequency similar to the resonance frequency, and couple to the excitation of the resonator via the electric field. The origin of these TLS is an ongoing debate in literature as well as ways of improving the quality factor of resonators, e.g. [80, 81, 82, 83]. Characteristic properties of such TLS are, that they can be saturated with increasing power and temperature, meaning that the quality factor of the resonator increases. The power dependence of the quality factor on TLS is given by [80, 84]

$$\frac{1}{Q_i}(\bar{n}_c) = p_{\mathsf{TLS}} \tan\delta^0_{\mathsf{TLS}} \frac{\tanh\left(\frac{\hbar\omega_c}{2k_bT}\right)}{\sqrt{1+\left(\frac{\bar{n}_c}{\bar{n}^{\mathsf{crit}}_{\mathsf{TLS}}}\right)^{\beta}}}. \tag{5.27}$$

Here, p_{TLS} is the filling factor, which can be seen as the participation ratio and $\tan\delta^0_{\mathsf{TLS}}$ is the loss tangent at zero temperature. As those parameters are not necessarily easy to distinguish, they can be combined to a loss parameter $k = p_{\mathsf{TLS}} \tan\delta^0_{\mathsf{TLS}}$. Further, n_c is the circulating power, here given as photons in the resonator, with a critical value $\bar{n}^{\mathsf{crit}}_{\mathsf{TLS}}$, above which TLS are excited, leading to saturation and an increase in quality factor [80]. Further, β is usually on the order of unity and takes the non uniformity of the electric field distribution around the resonator into account [80]. The energy of the TLS, $\hbar\omega_c$, is compared to the thermal bath. As it is a resonant process it is sufficient to consider TLS having a frequency close to the resonator's

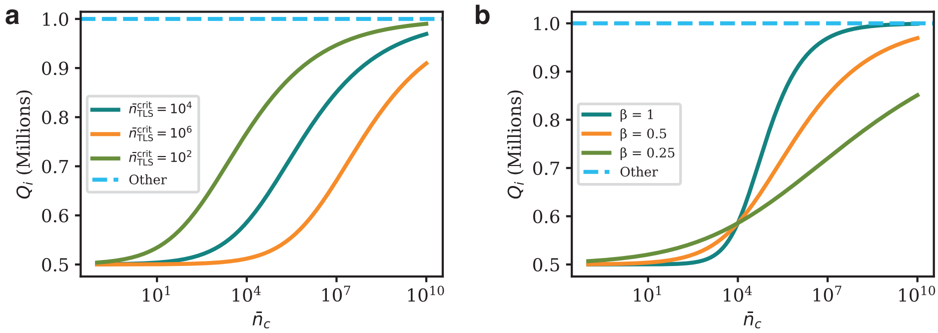

Figure 5.3: Change of quality factor due to TLS related losses with increasing drive strength. The following parameters are used: $\omega_c/2\pi = 8\,\text{GHz}, Q_{\text{other}} = 1 \times 10^6$ and a combined loss parameter of $k = 1 \times 10^{-6}$. **a.** Change of internal quality factor with $\bar{n}^{\text{crit}}_{\text{TLS}}$, while β is kept constant at 0.5. **b.** $\bar{n}^{\text{crit}}_{\text{TLS}}$ is kept constant at 10^4 and β is varied. We see that $\bar{n}^{\text{crit}}_{\text{TLS}}$ mainly influences, at which photon number TLS start to get saturated and Q_i increases, while β has most impact on the steepness of the curve. Generally, the quality factor increases, until limited by another loss mechanism (Q_{other}).

frequency. Fig. 5.3 shows the power dependence of the internal quality factor. Comparing what happens when either changing $\bar{n}^{\text{crit}}_{\text{TLS}}$ or β.

The change of quality factor with temperature is given by [84]

$$\frac{1}{Q_i}(T) = p_{\text{TLS}} \tan \delta^0_{\text{TLS}} \tanh\left(\frac{\hbar\omega}{2k_bT}\right). \tag{5.28}$$

This equation is valid in the weak field limit, such that the drive does not saturate TLS.

Next to influencing the quality factor, TLS also lead to a shift in resonance frequency [84, 80]

$$\Delta\omega_c(T) = \omega_c(0)\frac{p_{\text{TLS}} \tan \delta^0_{\text{TLS}}}{\pi}\left(\text{Re}\Psi\left(\frac{1}{2} + \frac{1}{2\pi i}\frac{\hbar\omega_c(T)}{k_bT}\right) - \log\left(\frac{\hbar\omega_c(T)}{k_bT}\right)\right). \tag{5.29}$$

Here, Re(Ψ) is the real part of the complex digamma function. In contrast to the effect on Q_{int} (Eq. 5.28), off resonant TLS contribute to the frequency shift, which also makes the frequency shift independent of power.

Another loss mechanisms is due to quasiparticles, when Cooper pairs start to break due to thermal activation [85, 86]. This effect becomes dominant when the bath temperature exceeds around 10% of the critical temperature of the superconductor [85]. We can approximately model this effect by using a two fluid model, where the resistance in dependence on temperature is described by Eq. 5.3.

Fig. 5.4 shows the influence of TLS and quasiparticle loss on a superconducting resonator, by plotting the dependence of the internal quality factor on the temperature, also another temperature independent loss mechanism, Q_{other}, is included. With increasing temperature, the quality factor initially rises due to saturation of TLS. In case of aluminium, having a lower critical temperature, losses from quasiparticles start to dominate from 200 mK onwards. In contrast to that, owing to the higher T_c, in case of niobium, the quality factor rises much higher, before being dominated by quasiparticles loss form around 2 K onwards.

Fig. 5.5 shows the change of resonance frequency introduced by TLS (Eq. 5.29) for different loss parameters k, where we always see a characteristic dip for low temperatures independent of the loss parameter, before a steady increase of frequency. With increasing temperature, we also expect to see an effect due to quasi particles, where it depends on the critical temperature of the superconductor, at which temperature this becomes relevant. More information on this can be found in [86, 87].

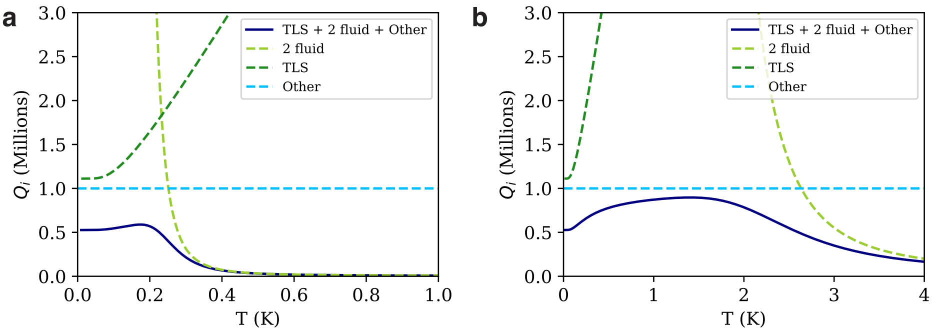

Figure 5.4: Change of quality factor due to TLS related losses and quasi particles with increasing bath temperature. Besides a prefactor $A = 1$ used to calculate the Q within the two fluid model, Eq. 5.3, the parameters are the same as in Fig. 5.3. **a.** Change of Q_i with increasing temperature in the case of aluminium. Initially the quality factor rises, as TLS get saturated, but above about 200 mK the breakdown of superconductivity dominates and leads to a drastic decrease of the Q factor. **b.** Same as in (a), but for niobium having a much higher critical temperature. Here the quality factor rises until about 1.5 K and only above it is limited by a breakdown of superconductivity.

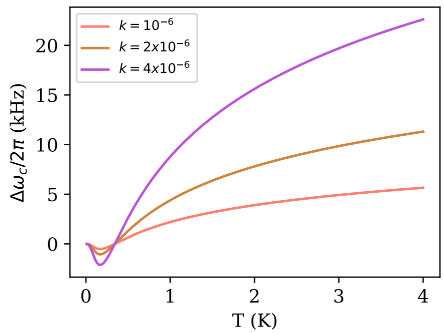

Figure 5.5: TLS induced frequency shift against bath temperature shown for three different values of the loss parameter k and using $\omega_c/2\pi = 8$ GHz.

5.3 SQUIDs as magnetic field sensors

In Chapter 5.1.3 we have already discussed that the properties of a SQUID depend on the external magnetic field. Thus, a SQUID can be utilised as a magnetic field sensor. Even more though, they are among the most sensitive magnetic field sensors which exist. SQUIDs are widely used for medical purposes, i.e. for neurological screening of the brain, where fields down to fT are measured [71]. Also they are sensitive enough to detect spins of single electrons [88]. On the one hand, SQUIDs can be operated with a DC bias current, where the change of critical current with field is directly detected [71] (DC-SQUID). On the other hand, a SQUID can be embedded in an LC resonator, like it is for example done in [89, 90]. A sketch of such a circuit is shown in Fig. 5.6. As a SQUID is a flux tunable inductance, Eq. 5.15, the inductance and thus the resonance frequency of an LC resonator (Eq. 5.18) depends on the magnetic field through the SQUID loop. This approach can be especially favourable, as it is free of dissipation in comparison to DC operation, where the critical current of the junctions is exceeded during the course of operation, which produces local heating [90]. As shown in Fig. 5.6, a circuit with an embedded SQUID has an additional linear inductance, which cannot necessarily be neglected. Assuming that the linear inductance, L_{lin}, is in series with the SQUID and further $L_{\text{lin}} \gg L_{\text{SQ}}$ we find the following equation for the shift of the resonance frequency

$$\frac{\Delta\omega_c}{\omega_c} \simeq -\frac{L_{\text{SQ}}(\Phi_{\text{ext}} = 0)}{2L_{\text{lin}}} \frac{1}{\left|\cos\left(\frac{\pi\Phi_{\text{ext}}}{\Phi_0}\right)\right|}. \tag{5.30}$$

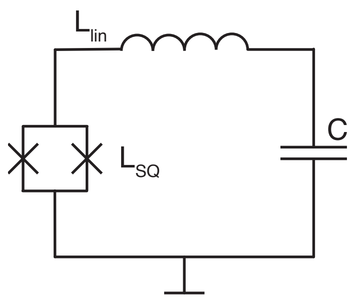

Figure 5.6: SQUID in series with an LC circuit. This leads to a resonator with a nonlinear inductance and its frequency depends on the magnetic field through the SQUID loop.

Here, we neglected the geometric inductance of the SQUID loop itself ($\beta_l \ll 1$), which would prevent the calculation of an analytical solution. In Fig. 5.7 we show the tunability of an LC

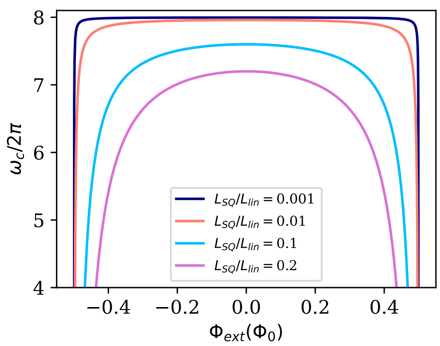

Figure 5.7: Flux tunability for an LC resonator with an embedded SQUID according to Eq. 5.30. We use $\omega_c/2\pi = 8\,\mathrm{GHz}$. When the ratio $L_{\mathrm{SQ}}/L_{\mathrm{lin}}$ increases, the total inductance increases, which lowers the unbiased resonator frequency.

resonator with a SQUID embedded for different ratios of the linear resonator inductance to the SQUID inductance. While for an increasingly dominating linear inductance, the resonator frequency is barely influenced for most flux bias points, it is highly sensitive close to a flux bias of $\pm 0.5\phi_0$.

5.4 A circuit with a Josephson junction as a Duffing oscillator

In here, we will discuss how to describe a circuit having a junction within the Duffing framework, introduced in Chapter 3.2. For simplification, let us only consider a single junction, with its nonlinearity coming from the first Josephson equation 5.5. There is fundamental no difference of treating a single junction or a SQUID in terms of nonlinearity. However, by biasing the SQUID, the inductance can be changed, which does not only change the resonance frequency of the circuit, but also the strength of the nonlinearity. This aspect will be discussed in more detail in Chapter 5.5. For an unbiased SQUID, the critical current is double compared to a single junction which halves the inductance, besides that both can be treated identically.

For now, let us consider a junction in parallel with a capacitor and a resistor, driven by a current source (Fig. 5.8). As will be briefly discussed in the end, identical conclusions can be drawn for a series circuit.

To solve this circuit, it makes sense to use the generalised flux introduced in Eq. 5.19. Furthermore we rescale it as $\delta = \Phi\frac{2\pi}{\Phi_0}$, where we see that δ is also the phase across the junction, as introduced with the second Josephson equation, Eq. 5.6. Using Kirchhoff's law,

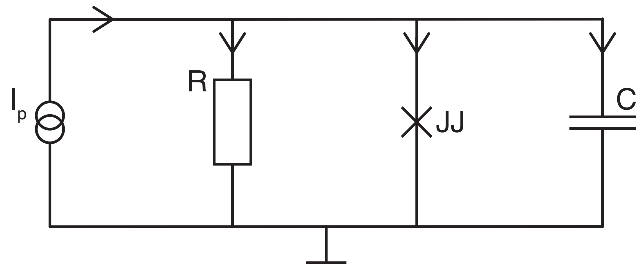

Figure 5.8: Circuit of a resistor, Josephson junction and capacitor in parallel, driven by a current source. As the junction is a nonlinear element, this circuit can be approximately described by the Duffing model, introduced in chapter 3.

we arrive at

$$C\frac{\Phi_0}{2\pi}\ddot{\delta}(t) + \frac{\Phi_0}{2\pi R}\dot{\delta}(t) + I_c \sin\left(\delta(t)\right) = I_p(t), \tag{5.31}$$

where I_p is the drive current, R the resistance, which can be also seen as the resistance of the current source. To simplify, we use that the inductance of the circuit is only given by the junction such that $\omega_c = 1/(L_{J0}C)$ and further use that the linewidth $\kappa = RC$, which can be seen form Eq. 5.24. We further develop the sine to third order and obtain after re-arranging

$$\ddot{\delta}(t) + \kappa\dot{\delta}(t) + \omega_c^2\left(\delta(t) - \frac{\delta(t)^3}{6}\right) = \omega_c^2\frac{I_p}{I_c}\cos(\omega_p t). \tag{5.32}$$

Where we also assumed a sinusoidal drive. This equation is now identical to the Duffing equation, introduced with Eq. 3.28, by using $\beta \mathrel{\widehat{=}} -\omega_c^2/6$, $F \mathrel{\widehat{=}} \omega_c^2\frac{I_p}{I_c}$ and $x \mathrel{\widehat{=}} \delta$. Thus, the Duffing model is a valid model for describing the behaviour of such a circuit and we also expect to see effects like gain, as investigated in Chapter 3.1.1.

What we discussed here is a circuit with its elements in parallel. As it will become apparent later, the circuit used in the experiment is closer to a circuit having the elements in series. While it is more complicated to derive such a circuit, it also comes down to the Duffing model, as does any cubic nonlinearity added to a linear resonator. A more in-depth discussion can be found in [91].

It is worth noting, that the critical point, where bistability is achieved (Eq. 3.9), can only be achieved if the current necessary for this critical point is (sufficiently) below the critical current of the junction. Sufficiently means that the Taylor expansion of the sine is still valid. The condition which needs to be fulfiled is

$$\frac{4}{3^{1/4}}\sqrt{\frac{L_{\text{tot}}}{L_{\text{SQ}}}}\frac{1}{Q} = \frac{4}{3^{1/4}}\sqrt{\frac{1}{pQ}} = \frac{I_{crit}}{2I_0} < 1 \tag{5.33}$$

Here, L_{tot} is the total inductance of the resonator and p is the participation ratio of the inductances $L_{\text{SQ}}/L_{\text{tot}}$. Here, the conditions for a SQUID are already used, having double the critical current and half the inductance compared a single junction.

5.5 Equivalence of a junction to a Kerr nonlinearity

In Chapter 3 we started with the Hamiltonian for a nonlinear system, Eq. 3.1. In that chapter we later saw that this formulation is identical to the Duffing model. Here, in Chapter 5.4, we have seen that a circuit with a Josephson junction can be treated within the Duffing model. This implies, that that the nonlinear junction is a Kerr nonlinearity. Still, it is worth directly showing, that the Hamiltonian used as a starting point in Chapter 3 can be found using the circuit elements and the junction introduced in this chapter. For this we will consider a series circuit, similar to the one depicted in Fig. 5.6, however having a single junction instead of a SQUID, where the only difference is that the Josephson energy E_{J0} would simply double in case of the unbiased SQUID. We start with the Hamiltonian of the LC circuit, Eq. 5.20, and add the influence of the junction using the Josephson energy (Eq. 5.11) [92]

$$H_{\mathsf{LC}}^{\mathsf{NL}} = \frac{Q_C^2}{2C} + \frac{\Phi_L^2}{2L} - E_{J0}\cos\left(\frac{\Phi_J 2\pi}{\Phi_0}\right) \tag{5.34}$$

Here, Φ_J (Φ_L) is the generalised flux over the respective branch of the circuit and Q_C is the generalised charge. Also it should be noted, that we did not rescale the generalised flux here, which is the reason for the $2\pi/\Phi_0$ in the cosine term related to the junction. It should be noted, that here it is possible to simply add the Josephson energy to the Hamiltonian as the considered circuit is a parallel circuit with a single node. For more complex circuits, the Hamiltonian has to be derived from the Lagrangian.

Assuming a small Φ_J, we can develop the cosine to fourth order and absorb the $\propto \Phi_J^2$ term in the linear inductance, while the $\propto \Phi_J^4$ provides us with the nonlinearity. Now, using the operators introduced in Eq. 5.21 and ignoring fast rotating terms we find [92]

$$H_{\mathsf{LC}}^{\mathsf{NL}} = \hbar\omega_c \hat{a}^\dagger \hat{a} + \hbar\frac{\mathcal{K}}{2}\hat{a}^\dagger\hat{a}^\dagger\hat{a}\hat{a}, \tag{5.35}$$

where we used

$$\mathcal{K} = -\frac{\pi p^3 \omega_c Z_0 e^2}{h}, \tag{5.36}$$

with p being the participation ratio of the inductances, L_J/L_{tot}. This is exactly what we started with in Chapter 3 to derive the expressions for the gain and shows that such a Hamiltonian is a good model for our system.

In the previous chapters, we have introduced linear optomechancis, which we combined with nonlinear cavities, to arrive at the field of nonlinear optomechanics. In this chapter, we have discussed that a nonlinear cavity can be realised as a superconducting resonator. In addition, we also discussed the capabilities of such a superconducting cavity with an embedded SQUID as a magnetic field detector. Now, we have a sufficient theory background to understand the experiment, where a discussion of the setup follows.

6 Experimental platform

In this chapter, we will discuss our experimental platform, being microstrip cavities in 3D waveguides. We will consider the working principle of the cavities and how they are coupled to the waveguide. Further, we will discuss which different cavity designs were used, the design considerations and how our optomechanical setup was built. Lastly, we will consider the complete measurement setup.

6.1 Microstrip cavity in a 3D waveguide

A 3D rectangular waveguide forms the environment for our cavities, allowing to readout and excite them [79, 44].

6.1.1 The 3D rectangular waveguide

3D rectangular waveguides are hollow tubes made from a conducting material with a rectangular cross section. Here the key properties of such waveguides are introduced, where a much more sophisticated description can be found in [77].

Electromagnetic fields can propagate in such waveguides and the fields of the propagating modes can be solved analytically using Maxwell's equations. Fig. 6.1a shows a sketch of a rectangular waveguide with the propagation in z direction. In Fig. 6.1b there is a picture of an assembled aluminium waveguide, where already an input and output coupler are connected to a central waveguide section. This section has five slots for samples in each of the three rows with a sample holder already mounted above the central row.

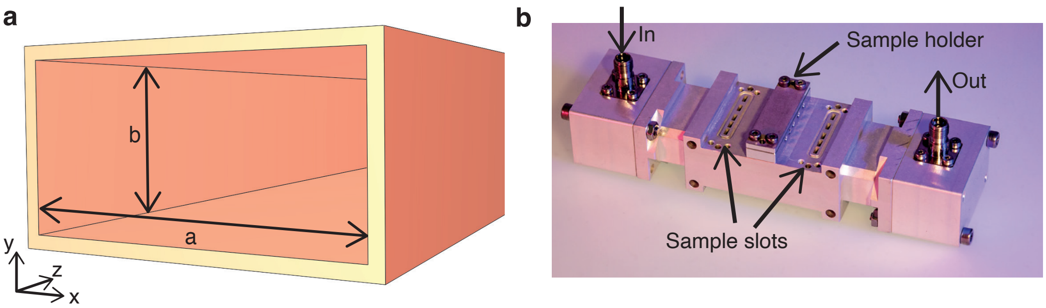

Figure 6.1: Illustration and picture of a rectangular waveguide. **a.** Illustration of a rectangular waveguide, being a rectangular tube, with the propagation in the z direction. We assume $a > b$. **b.** Picture of the aluminium waveguide used in some of the experiments. In the beginning and the end, there are couplers to connect a coaxial cable, which allow to excite waveguide modes and thus to couple into and out of the waveguide. Three rows of slots in the central waveguide section allow to place samples in the waveguide. Over the central row of holes, there is a sample holder installed. Picture by M. Knabl/IQOQI.

To solve the fields inside waveguides, we generally distinguish between TE and TM modes, where either no electric field component (TE mode) or no magnetic field component (TM mode) exists along the propagation direction. The propagation along the z direction of the respective field can be written as $e^{-i\beta z}$, where β is the propagation constant, which generally depends on frequency and the shape of the waveguide. A distinct feature of waveguides consisting only of a single conductor is, that every mode has a certain cutoff frequency, depending on the dimensions of the waveguide. Only above the cutoff frequency, the mode can propagate, while below its amplitude is exponentially attenuated. The cutoff wave number, k_c, is given by $k_c = \sqrt{k^2 - \beta^2}$, where k is the wave number $k = 2\pi/\lambda$.

Now, considering the rectangular waveguide and using the boundary conditions that the electric field along the walls vanishes, we see after some calculation for the component of the magnetic field along the propagation direction [77]

$$h_z(x, y) = A_{mn} \cos \frac{m\pi x}{a} \cos \frac{n\pi y}{b}. \tag{6.1}$$

Here, $H_z(x, y, z) = h_z(x, y)e^{-i\beta z}$, m, n are integers and A_{mn} is a constant. For the electric field, we find the following expressions for the components along x and y:

$$E_x = \frac{i\omega\mu n\pi}{k_c^2 b} A_{mn} \cos \frac{m\pi x}{a} \sin \frac{n\pi y}{b} e^{-i\beta z} \tag{6.2}$$

$$E_y = -\frac{i\omega\mu m\pi}{k_c^2 a} A_{mn} \sin \frac{m\pi x}{a} \cos \frac{n\pi y}{b} e^{-i\beta z}. \tag{6.3}$$

Further, the propagation constant β is given by

$$\beta = \sqrt{k^2 - k_c^2} = \sqrt{k^2 - \left(\frac{m\pi}{a}\right)^2 - \left(\frac{n\pi}{b}\right)^2}. \tag{6.4}$$

In order to allow propagation, β has to be real-valued, thus $k^2 > k_c^2$, leading to the formulation of the cutoff frequency for each mode given by

$$\omega_{mn}^c = \frac{k_c}{\sqrt{\mu\epsilon}} = \frac{1}{\sqrt{\mu\epsilon}} \sqrt{\left(\frac{m\pi}{a}\right)^2 + \left(\frac{n\pi}{b}\right)^2}, \tag{6.5}$$

with ϵ and μ being the permeability of the electric and magnetic field. Here we assumed without loss of generality that $a > b$. The cutoff frequency of the fundamental mode, the TE$_{10}$ mode, is given by $\omega_{10}^c = \pi/(a\sqrt{\mu\epsilon})$, and thus it depends on the electric and magnetic field permeabilities as well as on the width of the waveguide. This is also the mode, which is used throughout all discussed experiments.

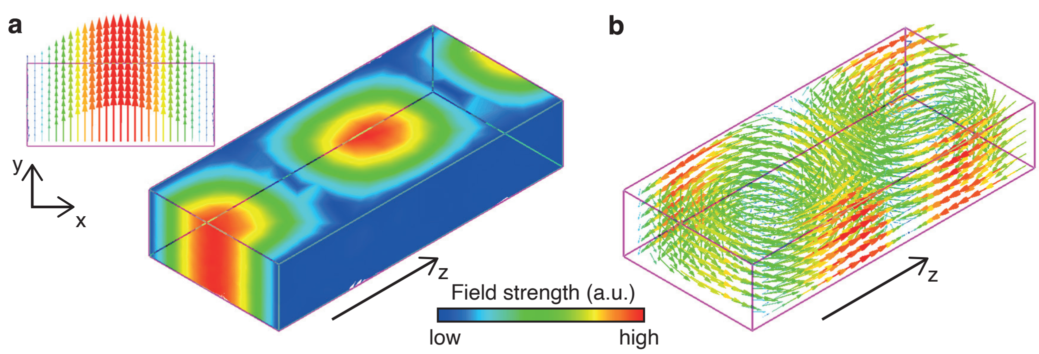

Figure 6.2: Electric and magnetic field of the fundamental TE$_{10}$ mode above cutoff. **a.** Magnitude of the electric field and (top left) vectorial depiction on the $x - y$ plane. The electric field is strongest in the centre and vanishes towards the sidewalls. There are only electric field components along the x direction. **b.** Vectorial depiction of the magnetic field. The magnetic field has its strongest components along the sidewalls, and as expected for a TE mode, has components along the propagation direction, while it has no components along the y direction.

Fig. 6.2 shows the electric and magnetic field of the fundamental TE_{10} mode. As seen in the vectorial inset, there is no electric field component along the propagation direction. Further, the electric field is strongest in the centre and symmetrically decreases towards the walls to both sides. The magnetic field on the other hand has components along the propagation direction and is strongest (in some regions) close to the walls. It further rotates along to the propagation direction.

6.1.2 The microstrip cavity

The cavities we are using are similar to microstrip resonators, which are thin conducting films on top of a dielectric substrate with a ground plane on its other side [77]. We are using films of superconductor on top of a silicon substrate having the shape of an inverted U (Fig. 6.3(a)). This shape makes them more compact in space, while it does not change their modes. Those cavities are placed in a rectangular waveguide (Fig. 6.3(b,c)), where the walls of the waveguide serve as a ground plane. The coupling to the waveguide, used for excitation and readout, will be addressed in Chapter 6.1.3. We operate the cavities on their fundamental $\lambda/2$ mode, with

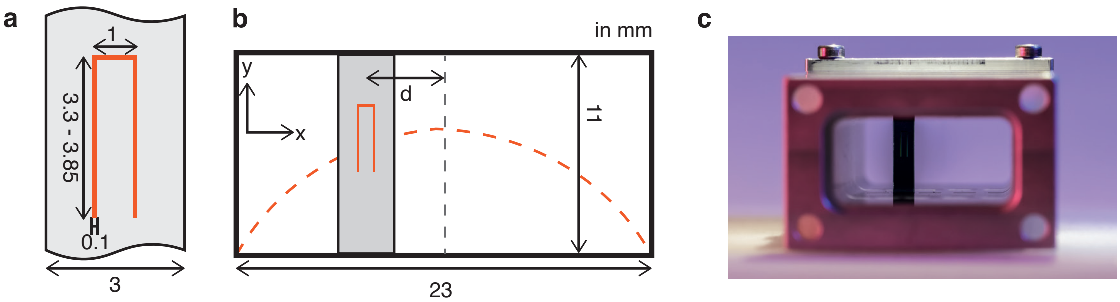

Figure 6.3: Sketch of the cavity and placement inside the waveguide. **a.** The cavity, a thin stripe of superconductor in the form of an inverted U (orange), patterned on a silicon substrate (gray). The length of the cavity legs were slightly modified for different experiments, where the range of leg lengths is given here. **b.** Sketch of the cavity inside the waveguide. The electric field strength symmetrically reduces from the centre towards the walls (dashed line). When the cavity is placed off-centre, it is excited by the potential difference between both legs. Here, d is the distance between the centre of the cavity and the centre of the waveguide. **c.** Picture of the aluminium waveguide with the cavity on the silicon substrate inside. The inner dimensions of the waveguide are given in (b), for some experiments we also used a copper waveguide of the WR-90 standard, with slightly different dimensions. Picture by M. Knabl/IQOQI.

electric field maxima at the ends of the legs and current maxima in its centre (also discussed in more detail in Chapter 6.1.3 and Fig. 6.4). Such a cavity can be modelled as a capacitively shunted transmission line, where its frequency depends on the total length and the capacitive coupling between both legs [79]. Also, due to the presence of the silicon substrate and its high permittivity, the frequency is much lower than it would - hypothetically - be in free space. As only parts of the field are stored in the substrate, while others are stored in vacuum, the exact frequency depends on the dimensions of the substrate, but also its exact dielectric constant [77]. As materials we use niobium for most cavities, while some early generation cavities were also made from aluminium. This cavity design is beneficial in terms of losses, Chapter 5.2.3, as the participation of lossy mechanisms is reduced, with parts of the field stored in (lossless) vacuum and the field stored in regions susceptible to loss is diluted over a large area.

6.1.3 Waveguide-cavity coupling

When we place a cavity off-centre in the waveguide (Fig. 6.3b,c), electric field differences arise between both legs. This potential differences excites the cavity mode, where the magnitude of the electric field is shown in Fig. 6.4(a) and the current along the cavity in Fig. 6.4(b). We

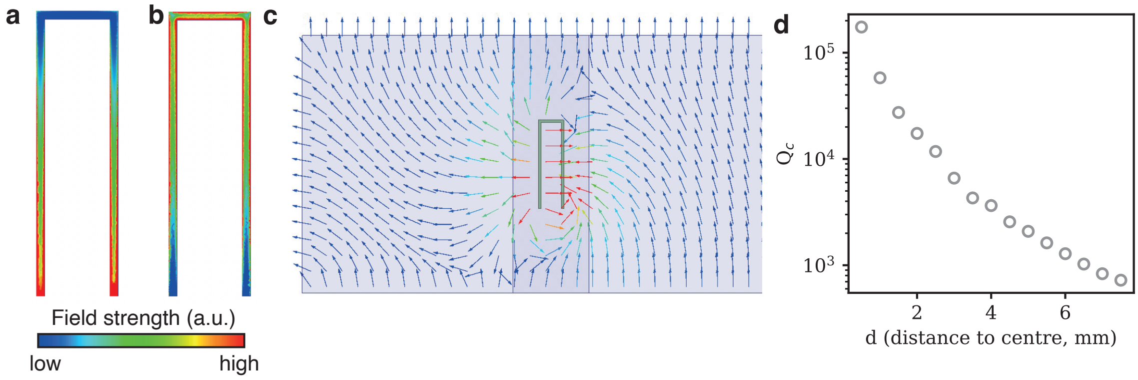

Figure 6.4: Fields along the cavity and coupling to waveguide. **a.** Electric field along the cavity of the fundamental $\lambda/2$ mode. The field is strongest at the ends of the legs and has a node in the centre. **b.** Surface current along the cavity, where the maximum current is in the centre and no current flows at the ends of the legs, as this is an open. This is $\pi/2$ out of phase compared to the field plot in (a). **c.** Vectorial depiction of the electric field in the waveguide in the plane of the cavity (right to the cavity only parts of the waveguide is shown). **d.** Simulated coupling quality factor when shifting the cavity outwards from the centre (d is the distance to the centre, compare Fig. 6.3). We see that the coupling changes over several orders of magnitude and can be set precisely by choosing the position in the waveguide. Here we already used the dimension of the WR-90 standard, having a width of 22.86 mm

clearly see that the excited mode is the fundamental $\lambda/2$ mode with an electric field node and a current anti-node in the centre. Fig. 6.4(c) shows the vectorial depiction of the electric field in the plane of the cavity, plotted at the resonance frequency of the cavity. It is strongest in the region of the cavity and perpendicular to conducting surfaces. The coupling strength depends on the gradient of the electric field over the extend of the cavity, which changes as the cavity is moved from the centre towards the wall. Exactly in the centre, we do not expect any coupling, as the field should be identical at both legs. As we shift it towards the wall, the stronger of a coupling we obtain, Fig. 6.4(d), where the coupling quality factor against the distance from the centre is plotted. For the parameters chosen in the simulation, quality factors from above 10^5 to below 10^3 could be reached. If even higher quality factors (lower couplings) are required, the cavity can be placed in the centre, with a neighbouring bare silicon or sapphire piece, to lift the symmetry of the electric field over the cavity. This was also done in the experiment, Chapter 7.1.1, and we reached coupling quality factors above one million. An alternative to adjust the coupling by the position, would be to make the legs asymmetric [79], however this is not followed within this work.

With this we see, that such a cavity in a rectangular waveguide is an approach with several benefits. It allows to simply adjust the coupling by choosing the position in the waveguide. Further, it is a low loss platform, as parts of the fields are stored in lossless vacuum. The parts stored near lossy surfaces and interfaces are diluted due to the large size of the cavity, which reduces the participation of loss mechanisms (Chapter 5.2.3).

6.1.4 Circuit model and circle fit

This measurement configuration of the cavity in a rectangular waveguide is also favourable for characterising a resonator, as internal and external (coupling) losses can be measured simultaneously, in contrast to a pure transmission measurement. The reason is, that there is also transmission through the system, when the waveguide is probed off the cavity resonance, which provides the necessary base line. A sketch of this configuration, which is known as the notch or hanger configuration, is shown in Fig. 6.5. The measurement is typically performed from port 1 (input) to port 2 (output), which is known as measuring the scattering parameter S_{21}. The

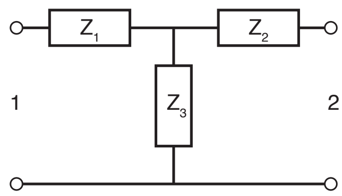

Figure 6.5: Model for a cavity in the notch configuration. The transmission line is represented by the impedances $Z_{1,2}$, the cavity by Z_3. Usually the scattering parameter from port 1 to port 2 is measured, giving a S_{21} measurement.

response of a cavity in notch configuration is given by [93]

$$S_{21}(\omega) = 1 - \frac{Q_l/|Q_c|e^{i\phi_0}}{1 + 2iQ_l\frac{\omega-\omega_c}{\omega_c}}. \tag{6.6}$$

Here, Q_l is the total quality factor and Q_c is the coupling (external) quality factor, while ϕ_0 accounts for an impedance mismatch in the microwave transmission line before and after the cavity, which makes Q_c a complex number ($Q_c = |Q_c|e^{-i\phi_0}$). The real part of the coupling quality factor determines the decay rate of the resonator to the transmission line, in our case the emission to the waveguide. The physical quantity is the decay rate, κ, which is inversely proportional to the quality factor [94] and therefore the real part is found as[1] $1/Q_c^{Re} = \mathrm{Re}(1/Q_c) = \cos\phi_0/|Q_c|$. Knowing Q_c^{Re} and Q_l, the internal quality factor can be obtained, as $1/Q_l = 1/Q_c^{Re} + 1/Q_{\mathrm{int}}$ [94] (Eq. 5.26). In case $Q_c^{Re} \simeq Q_i$, the setup is considered as being critically coupled. In case $Q_c^{Re} \ll Q_i$, the setup is known as being undercoupled and the opposite is an overcoupled setup. Plotting the imaginary versus the real part of S_{21} forms a circle in the complex plane, thus fitting the cavity response with this model is known as performing the circle fit.

Eq. 6.6 represents an isolated resonator, not taking effects from the environment into account. With the environment, which arises by including the whole measurement setup before and after the cavity, Eq. 6.6 becomes [93]

$$S_{21}^{\mathrm{full}}(\omega) = (ae^{i\alpha}e^{-i\omega\tau})S_{21}(\omega). \tag{6.7}$$

Here a and α are an additional attenuation and phase shift, independent of frequency and τ is the electrical phase delay of the microwave signal over the measurement setup.

6.2 Different cavity designs

We made several different designs of the U-shape microstrip cavity, introduced in Chapter 6.1.2. The first generation of cavities aimed at understanding the properties of such a cavity design, with a special interest on investigating internal losses. In this generation we had cavities made from aluminium and niobium. The second generation made soley from niobium came with a junction or a SQUID in the centre, to determine their influence on the cavities and to especially see the sensitivity to magnetic fields using the SQUID setup. Those samples were then also used in the final optomechanical setup. Here, we will consider how each of those samples was fabricated and which specific considerations were made in the design.

6.2.1 Cavities without a feature in the centre

As we did not have a cleanroom at our university until summer 2018, the Fachhochschule Vorarlberg fabricated those samples for us. Standard optical lithography techniques were used

[1]When speaking of Q_c while discussing the results, usually one refers to Q_c^{Re}.

in the fabrication together with sputter deposition of the metallic films. Structuring of the metal layer was done using a wet etching process for the aluminium samples and a reactive ion etching (RIE) process for niobium. After completely removing the photoresist, both samples were cleaned in an oxygen plasma.

For finding the optimal dimensions, finite element simulations were performed using HFSS [95]. We used a leg length of either 3.65 mm or 3.85 mm and expect a frequency of either around 8 GHz or 7.5 GHz. The initial design as well as first simulations of those resonators were performed by a former PhD student in our group, Phani R. Muppalla.

The internal quality factor we expected was in the range of a million. Simulations showed that putting the sample one slot off centre in the waveguide would lead to much lower coupling quality factors (Fig. 6.4(d)), which is not ideal for the circle fit. Thus, we decided to place the samples in the central slot and add a bare silicon substrate in a neighbouring slot. This lifts the symmetry of the electric field in the waveguide and also leads to coupling quality factors in the range of one million.

6.2.2 Cavities with a via, a single junction or a SQUID in the centre

Our second generation was fabricated by a company called Star Cryoelectronics (Starcryo), which was necessary due to the sophisticated Nb/Al/Nb trilayer process typically used making Josephson junctions in niobium, as it gives reliable parameters for the junctions [96].

First, let us discuss some details about the fabrication process for those samples. All samples of the second generation were fabricated within a single run. In the first step, the base electrode, a Nb/Al-AlOx/Nb trilayer is deposited, which is the layer with the junction and AlOx serves as the insulating barrier. The trilayer has a total thickness of around 270 nm, where the Al has a thickness of 9 nm. In a next step, the junctions are defined using a resist mask and the top Nb is removed by RIE in all regions besides the junctions. Afterwards, the base electrode is defined from the trilayer by etching it away in areas where it is not needed. With this, the bottom layer is completely defined. To separate this layer from the top wiring layer, a SiO_2 dielectric layer of around 300 nm is deposited, serving as an insulator. To connect to the bottom layer, vias are etched through this dielectric layer. Then another Nb layer of around 300 nm is deposited, serving as the top electrode, and a RIE is again used to define it. On a special request, the SiO_2 was removed in areas far from the junction, as this layer is a possible source of dielectric losses and we wanted to avoid having this layer in areas of high electric field (at the ends of the cavity legs, Fig. 6.4). The region where the SiO_2 remained can for example be seen in Fig. 6.6 or Fig. 6.8.

We ordered three different cavity designs, with either a via in the centre connecting both electrodes, a single junction or a SQUID, Fig. 6.6. We used two different variants for the SQUID, defined either with thin wires or a SQUID washer feature. In total, we got 18 samples, with two having only a via, eight having a single junction, with four of them having also a via and four samples for each different SQUID variant. The samples with the via and single junctions aimed at testing the behaviour when adding the junction. Also the nonlinearity could be tested with the single junction devices. The idea for the SQUID samples was, to test them as magnetic field sensitive detectors and eventually use them in our optomechanical setup, as explained in Chapter 5.3. Additionally, we also got a planar microcoil, with the intention to test the SQUID's tunability and its response to a fast alternating flux, some details on this will be given in Chapter 7.1.4.

Now, to the design parameters we chose for the samples. The outer dimensions are similar to the first generation samples, Chapter 6.2.1. Only the leg length was slightly modified to 3.5 mm and 3.3 mm to increase the resonance frequency. The critical current of the junctions can be chosen in the design process, and is given by the critical current density and the junction area. Deciding for the smallest critical current possible in the Starcryo process, we ended up with a design value of 8.4 μA. For deciding on a loop size for the SQUID, a smaller loop is preferable

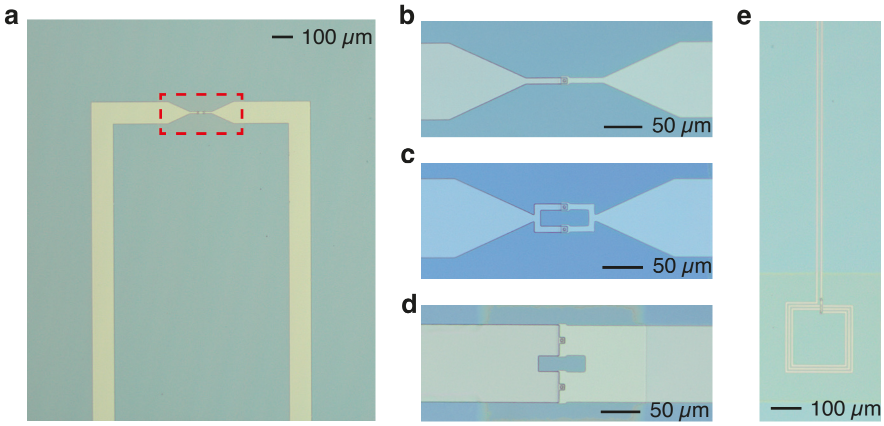

Figure 6.6: Microscope images of different Starcryo cavity designs. **a.** Image of the cavity taken with an optical microscope and indicated magnified region in b-d. **b.-d.** Microscope zoom in on different cavity designs. In (b) the cavity with a single junction, in (c) with a conventional SQUID design and in (d) with the SQUID washer design. Additionally we also had designs of a single junction followed by a via or only a via. **e.** Image of the microcoil used for some flux biasing tests in the early stages of the experiment. In (d) and (e) the slightly different coloured section shows where the separating SiO_2 layer was not removed.

to reduce the linear inductance, and thus β_l (Eq. 5.16). However, for detecting magnetic fields, a large loop having a bigger area is preferable to be more sensitive to fields. As will be discussed in Chapter 6.3, we added a magnetic cantilever with a width of about 50 μm above the SQUID loop, where we wanted to approximately match this size for ideal coupling. Keeping this in mind, we settled for a loop size of 60 μm × 20 μm, as an ideal compromise, between a comparable size to the cantilever and still an acceptable β_l of 0.7 for the conventional SQUID and 0.5 for the SQUID washer. In addition, we ran several simulations using HFSS to learn about the behaviour of a SQUID in the centre of the cavity. We accounted for the junctions by adding a fixed value for the inductance, which we also tuned to simulate the tunability with a changing magnetic field.

6.3 Mechanical cantilever

Up to now, we have discussed the microwave (photonic) part of our setup, with the waveguide and the cavity itself. As already discussed in Chapter 5.3, a cavity with an embedded SQUID is sensitive to magnetic fields, which we want to use for coupling a mechanical element. The mechanical element is a cantilever - a single clamped beam - which we equip with a magnet.

We use commercial atomic force microscopy cantilevers from BudgetSensors, which come without a tip. The typical frequency range for the used cantilevers is 200 to 500 kHz. Their dimension is typically 100 μm × 50 μm with a thickness of about 3 μm. As they do not come with a (magnetic) tip, we decided to in-house equip them with a tip. This protocol was developed Mathieu L. Juan, a former PostDoc in our group. Here, the basic recipe of how a magnetic cantilever can be prepared and put on top of the microwave cavity is given:

- First, the magnetic powder is ground, where we are using Neodymium Iron Boron powder from a company called Nanoshel. The grain size we aim for is around 20 μm, to be below the width of the cantilever, where the grains in the powder are typically too large.

- To deposit the magnet on top of the cantilever, we work below an optical microscope and use micro manipulators. To aid the pickup with the needle attached to the micro manipulator, we add a small amount of Stycast to its tip. We also put a small drop of Stycast on the tip of the cantilever, to ensure that the magnet sticks.

- After deciding for a magnet, we pick it up with the needle and use the micro manipulators to bring it close to the cantilever. As soon as the magnet is close to the tip of the cantilever, it is usually sucked by the Stycast drop on its tip. Afterwards, the Stycast has to dry. Fig. 6.7a,b shows the magnet on top of the cantilever, with either the cantilever or the top of the magnet in focus.

- In the next step, we magnetise the cantilever tip using a home built magnet, with a magnetic field of 2 T. With this the cantilever is ready to be placed on top of the microwave cavity.

- To glue the cantilever chip to the silicon chip of the cavity, we use a drop GE Varnish. We place this drop in the vicinity of the SQUID on top of the silicon substrate, as the cantilever only extends 100 µm out of its chip.

- We then place the cantilever chip on top of the Varnish drop, with the magnet facing down. To make sure, that both chips stick together, we firmly press the cantilever chip against the cavity chip using a pair of tweezers for a about a minute. A second pair of tweezers is used to control the positioning of the cantilever directly above the SQUID loop. Also this procedure is performed below the optical microscope. Fig. 6.7c,d shows two pictures of the cantilever above the SQUID loop. Again one time focusing on the SQUID and one time on the tip of the cantilever, which is used to read off the SQUID-cantilever distance. The distance can be roughly controlled, by the size of the Varnish drop, where exactly it is placed on the cavity chip and the amount of force applied when pressing the cantilever chip. However, this is not very well controlled, and a better alignment procedure might be useful in the future. After drying, the sample is ready to be put into the waveguide.

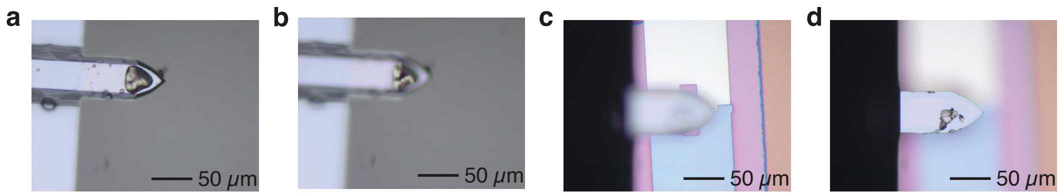

Figure 6.7: Placement of the magnet on the cantilever and afterwards of the magnetised cantilever on top of the SQUID loop. **a.,b.** Cantilever with magnet on top and changing the focus from the tip of the cantilever to the highest feature of the magnet to measure its height. Here the magnet is approximately 8 µm high. **c.,d.** Cantilever on top of the SQUID loop, in (c) focusing on the cavity and in (d) on the backside of the cantilever. With this we could estimate a distance of around 30 µm including the height of the magnet and the cantilever. As can be seen, the cantilever can be placed with high accuracy above the SQUID loop. Picture by D. Jordan/IQOQI.

- To slide the sample into the waveguide, we screw it into a sample holder, made from aluminium or copper. Such a holder can be e.g. seen in Fig. 6.3 or 6.8. In the first iterations, this was a simple holder, where the sample was fixed with a screw, and a small indium sphere provided cushioning. In later iterations, a screw pressed against thin metal plates, which deformed and allowed to fix the sample more gently.

Fig. 6.8 shows a photograph of the complete experimental device. This device is then put into the waveguide, where the copper clamp, used to hold the sample in place is seen in the background. This clamp is then screwed to the top of the waveguide, e.g. similar to what is seen in Fig. 6.1(b).

Such an approach, where a mechanical element is coupled to a cavity using inductive coupling became increasingly popular over recent years and is implemented by multiple groups [43, 2, 3], while already in 2008 a approach using a DC-SQUID was demonstrated [97]. The reason

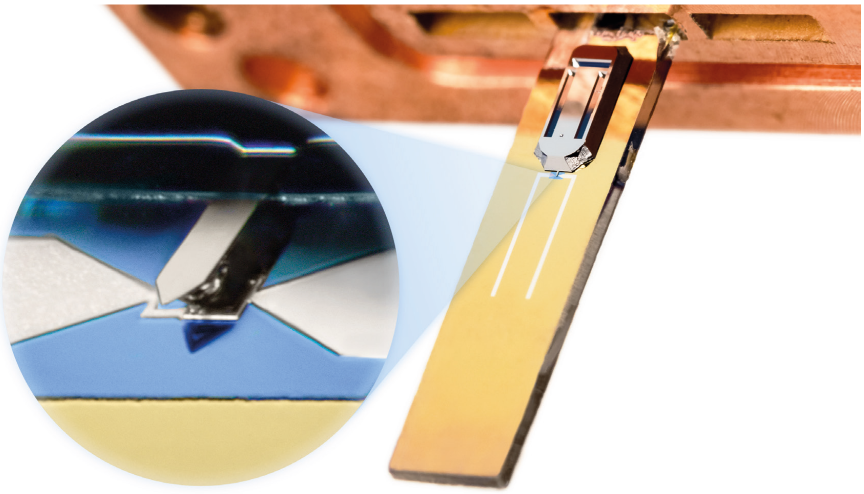

Figure 6.8: Photograph of the complete setup. U-shaped cavity (white) patterned on the silicon chip (golden). Directly above is the cantilever chip (grey), where the cantilever can be seen in the vicinity of the SQUID loop. In the background, we can see the copper clamp, necessary to mount the sample in the waveguide. The inset shows a microscope picture of the central region, where we can see the cantilever with its magnet, placed directly above the SQUID loop. The blue part on the cavity chip is the area, where the SiO_2 layer, separating the two niobium wiring layers was not removed.

to follow this approach is the expectation of much higher coupling strengths compared to the usual capacitive coupling, which already showed very encouraging results [23, 98, 99]. Our approach is also based on a proposal developed in Innsbruck [1].

In this section, we discussed the experimental device. In the final part of this chapter, we will consider the full measurement setup, including the wiring of the cryostat.

6.4 Cryostat and wiring setup

To perform the measurements it is necessary, that our cavities are in a superconducting state. The critical temperature of aluminium is around 1.2 K, however as we have seen in Chapter 5.2.3 the breakdown of superconductivity already limits high quality cavities above a few 100 mK. Additionally, it is desirable to avoid thermal occupation of the cavity, which is especially relevant working with qubits and given by the bosonic occupation statistics (Eq. 2.15). For a 8 GHz cavity we expect to be in the ground state below approximately 350 mK. All of this requires us to work at very low temperatures. To comply with this, our experiments are housed in a dilution refrigerator, which allows cooling the samples down to around 30 mK. A picture of our cryostat is shown in Fig. 6.9 including labelling of the main components. To reach such a low temperature, the cryostat has two cooling circuits. Cooling down to 4 K is provided by the pulse tube cooler, which is a powerful cooler and uses Helium injected at around 21 bar. The expansion of Helium provides the cooling similar to a domestic fridge. For cooling to lower temperatures, a mixture from ^{4}He and ^{3}He is used. While ^{4}He becomes liquid below 4 K and remains in the so-called mixing chamber at the base plate of the cryostat, ^{3}He cycles through the cryostat (and outside pumps). As it goes through the mixing chamber it dilutes the ^{4}He mix and removes heat to provide the cooling. More details about this cooling mechanism are found in [100] or [101], having also additional information about the cryostat and wiring used in our lab.

A schematic of our complete measurement setup is shown in Fig. 6.10. It shows the setup in its final form, as its complexity increased with the experiments getting more sophisticated. While the setup outside of the cryostat changed, the wiring setup inside remained mostly unchanged, besides using different waveguides and adding coils. We estimated the input attenuation to the sample with (73.0±1.5) dB. For the first generation of samples we only used the VNA, as this was sufficient to characterise their basic behaviour. This also made the power splitters unnecessary and also we did not use a coil, as those samples were not tunable by magnetic fields. We switched between different copper and an aluminium waveguide to see the influence when using different waveguides. Shielding the experiment from external magnetic field is also of major importance. For this we are using three layers of shielding directly surrounding the experiment (Fig. 6.10). For this shielding, we are using two layers of mu-metal with a layer of niobium in between. Due to its high magnetic permeability, mu-metal is well suited to protect from magnetic fields. The niobium, used as the middle layer, becomes superconducting and is therefore naturally also a very good shield from magnetic fields below its critical temperature.

While measuring the Starcryo samples, we gradually expanded the setup. In the first stages, we continued with the same VNA setup using the aluminium waveguide. Later we added a microwave generator to measure the gain on the single junction and SQUID devices. In a next step, we wanted to characterise the (fast) flux response of the SQUID samples. For this we first utilised the on chip microcoils in the aluminium waveguide. Those had to be wirebonded using the printed circuit board (PCB, see e.g. in Fig. 6.11), which proofed to be a limiting factor, as superconductivity seemingly broke there and the coils started to heat up the cryostat when applying fields in the region of a Φ_0. While we could do some tests on fast flux signals in the MHz range with those micro coils, we switched to a copper waveguide and waveguide coils subsequently (Fig. 6.11d). Adding the magnetic cantilever to the setup, we also added the spectrum analyser for measuring the modulation due to the mechanical mode. For calibration reasons, it was also required to add a delay line, something which will be explained in more detail in Chapter 7.2.3. The setup was then subsequently modified in minor regards, like changing an analogue for a digital phase shifter or changing to a digital attenuator.

This gives an overview of the used setup, the measurement results are discussed in the next chapter. Additional details, like why we decided for a specific component in the setup or an attempt to do a simply mechanical isolation will also be discussed, when the respective measurements are discussed.

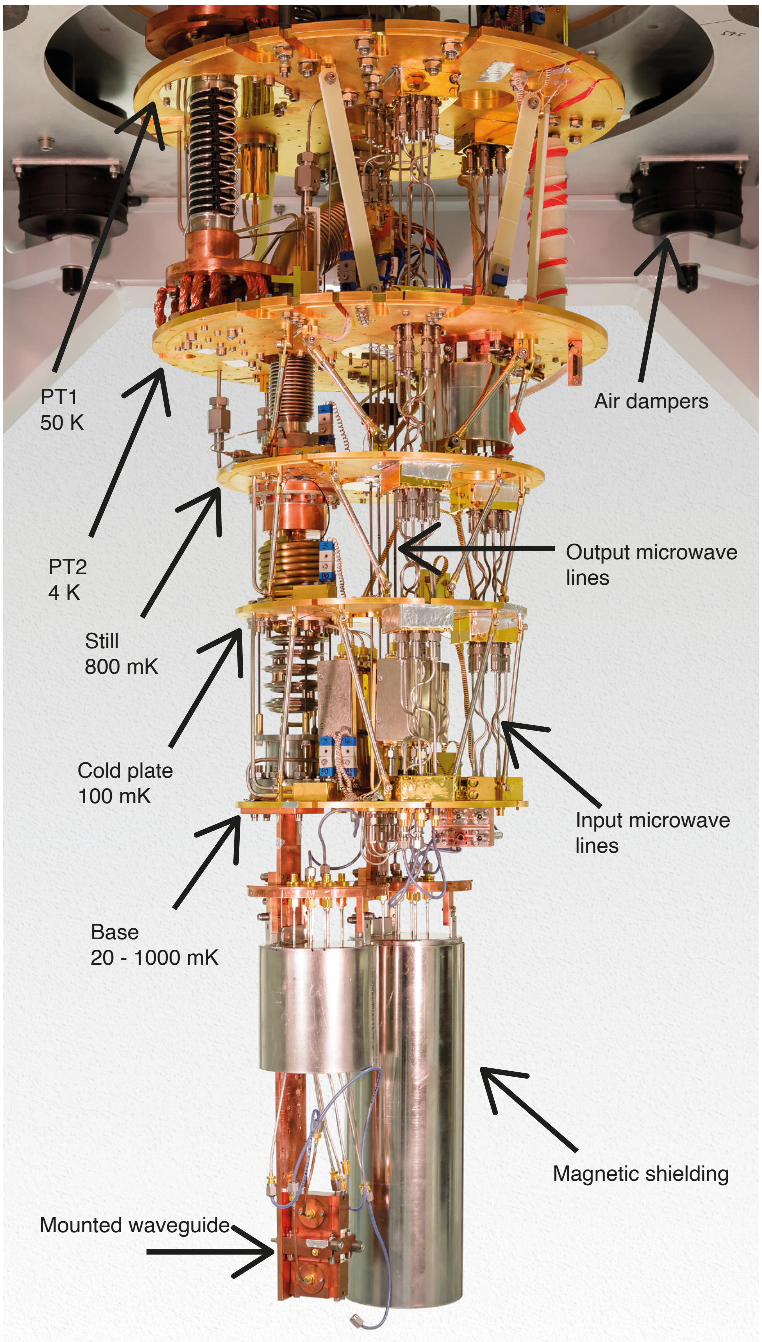

Figure 6.9: Picture of the cryostat with labelling of main components and a waveguide mounted. Picture by M. Knabl/IQOQI.

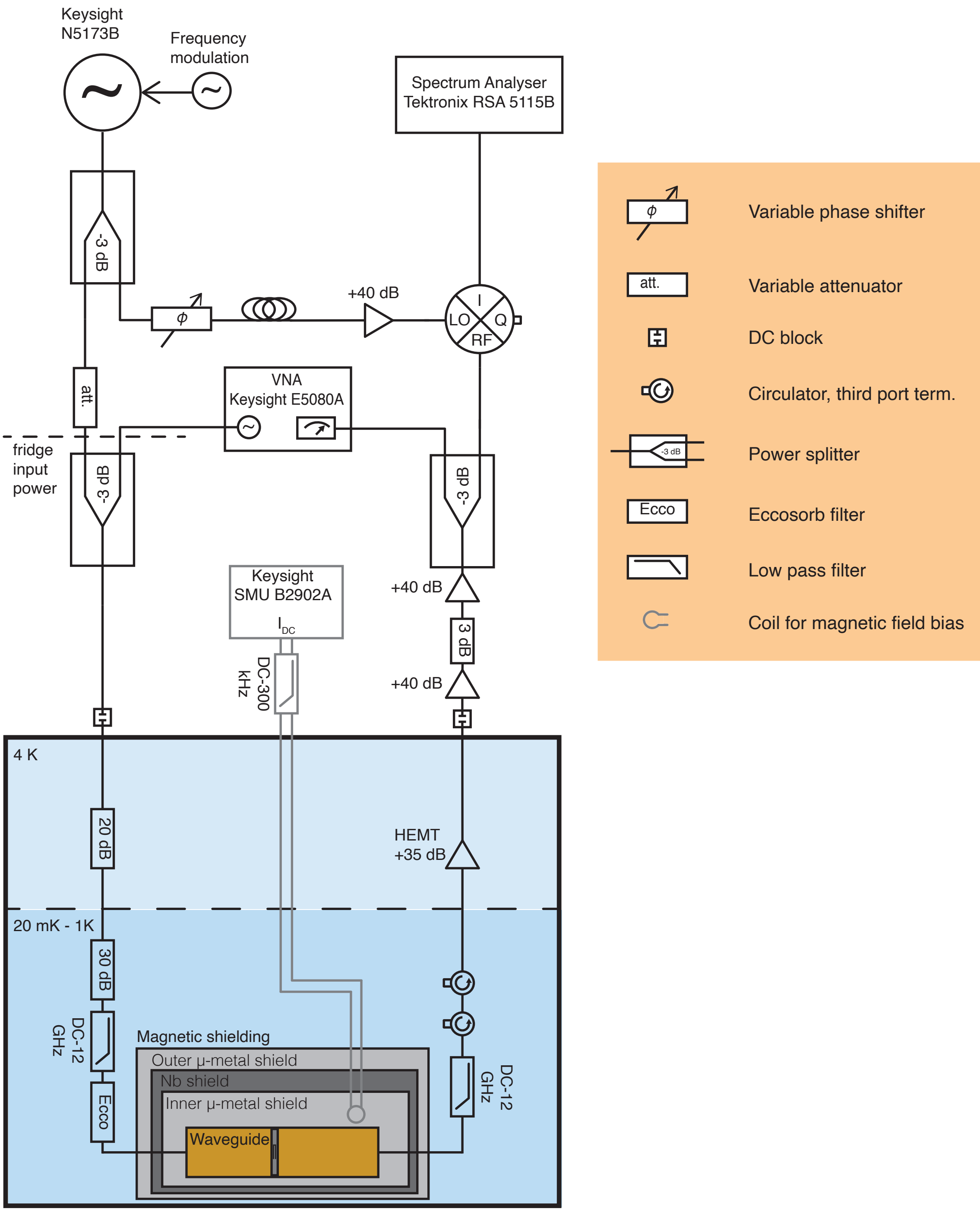

Figure 6.10: Full measurement setup. Over the range of the experiment, the complexity of the setup increased, here it is shown in the final version. For some earlier measurements, only parts of this setup were used, which is stated in the main text. While the setup outside of the cryostat changed and the coil for magnetic field biasing was added later, the microwave wiring in the cryostat remained similar. This figure was also shown in [46].

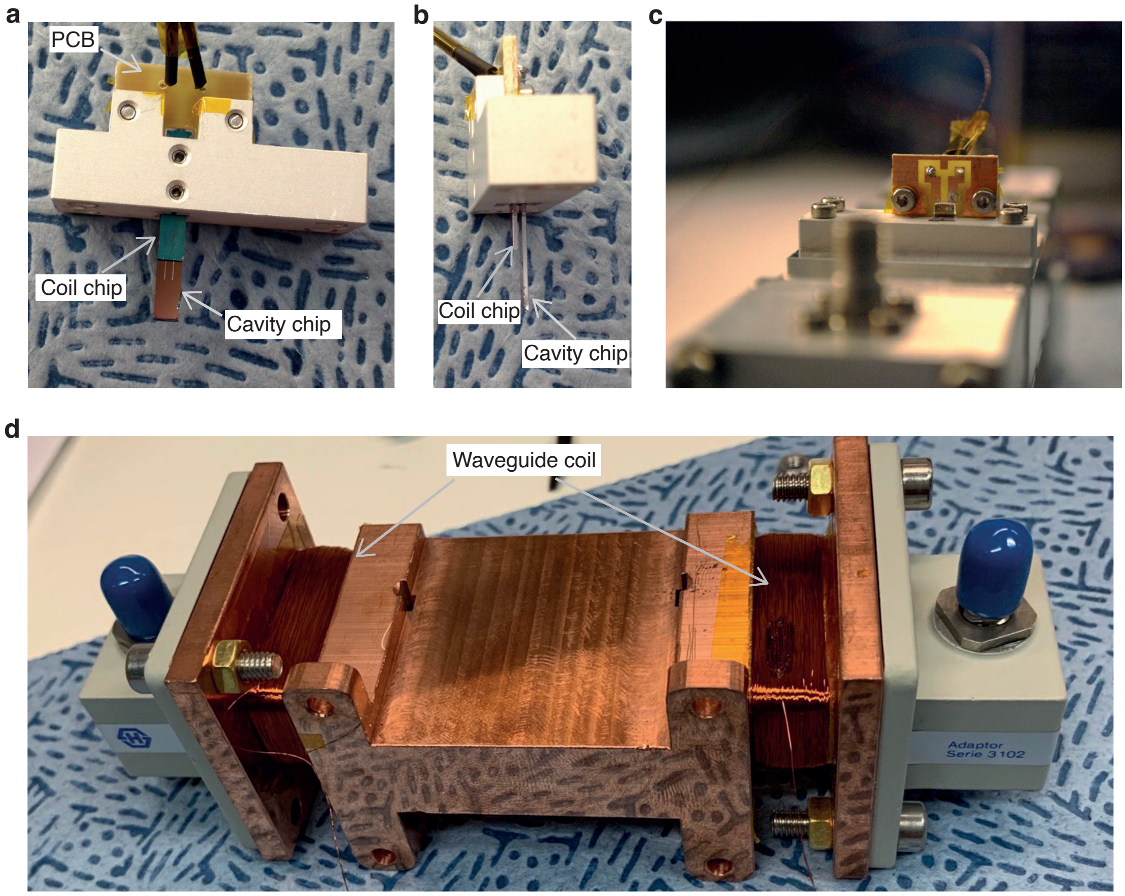

Figure 6.11: Different coil setups. **a.-c.** On chip coil. In (a) seen from the back, with the PCB on top of the two chip sample holder, which is wirebonded to the coil chip. As the microcoil is at the bottom of the chip, this chip does not reach that far into the waveguide. This chip is seen from the back and the cavity chip (below) is seen from the front. In (b) there is a side view, where the alignment can be seen, which is crucial to have a strong enough field at the SQUID. In (c) it is shown how the microcoil setup looks when mounted in the aluminium waveguide. **d.** For the copper waveguide, we used waveguide coils, where we wound the coil around the waveguide body. We used between 30 and 3000 windings for those coils.

7 | Results

In this chapter we will discuss all main measurement results using the theory and setup introduced in the previous chapters. This chapter consists out of four main parts. First, the different cavity samples before putting the cantilever on top will be discussed. We will be starting with cavities without a feature in the centre, later we will discuss cavities with a single junction in the centre to arrive at the SQUID samples. Of main interest are their internal losses, the dependence on temperature, the nonlinear properties of samples with junctions and also the unique feature of the SQUID samples, the magnetic field sensitivity. Second, the optomechanical setup, where a magnetic cantilever is put on top of the SQUID samples will be investigated. Different cantilevers could be detected with the used SQUID samples. We will review how such cantilevers are measured and a detailed characterisation of our main sample, used for all the backaction measurements, will be presented. Third, we will focus on optomechanical backaction, starting with measurements in the linear (low power) regime. Owing to the large coupling strength, backaction can be achieved with a single photon. Finally, we will discuss the main results, measuring backaction in the nonlinear (high power) regime. There we will see how linear backaction on an otherwise identical system can be outperformed, and discuss the cooling limits for the current state of the experiment.

7.1 Cavity characterisation

In this first section, we will focus on the cavities and discuss their properties before adding the magnetic cantilever. The setup discussed in this chapter consists out of a microstrip cavity in a rectangular waveguide measured in transmission (Chapter 6.1.3).

7.1.1 Cavities without a feature in the centre

Here, we will discuss the behaviour of the first generation samples fabricated by the Fachhochschule Vorarlberg in a single layer process without any feature in the centre of the cavity (Chapter 6.2.1). The aim of those samples was to understand how such cavities perform, if the coupling can be set as expected and the frequencies are in the desired range. Also it should be investigated how the choice of waveguide and cavity material influences the internal losses. Table 7.1 summarises the parameters of the samples discussed here. We used two niobium samples, one in a copper and one in an aluminium waveguide and one aluminium sample in an aluminium waveguide. The resonance frequencies of those samples were all between 7 and 8 GHz, while we even backed some cavities with an additional empty substrate to lower their frequency (required to avoid frequency crowding when measuring multiple samples in a single waveguide).

Fig. 7.1 shows a low and high power measurement of the cavity made from niobium placed in an aluminium waveguide. The high power measurement shows a much improved signal to noise ratio and it is evident that the quality factor increases with power, as the resonance gets much narrower and deeper. To extract the quality factors we used the circle fit routine, Chapter 6.1.4, a solid line also shows the fit in Fig. 7.1. The extracted single photon internal quality factor was

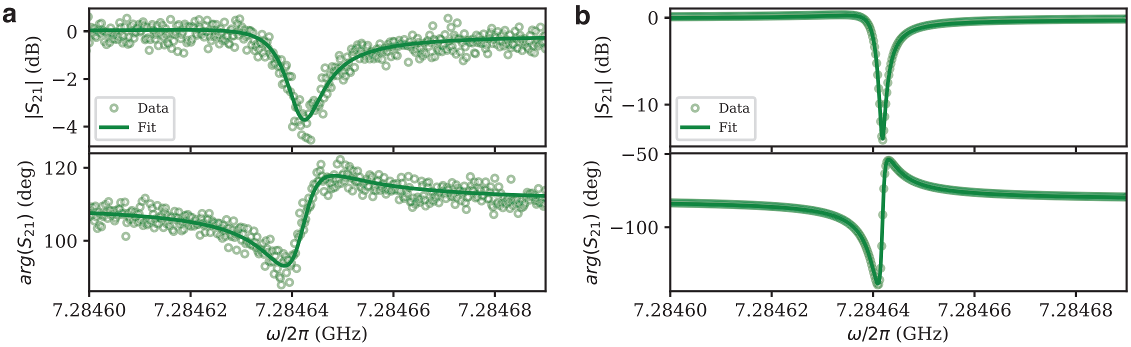

Figure 7.1: VNA measurement of the niobium sample in the aluminium waveguide. **a.** Low power and **b.** high power measurement. Next to the signal to noise ratio improving, it is also evident from the more pronounced resonance, that the internal quality factor is much increased for the high power measurement. The offset was shifted in both plots, such that the background is around 0 dB. The solid line is a fit using the circle fit routine, Chapter 6.1.4.

Table 7.1: Parameters of samples without a feature in the centre. The niobium and aluminium sample in the aluminium waveguide were measured in the same cooldown. The niobium sample was backed by a Silicon substrate to lower its frequency [79].

Cavity (WG) material	$\omega_c/2\pi$ (meas.)	$\omega_c/2\pi$ (sim.)	Leg length	Q_c	Q_i (low power)
Nb (Cu)	7.92 GHz	7.94 GHz	3.65 mm	0.6×10^6	0.7×10^6
Nb (Al)	7.28 GHz	7.23 GHz	3.85 mm	2.2×10^6	1×10^6
Al (Al)	7.9 GHz	7.94 GHz	3.65 mm	1.7×10^6	0.6×10^6

between half a million and one million for all samples, where we measured the highest quality factor for the niobium sample in the aluminium waveguide. Niobium generally showed higher quality factors, additionally the aluminium waveguide helps in two ways: first it shields from stray fields, second the waveguide walls, which are the ground plane for the cavity mode, become superconducting. As preliminary measurements showed such a high internal quality factor, we put them in the central slot of the waveguide and used an empty substrate in a neighbouring slot to create an asymmetry in the field. With this the cavities were approximately critically coupled. More considerations about this setup are discussed in Chapter 6.1.3 or in [79].

Next to the internal quality factor in the single photon limit, where TLS are usually not saturated by power, it is interesting how the internal quality factor changes with power and temperature (Chapter 5.2.3).

In Fig. 7.2 the internal quality factor of the cavity is plotted against power (a) and temperature (b). To convert the input power to photon number we estimate the fridge input attenuation with 69 dB[1] and use the relation converting power to circulating photon number, found e.g. in [79]. The quality factor for all samples increases with photon number, the highest quality factor of nearly 10 million is measured for the niobium sample in the aluminium waveguide and seems to increase even beyond the measured range. Simulations showed, that the quality factor in the copper waveguide could be limited by the finite conductivity of the walls to the values we measure. We fit all curves to the TLS model, Eq. 5.27, where we find very good agreement and the results are given in Table 7.2. Also for increasing temperature, we see an increase in quality factor. However, the breakdown of superconductivity in aluminium has an influence on this measurement. While the niobium cavity in the copper waveguide shows an increasing quality throughout the whole measurement range, explained solely by TLS saturation (Eq. 5.28), the niobium cavity in the aluminium waveguide is limited by the breakdown of superconductivity in the waveguide walls above 400 mK and the aluminium cavity by the breakdown of its own su-

[1]This is slightly different to the 73 dB estimated for the latest version of the setup, due to a slightly different wiring setup used for those measurements.

perconductivity already from 200 mK onwards. Thus for fitting the behaviour of the aluminium cavity, we combine the TLS saturation with the change resistivity predicted by the two fluid model, Eq. 5.3, which gives good agreement.

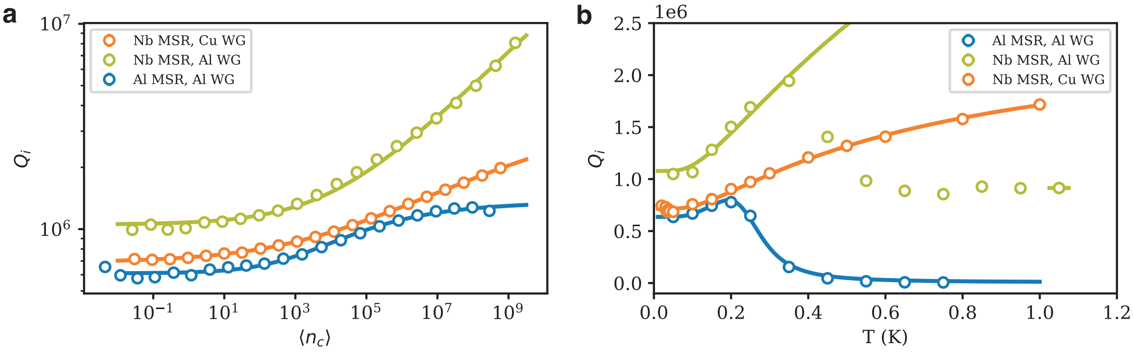

Figure 7.2: Change of internal quality factor when changing power and temperature. **a.** Change of the quality factor of the sample without a feature in the centre, for increasing photon number. The quality factor increases for all samples, which is well captured, by the TLS model, Eq. 5.27. The fit results are given in Table 7.2, where the loss parameter k, the saturation parameter $\bar{n}^{\text{crit}}_{\text{TLS}}$, β and a limiting quality factor due to other loss channels are used as free fit parameters. While the quality factor of the aluminium cavity saturates, the one of the niobium cavities keep increasing throughout the complete measurement range. **b.** Change of Q_i with temperature. While only the TLS model is considered for describing the behaviour of the niobium cavities (Eq. 5.28), we also have to take the breakdown of superconductivity into account for the aluminium sample (Eq. 5.3). The niobium sample in the aluminium waveguide is also limited by the breakdown of superconductivity in the waveguide walls. The fitted loss parameters are given in Table 7.2, further details are discussed in the text.

TLS also induce a change of frequency when increasing the temperature. Fig. 7.3 shows this for the niobium cavities, while the aluminium cavity is dominated by the breakdown of superconductivity, see data in [44]. Also here, the niobium cavity in the aluminium waveguide only shows good agreement to the TLS model, Eq. 5.29, until 400 mK, where the breakdown of superconductivity in the waveguide walls occurs. The niobium cavity in the copper waveguide shows good agreement throughout the whole range. Also those fit results are given in Table 7.2.

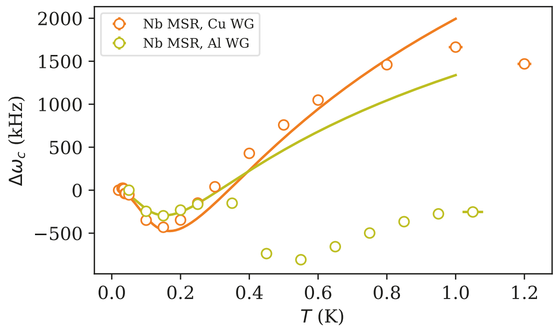

Figure 7.3: Shift of cavity frequency with temperature for the niobium samples. Fitting the data with the TLS model for the frequency change, Eq. 5.29, we find good agreement for the cavity in the copper waveguide, while for the one in the aluminium waveguide, the model deviates above 400 mK. The loss parameter k is the only free fit parameter, given in Table 7.2.

Comparing the loss parameter from the different fits (either fitting the change of the internal quality factor with power or temperature or fitting the frequency shift with temperature), we always find values of the same order. This already suggests, that the losses are independent from the material of the cavity, but are rather arise form the substrate itself and lossy interfaces or surfaces.

Table 7.2: Fit parameters, fitting the change of internal quality factor with input power/temperature and the change of frequency with temperature to the respective models discussed in Chapter 5.2.3. We give the combined loss parameter k for all shown fits. For the power dependence of Q_i additionally the critically photon number and the β parameter are given (Eq. 5.27). We only fit the frequency change with temperature for the niobium samples, as the aluminium samples are dominated by the breakdown of superconductivity (see data in [44]).

Cavity (WG) material	k ($Q_i/\langle n_c\rangle$ fit)	k (Q_i/T fit)	k (ω_c/T fit)	$\bar{n}_{\text{TLS}}^{\text{crit}}$	β
Nb (Cu)	$1.22(2)\times10^{-6}$	$1.00(2)\times10^{-6}$	$0.91(5)\times10^{-6}$	$3.3(3)\times10^{3}$	0.240(6)
Nb (Al)	$0.95(5)\times10^{-6}$	$1.6(2)\times10^{-6}$	$0.61(4)\times10^{-6}$	$8(4)\times10^{3}$	0.33(2)
Al (Al)	$0.90(4)\times10^{-6}$	$0.79(7)\times10^{-6}$	-	$0.7(3)\times10^{3}$	0.47(5)

With this we have done a basic characterisation of the microwave cavities fabricated in a single layer process and without a feature in the centre. The cavities work well showing a high internal quality factor of up to one million for low powers, limited by TLS. Fitting the TLS model to the power and temperature dependence gives a good agreement. Also the coupling of the cavities can be chosen by the position in the waveguide, where we had an approximately critically coupled setup for those measurements. Now we want to investigate the second generation of devices from Starcryo, starting with the cavities with a via in the centre.

7.1.2 Cavities with a via in the centre

In here the most simple samples from the second generation, a cavity with a via[2], but no junction in the centre, will be discussed (Fig. 6.6). All of those second generation samples are made from niobium in a multi-layer process by Starcryo on a single silicon wafer. These samples aimed at learning how cavities fabricated by Starcryo perform and the results will be used as a reference for the more sophisticated samples with a Josephson junction. We had two samples with a via available, which both performed similar. Here we will discuss the results from one of those samples. Similar to Chapter 7.1.1, we characterised their behaviour for increasing power, however we did not do measurements with increasing temperature.

In Fig. 7.4 a low and a high power measurement of the cavity is shown. Again we see an improvement of the internal quality with increasing power. The solid line is the fit using the circle fit routine (Chapter 6.1.4). Table 7.3 summarises the parameters of the discussed

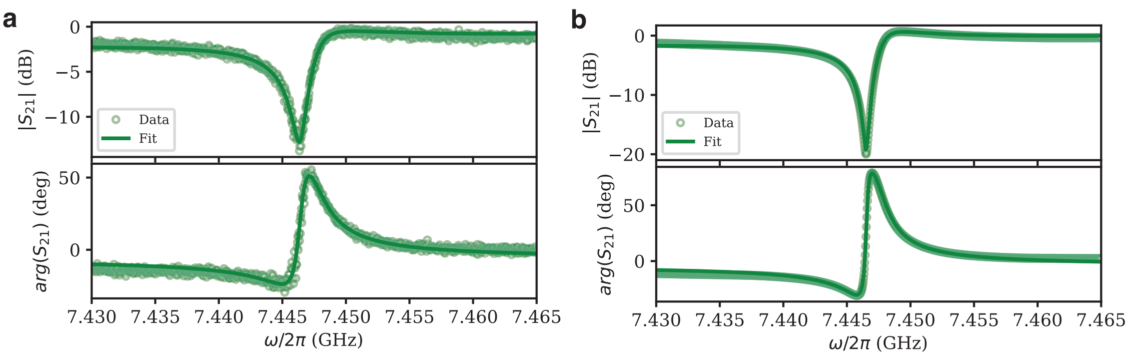

Figure 7.4: VNA measurement of a sample from Starcryo with a via. **a.** Low power and **b.** high power measurement. Comparing them to the samples from the Fachhochschule Vorarlberg (Fig. 7.1), the quality factors are much lower, and thus the linewidth is much wider. The offset was shifted in both plots, such that the background is around 0 dB.

sample. The internal quality factor is drastically below the one from the samples from the

[2] A via is a solid superconducting connection between both wiring layers, more details can be found in Chapter 6.2.2.

Table 7.3: Parameters of the sample with a via connecting both legs. It was further backed by a bare silicon substrate, to lower its frequency and avoid frequency crowding, as there were multiple samples in the waveguide. The difference between measured and simulated frequency can be explained with the dielectric constant of the substrate being higher than estimated.

$\omega_c/2\pi$ (meas.)	$\omega_c/2\pi$ (sim.)	Leg length	Q_c	Q_i (low power)
7.45 GHz	7.67 GHz	3.5 mm	3300	7500

Fachhochschule Vorarlberg, which was already expected as the fabrication process is much more sophisticated (Chapter 6.2), thus we put the samples one slot off centre in the waveguide, to increase the cavity-waveguide coupling. Indeed, the coupling quality factor is about half of the low power internal quality factor, which is a good regime for determining both quality factors with high accuracy. Again we shifted the frequency of this sample, by backing it with an empty silicon substrate, to avoid frequency crowding in the waveguide, measuring multiple samples simultaneously.

Figure 7.5 shows the increasing internal quality factor with power, which increases to around $2{\times}10^4$. We again fit with the TLS model (Eq. 5.27), where we see good agreement. Comparing the fit parameters to what we obtained for the samples without a feature in the centre from the Fachhochschule Vorarlberg (Chapter 7.1.1), we have a much lower loss parameter (which means that the loss rate is increased) and a higher saturation photon number, $\bar{n}_{\text{TLS}}^{\text{crit}}$. This is further evidence, that those samples are much more susceptible to loss than the first generation. Still the quality factor seems to be good enough for building the optomechanical setup and a

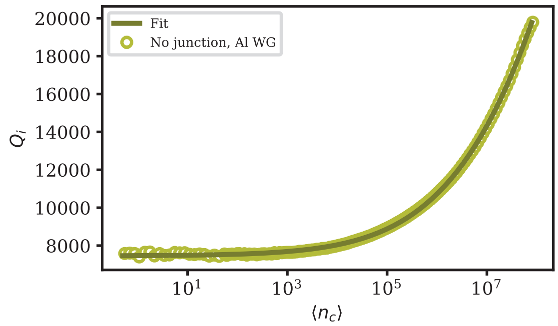

Figure 7.5: Increasing internal quality with power and fit with the TLS model (Eq. 5.27). The fit gives the following parameters: $k = 1.35(2) \times 10^{-4}$, $\bar{n}_{\text{TLS}}^{\text{crit}} = 1.29(6) \times 10^6$, and $\beta = 0.41(1)$. Also a limiting quality factor due to other loss mechanisms is used as a free fit parameters, however as the quality factor keeps rising even for the highest powers used here, this cannot be usefully determined.

low quality factor was expected due to the multi-layer fabrication process as well as Starcryo using one of their standard Si wafers for fabrication. While wafers exist, which are known for having low losses at microwave frequencies, the used wafer was not specifically intended for such frequencies. In the next step, we want to analyse the samples with a Josephson junction in the centre, investigate how their behaviour changed and - most importantly - characterise their nonlinearity.

7.1.3 Cavities with a single junction

Simultaneously to testing the samples with a via, we also tested samples with a single junction. One interest was of course if we see a change of the quality factor simply due to the junction, but also with input power, as it was the case for the previously discussed samples. Secondly, and also more interesting was the nonlinearity due to the presence of a junction. We had some samples with only a single junction and others with a single junction followed by a via. For those two, we did not see any noticeable difference in any measurement. The internal quality factor was similar to the (low power) case with only a via, so the junction does not seem to have any significant influence on the losses at the current level of the quality factors, which is good news, since then the junction does not impose any limit. The internal quality factor further remained nearly the same for all accessible powers, as nonlinear effects dominated before any saturation of TLS was reached. For characterising the nonlinearity, we performed a power sweep, focusing on the nonlinear frequency shift (Fig. 7.6). In (a) the power sweep over the whole range is shown. While for low powers, the cavity remains unchanged, it shifts to lower frequencies with increasing power. By further increasing the power, the resonance nearly vanishes and it becomes a wide and shallow feature, as the cavity probably enters a chaotic regime. This might be, as we are operating close or even above the critical current of the junction in this power range. In this regime, where the cavity nearly vanishes, we typically also do not see a difference between low and high photon state.

We can use the data where the frequency already shifts due to the nonlinearity, but the line shape is still approximately a Lorentzian to extract the Kerr constant. This is done in Fig. 7.6b, where we estimate the photon number using the input attenuation, similar to how it is described in Chapter 7.1.1. With this we extract a Kerr of $\mathcal{K}/2\pi = [-27.4 \pm 0.1(\text{fit}) \pm 9.7(\text{sys.})]\text{kHz}/\bar{n}_c$. The systematic error here and for the Kerr values given in the following arise from the uncertainty in input attenuation, where we assume an uncertainty of 3 dB.

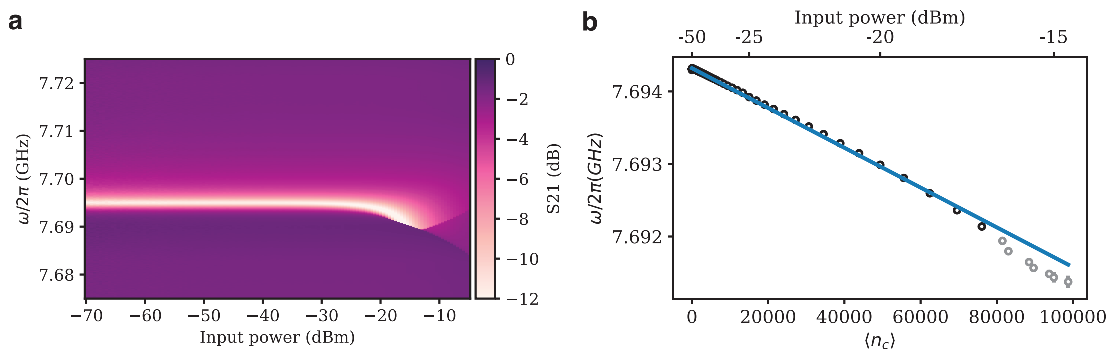

Figure 7.6: Change of cavity frequency with increasing power. **a.** 2D map of VNA traces with increasing input power. For higher powers, the cavity frequency shifts to lower values due to the nonlinearity from the junction. This happens in a range of a few dB of input power. When the power increases further (here around −10 dBm) the cavity enters the chaotic regime. The baseline is again shifted to be at 0 dB **b.** Frequency of the cavity against cavity photon number, estimated via the input attenuation. Black points are used for the linear fit to obtain a Kerr of $\mathcal{K}/2\pi = [-27.4 \pm 0.1(\text{fit}) \pm 9.7(\text{sys.})]\text{kHz}/\bar{n}_c$. The grey points are ignored, as the circle fit starts to break due the distorted cavity line shape and the frequency cannot be trusted.

We also did a more sophisticated analysis of the nonlinearity, by directly fitting the Duffing model (Chapter 3.2) to the nonlinear line shape. In contrast to what has been done above, this is then mainly relevant for line shapes, which are clearly different from a Lorentzian peak. The exact model used in the fit and additional considerations are given in Chapter B of the appendix. Fig. 7.7 shows fits to the resonance at different powers using the Duffing model. The fit works well until bistability and starts to slightly deviate above. To extract a Kerr, we have to be careful, as for the fit we work if a reduced parameter model and the parameter characterising the nonlinearity, η, is set to 1 (Chapter B of the appendix). However, the power itself is a fit parameter, and we use one of the fitted powers and convert it to the photon number using the input power attenuation (as it was done in Fig. 7.6b). By scaling this, we obtain the photon numbers for all the powers, with more details given in Chapter B of the appendix. Knowing the photon number for any given power and the critical power, we can estimate the Kerr for every single fit. Averaging the Kerr values up to bistability gives $\mathcal{K}/2\pi = [-34 \pm 2(\text{fit}) \pm 11(\text{sys.})]\text{kHz/Photon}$. Even though the Kerr value is slightly above what was found estimating the Kerr via the frequency shift, there is good agreement between both values given by the very different approaches. Also those numbers were extracted using very different power ranges.

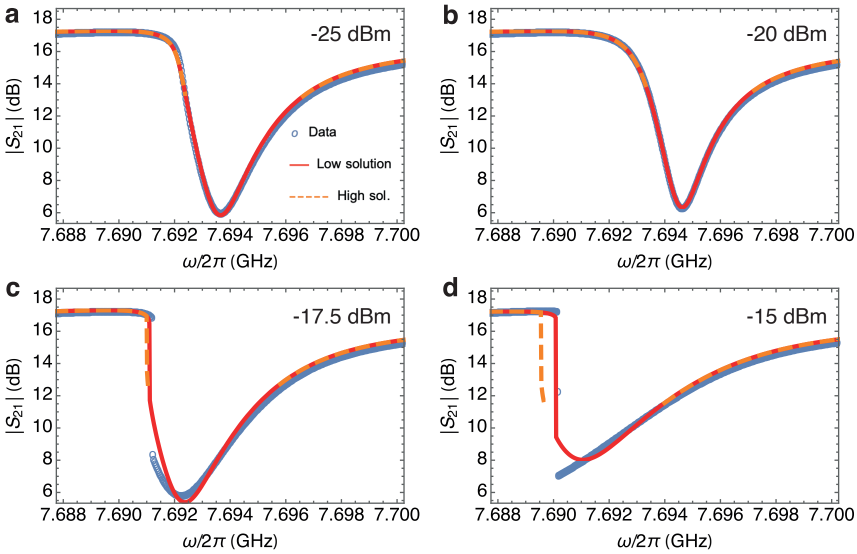

Figure 7.7: Fitting the Duffing model to the nonlinear line shape of the cavity with a single junction in its centre at different powers (input power given in each panel). This model (details in appendix, Chapter B.1) includes the circuit model with the impedance mismatch (see Chapter 6.1.4). **a,b.** Cavity below bistability. There is a slight shift in frequency at the measurement in (b), taken already at higher power, but below bistability. The model is in excellent agreement with the data. **c.** Slightly above bistability. The model accurately fits the detuning, where bistability occurs, however the line shape around the region of bistability is slightly different, but otherwise the data and model show good agreement. **d.** Further above bistability, we still obtain good agreement with some deviation of the curve at the bistable detuning. As we only measure sweeping to increasing frequency, we only measure the solution with low photon number. We obtain values for the Kerr for all individual fits. Averaging the values up to bistability gives an average of $\mathcal{K}/2\pi = [-34 \pm 2(\text{fit}) \pm 11(\text{sys.})]\text{kHz}/\bar{n}_c$, in good agreement with the value obtained from the linear fit to the frequency change (Fig. 7.6). The values for the Kerr at all measured powers are plotted in the appendix, Chapter B.1.

In principle, the nonlinearity of those samples can be used to realise a parametric amplifier. However we mainly focused on the gain measurement for the SQUID samples and did not measure gain using the single junction samples. The reason was, that the SQUID samples are the relevant samples for the optomechanical experiment. Measurements of the gain in the SQUID samples is discussed in Chapter 7.1.5.

7.1.4 Cavities with a SQUID

Now, we can discuss the samples with a SQUID in the centre, which are also the samples used in the optomechanical setup. The quality factor remained mainly unchanged, which is also expected, as this was already the case for the samples with a single junction. We also continued with the same waveguide-sample configuration in terms of placement, mounting those samples one slot off the centre of the waveguide. Inhere, we will discuss a basic characterisation of the nonlinearity and later on the flux tunability, which will be essential for detecting the cantilever. We did the same power sweeps as already discussed in the previous Chapter 7.1.3, to learn about the nonlinearity. Fig. 7.8 shows fits with the Duffing model to traces taken at different powers, where we can extract the Kerr constant similar to the previous part. We find a Kerr of $\mathcal{K}/2\pi = [-10 \pm 2(\text{fit}) \pm 3(\text{sys.})]\text{kHz}/\bar{n}_c$, which is smaller than for the single junction, as expected, as the nonlinearity is effectively reduced due to a second junction in parallel. Again, the fit is in good agreement with the data and only slightly diverges above bistability, where it still predicts the bistable splitting very accurately.

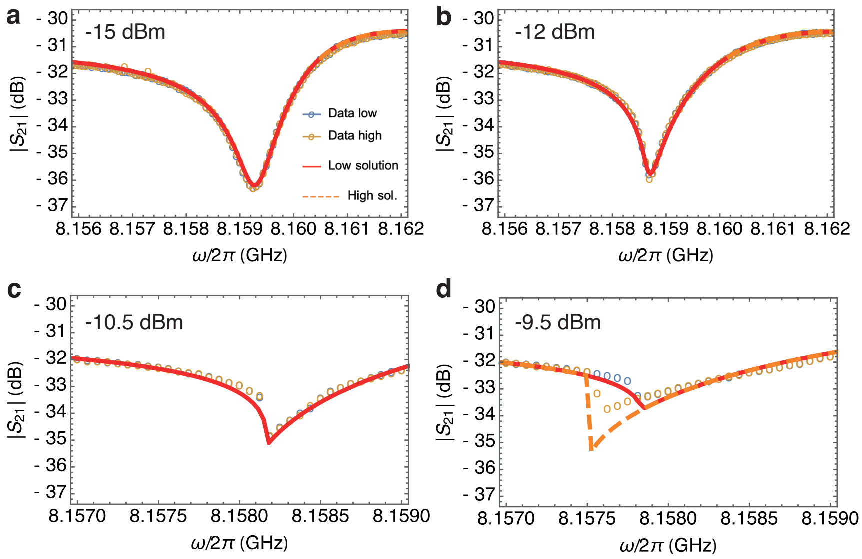

Figure 7.8: Fitting the Duffing model to the nonlinear line shape of the cavity with a SQUID in its centre for different powers, similar to what is seen in Fig. 7.7 for a single junction. Here we additionally measured the opposite sweep direction from high to low frequencies. Still we continued to do individual fits for each power using the low state data. The input powers are noted in the respective panels. **a,b.** Cavity far below bistability, where we see excellent agreement with the fit, for lower (a) and higher power (b). **c.** Just before bistability, we still have a very good agreement to the fit. **d.** Above bistability, there is still good agreement to the theory. The frequencies of the low and high state are well predicted, only the shape of the high state is different from theory. This could come from limiting effects, where we approach the critical current of the junction. Again, we extract a Kerr using the fits below bistability and obtain $\mathcal{K}/2\pi = [-10 \pm 2(\text{fit}) \pm 3(\text{sys.})]\text{kHz}/\bar{n}_c$.

As a secondary approach, we can also do a fit to the data, by modelling the nonlinear change of the photon number, Eq. 3.6. We implemented the fitting routine slightly differently than the one using the Duffing model. This routine now requires subtracting the background[3], and additionally it gives a single value of the Kerr fitted simultaneously to all traces. The background subtraction was also the reason for not fitting the single junction sample with this method, as this is not flux tunable. Also for this dataset, the subtraction did not work ideally, as we did not take a dedicated background trace, but used a suitable one from the flux map (Fig. 7.10). The fit shown in Fig. 7.9, worked reasonably well and we could extract a Kerr of $\mathcal{K}/2\pi = [-9.0 \pm 0.5(\text{fit}) \pm 3.1(\text{sys.})]\text{kHz}/\bar{n}_c$, which is in very good agreement with the value obtained from fitting the Duffing model.

It should be noted, that operating the cavity at different flux bias points/frequencies (Fig. 7.10) also changes the nonlinearity (Eq. 5.36) as the participation ratio of the nonlinear junction inductance changes. So the Kerr value extracted with both methods is only correct for the flux bias point used here.

Now, we want to investigate the magnetic field sensitivity of the SQUID based cavities. To do this, we measured these samples in a copper waveguide with two coils around it (seen in Fig. 6.11d). In Fig. 7.10 a flux map for two different samples, a SQUID and a SQUID washer (Fig. 6.6), is shown. We clearly see that the samples are hysteretic, due to a large geometric inductance of the SQUID loop compared to the junction inductance, such that $\beta_l > 2\pi$ (Eq. 5.16) [73]. The tunability for these samples is about 100 MHz.

Additionally to the large coil, we also used a microcoil placed in the vicinity of the SQUID

[3]When subtracting the background, we use a VNA trace with the sample far detuned, to only measure the background. Ideally the background has a flat frequency response. However often there are ripples, which also degrade the quality of the fit, therefore it is helpful to subtract the background prior to fitting the data, if possible.

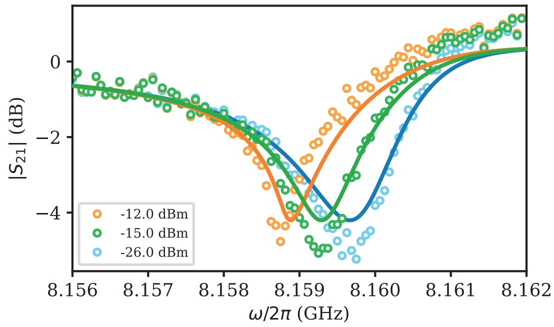

Figure 7.9: Fitting the background subtracted data to the nonlinear response of the photon number, Eq. 3.6. The fits are the solid lines, the datapoints of the measurement are directly shown. This model was only implemented up to bistability, thus we use three measurements with increasing power up to bistability (lowest power in blue, then green and orange). The intermediate power measurement (green) is the same as in Fig. 7.8(a) and the highest power measurement (orange), is the same as in Fig. 7.8(b). From those two measurements, we also see that the Kerr seems to be slightly underestimated, and obtain a value of $\mathcal{K}/2\pi = [-9.0 \pm 0.5(\text{fit}) \pm 3.1(\text{sys.})]\text{kHz}/\bar{n}_c$. This value is within the error to the value we obtained when using the Duffing model implementation for the fit.

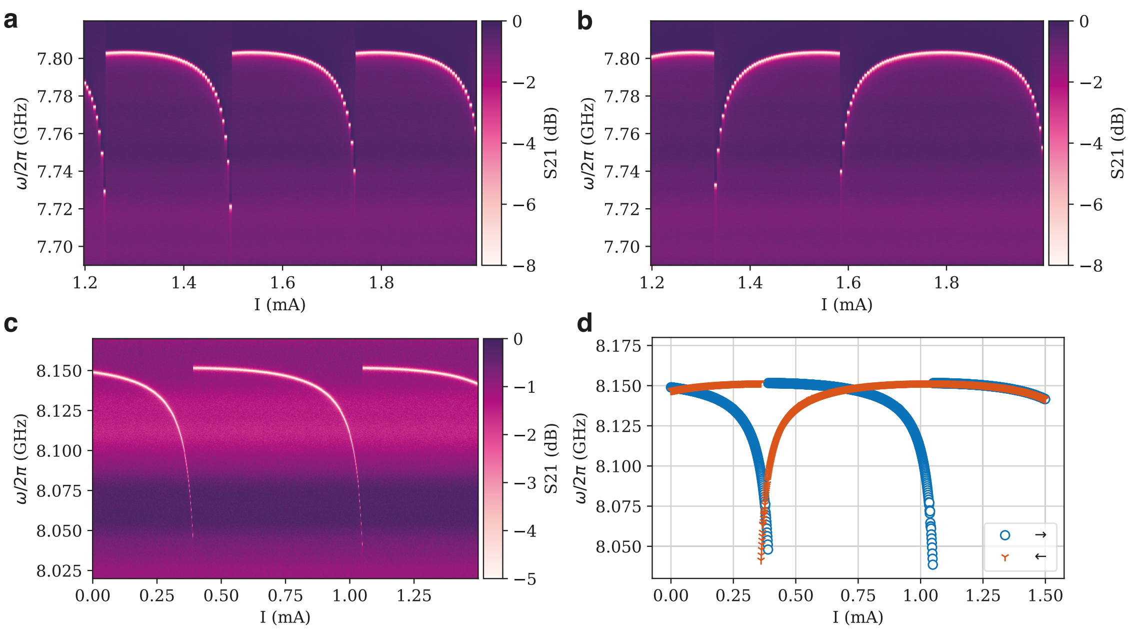

Figure 7.10: Flux maps of two different samples. **a,b.** Flux maps of the SQUID washer sample either for increasing (a) or decreasing the current through the coil (b). We can clearly see the hysteric behaviour and the tunability is a bit below 100 MHz. **c.** Flux map of the SQUID sample for increasing coil current. Here the tunability is about 100 MHz. In these flux maps, the offset was set such that the signal is at 0 dB far off resonance. **d.** Fitted frequency of the SQUID sample for increasing and decreasing the current in the coil, where again the hysteric behaviour can be clearly seen.

loop (Fig. 6.11) to simulate a fast flux signal, similar to what is expected from the cantilever. In Fig. 7.11 two measurements of the cavity are shown, where a fast flux signal is applied with two different frequencies. The onset of the sidebands can be seen, which are stronger pronounced for the higher modulation frequency. We also perform a fit using a single central Lorentzian with two symmetric Lorentzians around it, which is in good agreement to the measured data. In the next part, we will investigate the capabilities of using such a SQUID sample as a parametric amplifier.

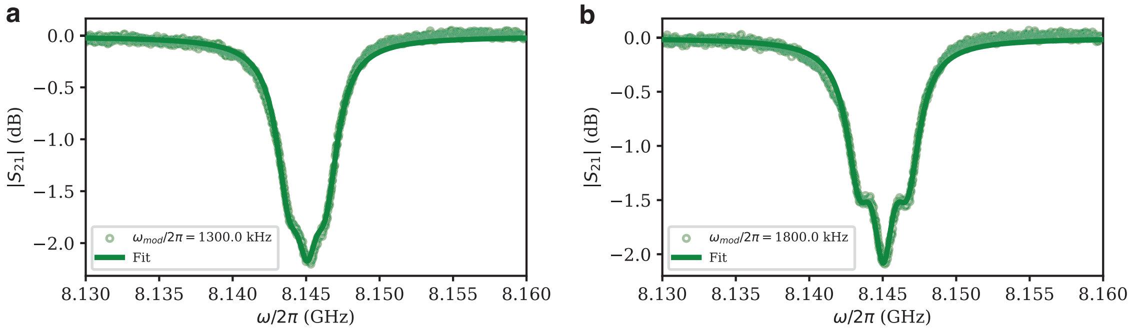

Figure 7.11: Using the micro coil for simulating the influence of a magnetic cantilever. **a.** Driving the microcoil at 1300 kHz we see the onset of sidebands, which are not clearly distinguishable from the main peak. **b.** Using 1800 kHz, the sidebands can be clearly distinguished. We fit both data sets with three Lorentzians, consisting of a main peak and two symmetric side peaks. This gives good agreement to the measured line shape. Also here the background was set to be at 0 dB far off resonance.

7.1.5 SQUID based cavities as parametric amplifiers

In this part, we will investigate the possibilities of using our cavities as parametric amplifiers, which was theoretically investigated in Chapter 3.1.2. The typical measurements were always performed using the same scheme. First, we did a power sweep with the VNA (similar to what is shown in Fig. 7.6) to learn about the bistable power. Then we did two tone measurements with powers close, but below, the bistable power. To find the frequencies with highest gain, we changed the frequency of the pump tone and did a VNA scan with a weak probe tone (signal tone) for each frequency. We repeated this for different powers to find the ideal setup parameters to achieve highest gain. Fig. 7.12 shows such a typical gain map measured in transmission. The pump tone, which is swept through can be seen, as well as the region with most gain, being the bright region. As we are operating our cavity in the notch configuration, the signal can be either scattered forward (transmission) or backwards (reflection). This proofed to be a challenge when doing gain measurements, as depending on pump frequency and the detuning, gain could occur in reflection, but is not seen in transmission (and vice versa). This can be also seen in this figure, as the gain seems to drop below −10 dB for some combination of detuning/pump frequency. For the discussed measurement, this seems to especially happen for lower pump frequency (compared to the one where highest gain occurs in transmission) and being detuned below the frequency of the pump. Also it should be noted, that the signal is offsetted, such that it is at 0 dB when far detuned.

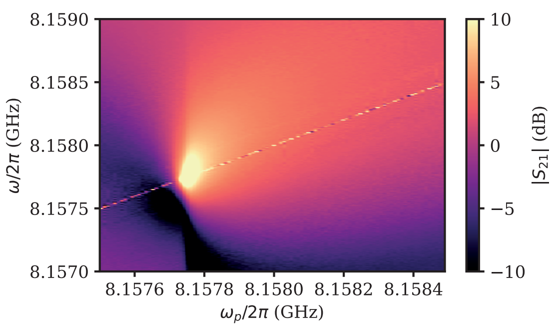

Figure 7.12: Gain map. The pump (ω_p) is swept through and for each pump frequency a weak VNA signal is measured. We offset the traces, such that they are at 0 dB when far detuned. High gain only occurs for a small range of pump frequencies in a narrow region around the pump. The frequency of the cavity without the strong pump is around 8.159 GHz.

To investigate this further, we used a circulator in our setup, to also enable measurements in reflection. Such a measurement is shown in Fig. 7.13a, where the difference of the two configurations can be clearly seen. Again, we offsetted those traces, to be at 0 dB far from the pump. To get the full gain profile, both traces have to be added, which is depicted in Fig. 7.13b. Several traces with different pump powers can be seen, the powers are given relative to the highest power used. We achieve a gain of nearly 20 dB, however the bandwidth is limited to a few hundred kHz.

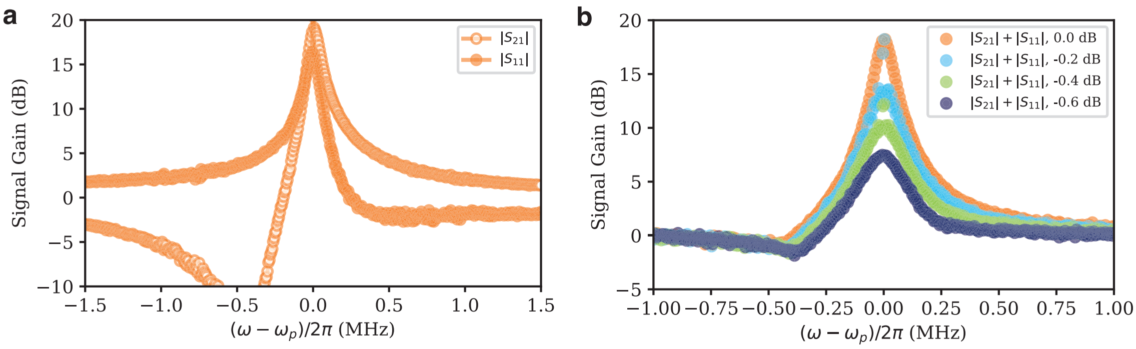

Figure 7.13: Gain traces. **a.** Due to our measurement configuration - the notch configuration (Chapter 6.1.4) - parts of the signal are reflected, while others are transmitted (usually we only measure the transmitted signal). Here, shown are the reflected and transmitted signal, shifted such that far away from the pump we see no gain. **b.** Gain profiles when summing transmission and reflection for different pump strengths, relative to the pump strength where we see highest gain.

Using Eq. 3.18 we can also compute gain profiles and compare them to the data. This model requires the quality factor/linewidth (known from fitting the cavity response) and the drive strength (which we parametrise in units of the critical drive strength). As a third parameter, the pump-cavity detuning is required. However, similar to the experiment, we adjust the probe-cavity detuning to achieve the highest gain for a given drive strength. With that, the only required parameters are the cavity linewidth and the drive strength in units of the critical drive. Such a comparison of a calculated gain profile to a measured one is shown in Fig. 7.14. However to get a decent agreement, the linewidth had to be decreased by a factor of eight, and 0.7 of the bistable power was used for the drive strength. It could be expected that the power was closer to the bistable one, as we could not measure a gain profile with higher gain for this measurement set. With this it can only be concluded that the line shape is the one expected from a gain profile, but the discrepancy in power and linewidth is currently unexplained. However, as the setup is approximately critically coupled, half of the losses are dissipated internally, which might be a reason for the lower gain. Also it should be noted, that shown here is not a fit, but simply a calculated gain profile based on our parameters. This is rather straight forward, as the maximum gain is adjusted by the drive strength and the width of the gain profile by the linewidth of the cavity.

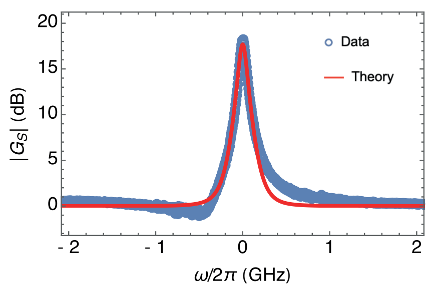

Figure 7.14: Comparison of a theory predicted gain profile to a measured gain profile (profile with most gain in Fig. 7.13). For the theoretical prediction of the gain profile (red line), we use 0.7 of the bistable drive and furthermore eight-fold decrease the measured linewidth to obtain a similar line shape.

With this, we have investigated the amplification capabilities of our SQUID based samples. As expected, those samples work as parametric amplifiers. We could see gain of around 20 dB with a linewidth of several hundred kHz. While this is not particularly wide, it is the frequency range, we expect our cantilevers in. With this we can expect to amplify the measurement signal of the mechanical cantilever, when operating close to bistability. So far we only discussed the samples without a cantilever, from now on we will focus on the optomechanical setup.

7.2 Characterisation of the optomechanical setup

Here, we will discuss the characterisation of the optomechanical setup in detail. First, we will review what changed after adding a magnetic cantilever to one of the SQUID cavities completing the optomechanical setup. Afterwards, we will discuss early characterisation measurements of the optomechanical setup, as well as a comparison between different mechanical cantilevers. We will also see the issues we faced and how they were overcome. We mainly used one cantilever/cavity sample for all optomechanical measurements. In case measurements of a different samples are shown, it will be explicitly mentioned .

7.2.1 Changes of the cavity after adding the cantilever

After adding the mechanical cantilever (Chapter 6.3) several properties of the SQUID samples changed, likely due to the strong magnetic field in the vicinity of the junctions. Among one of the most significant things which changed, was the flux tunability. Before mounting the cantilever, this was limited to around 100 MHz (Fig. 7.10) and hysteretic , afterwards the hysteresis was (nearly) gone and the tunability exceeded several hundred MHz (Fig. 7.15a). The tunability of the cavity to even lower frequencies is shown in Chapter 7.2.6 (Fig. 7.30b). With the likely reduction of I_c due to strong magnetic field in the vicinity of the junctions, β_l (Eq. 5.16) reduces and this leads to a non-hysteretic sample. This also allows to fit the model for the frequency change with flux bias point to the data along the flux map (Eq. 5.30), Fig. 7.15b. We see excellent agreement between this model and the data, which points to a nearly negligible β_l. The fit gives a participation ratio of 0.86(5)% for the SQUID compared to the linear inductance of the cavity. Comparing this to the approximately 5 nH we estimated for the linear inductance doing finite element estimation [95, 79] and using Eq. 5.10 gives a critical current of around 4 µA. This is lower than the designed critical current (8.4 µA), but probably not as low as expected due to the presence of the magnetic cantilever, as will be discussed below within this section of thesis. The difference can be of course, that the critical current was higher than expected or that the inductance is above the simulated value.

Another aspect, which is of key interest, is the internal quality factor. Fig. 7.15b shows the internal quality factor extracted along the flux map, in comparison to the quality factor obtained from all other measured SQUID samples before putting the cantilever (green line). Here, the quality factor with cantilever is only slightly below the one measured without cantilever (7100(100) against 6800(300), where the error here is the standard error). However this result should be interpreted with care, as the traces from the flux map are not ideal for the circle fit, as the point density in the region of the resonance is low, which leads to a high spread of the measurement data. Unfortunately, this is one of the few measurements of the cavity at low flux sensitivity, where the pulse tube was turned off (otherwise the mechanical mode was highly excited, also leading to a distortion of the cavity line shape, see e.g. Fig. 7.24). Extracting the internal quality factor from another pulse tube off measurement (Fig. 7.23a, top of the flux map), gives a quality factor of about 5900. Using measurements done within measuring a cooling trace (Chapter 7.4.2) at a still low flux sensitivity gives a quality factor of around 6000. As the measurement presented in Fig. 7.15b suffers from a low data quality, it it seems that the internal quality factor reduced by around 1000 due to the presence of the magnetic

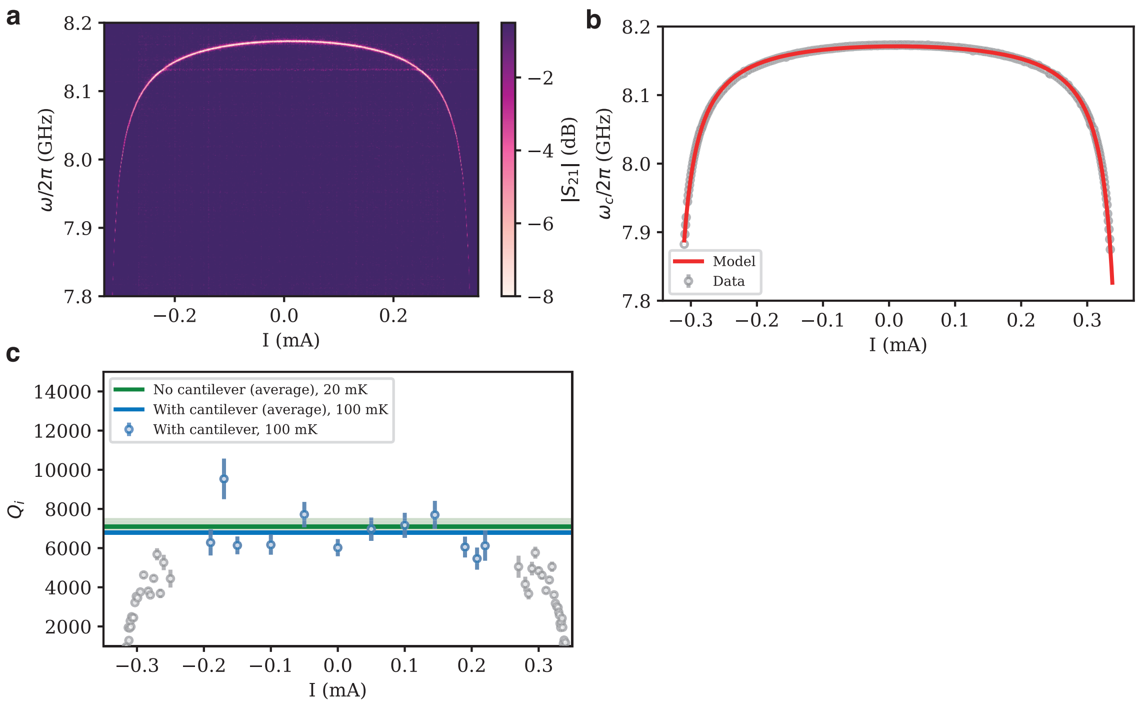

Figure 7.15: a. Flux map after placing the cantilever with background trace subtracted. In contrast to without the cantilever (Fig. 7.10) the flux map does not show a hysteresis and the tunability is much increased. **b.** Frequencies measured along the flux map and fit with the model for the frequency change with applied field (Eq. 5.30 and including an additional offset in the current as there might be a reminiscence magnetic field, even though no current is applied). The fit gives a participation of 0.86(5)% for the SQUID. **c.** Internal quality factor along the flux map. The blue points are used to extract an average, far enough from the region where the quality factor becomes systematically lower, due to magnetic noise. In green is the average value of the internal quality factors of all samples measured without a cantilever, in shaded green the standard deviation. In contrast to (b) only several fits are shown, where the fitting range and initial parameters are hand picked. While the frequency was usually nicely fitted with standard parameters, additional care was required when extracting the quality factor.

cantilever. Doing a rough estimation, assuming a quality factor of 7000 before the cantilever, and 6000 with the cantilever, leads to an additional quality factor (Eq. 5.26) of 40000 arising from the presence of the magnetic cantilever. It should be pointed out, that this number is specific to the main sample, of which the measurements are discussed here and will depend on the size/spacing between SQUID and cantilever. Still, this number can be considered as a rough estimate for the limit arising from the cantilever. Thus, the total linewidth of the cavity, remained similar to before mounting the cantilever, as it is also dominated by the coupling losses (Tab. 7.3) at a value of $\kappa \simeq 3.5\,\text{MHz}$. It slightly changed during different runs, mainly depending on the exact environment and placement in the waveguide, slightly changing the coupling.

As the critical current changes, also the Kerr constant changes, due to an increase of the participation of the junctions (Eq. 5.36). Fig. 7.16 shows two traces of two power sweeps at different flux bias points of our sample.

Comparing the nonlinear frequency shift of the resonator with and without mounted cantilever, (Fig. 7.6) shows, that the shift now happens at lower power, consistent with a larger Kerr constant. Fitting the samples with the response of a nonlinear cavity (Eq. 3.6), we extract a Kerr constant in the range of $10\,\text{kHz}/\bar{n}_c$, an increase of around three orders of magnitude. As the participation ratio of the junction inductances has a cubed dependence on the ratio (Eq. 5.36), we can estimate around a 10 fold decrease of the critical current. This value is also

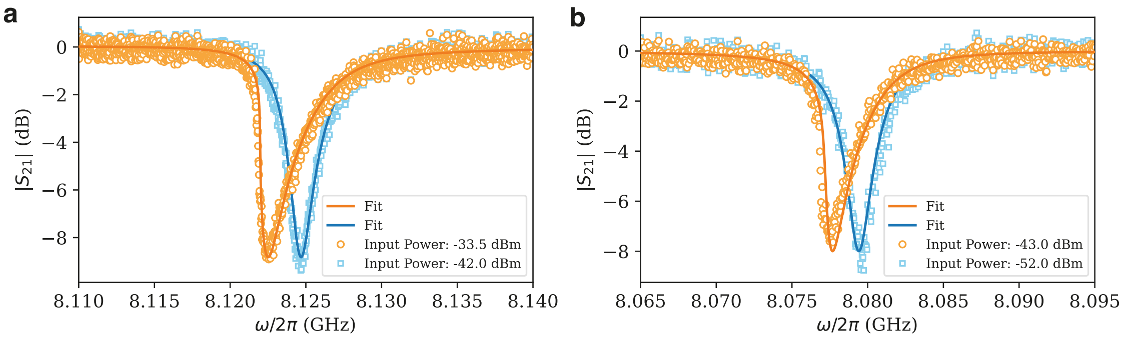

Figure 7.16: Power sweeps at two different bias points with the cantilever mounted. **a.** Power sweep at around 8.125 GHz. The fit gives an accurate description of the data and yields a Kerr of $\mathcal{K}/2\pi = [-14.75 \pm 0.04(\text{fit}) \pm 1.3(\text{sys.})]\text{kHz}/\bar{n}_c$, where the systematic error arises from the uncertainty of the input power to photon number conversion. **b.** Power sweep at a lower frequency of 8.08 GHz, as the participation of the junctions is increased, we expect a larger Kerr (see Eq. 5.36). The fit finds a Kerr of: $\mathcal{K}/2\pi = [-56.6 \pm 0.8(\text{fit}) \pm 24(\text{sys.})]\text{kHz}/\bar{n}_c$.

compatible with the change of the maximum frequency of the flux map when adding the cantilever. Measuring the cavity before and after mounting the cantilever, the maximum frequency decreased by around 40 MHz to 50 MHz. Assuming a lower critical current by a factor of 10, as well as the SQUID participation ratio extracted when fitting the flux map, Fig. 7.15, we expect a decrease of the maximum frequency by 35 MHz. Additionally it is worth noting, that the top frequency of the flux map sometimes even decreased by an additional 20 MHz to 30 MHz, which can arise for instant from a slightly different field from the magnet of the cantilever or a slightly different position of the cantilever, changing from cooldown to cooldown. Still the decreased frequency of the flux map seems to agree with what is expected from the assumed change of critical current.

We further see the clear increase in Kerr when operating at lower frequencies (and thus higher flux sensitivities), when we compare the power sweeps taken at the two different flux bias points in Fig. 7.16. There we see, that a similar nonlinear shift already appears at 10 dB lower input power when working at 8.08 GHz instead of 8.125 GHz.

As discussed, the reduction of critical current is believed to arise from the magnetic field in the vicinity of the junctions, which is a known phenomena [68, 102]. This effect was also observed in an earlier DC SQUID experiment performed in our group. It is actually a welcoming change to our samples, as with this the tunability and thus expected coupling strength dramatically increases.

7.2.2 Measurements of the mechanical mode

In this part, we will review how the mechanical mode is measured and discuss several of the different samples measured. Fig. 7.17 shows a sketch of how the mechanical signal is measured. Due to the coupling, the position of the mechanical cantilever changes the frequency of the cavity. To measure this, we use a fixed frequency probe tone, which experiences an amplitude/phase modulation, depending on the probe-cavity detuning. Taking the Fourier transform, two sidebands symmetric to the probe tone occur, arising from that modulation.

To perform those measurements, nearly the complete setup shown in Fig. 6.10 is required. Only the mixer is optional and the signal can be measured directly. However to extract coupling strengths, also the mixer is required for calibration in our setup, which will be discussed in detail in Chapter 7.2.3.

Fig. 7.18 shows such a measured spectrum, in this case of the main sample used for all discussed backaction measurements. In this spectrum we clearly see the main peak and the two sidebands due to the mechanical mode at a frequency of around 270 kHz.

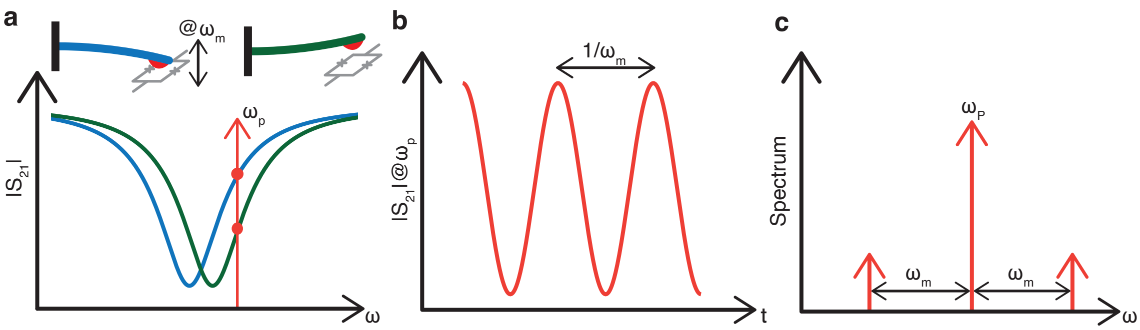

Figure 7.17: Sketch of how the mechanical signal is measured. **a.** As the cantilever moves between its extrema, the frequency of the cavity changes. To measure this, we use a fixed frequency probe tone at ω_p, which is, depending on the probe-cavity detuning, either amplitude or phase modulated. With a detuning as sketched here, the amplitude modulation is the dominating component. **b.** The amplitude of the probe tone varies with the mechanical frequency. **c.** To measure this, we use the spectrum, where the modulation appears as sidebands with a spacing of the mechanical frequency ω_m around the probe tone.

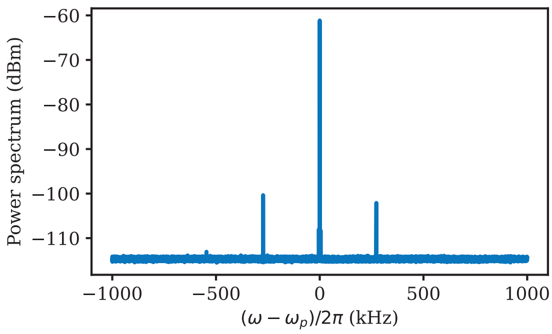

Figure 7.18: Measured spectrum. We see the central probe tone, the mechanical signature appears as expected with two sidebands symmetric around the probe tone. Magnifications of those sidebands for different cantilever samples are shown in Fig. 7.19.

We tried several different cantilevers mounted on different SQUID cavities. Some of those spectra are shown in Fig. 7.19, giving an overview. The cantilevers had different frequencies ranging from around 200 kHz to around 1.5 MHz. The samples shown here had a nice single peak feature and could be fitted with the model of a damped harmonic oscillator

$$S_{II}(\omega) = \frac{A\Gamma}{(\omega^2 - \omega_m^2)^2 + \Gamma^2\omega^2}, \tag{7.1}$$

where A is the amplitude, Γ the linewidth and ω_m being the resonance frequency. Two of those fits are shown in Fig. 7.20 where in (a) a fit to our main sample and in (b) a fit to the sample seen in Fig. 7.19c is shown. Even though the data for this sample is very noisy, it is still possible to perform a faithful fit. In contrast to Fig. 7.19, the data here is shown (and fitted) in linear scale. In Table 7.4 the extracted fit parameters are given. Next to the frequency, also the linewidth is determined. It ranges from sub-Hz to nearly 100 Hz for the high frequency sample. Those numbers should be taken with care, as the cantilevers were measured at different temperatures and for example sample Fig. 7.19b could only be measured with the pulse tube turned on.

Some of the measured samples had an odd line shape, or were simply double peaks. Those samples were disregarded and not investigated further, two examples of this are shown in Fig. 7.21. In (a) the peak has a narrow double feature, while in (b) it is clearly two distinguishable peaks, with a third side peak. While we saw several of those odd spectra, most samples were well behaved.

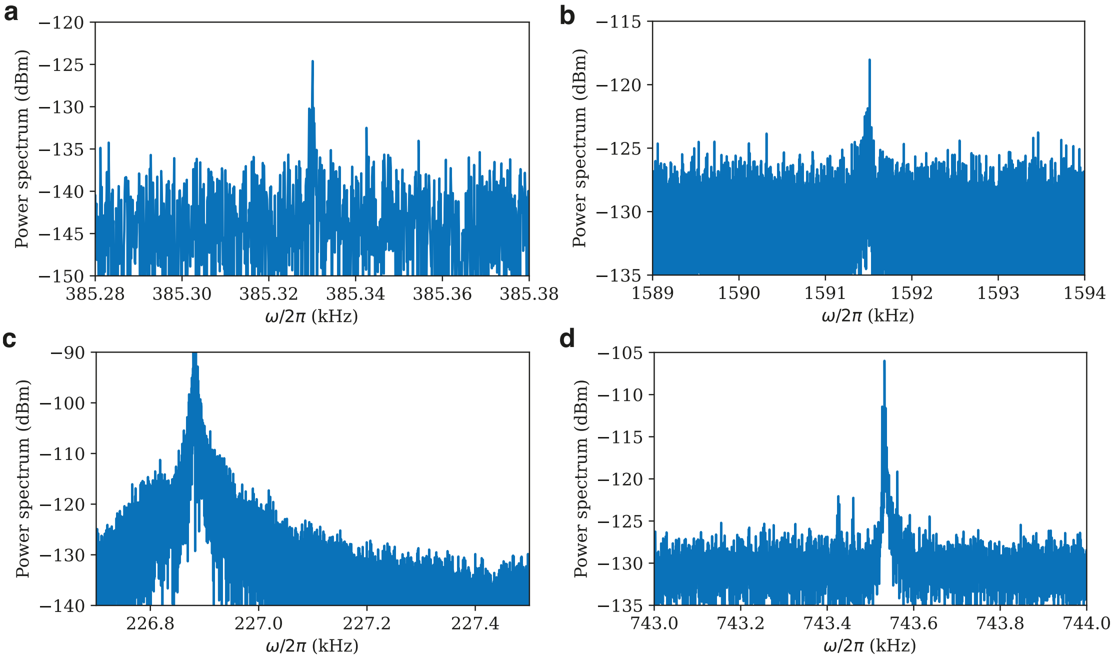

Figure 7.19: Zoom in on the mechanical peak of different samples, the frequency axis is relative to the probe tone. **a-d.** The spectra plotted here should give an overview of the range of cantilever frequencies and peak shapes. However they cannot be compared directly to each other, as not all of those peaks were/could be measured with the pulse tube switched off and they were also measured at different temperatures. Additionally, slightly different setups were used, explaining the different offsets in the spectra.

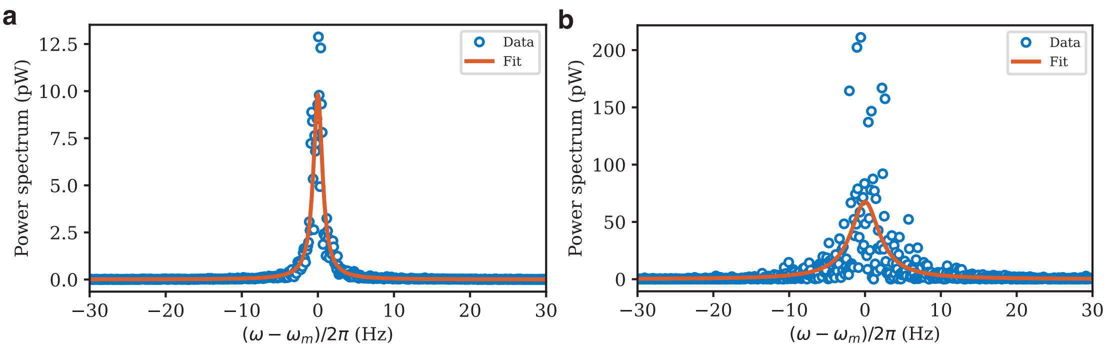

Figure 7.20: Fit with the damped harmonic oscillator model (Eq. 7.1), to two different mechanical peaks. **a.** Fit to the mechanical spectrum of our main sample, where its full spectrum is shown in Fig. 7.18. **b.** Fit to the spectrum seen in Fig. 7.19c. While the mechanical peak is rather noisy, the fit seems to give a valid description of the line shape. The fit results are given in Table 7.4.

Table 7.4: Results of fitting the harmonic oscillator model to the mechanical peaks. These fit results only give some guidance of which parameter range is possible, as they were taken at different temperature, and partly also with the pulse tube cooler turned on (an issue which will be discussed in this chapter).

Sample	$\omega_m/2\pi$	$\Gamma_m/2\pi$
Fig. 7.19a	385.3 kHz	0.06 Hz
Fig. 7.19b	1591 kHz	79.8 Hz
Fig. 7.20a	272.9 kHz	1.4 Hz
Fig. 7.20b	226.9 kHz	4.6 Hz

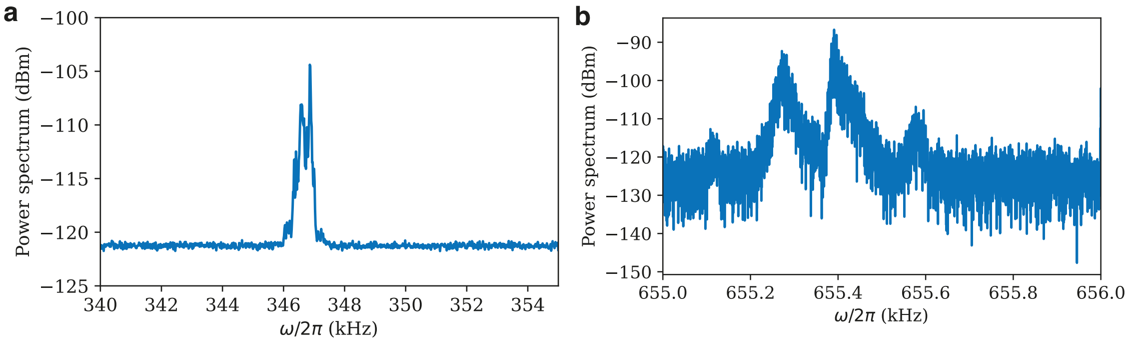

Figure 7.21: Mechanical peaks with an odd line shape. While most mechanical cantilevers showed nice single peaks, which could be described by a damped harmonic oscillator model (see Figures 7.19 and 7.20), we also saw cantilevers with different line shapes. The peaks shown here, should give two examples of such samples. We did not do any further investigation of those cantilevers. **a.** Peak with a narrow double feature. **b.** Double peak, with two nearly identical features and an additional side peak.

It is also worth mentioning, that the pulse tube cooler had a dramatic influence on the mechanical occupation. This is seen in Fig. 7.22 where a measurement with the pulse tube turned on and one with the pulse tube turned off of our main sample is compared. The height of the spectrum is more than an order of magnitude different. However, this was also beneficial when searching for the mechanical mode of a sample, as due to this high occupation, it was easier to find the mode.

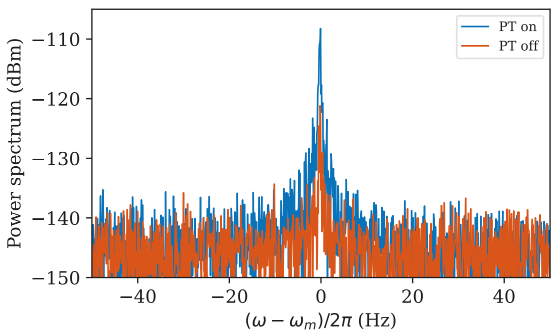

Figure 7.22: Comparison of two spectra with the pulse tube switched on or off. When the pulse tube is switched off, the peak height is reduced by more than an order of magnitude. Hence the vibrations induced by the pulse tube cooler, lead to a dramatic increase of the excitation of the cantilever.

Investigating the high occupation due to the pulse tube further, there are two measurements of the cavity worth discussing. The first is the flux map, where a comparison between pulse tube switched on and off is shown in Fig. 7.23. While the cavity is similar at the top of the flux map, where it is also most flux insensitive, the behaviour changes going to lower frequencies, where the cavity clearly widens and even vanishes in the background with the pulse tube turned on, while it is clearly visibly with the pulse tube turned off. The second measurement, Fig. 7.24, is simply measuring the cavity at a given - flux sensitive - bias point, turning the pulse tube on and off during the measurement. Also here it is clearly visible when the pulse tube is turned on, leading to a very wide resonant feature. As discussed, the reason is the highly excited cantilever, which changes the cavity frequency due to the coupling. This happens at the mechanical frequency and owing to the large mechanical occupation, it drags the cavity by several linewidths, leading to the distorted cavity line shape. In conclusion, only measuring with the pulse tube turned off works well, which gives a measurement time window of up to ten minutes with a wait time afterwards. Either we could concatenate several of those measurements within a short time period of around one hour and waited afterwards for one to two hours or we did one or two

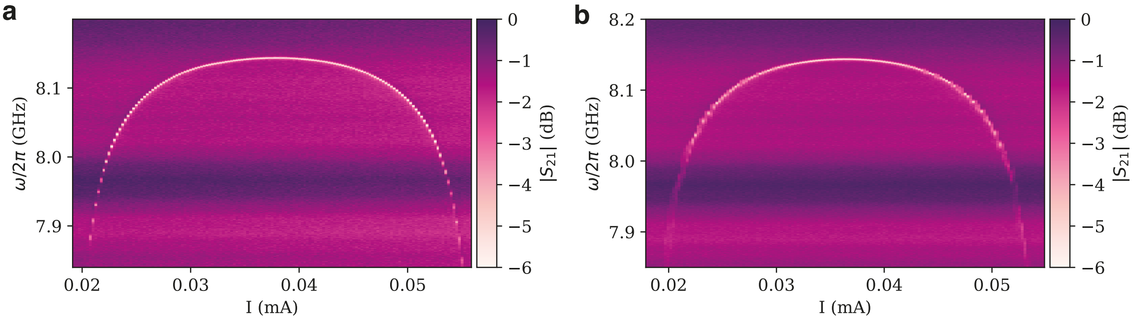

Figure 7.23: Flux map with **a** the pulse tube switched off or **b,** switched on. Only for lowest flux sensitivities, the cavity is nicely behaved with the pulse tube turned on. It is evident, that at higher sensitivities, the cavity is broadened over a large range of frequencies. The reason is, that due to the highly excited cantilever the cavity frequency is changed significantly, leading to a distorted line shape.

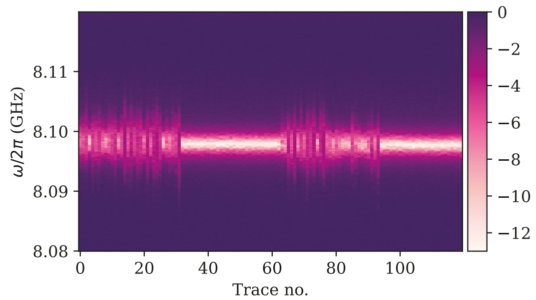

Figure 7.24: A final way to confirm the harmful influence of the pulse tube, is to continuously measure the cavity, while switching the pulse tube on and off. The pulse tube is switched off after the first 30 traces, switched on again after around 70 traces and off just before the 100^{th} trace. It is highly evident, that the cavity line shape is heavily distorted as the pulse tube is switched on, due to a high excitation of the mechanical mode.

pulse tube off measurements per hour.

Now we have seen first measurements of the mechanical mode of several samples. From now on, we will focus on our main sample, which proofed to be well behaved, has a high mechanical quality factor and a decent coupling rate (see Chapter 7.2.6).

7.2.3 Calibration routine to extract the coupling strength

In order to extract the coupling strength[4], we use a calibration routine, introduced in [103], which we will review in this chapter.

The necessity for calibration is due to the fact that we measure S_{II}, so fluctuations of the power (intensity) using the spectrum analyser, but are actually interested in S_{xx}, so the position fluctuations of the mechanical mode. Via the coupling to the cavity, the position fluctuations lead to fluctuations of the cavity frequency, related via the coupling strength

$$S_{\omega\omega} = \frac{g_0}{x_{x_{\text{ZPM}}}} S_{xx}. \tag{7.2}$$

Now, we have to find a connection between the frequency fluctuations of the cavity and the measured intensity fluctuations. For this we frequency modulate our pump tone [103], which scans the response of the system, sketched in Fig. 7.25. As the frequency of the probe tone varies, the transduction changes due to the presence of the cavity, which gives an additional

[4]The coupling strength can be only determined in combination with the phonon number, which will become evident within this chapter.

sideband. This is exactly the required calibration between S_{II} and $S_{\omega\omega}$, as we know the development (and frequency) of the frequency modulation

$$S_{II} = \frac{K(\omega_{\mathsf{FM}})}{\omega_{\mathsf{FM}}^2} S_{\omega\omega}(\omega_{\mathsf{FM}}). \tag{7.3}$$

The calibration factor K is obtained with the frequency modulated tone at ω_{FM}. Usually ω_{FM} is chosen to be in the vicinity of the mechanical frequency, which justifies that the calibration is valid at the mechanical frequency, but also for practical reasons, such that the calibration tone is in the same window of the spectrum analyser as the mechanical peak. With the following relation, we can extract $g_0^2 n_m$, which corresponds to $S_{\omega\omega}$ [103]

$$g_0^2 n_m \simeq \frac{1}{2}\frac{\phi_0^2 \omega_{\mathsf{FM}}^2}{2}\frac{S_{II}^{\mathsf{meas}}(\omega_m)}{S_{II}^{\mathsf{meas}}(\omega_{\mathsf{FM}})}\frac{\Gamma/4}{\mathsf{ENBW}}. \tag{7.4}$$

In the above equation ϕ_0 is the modulation index of the frequency modulation, S_{II}^{meas} are the measured intensities in the spectrum at the respective frequencies and Γ is the linewidth of the mechanical feature. ENBW is the bandwidth set on the spectrum analyser, which is directly given in Hz [103], in contrast to all other quantities which are given in angular frequency. The approximation comes from the fact that the calibration cannot be measured exactly at the mechanical frequency, but is measured slightly detuned. As noted before, only $g_0^2 n_m$ is measured, giving the frequency change of the cavity due to the mechanical mode, which makes it impossible to measure g_0 and n_m independently. To extract n_m, g_0 has to be calibrated, which is done by doing a temperature ramp measurement, discussed in Chapter 7.2.5.

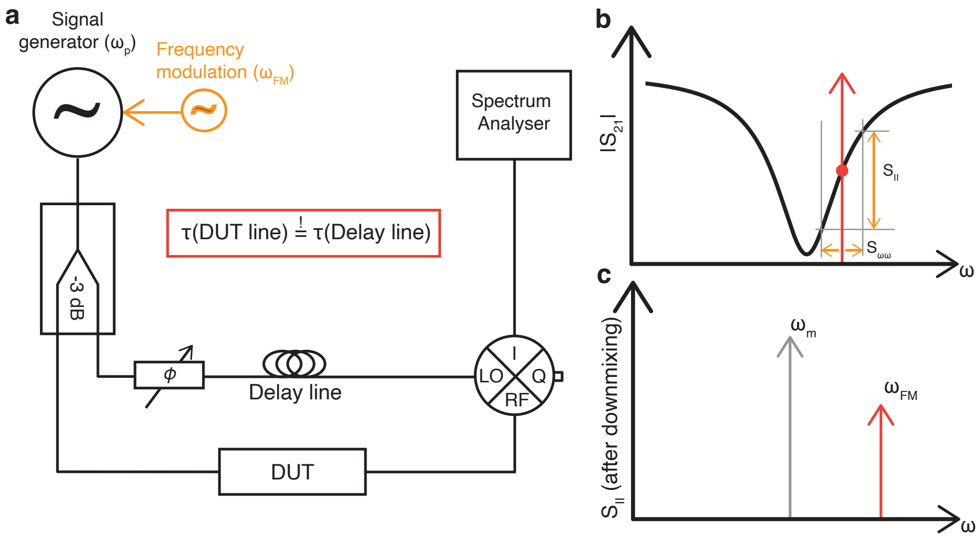

Figure 7.25: Sketch of how the calibration procedure works. **a.** Simplified sketch of the measurement setup. For the calibration routine, we split the signal from the microwave generator, which is frequency modulated. One path of the signal goes to our device under test (DUT), so into the cryostat and to our sample, and to the RF port of our IQ mixer. The other path is used as the LO for the mixer. It is required, that the electrical length of both paths is identical, thus it is also called the delay line. Due to this setup, the signal is always mixed down with the LO being at the same (modulated) frequency. **b.** An additional modulation of the tone occurs in the vicinity of the cavity, converting frequency modulation to an intensity modulation. This is identical to what happens to the signal due to the motion of the mechanical cantilever and with this calibration tone, the coupling rates can be determined. **c.** In the spectrum, an additional peak appears due to the frequency modulation at the modulation frequency, which depends on the transduction of the cavity. Usually we chose a frequency only a few 100 Hz detuned from the mechanical frequency, which is typically at several 100 kHz.

Before actually putting the measured signal from the cryostat in the spectrum analyser it has to be down mixed. The reason is, that any frequency modulated signal creates a sideband, but we are only interested in the additional part due to the presence of the cavity. Otherwise part of the calibration signal would arise from the original modulation, independent of the cavity slope, and would thus falsify the result. This can be circumvented using an IQ mixer and a delay line for the LO port with exactly the same electrical length as the line through the experiment, indicated in Fig. 7.25. With this, the LO and the RF are at the same phase of the frequency modulation, and only the additional modulation due to the cavity creates the sideband, being the calibration peak. It turned out that this procedure was rather cumbersome, as also the mixer is operated at the limits of its internal leakage, and thus the calibration only worked at certain frequencies. To fine tune the electrical length, we first used a manual and later on a digital phase shifter.

In Fig. 7.26 a spectrum with the mechanical peak and the calibration tone is shown. One time the full range (a) and the magnifications of the mechanical peak and the calibration tone (b), also showing the fit of the mechanical mode.

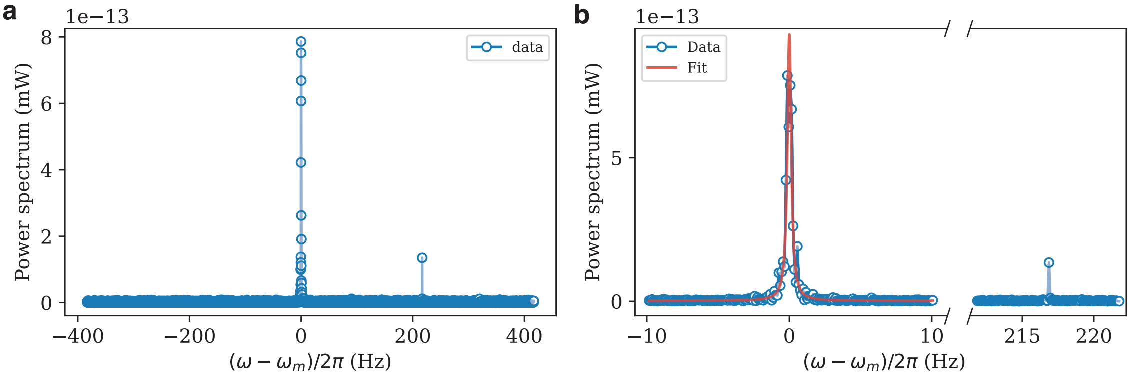

Figure 7.26: Spectrum with the mechanical and the calibration peak. **a.** Full spectrum, the calibration tone is around 200 Hz detuned from the mechanical peak. **b.** Magnification of the mechanical and the calibration tone. While the mechanical feature has a given width and is fitted with the harmonic oscillator model, the calibration tone is typically only on a single point in the spectrum and its height can be directly used.

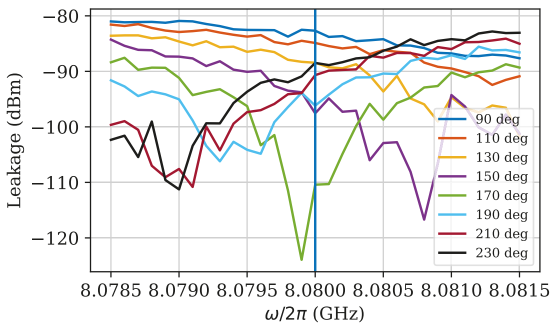

Figure 7.27: As illustrated in Fig. 7.25, the electrical length of the delay line has to be identical to the line through the experiment. If this is not the case, a calibration tone appears, even in case the cavity is detuned. Additionally, leakage in the mixer also leads to a spurious calibration peak. To find a good working frequency, we typically sweep the probe tone with the cavity detuned, for different phases of the phase shifter placed in the delay line. In this example, we chose to work at 8.08 GHz, where a phase of 170° would be a good choice.

As discussed above, the mixer seems to have an internal leakage, which only allows to use the calibration at certain frequencies. We usually measured this beforehand by measuring the calibration tone with the cavity detuned, thus we do not expect any mechanical or calibration signal. For this measurement we also increased the development of the frequency modulation, to be additionally sensitive to a spurious calibration signal. By changing the phase shifter's phase, shown in Fig. 7.27, we aimed to find a setting, where the leakage would vanish below -100 dBm, close to the noise floor for this set of measurements. In this example we aimed for a measurement at 8.08 GHz and found a phase where the leakage was sufficiently low.

7.2.4 Data acquisition and data treatment routines

Sophisticated data acquisition is required, as a narrow mechanical resonance feature as well as magnetic and mechanical noise put challenges on the measurements. The data acquisition changed for different data sets, key aspects will be given when those measurements are discussed and a thorough discussion is found in Chapter A of the appendix, where further technical details about the general data acquisition are given. Here, a concise overview of how the measurements were done will be given.

As the linewidth of the mechanical mode was below 1 Hz down to nearly 0.1 Hz without backaction, we typically used the spectrum analyser at a bandwidth of 0.1 Hz leading to a measurement time of 10 s. Initially, we took 40 consecutive traces for a single data point within one slot where the pulse tube remained switched off, which we reduced to 20 traces later on to safe time. To take such a data point required around 10 minutes for 40 traces, including the overhead mainly from the VNA traces. We fit those traces in groups of four traces, yielding 10 (or 5) independent values for each data point, which provides us then with statistics. A critical point, especially when measuring backaction, is the detuning between the probe tone and the cavity. We used the VNA to determine the detuning. In the early measurements, which were comparably unsensitive to flux noise, we set the detuning before taking all traces. Later, we used VNA measurements before, or even during the acquisition of the spectrum to determine the detuning.

7.2.5 Temperature ramp to determine the optomechanical coupling rate

As discussed in Chapter 7.2.3, we only have access to measuring $g_0\sqrt{n_m}$. To extract the optomechanical coupling rate g_0, we have to assume that the mechanical mode is thermalised (thus we know n_m). To ensure exactly this, we measure the mechanical mode at different temperatures, but the same coupling rate, with a low enough power to avoid backaction. The occupation of the mechanical mode should increase linearly with temperature, given by the Bose-Einstein distribution, Eq. 2.15.

Fig. 7.28 shows such a temperature ramp up to 700 mK. In panel (a) with the pulse tube

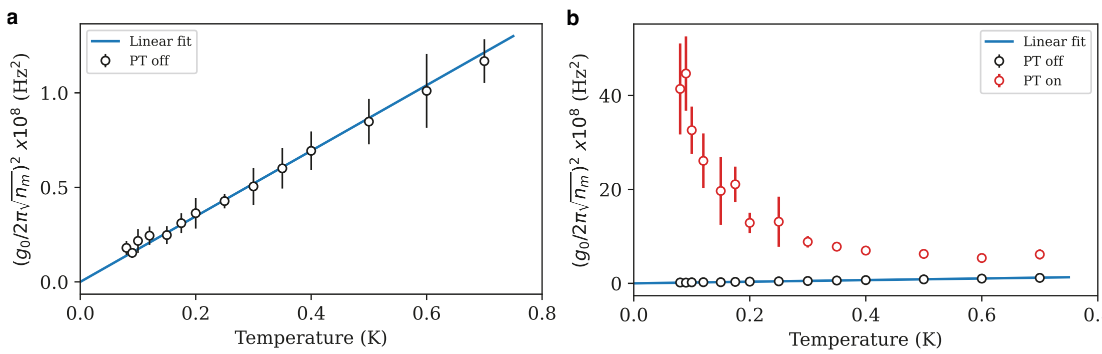

Figure 7.28: Temperature ramp to ensure thermalisation of the mechanical mode and to calibrate the coupling, as only $g_0\sqrt{n_m}$ can be measured. **a.** Pulse tube off. The mechanical occupation increases linearly with the temperature, as expected for a thermalised mode. The linear fit extracts $g_0/2\pi$ = 47.8(4) Hz. The sample was measured down to 80 mK, a measurement to even lower temperatures can be found in Chapter A.2 of the appendix. **b.** Pulse tube on. The mechanical mode is excited dramatically above the thermal equilibrium, however the occupation decreases with temperature. This can be explained with an increasing linewidth with temperature (see Fig. 7.29 and main text).

turned off, we see that the occupation increases linearly with temperature and extrapolated goes through zero, ensuring that there is also no offset. We additionally confirmed, that we are not inducing any backaction, by measuring at different powers around the power used for the temperature ramp, shown in Chapter A.2 of the appendix. A linear fit gives the coupling strength, which is in this case close to 50 Hz. In (b) additionally data with the pulse tube turned on is shown, where we clearly see the much higher mechanical occupation. Interestingly, the mechanical occupation with pulse tube on increases with lower temperature. An explanation for this can be found in the increasing linewidth with temperature, Fig. 7.29a.

As the pulse tube has a repetition rate of around 1.4 Hz, which is similar to the linewidth of the cantilever. With increasing linewidth the mechanical excitation decays faster and the pulse tube can excite it less efficiently, leading to a lower occupation number. In Fig. 7.29b the

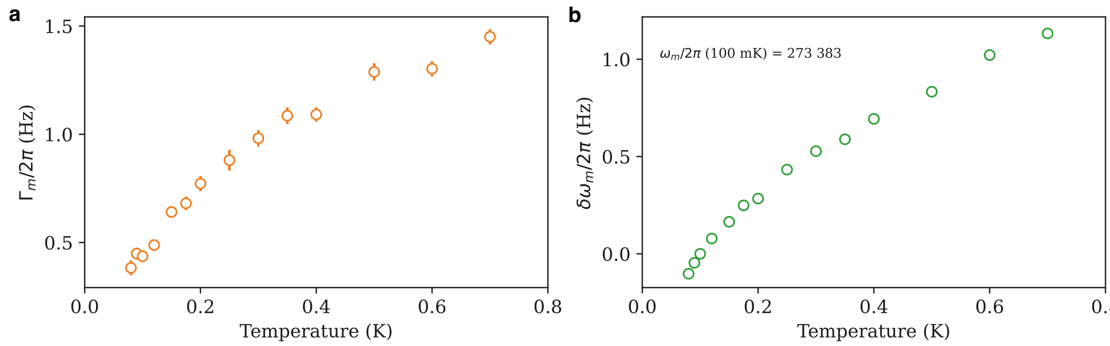

Figure 7.29: Change of mechanical linewidth and frequency with temperature. **a.** The linewidth increases with temperature. Below 100 mK the linewidth is far below 0.5 Hz, while it increases up to 1.5 Hz approaching 1 K. **b.** Change of mechanical frequency with temperature, where the frequency at 100 mK is used as a reference. The frequency slightly increases with temperature. The change of both, linewidth and frequency, can be explained by changes of the material properties of the cantilever.

frequency change with temperature is shown, where the slight change of frequency is explained with changes of the cantilever's material properties.

7.2.6 Tunability of the coupling strength

We know from Chapter 2, that $g_0 = \partial\omega_c/\partial x \, x_{\mathsf{ZPM}}$. In our case, we can re-write it as the following

$$g_0 = \frac{\partial\omega_c}{\partial\Phi_{\mathsf{ext}}}\frac{\partial\Phi_{\mathsf{ext}}}{\partial x}x_{\mathsf{ZPM}}, \tag{7.5}$$

where Φ_{ext} is the external magnetic field, which is (also) the field from the cantilever. The first part of this equation is the frequency change per field change, which depends on the bias point, as seen in the flux map, Fig. 7.15. This means that the coupling strength is in-situ tunable during the experiment. The second part, $\partial\Phi_{\mathsf{ext}}/\partial x$ is a geometric factor, depending on the size of the magnet, its magnetisation and the cavity-cantilever alignment.

With the coupling strength characterised via the temperature ramp, Chapter 7.2.5, we can extrapolate the coupling strength at any given bias point using the slope of the flux map. Fig. 7.30a shows the change of coupling strength with the cavity frequency. Whenever we performed cooling traces, we did a local flux map to determine the coupling, the data points using local flux maps are shown as well. The expected g_0 is then also checked to be in agreement with the tail of the cooling traces. On a secondary axis, the single-photon cooperativity (Eq. 2.40) is shown, which exceeds 100 for coupling strength accessible in the experiment. Beyond a coupling of around 10 kHz, flux noise becomes too large to measure the mechanical signal directly. However, we can still measure the cavity itself, shown in Fig. 7.30b. Here we see that the cavity tunes more than 1 GHz and estimate a $g_0/2\pi \simeq 90$ kHz. This can be seen

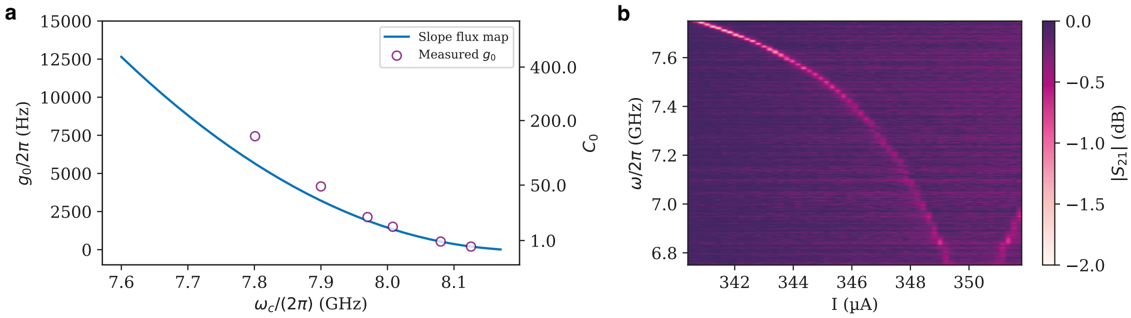

Figure 7.30: Change of coupling with flux bias point point. **a.** Comparison of the expected g_0 via the slope of the full flux map (Fig. 7.15) and local flux maps (For a local flux map, we took a flux map in a narrow range of cavity flux bias points. For these we do not have to rely on the model fitted to the complete flux map (Fig. 7.15), but use a polynomial fit.). This shows the tunability of the coupling strength from (first order) no coupling up to several kHz. On a secondary axis, the corresponding single photon cooperatives C_0, Eq. 2.40, are given. While the slope of the flux map allows higher coupling strengths, increasing flux noise prevents us from measuring the mechanical mode there. **b.** Flux map with the background subtracted down to low frequencies. While we cannot measure the mechanical mode when the cavity is very flux sensitive, we can still measure the cavity itself. Using the slope of the flux map, we expect a coupling of $g_0/2\pi \simeq 90$ kHz at the highest sensitivities of the cavity.

as a lower bound, as the cavity still seems to tune further down. In this range we also expect a single-photon quantum cooperativity, Eq. 2.41, beyond unity.

While working at large g_0 is beneficial for achieving a large backaction, it also makes the cavity more flux sensitive. This will be seen in the backaction measurements discussed later, where a good trade off between coupling strength and flux noise has to be found. This gets additionally complicated, as the Kerr increases with flux sensitivity (Eq. 5.36), which also means that bistability is already reached at a lower photon number.

7.2.7 Flux stability

Being sensitive to magnetic signals is crucial for detecting the magnetic cantilever, however it also makes the setup intrinsically sensitive to magnetic flux noise. We recognised, that low frequency flux noise influences the VNA traces and limits the stability of our operational point. Fig. 7.31a shows three VNA traces at different flux sensitivity, all measured with the pulse tube turned off. One notices that the cavity peak gets increasingly less pronounced with flux sensitivity and nearly vanishes in the background for the highest sensitivity shown. In addition however, there is a very regular pattern which is seen in all of the traces, which also gets increasingly dominant with flux sensitivity. These features change with the scan rate of the VNA and average out when taking a certain number of averages. Eventually they even come back when averaging even longer. Taking the spectrum by using a fixed frequency tone, Fig. 7.31b, we see the main components of this noise, which are between 50 Hz and 100 Hz, with typically the highest peaks close to 70 Hz and 80 Hz. At first, the cause of this noise was not evident and we suspected issues with our DC coils. At some point, we compared the spectrum using an accelerometer on the top of the cryostat to the flux noise of the cavity and all major peaks seen in the cavity spectrum coincide with mechanical noise peaks. This means that mechanical noise is converted to flux noise in our setup.

We came to the conclusion, that it is the magnet of the cantilever moving relatively to the SQUID at these low frequencies. This is also backed by the observation, that we do not see such flux noise for samples without a cantilever. To reduce vibrations, we subsequently did several steps. To track the influence of each step, we typically measured with the accelerometer as well as measuring the noise directly on the cavity. In the following is a list of the improvements, which were partly also done in parallel to each other:

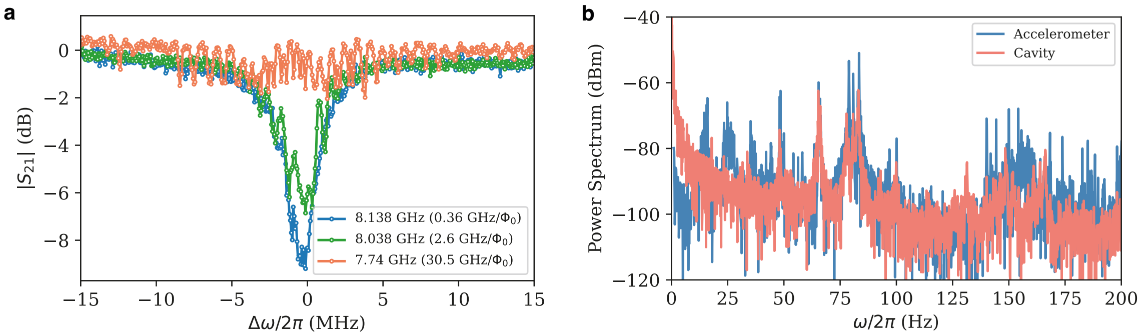

Figure 7.31: VNA traces at different flux sensitivities and noise spectrum. **a.** As the flux sensitivity of the cavity increases, the cavity response is increasingly governed by a noise pattern. This pattern depends on the VNA scan speed and seems to have its main components below 100 Hz. For high flux sensitivity it completely dominates the cavity response and prevented us from measuring in those regions. **b.** A noise spectrum of the cavity reveals that the dominating components of the flux noise are between 60 and 90 Hz. We also took a spectrum using the accelerometer (offsetted) on the top of the fridge and all noise peaks seen in the cavity spectrum coincide with mechanical peaks. Hence, mechanical noise is transduced to flux noise.

- Optimise air pressure in all the air dampers (Fig. 6.9). There are eight dampers, with one bottom and one top damper in each of the four corners of the suspension. With those dampers, the plate where the cryostat is mounted can be be lifted from its resting pillars, but also the clamping force can be varied by the air pressure. This involves optimising the air pressure in eight pillars, and the ideal configuration is not straight forward. However some configurations are clearly worse than most, like putting a very high or low pressure in all dampers. In the end, a configuration where it worked reasonably well was found and also used as a reference for subsequent cooldowns.

- Avoid vibrations coupling into the system via all connected hoses as much as possible. We tried separating the hoses which carried vibrations form touching each other in the laboratory. Sometimes we saw vibrations from the pulse tube cooler of the other cryostat coupling into our system, which we avoided by making sure that there was no connection between the two systems, via any of the cables and hoses.

- Below the laboratory there is a pump room, where all vacuum pumps, necessary for the operation of the cryostat, being the compressor, the forepump and the turbo pump are located, which are all vibrating at different frequencies and intensities. To reduce coupling of their vibrations into our system, we pursued a two fold approach. Originally, all of those pumps where mounted on a single rack. We first suspended all of these pumps separately, by building for instance a mount fixing the turbo pump to the ceiling or a table for the forepump. Second, we clamped all the hoses carrying vibrations from the pumps first individually and then all together, to reduce the amount of vibrations coupling into our system. Fig. 7.32a shows the mounting for the turbo pump from the ceiling and the hoses clamped together.

- Lastly, we built a sandbox filled with around 300 kg of sand to damp vibrations. We placed this box in the laboratory, directly above the pump room, routing all of the hoses through. In Fig. 7.32 a picture of the empty sandbox with the holes in the bottom (b) and the final setup in the laboratory (c) with all hoses and cables routed through is seen.

All of this helped to damp the vibrations. While doing the experiment and taking more sensitive data, we continuously learned about the significance of vibrations in our system and the importance of reducing them. Thus, those improvements were done in between the backaction

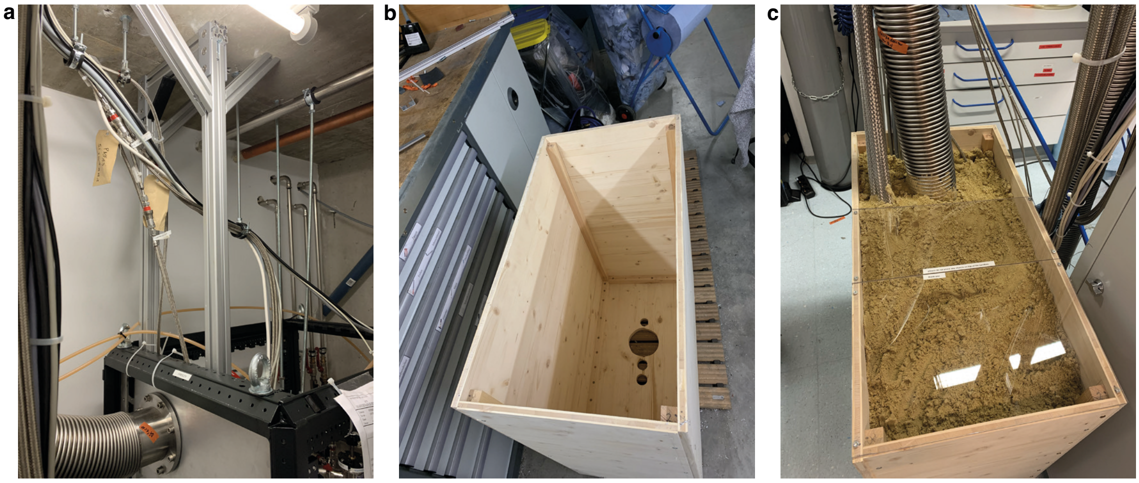

Figure 7.32: We made several improvements to reduce vibrations coupling from the vacuum pumps into our system. **a.** We suspended all three pumps separately, which were on a single cart previously. Here one can see the structure, which supports the turbo pump, mounted to the ceiling. Also all hoses going to the cryostat carry vibrations. These were first fixed separately (not seen) and then also clamped to the ceiling. **b.** In addition, we built a sandbox, to reduce vibrations further. Here the empty sandbox can be seen with cutouts for the hoses being routed through. **c.** Filled sandbox in the laboratory. All hoses and cables were routed through the sandbox. The pump room is directly below the pump room, thus we placed the sandbox exactly above the pump room, to easily guide everything through.

measurements. However all major improvements were done before doing the measurements on the nonlinear cooling, presented in Chapter 7.4. Fig. 7.33 shows a comparison of the spectrum measured using the cavity before and after doing most of the improvements. As can be seen, all noise peaks could be suppressed dramatically, by around 20 dB. It should be noted, that the vibrations also changed on a day to day period and the setup seems to be very sensitive to minimal changes in the environment. Still overall the flux stability could be improved by a lot doing all of the steps discussed.

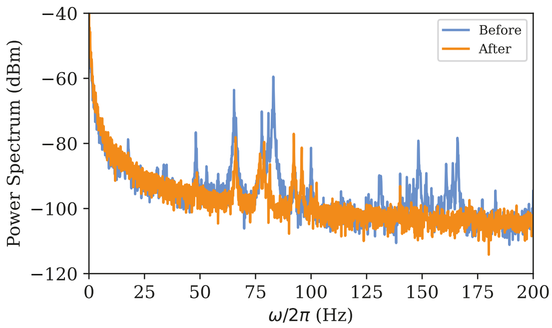

Figure 7.33: Noise spectrum before and after all improvements. While the frequency of the main noise components remained mostly the same, their height was drastically lower than originally. It should be noted, that the noise also changed on a daily bases, as it seems to be very sensitive on the environment. However the improvements led to an overall much more stable setup.

At some early point, we also measured an extremely high mechanical excitation, without any backaction. Initially we suspected a mechanical source to drive the mechanical excitation. However trying to reduce vibrations going to the cryostat did not result in any change. Eventually we discovered, that the reason was the box connecting the DC coil to the current source. Only if the outside of this box was properly grounded, the mechanical excitation was in the thermal equilibrium (when not doing measurement with backaction). Fig. 7.34 shows the phonon occupation for two similar detunings, where one time this box was grounded and the other time it was not grounded. The difference in occupation is nearly two orders of magnitude. We concluded, that the reason for those high excitations was flux noise at a frequency similar

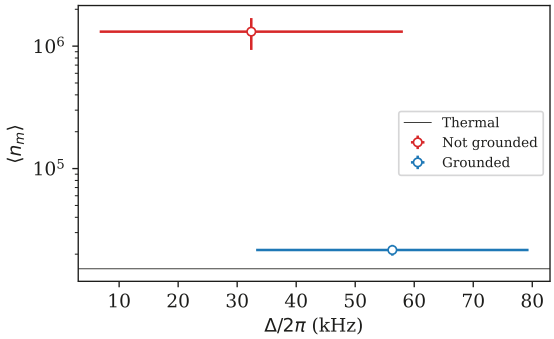

Figure 7.34: Sometimes we measured very high mechanical occupation. The reason was found in whether the box used to connect the DC cables running from the coil around the waveguide to the current source was grounded or not. In case this box was not grounded, the mechanical occupation number was nearly two magnitudes above the thermal expectation. Here two measurements are shown, measured at low enough power to avoid any backaction with similar detunings, one time grounding the box and another time not grounding this box.

to the cantilever frequency, driving it resonantly to very high excitation numbers. From this time on, we properly grounded the box and this problem did not occur anymore.

7.3 Backaction in the linear regime

Below we will discuss the backaction measurements done in the linear regime. For this measurements, a weak enough drive is used, such that the cavity remains in the linear regime. At first, we will discuss measurements at low coupling and intermediate powers, and afterwards measurements at high g_0 and very weak power. As the Kerr increases when operating at higher couplings (Eq. 5.36) we have to lower the power to remain in the linear regime. The setup used is the complete one shown in Fig. 6.10, where we utilised the manual phase shifter to change the length of the delay line. Additionally, we only used a single room temperature amplifier in contrast to the two shown in the diagram.

7.3.1 Cooling at low coupling

In this part, we will discuss a backaction measurement at a coupling of around 60 Hz. The data acquisition is already discussed in Chapter 7.2.4, additional information is also given in Chapter A of the appendix. A crucial aspect for measuring backaction is the detuning between the probe tone and the cavity. To change the probe-cavity detuning in this dataset, we tune the probe to different frequencies, while we keep the cavity frequency fixed. This is in contrast to all other datasets, where we changed the cavity frequency itself. Here, for tuning the cavity, we turn on the pump and tune the cavity frequency always to the same value. This is done to compensate for flux drifts occurring over a day. Then we detune the pump to the desired frequency and take the measurement.

Fig. 7.35 shows a backaction measurement and the data is fitted with the linear theory (Chapter 2.2). The fit, being in good agreement with the data, extracts a coupling of 57(1) Hz and a cavity photon number of 186(6). It should be noted, that we shifted the x-axis such that no backaction occurs at zero detuning, as we did not correct for the cavity/waveguide impedance mismatch when analysing the data. In this power regime, the cavity shows the typical linear line shape and the theory works well. However, already for this power we see systematically higher backaction in the cooling and weaker backaction in the heating area, as expected for a nonlinear cavity. This discrepancy is small, but it shows for the phonon number, linewidth and frequency shift.

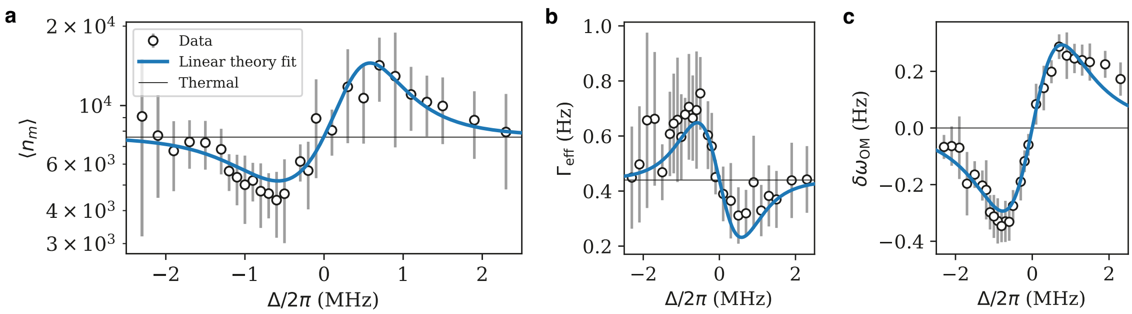

Figure 7.35: Backaction cooling for a coupling of nominally $g_0/2\pi = 57(7)$ Hz. **a.** Phonon number against probe-cavity detuning. Due to a small enough power, the cavity is in the linear regime, which allows us to fit with the linear theory, discussed in Chapter 2.2.2. The fit gives a cavity photon number of 186(12) and a coupling of $g_0/2\pi = 57(1)$ Hz. **b,c.** Mechanical linewidth and frequency shift under backaction. The theory is plotted using the fit results obtained from fitting the phonon number. In all three plots, we see decent agreement between data and theory.

Due to the low power, the overall backaction is small, with only lowering the thermal phonon number by around 40%. The mechanical frequency shift shows the backaction most clear, as we can extract the mechanical frequency with most accuracy.

In addition, it should be noted that due to the low coupling strength as well as the low powers, flux noise was not a limiting issue when measuring this data. Even though most of the discussed setup improvements (Chapter 7.2.7) were not implemented at that point.

With this measurement, we clearly show that we can see backaction in our optomechanical device. In the next part, we will discuss backaction at higher couplings, but still using a power, such that the cavity remains in the linear regime.

7.3.2 Cooling at high coupling

For this measurement we increased the coupling to around 2.4 kHz. To still operate in the linear regime, we decreased the power to be in the limit of nearly a single photon, compensating the Kerr increase with coupling (Eq. 5.36). Owing to the large coupling it is still possible to see backaction despite this very low power. However due to the large coupling, flux noise has a significant impact and we had to be much more careful when analysing the data, where especially flux drifts on time scales above our 10 s measurement time concerned us. In order to determine the detuning for each trace from the spectrum analyser, we fitted a VNA trace taken in parallel. Afterwards, we binned the traces together with respect to their detuning using a width of 1 MHz for each detuning bin. Details on this are given in Chapter A.4 of the appendix.

Fig. 7.36 shows the backaction traces when using a coupling of 2.38(6) kHz and a cavity photon number of 2.1(4) on resonance. At this coupling the single photon cooperativity (Eq. 2.40) is around 10 and at the detuning of most cooling, we estimate a photon number of 1.4 in the cavity[5]. Despite the low photon number, there is significant backaction, reducing the thermal population by around a factor of 3. In the heating region we enter the regime of dynamical instability and cannot trust the data/fit there. Besides, there is very good agreement for the fit of the photon number and frequency shift, however the fit systematically underestimates the linewidth in the most cooling region.

The discrepancy in the linewidth can however be explained with flux noise. The probe-frequency detuning is not fixed due to flux noise, which changes the backaction on the me-

[5]As the detuning with most cooling is red detuned from the cavity resonance, we have a smaller cavity population.

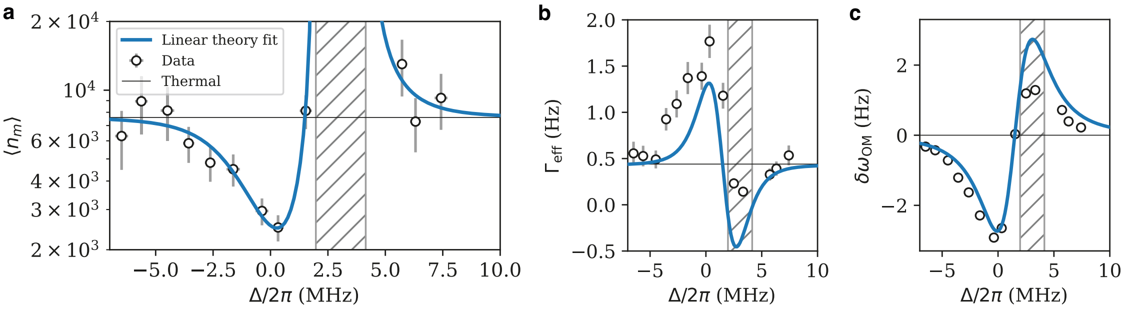

Figure 7.36: Backaction for a large coupling of around 2.4 kHz, where we also expect C_0 to exceed around 10. **a.** Phonon number against detuning. The fit gives a photon number of 2.1(4) on resonance and $g_0/2\pi = 2.38(6)$ kHz. At the detuning of most cooling, we estimate a circulating photon number of 1.4. **b,c.** Mechanical linewidth and frequency shift against detuning. We use the fit parameters obtained when fitting the phonon number and plot the results here. While there is good agreement with the frequency shift, the linewidth is systematically underestimated in the cooling region. We believe this occurs due to flux noise and is further investigated in Fig. 7.37. The hashed region marks the region of mechanical instability, which occurs when the linewidth drops below zero. There the results cannot be trusted. The horizontal line in (b) shows the expected linewidth without backaction.

chanical mode. This change of backaction leads to a frequency shift due to the optical spring effect (Eq. 2.25), which is seen as an effective broadening of the linewidth. This flux noise especially became an issue for the measurements operating in the nonlinear regime, close to bistability and at high couplings. This is addressed in Chapter 7.4.4, where a model for the backaction including flux noise is developed and applied to the data. Already here, we use this model to fit our data. We fit the linewidth and frequency shift, where we use the strength of the flux noise and the cavity photon number as free fit parameters. The results of this fit are shown in Fig. 7.37. There the prediction of the flux noise model for the phonon number and the

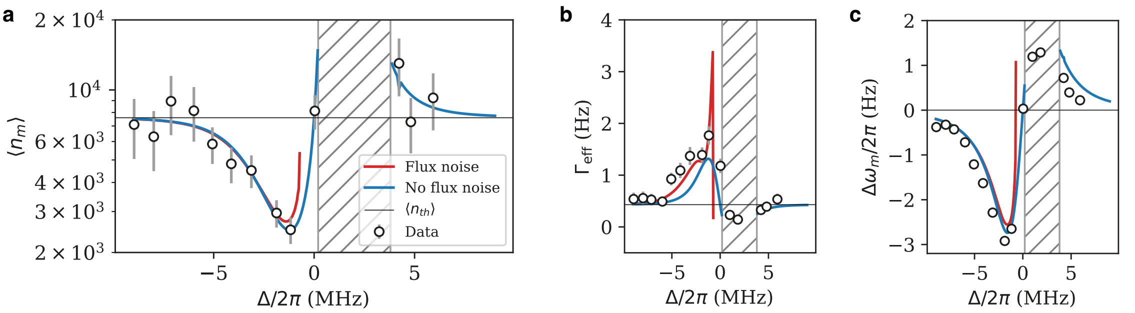

Figure 7.37: Fitting the cooling trace shown in Fig. 7.36 with the flux noise model, discussed in detail in Chapter 7.4.4. We fit the change of linewidth and mechanical frequency versus detuning, using the strength of flux noise and cavity photon number as free fit parameters. **a.** Phonon occupation against probe cavity detuning. The flux noise model only predicts a minor difference in the cooling strength. The effect of the mechanical instability already shows further red detuned, as instead of a single detuning, a range of detunings are used. The trace without flux noise uses the same parameters, only the flux noise is set to zero. **b.** Linewidth against probe cavity detuning. Here we see the same characteristics as in the experiment. The linewidth in the cooling region is systematically increased in the case of flux noise. Also a dip just before the highest linewidth is predicted, similar to the experiment. The horizontal line shows the expected linewidth without backaction. **c.** Mechanical frequency against detuning. Here, similar to the phonon number, the model with and without flux noise are very similar, while there is still a slight discrepancy to the measurement data throughout the cooling region for both models.

linewidth is plotted. While it does not seem to have a huge impact on the phonon number, the predicted linewidth under flux noise is much closer to the measurement data than the model without flux noise. Especially the spike around largest cooling backaction seems to be similar to the effect we observe in the experiment. For the frequency shift, flux noise only seems to have a minor influence, by slightly reducing the expected frequency shift. As the impact on the phonon number is small, we can trust the fit parameters obtained when fitting the phonon number without taking flux noise into account (Fig. 7.36).

With this we have seen that in the low power regime, our cavity can be approximately treated as being linear. A single photon in the cavity is sufficient to see significant backaction on our system, due to the large coupling, at which this measurement was taken. At this high coupling, flux noise has a non negligible impact on our measurements. For the data treatment, we solved this by binning the data with similar detunings together. Furthermore, the impact of flux noise on the mechanical linewidth can be well described by our flux noise model.

7.4 Nonlinear enhanced cooling

In this part the backaction measurements using the enhanced cooling capabilities of our nonlinear cavity will considered and discussed. We want to experimentally demonstrate that the theoretical predictions from Chapter 4 are correct. To our knowledge, such a nonlinear cooling has not been shown so far experimentally, while it was already predicted several years ago by theory [4, 5].

7.4.1 Measurement specific information

The setup we used is identical to the one depicted in Fig. 6.10. For the phase shifter, we now used a digital model from the Vaunix Lab Brick series. This makes the setting of the phase in the delay line more controlled, and also more convenient, as it allows to adjust the phase remotely. In addition, we added a second room temperature amplifier, in contrast to the previous measurements, Chapter 7.3, to boost the signal before downmixing.

Measuring cooling traces approaching bistability, the sensitivity to flux noise increases, as the cooling happens over an increasingly narrow range of detunings. To improve flux stability, we did all the modifications on our setup, as discussed in Chapter 7.2.7. The improvements can be also seen directly in the cooling traces, where bottoming out is avoided, which will be addressed later on in Fig. 7.43. To further increase our resilience against flux noise, we modified our data taking routine. To determine the detuning of each trace, we use a VNA trace taken before the spectrum analyser measurement. In contrast to the cooling with low power (Chapter 7.3), we cannot use the VNA trace measured during the acquisition of the spectrum, as the cavity line shape is distorted due to the large pump power. To further increase the stability of the chosen detuning during a pulse tube off measurement, we check the cavity detuning several times during the data taking and retune if necessary, which is all done automatically. When analysing the data, we bin the data with similar detunings using the VNA traces and also apply several automated goodness of fit criteria to make sure that the fit is reliable and there was not a significant change of flux bias point during the measurement. We further also integrate the area under the mechanical peak numerically, to get a fit independent estimate of the phonon number.

More details on the measurement protocol and the data treatment are given in Chapter A of the appendix.

7.4.2 Nonlinear cooling at low coupling

Here, we will discuss nonlinear cooling measured at low coupling strength and different powers, where the nonlinearity gets increasingly relevant with higher power. For the measurements shown here a coupling strength of around 201 Hz was used.

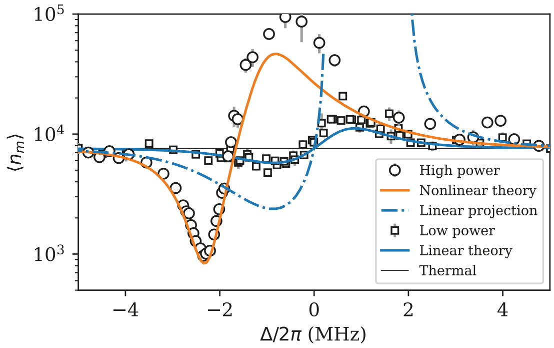

Figure 7.38: Comparison of two cooling traces taken at low and high power by showing the mechanical occupation against the probe-cavity detuning. For the low power trace, the cavity is in the linear regime, and a fit with the linear theory works well. Increasing the power to around half the critical power, the cavity is in the nonlinear regime. The frequency shift of the cooling trace is evident and only the nonlinear theory is capable of describing the data. Characteristic for the nonlinear cooling is the large asymmetry between cooling and heating backaction strength. This is also evident, plotting the linear projection for the high power trace with - besides the nonlinearity - identical parameters.

Fig. 7.38 compares two cooling traces taken at low and high power. The detunings are the low power detunings measured with a VNA measurement directly before the acquisition of the spectrum. For the low power trace, we see the much lower backaction, but also the good agreement to the linear theory. For the high power trace we use a fit based on the nonlinear theory, Chapter 4, and find, especially in the cooling regime, excellent agreement. We also plot the linear projection using the same set of parameters for a linear system, and clearly see the difference to the data. Besides the nonlinear frequency shift, the cooling is significantly increased, while the amplification/heating is much decreased. The linear theory would predict negative linewidth, while the nonlinear theory accurately predicts not to reach instability. The discrepancy between data and nonlinear theory in the amplification/heating region can be explained with a high sensitivity of the mechanical mode to mechanical noise, as the linewidth is very low in this region.

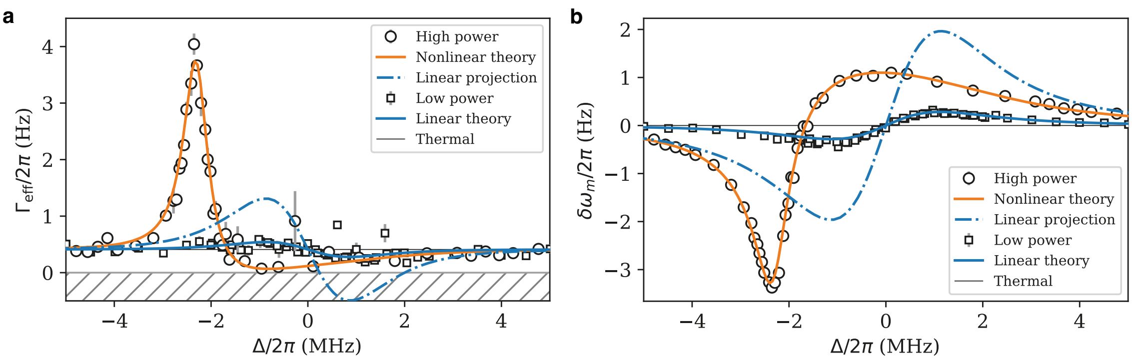

Figure 7.39: a. Mechanical linewidth **b.** and frequency shift for the cooling trace plotted in Fig. 7.38. The features are similar to what is discussed in Fig. 7.38. Also here the asymmetry in the cooling and amplification backaction strength is evident, where due to the nonlinearity, the regime of dynamical instability is not reached in the high power case. In both plots, we observe excellent agreement between nonlinear theory and the (high power) data, while the linear theory is clearly unable to reproduce the measurement.

Fig. 7.39 shows the corresponding linewidth and frequency shift. Also there we see excellent agreement between the high power data and the nonlinear theory. Especially in these plots the asymmetry between cooling and heating strength can be observed, induced by the nonlinearity of the cavity line shape. For fitting the nonlinear theory to the data, we always perform the fit on the linewidth and the frequency shift simultaneously and calculated the results for the phonon number.

For the high power measurement, the fit extracts a photon number of around 126, while for the low power data we had around 24 photons in the cavity. With this, we have shown that the nonlinear line shape of the cavity has to be crucially taken into account and as predicted, we see much enhanced cooling backaction due to the nonlinearity.

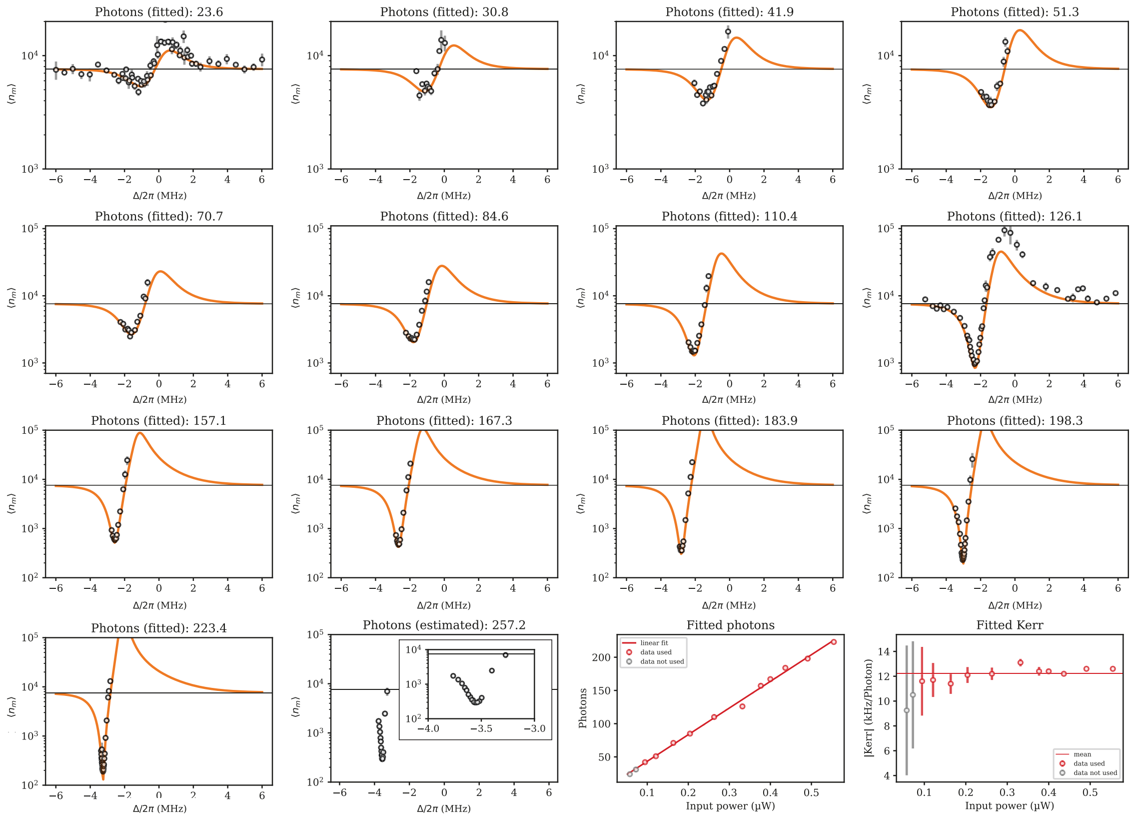

Figure 7.40: Cooling traces for increasing power together with an independent fit for each trace. In the bottom right, the extracted fit parameters against fridge input power are shown, the negative Kerr is given as an absolute value.

Fig. 7.40 shows all the cooling traces taken at different powers, while Fig. 7.38 already shows the two where both tails, cooling and heating, were measured. For all traces the nonlinear fit is shown and the extracted photon numbers are given, except for the one with highest power, which is above bistability. As shown in the inset, the cooling backaction happens on a very narrow range. It is evident, that the cooling backaction shifts to lower frequencies with increasing power, as expected from the nonlinearity. The nonlinear fit shows excellent agreement with the data. For the highest power before bistability, we seem to be limited by flux noise, which will be discussed in Chapter 7.4.4. In the two bottom right panels, the extracted Kerr values and photon numbers are shown, which are also the only two fit parameters. As expected, the photon number linearly increases with input power, while the Kerr remains the same over all powers. The bias point of the cavity is similar to the one used for the power sweep, shown in Fig. 7.16a. Comparing the values of the Kerr from the power sweep to what we extract here by fitting the cooling traces, we find good agreement, even though the methods used to obtain the Kerr are very different. Here we used the nonlinear fit to the cooling trace, while before we fitted the cavity directly and estimated the photon number using the input attenuation.

Fig. 7.41 shows the lowest phonon number measured for each power, the linewidth and frequency shift at this point. Additionally the predictions from the linear and nonlinear theory are plotted, using the average Kerr value and an estimate of the photon number, from the fit to all individual traces, Fig. 7.40. While for lowest powers, the predictions from linear and nonlinear theory are similar, for higher powers, only the nonlinear theory gives a faithful prediction of the data. For highest power we see a slight decrease in cooling strength as the phonon number at best cooling increases, which can be explained with flux noise, Chapter 7.4.4. Interestingly, the frequency shift reduces operating close to bistability, seen in the data as well as in the theory. Already when introducing the theory, Chapter 4, this feature could be also observed. So far, we have no intuitive explanation for this feature, however it should be noted, that in the sideband resolved regime there is no frequency shift at best cooling (Fig. 2.3).

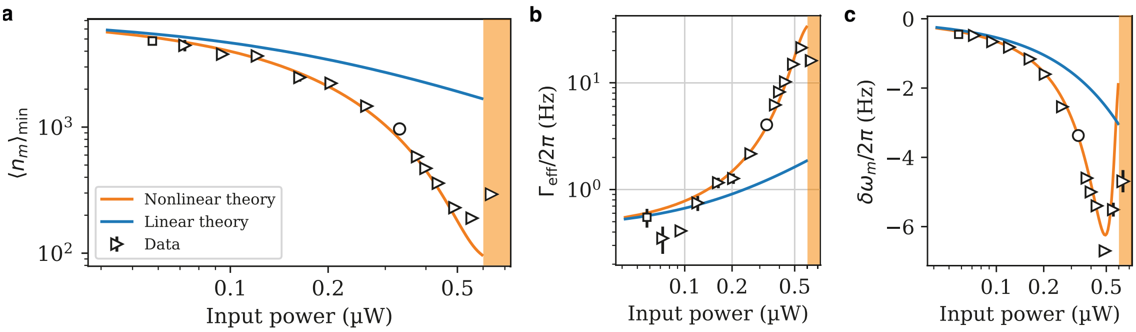

Figure 7.41: Best cooling against input power. **a.** Minimum phonon occupation for increasing power, together with predictions from linear and nonlinear theory. The parameters for calculating the predictions are obtained from the fit to all cooling traces (Fig. 7.40), where an averaged input power to photons conversion and an averaged Kerr is obtained. While for low powers linear and nonlinear theory are similar, at high powers the nonlinear cavity achieves a cooling enhancement of more than an order of magnitude. **b.** Mechanical linewidth at the point of lowest phonon number. Again, the nonlinear cavity gives excellent agreement with the data, while the linear theory predicts much weaker backaction. **c.** Mechanical frequency shift against detuning. Interestingly, the frequency shift reduces for strongest backaction, which is also seen in the data. In all plots, the circle and square symbols correspond to the symbols used in the Fig. 7.38, the shaded area is the region above bistability.

Fig. 7.42 shows that also performing an independent linear fit on the high power dataset from Fig. 7.38 does not give a faithful representation of the data. Here we also shifted the x-axis, such that we have no backaction at zero detuning. Still the cooling is significantly underestimated, while the heating is overestimated. This shows once more, that only the nonlinear theory is capable of describing this data.

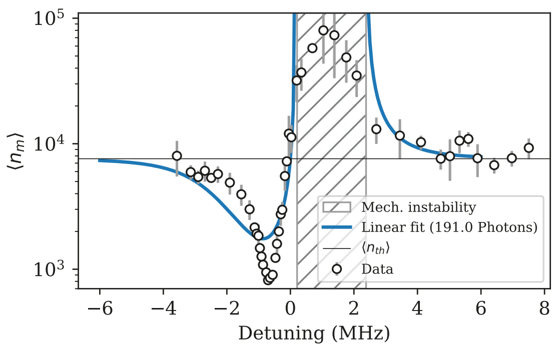

Figure 7.42: Linear fit to the high power dataset (also shown in Fig. 7.38), however with performing an independent fit with the linear theory. For this, we shift the data, such that we have no backaction exactly at zero detuning. Still, the linear theory is clearly unable to reproduce the data, where it underestimates the cooling and overestimates the heating. For the heating it even predicts that the mechanical linewidth drops below 0, leading to mechanical instability.

As described in Chapter 7.2.7, we did several steps to improve flux stability of our setup. Fig. 7.43 shows one cooling trace measured before and another one after doing most of the improvements, which is a trace from the dataset discussed here. The measurement shown in (a) is also the only one with a different coupling of 150 Hz shown in this part of the thesis. Both traces are taken at around 70% of the bistable power. While the one before the improvements clearly bottoms out in the cooling region, we do not observe this afterwards. This shows the direct impact of the work done on reducing the vibrations on the measurements results.

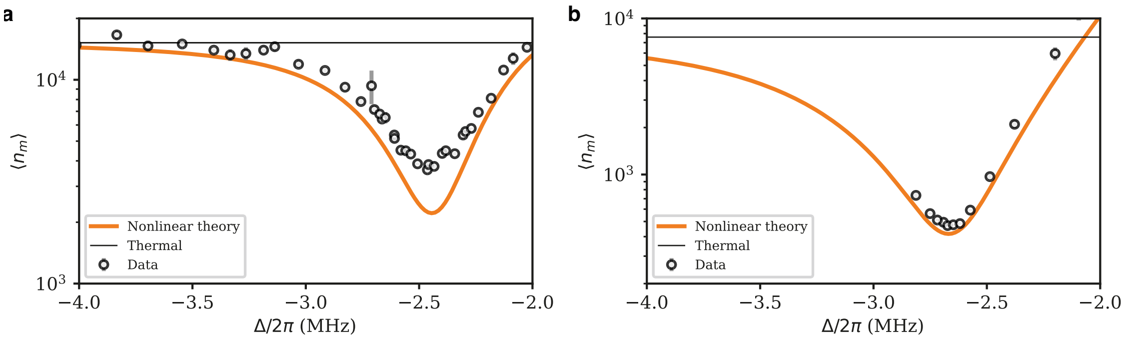

Figure 7.43: Improvements of the cooling traces due to reduction of mechanical vibrations. Here two cooling traces are compared, taken at around 70% of the bistable power. **a.** Cooling trace before doing most of the improvements discussed in Chapter 7.2.7. At most cooling there is clearly a bottoming out effect, which arises as the probe-cavity detuning is washed-out over a certain range of detunings. **b.** After reducing mechanical vibrations coupling into our system, a similar cooling trace follows the theory even at most cooling. Further, this trace is taken at a g_0 of around 200 Hz, while the trace shown in (a) is taken at a coupling 150 Hz, making it even more sensitive to flux noise. Also the thermal phonon number differs, with the measurements in (a) taken at 200 mK and in (b) at 100 mK.

Finally it should be noted, that the mechanical frequency shifts linearly with detuning of the cavity frequency, as shown in Fig. 7.44. This is only a minor correction, which was taken into account in extracting the mechanical frequency shift in all cooling traces discussed in this part. However it is especially significant for the lower power traces, where the backaction is small. There it is especially relevant as the frequency shift due to backaction is also small and the small shift due to the frequency change of the cavity is apparent.

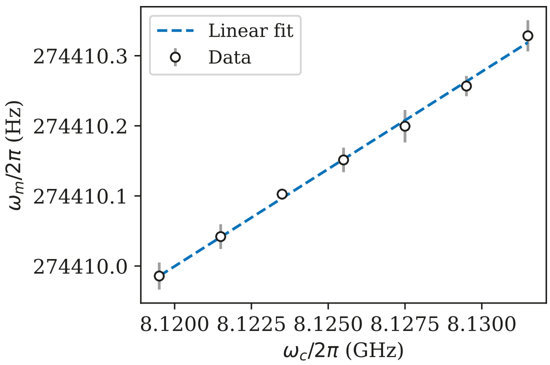

Figure 7.44: Change of the mechanical frequency with cavity frequency, fitted with a linear slope. This is measured at low power to avoid backaction and used to calibrate the mechanical frequency shift for the cooling traces.

This effect can be modelled with the instantaneous (conservative) backaction from current circulating in the SQUID loop on the cantilever. As we bias the SQUID, a circulating current forms around the SQUID, which also influences the equilibrium position of the cantilever. When the cantilever oscillates around its resting position, the bias through the SQUID changes, which - instantaneously - leads to a force on the cantilever. This effect influences the frequency of the cantilever, while it is still conservative. A colleague of mine, Christian Schneider, modelled this effect and the results are shown in Fig. 7.45. While for some parameters we can only do rough estimates, the magnitude of the frequency change agrees well with the observations in the experiment. Plotted is the mechanical frequency in dependence of the flux through the SQUID loop. The shape is similar to the frequency dependence of the cavity itself on the flux bias point (flux map, Fig. 7.15). Hence we can expect a (near) linear dependence between the mechanical frequency change and the cavity frequency. Thus we concluded, that instantaneous backaction of the current circulating in the SQUID indeed leads to the frequency shift of the mechanical mode.

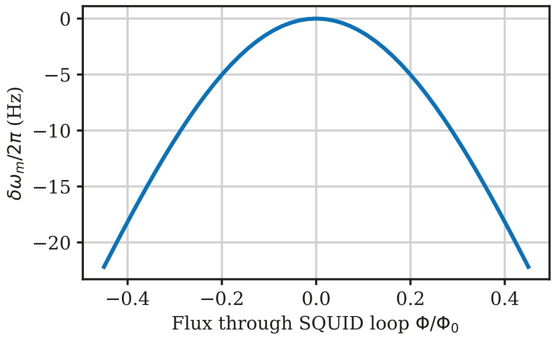

Figure 7.45: Simulated change of the mechanical frequency in dependence of the flux bias point. The parameters used for this calculation are: distance magnet-SQUID 5 μm, magnetic dipole moment on the cantilever tip 0.1×10^{-9} N m/T, SQUID radius 10 μm, critical current of the Josephson junction 1 μA, $\beta_l = 10^{-3}$. This figure is provided by a colleague of mine, Christian Schneider.

7.4.3 Nonlinear cooling at intermediate coupling

In this part we will discuss some cooling traces, taken at an intermediate coupling of around 800 Hz. As we will see, the cooling is clearly limited by flux noise. Fig. 7.46 shows three cooling traces at different power and a trace summarising the best cooling for each power. Here only the phonon number against detuning is shown and the nonlinear theory is used for fitting. For the lowest power in (a), the fit is in good agreement with the data. Already in (b) we see a slight deviation, as the cooling bottoms out for strongest backaction due to flux noise. In (c), flux noise becomes increasingly relevant, as the cooling backaction happens over a narrower range of detunings when operating deeper in the nonlinear regime. Thus, we are not able to pass a fit through the data and simply use the predictions based on the extracted parameters at lower power. In panel (d) we can see, that the nonlinear theory seems to be a much closer description to the data, but also that flux noise becomes increasingly limiting with power, as we already saw from the individual cooling traces. At this g_0 we managed to cool to around 1000 phonons, which is similar to low g_0, discussed previously (Chapter 7.4.2). In the next part we will consider the flux noise model we developed, to see if the behaviour we see can be indeed describe by flux noise.

7.4.4 Flux noise model

In Chapters 7.4.2 and 7.4.3 we have already seen that flux noise leads to a bottoming out of cooling traces. This limits the effective cooling strength we can obtain and becomes increasingly relevant when working closer to bistability. This is a consequence of the cooling backaction happening over a smaller range of detunings closer to bistability. Operating at higher coupling naturally makes the system also more sensitive to flux noise.

In this part we will discuss how we model the influence of flux noise on our setup. Modelling it very accurately is highly challenging, as the flux noise seems to be an interplay between fast

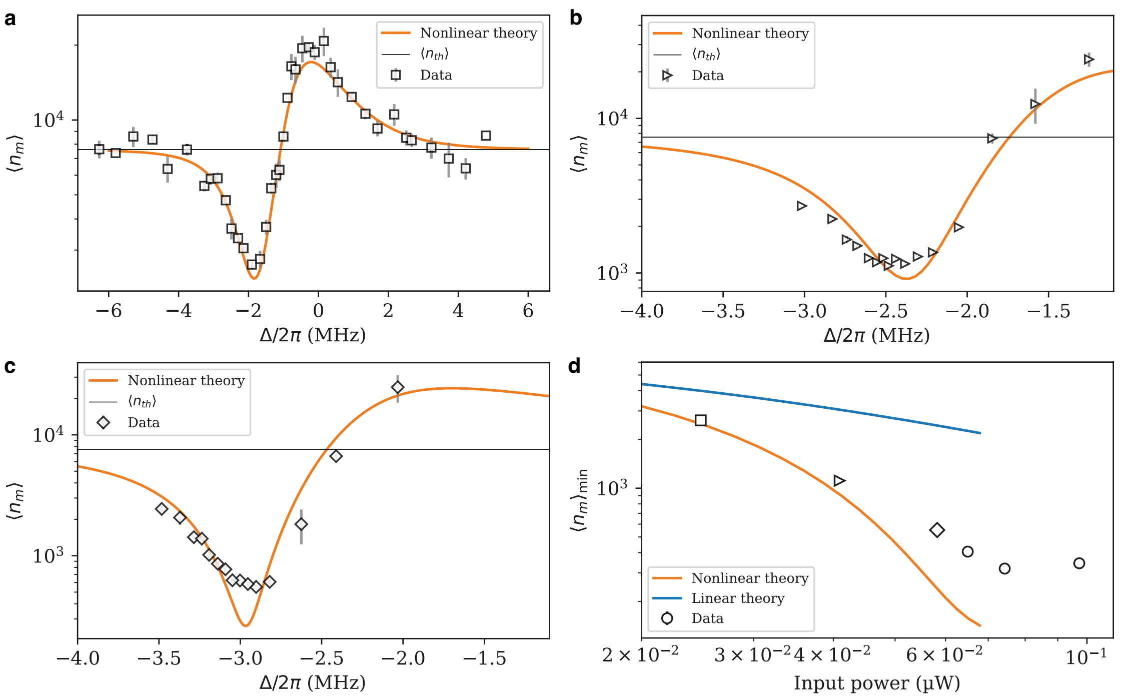

Figure 7.46: Cooling traces at intermediate $g_0/2\pi = 800\,\text{Hz}$. **a-c.** Cooling at increasing power. For low power we find good agreement between data and a nonlinear theory fit, while for higher power, the cooling is increasingly limited by flux noise and we see the bottoming out effect. In contrast to the other powers, we only use a prediction from lower power for (c) and not a fit with the nonlinear theory. **d.** Lowest phonon number measured against input power, with predictions form linear and nonlinear theory. The symbols match with the ones used for the traces in (a-c). Here we still see, that we benefit from the nonlinearity of the cavity, but the cooling is increasingly limited by flux noise, something which will be discussed in more detail in Chapter 7.4.4.

processes (compared to the measurement time and the mechanical linewidth) and processes on a timescale of the order of our measurement time. Furthermore the influence of flux noise also depends on the environment and is thus not constant over time. There are also observations, that the cavity stabilises using a strong drive [3], which makes it even more challenging to model.

For this model, we decided to use a simple model by assuming Gaussian distributed noise. We get decent qualitative agreement for measurements where we have a low to medium influence from flux noise. Generally for comparing measured cooling traces to theory, we simulate the mechanical spectrum using the nonlinear theory (Chapter 4) for given system parameters. One key parameter is of course the probe-cavity detuning. From this spectrum we then calculate phonon occupation, linewidth and frequency shift. In order to model the flux noise, we do not assume a single probe-cavity detuning anymore, but average multiple spectra with different detunings on top. For our model we assume Gaussian distributed noise, which is implemented by assigning a weight to each trace according to

$$\begin{aligned} W_i(\Delta\omega_i) &= \frac{1}{\sqrt{2\pi\sigma^2}} e^{-\frac{(\Delta\omega_i - \Delta\omega_0)^2}{2\sigma^2}} \\ w_i &= \frac{W_i}{\sum_i W_i} \end{aligned} \tag{7.6}$$

Here, w_i is the specific weight assigned to a spectrum at a given probe-cavity detuning $\Delta\omega_i$, while $\Delta\omega_0$ would be the intended probe-cavity detuning of the measurement. The width of the Gaussian, σ, gives an effective strength of flux noise. We calculate 50 spectra for equally distributed detunings up to 2σ to each side of $\Delta\omega_0$. We obtain the phonon number as the

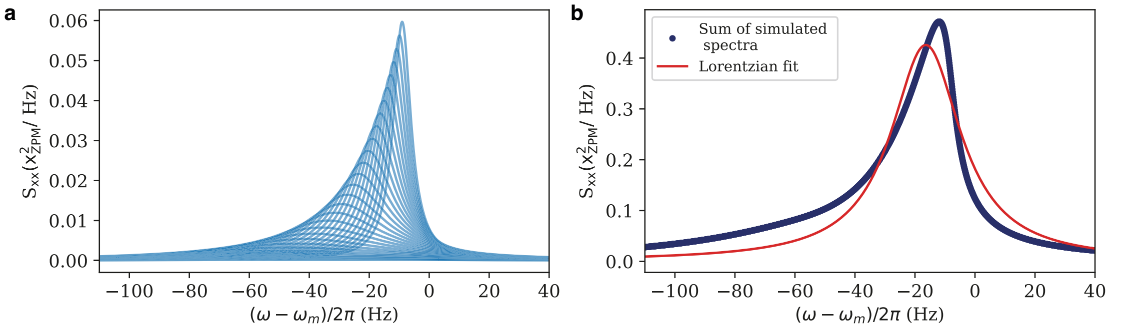

Figure 7.47: For modelling the flux noise, we assume a distribution of detunings instead of a fixed probe-cavity detuning. This leads to different mechanical spectra as the backaction changes. **a.** Weighted spectra plotted on top. **b,** Sum of weighted spectra to get a single spectrum. We fit this spectrum with a Lorentzian, which is not a representative prediction of the line shape, but is most similar to what we do in the analysis of the experiment. From this fit we obtain the mechanical linewidth and frequency. We get the phonon number from each individual spectrum as seen in (a), together with the weighting.

weighted area of each spectrum, while we fit the final, averaged spectrum using a Lorentzian for estimating the mechanical linewidth and frequency. Fig. 7.47 shows an example of how we obtain such a simulated spectrum influenced by flux noise. In (a) the weighted, normalised (Eq. 7.6) spectra on top of each other are shown. The asymmetry with a much flatter tail towards larger negative detunings can be clearly seen and comes from the fact that for large cooling backaction, there is also the highest mechanical frequency shift and highest linewidth. This can be especially seen in sub panel (b) where we show the sum of the weighted spectra shown in (a) together with a Lorentzian fit. The reason to use a Lorentzian fit, even though it is not very accurate, is that it comes closest to what we also do in the analysis of the experiment. We also see the asymmetry of the mechanical spectrum in the data, which can be seen later, when the best cooling currently achieved is discussed (Fig. 7.57). In contrast however, the numerical integration, which we also do within the analysis, is shape independent, as the total area below the curve matters and does not suffer from flux noise in determining the phonon occupation number.

Let us first consider the dataset measured at the intermediate $g_0/2\pi$ of around 800 Hz (Chapter 7.4.3) to see the capabilities, but also the limits of our flux noise model. Such an intermediate coupling is favourable for doing this, as the influence of flux noise is low enough to get a trustworthy estimate of the system parameters, while it has a clear influence at higher powers. Fig. 7.48 shows the cooling traces already shown before, but now including the predictions from the flux noise model. In (a), for intermediate power, the cooling is already slightly limited due to flux noise, while we still manage to fit the data with the usual nonlinear theory. This figure now also includes a trace including flux noise, taking the same parameters and assume a flux noise strength of $\sigma = 202.2 \cdot g_0$ used in the Gaussian distribution (Eq. 7.6). This corresponds to an absolute flux noise strength of

$$\Delta\phi = 76.8\,\mu\phi_0. \tag{7.7}$$

This was found by re-writing σ in terms of g_0 together with Eq. 7.5. The second part of Eq. 7.5 is the flux change from a single mechanical excitation, which is related to g_0 via the flux sensitivity of the cavity. We calculated the change of a zero point motion to $0.38\,\mu\phi_0$. After regrouping, we can re-express the flux noise strength σ as

$$\sigma = \Delta\phi \left(\frac{\partial\phi}{\partial x} x_{\mathrm{ZPM}}\right)^{-1} g_0 = 76.8\,\mu\phi_0 \cdot \frac{1}{0.38\,\mu\phi_0} g_0 = 202.2 \cdot g_0. \tag{7.8}$$

This flux noise strength is then used throughout all measured cooling traces where flux noise is shown. Sub panel Fig. 7.48b shows a cooling trace for higher power, and thus increased

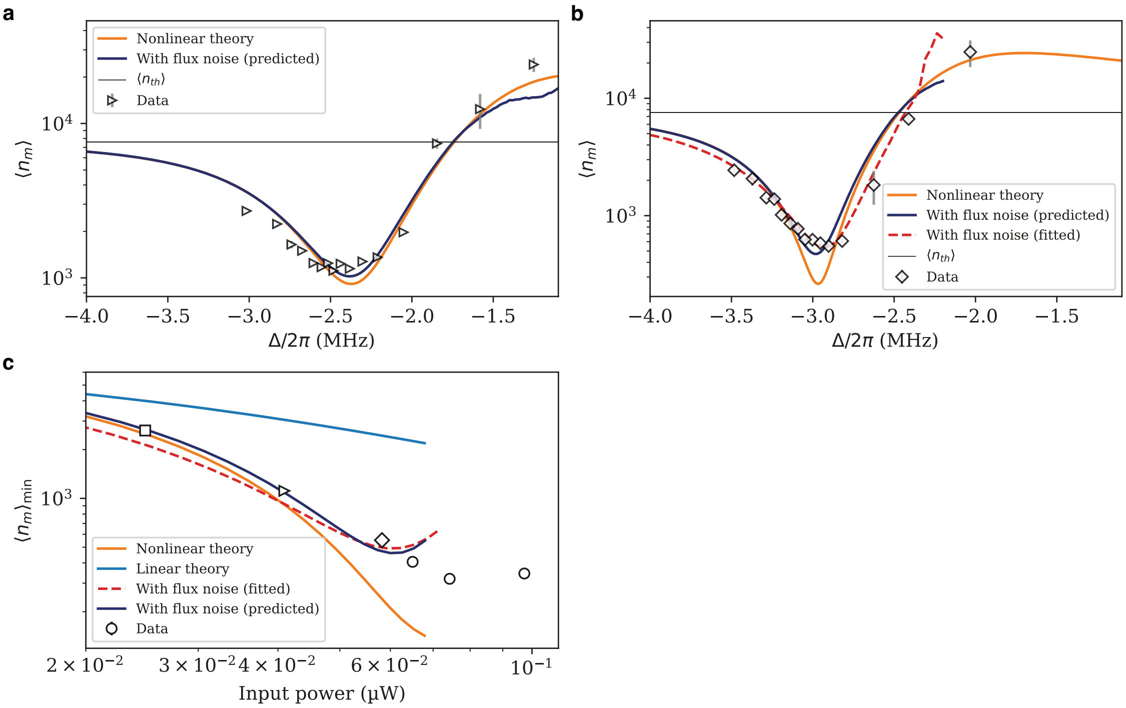

Figure 7.48: Flux noise model plotted to the data taken at intermediate g_0 (Fig. 7.46). **a.** For the measurement at intermediate power, flux noise only has a minor influence. However, the model with flux noise is in better agreement to the lowest phonon number measured than the model without. **b.** At higher power, we do a two fold approach. Next to plotting the prediction using the fixed flux noise strength, we also do a fit using the Kerr, photon number and the flux noise strength as free parameters and obtain excellent agreement to the data. **c.** Plotting the lowest phonon number against input power, the model with flux noise agrees better to the data, however also suggest a tailing up, which is stronger than observed. While the parameters fitted to the trace in (b) have good agreement to this data point, the agreement with the other points reduces.

sensitivity to flux noise. There, the nonlinear theory based on predictions from lower power, as well as the flux noise model with the flux noise strength stated above are plotted. Moreover, we also fit this dataset with the model, using the flux noise strength, the photon number and the Kerr as free fit parameters. There we get a very good agreement to the data, however extrapolating the parameters to other sets fails. Sub panel (c) shows the extraction of the lowest phonon number for different powers, together with the predictions from theory up to bistability. For the linear theory and the nonlinear theory (with and without flux noise), we use the parameters known from low power measurements (i.e. sub panel (a)). In addition, it is shown what the parameters obtained from the fit to the data in sub panel (b) would predict. Here, we already see the limits of our model. It manages good agreement with the data for low to medium influence from flux noise, but seems to fail when going to higher power, where flux noise has an increased impact. While we find parameters which agree well at a given power, agreement with traces from other powers is then not as good. As this is just a simple model, it is expected that the agreement is not perfect, especially in the regions of high sensitivity to flux noise. Among the shortcomings of this model are, that the flux noise is highly likely not Gaussian distributed and not constant over time. We further believe, that going into the nonlinear regime stabilises our cavity, effectively reducing the sensitivity to flux noise, something which was also observed in [3]. So the effective flux noise would reduce with increasing power, which seems to be also reflected in our data. While we see the tailing up in both the data and the flux noise model, in the model it seems to happen much quicker with increasing power. In case one assumes that the effective flux noise gradually lowers with power, a similar effect to the one seen in the measurements could be expected.

Expanding the model to other datasets, we can investigate the highest power dataset from low g_0 (Chapter 7.4.2), where we also saw limiting effects from flux noise. Fig. 7.49 shows the

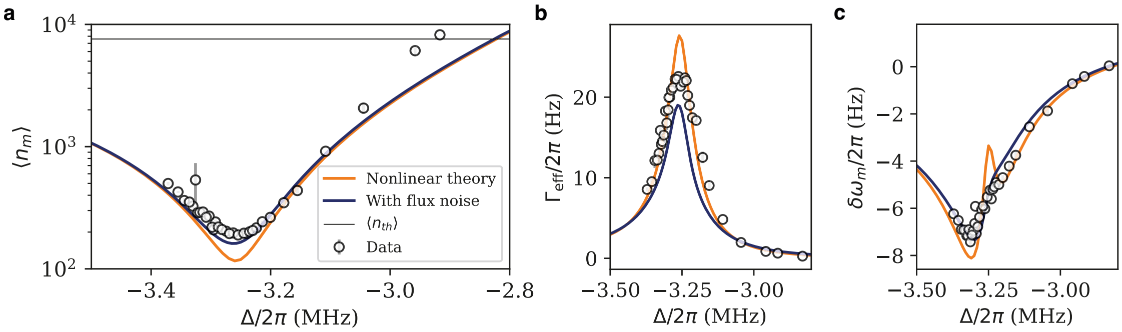

Figure 7.49: Model including flux noise plotted to the high power cooling trace measured at low g_0 (bottom left in Fig. 7.40), using the estimated flux noise strength (see main text). **a.** For the phonon number, we obtain much better agreement with flux noise than without , however the data still slightly deviates. **b.** For the linewidth, the model seems to overestimate the flux noise. **c.** For the shift of the mechanical frequency, the flux noise model is in good agreement with the data. Also the spike seen in the theory without flux noise vanishes, giving a much better agreement to the data.

predictions using the determined flux noise strength, Eq. 7.8 and the other parameters from the fit without flux noise. While it is not a perfect fit, the flux noise model is much closer to the data than without flux noise and also seems to predict the minimum phonon number well. Also for the mechanical frequency shift (c), the narrow peak vanishes, which is in agreement with the observations from the measurement.

We can then also extend this model to the lowest phonon number measured for a given pump power, plotted in Fig. 7.50 from the same dataset discussed in Chapter 7.4.2. Here the flux noise model seems to give a good estimate for the tailing up of the phonon number working close to bistability. Also it seems to give a better estimate for the linewidth, only for the frequency change it is not that accurate. This can be also due to fact, that we use the frequency shift at the data point with lowest phonon number. If the phonon number remains similar (low) for a range of detunings, while the frequency shift changes, this might lead to not extracting the frequency shift of the point with most backaction and could lead to a discrepancy.

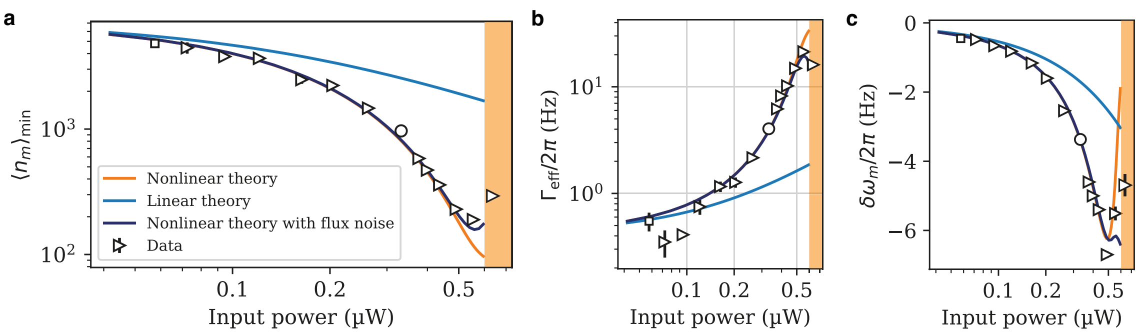

Figure 7.50: Model including flux noise plotted to the best cooling against input power for the low g_0 measurement (Fig. 7.41). Here again we plot the predictions with flux noise, using a fixed flux noise strength. **a.** The flux noise model, seems to accurately predict the tailing up just before bistability. **b.** This reduction of backaction is also seen in predicted in the linewidth. **c.** For the mechanical frequency shift, the tailing up suggested by the theory without flux noise, originating from the spike appearing when operating close to bistability (Fig. 7.49), is diluted due to flux noise. This effect seems to be overestimated in the model. The shaded region in all three panels is the region above bistability.

Even though the model is very simple it seems to capture the essential parts of the behaviour under flux noise for different datasets. From this we can conclude that we are with a high probability limited by flux noise.

A different way for learning about the strength of the flux noise, is the change of the cavity linewidth with increasing flux sensitivity. This is plotted in Fig. 7.51, where the cavity linewidth is already plotted in terms of coupling strength (which is directly proportional to the flux sensitivity). We fit the linear dependence of the cavity linewidth on g_0 and obtain a slope of 794(50), corresponding to a flux noise of 302(19) $\mu\phi_0$ (Eq. 7.8). Additionally plotted is a line with a slope of 202, corresponding to the flux noise extracted with the flux noise model, Eq. 7.8. While the flux noise estimated with the flux noise model and with the change of cavity

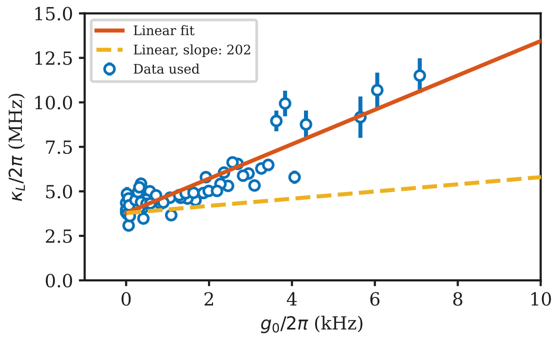

Figure 7.51: Change of cavity linewidth with flux sensitivity, parameterised using g_0 (i.e. Fig. 7.15). The flux noise is expected to increase linearly with flux sensitivity, where a linear fit gives a slope of 794(50). This translates to a flux noise amplitude of 302(19) $\mu\phi_0$. Additionally plotted is a line with a slope of 202, which is the extracted flux noise strength using the flux noise model (Eq. 7.8).

linewidth is in the same order of magnitude, the noise estimated from the cavity linewidth is nearly four times larger. The difference between the two methods arises in part from the Gaussian noise assumed in the flux noise model, where the width of the Gaussian is used as the flux noise strength. In addition, we observed that the flux noise becomes smaller as we are operating closer to bistability, something which also observed in [3]. While the flux noise model is mainly used for high power measurements, where the nonlinearity of the cavity has significant influence, we measure the broadening of the cavity linewidth at low powers. Also this could (partly) explain the difference in extracted flux noise amplitude.

7.4.5 Working at highest couplings

In this section cooling traces measured at high couplings are addressed, to demonstrate our ability of operating the system at those parameters. As flux noise has higher influence at higher couplings, we cannot necessarily fit traces at those couplings and our cooling is limited as well. Fig. 7.52 shows two cooling traces, one at a $g_0/2\pi$ of around 4 kHz, sub panel (a), and one at a $g_0/2\pi$ of around 7.5 kHz (b). For the 4 kHz trace, which is taken at around half the bistable power, we are still able to perform a fit using the nonlinear theory. However, in the region of most cooling we are clearly limited by flux noise. The flux noise model (Chapter 7.4.4), where we again estimate the strength of the flux noise using Eq. 7.7, predicts the overall behaviour and also the minimum phonon occupation very well. While we manage to cool to just below 200 phonons starting from around 7600 thermal phonons, according to the nonlinear theory, we would be able to cool to nearly 10 phonons if we had no flux noise. Assuming the same parameters for a linear cavity, we expect to cool to around 90 phonons.

Sub panel (b) shows a cooling trace taken at even higher $g_0/2\pi$ of nearly 7.5 kHz. Here, flux noise prevents us from fitting this data. Still we are able to measure a cooling trace, even though the data quality clearly suffers. As the mechanical spectra are also influenced by flux noise, we show the results from numerical integration along the results of fitting the spectra.

Here, we see good agreement. Only in the region of most cooling - where we are also most sensitive to flux noise - we see slight differences, which shows that we can trust the fit for such high coupling strengths.

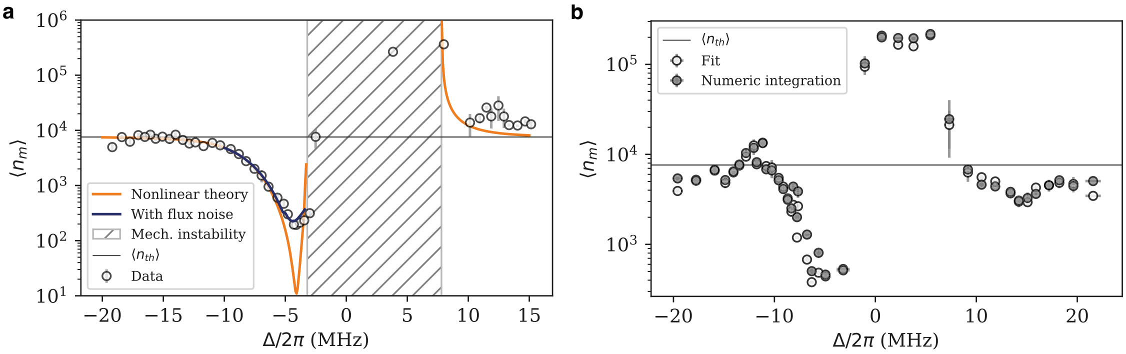

Figure 7.52: Cooling traces measured at high g_0. **a,** Trace at around $g_0/2\pi = 4\,$kHz. We are able to fit the cooling trace, however it is clearly limited by flux noise. Plotting the prediction of flux noise using the parameters from the fit, together with the flux noise strength discussed in Chapter 7.4.4 gives good agreement. We also highlight the region, where the mechanical mode is expected to be in the regime of mechanical instability. **b,** Cooling trace at around $g_0/2\pi = 7.5\,$kHz. Here, the data quality clearly suffers from flux noise and we are not able to pass the fit through the data using the nonlinear cooling theory. As some spectra are heavily influenced by flux noise, we also show the results from numerical integration, alongside the usual fits to the spectra. There is overall good agreement between both methods, however in the region of most cooling some differences occur.

With the data shown in this part, we demonstrate that we can operate our system at very large couplings of up to 7.5 kHz. While at those couplings strength there is too much flux noise to fit the cooling traces to theory, we can still do so at couplings of 4 kHz. However, already at those couplings, our cooling abilities are clearly limited by flux noise.

7.4.6 Kerr anomaly

Here we will discuss a model for the occurrence of the Kerr anomaly in our system. First, we will investigate in which frequency region this anomaly occurs. For this, we consider a flux map taken with high power, Fig. 7.53. The anomaly begins at around 8.05 GHz, where the response of the cavity gets very shallow in a narrow range of frequencies. Afterwards the cavity frequency is increased compared to the low power case (black dashed line). For a further increase of the flux bias, it returns to the expected shift to lower frequencies compared to the low power case.

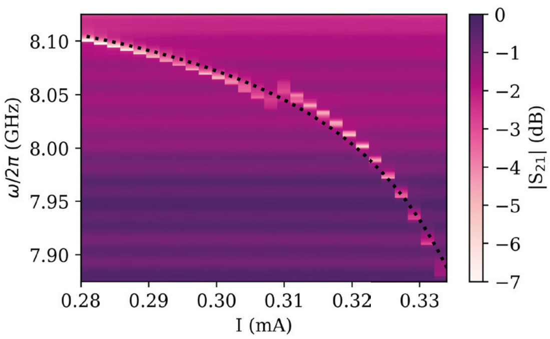

Figure 7.53: Flux map taken with a strong drive (-30 dBm fridge input power) in the region of the anomalous Kerr. The dotted black line shows the expected cavity frequency when performing a low power measurement. At a bias frequency of around 8.05 GHz we see the onset of the anomaly. There the cavity shifts to higher frequencies compared to the low power case, indicative of a positive Kerr. Afterwards we recover a negative Kerr again.

Now, we will discuss the behaviour of the cavity in this anomalous region, by investigating two power sweeps at different cavity frequencies, Fig. 7.54. As we can see, especially in the sweep taken at 8.01 GHz (sub panels (a), (c)), the frequency of the cavity first shifts up, due to a positive Kerr and shifts down for even higher powers. This can be also seen in the line cuts plotted below, where in the medium power measurement the cavity has a steep slope on the higher frequency side, indicative of a positive Kerr. For higher powers we obtain, as usual, the steep part on the low frequency side. Thus for high enough powers, the cavity behaves like a usual cavity with negative Kerr and this anomaly just pushes this regime to higher powers, effectively reducing the Kerr. This Kerr anomaly is actually beneficial for cooling the mechanical resonator. Typically, the nonlinearity of the cavity increases when going to higher coupling strengths, which allows for fewer photons at bistability. While the backaction strength increases with increasing coupling, operating at higher photon number and still having a nonlinear cavity is even more beneficial. Sub panels (b) and (d) show such a measurement at a bias point of 7.97 GHz, which we use for measuring the best cooling we currently achieve (Chapter 7.4.7). Here, the effect of the Kerr anomaly is already less dominant, but we still benefit from the overall reduced Kerr and thus higher photon numbers when reaching bistability. Remarkably, we can operate at similar powers as in the backaction measurements at low g_0, while having a more than ten times bigger coupling strength. However, it should be noted, that we are also more sensitive to flux noise, which limits the increase of backaction we can achieve.

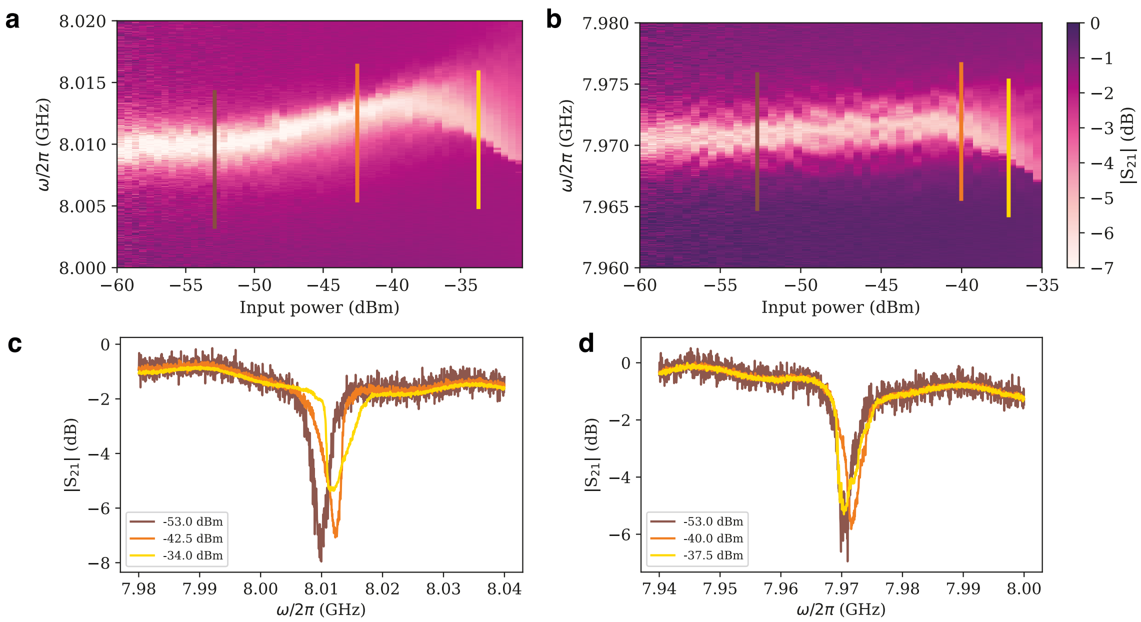

Figure 7.54: Power sweeps of the cavity for two different flux bias points in the anomalous Kerr region. **a.** Power sweep at a bias frequency of 8.01 GHz and **c.** line cuts at different powers. We see that the cavity shifts to higher frequencies for intermediate powers before shifting to lower frequencies for higher powers. At -42.5 dBm we see a steep slope on the right side of the cavity, a clear sign of a cavity with positive Kerr. Going to even higher powers, this changes to the other side, having the steep part of the cavity at the typical lower frequency side. **b,d.** Power sweep at the frequency we took the data for the highest cooling we achieve (Chapter 7.4.7). Here, the effect of the positive Kerr is reduced but it still has an influence, allowing us to work at higher powers when reaching bistability. Remarkably, as it can be seen in (d), at bistability the net frequency shift compared to low power is close to zero, as the shifts from positive and negative Kerr just cancel.

To get a qualitative understanding of the origin of this phenomenon, we model our circuit using lumped elements (Fig. 7.55a), and recover a similar behaviour as in the experiment. The simulations presented in this part were performed by Aleksei Sharafiev, a former Postdoc in our group. We use a software called PScan [104, 105] and simulate our circuit with the parameters

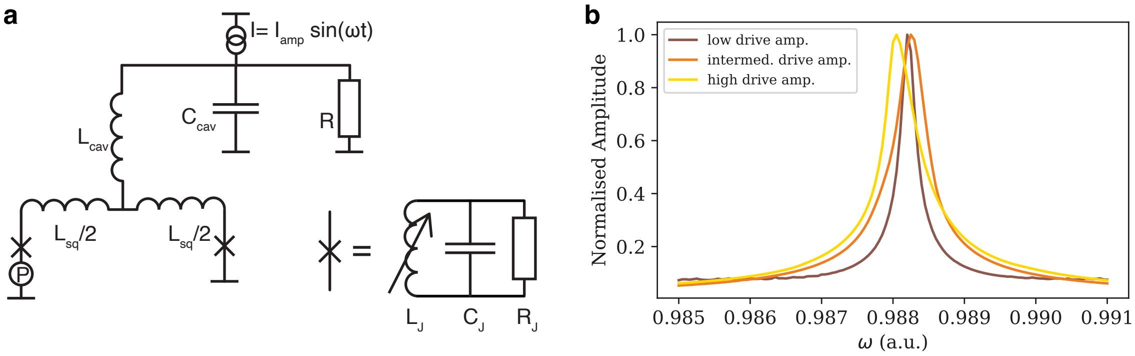

Figure 7.55: Simulation of our circuit to get better insight into the origin of the Kerr anomaly. **a.** Model used for simulating the circuit. **b.** In a certain region of frequencies, we see exactly the same qualitative behaviour as we see in the measurements (Fig. 7.54). There, the resonance frequency increases first for increasing power, before it decreases, when increasing the power further.

shown in Tab. 7.5. Those parameters are only estimates of the setup parameters and while they allow us to get a qualitative understanding of the effect, we cannot draw quantitative conclusions. We use the RCSJ model to describe the Josephson junctions together with the

Table 7.5: Parameter used to simulate our circuit. The inductance and capacitance of the cavity, L_{cav} and C_{cav}, are obtained from finite element simulations. The resistance R is chosen such that it matches the linewidth of the cavity. The geometric inductance of the SQUID, L_{sq}, is estimated from the flux map. The critical current of the junction I_c is obtained from the design parameters, where we estimate that it is lowered by a factor of 5 (When discussing the change of the Kerr (Chapter 7.2.1) we estimated a factor of 10. However this factor is just an estimation and such a Kerr anomaly would be found independent of the exact value for the critical current.) due to the presence of the magnet in its vicinity, obtained from a change in the flux map, when placing the magnet. To fully characterise the junction, we use the McCumber parameter β_c, which also depends on the junction capacitance (known from design parameters) and the gap resistance R_N. For the shown simulation, we use a phase drop P, to set the flux bias point, such that the third harmonic of the cavity is similar to the plasma frequency of the junction.

Parameter	Value
L_{cav}	4.96 nH
C_{cav}	144 fF
R	648.2 Ω
L_{sq}	0.0195 nH
I_c	1.67 μA
β_c	333420
R_N	13 100 Ω
P	0.13 ϕ_0

phase balanced method to simulate the circuit. To obtain the results, we use the voltage response of the system to an applied driving current with different frequency and amplitude. Fig. 7.55b shows the voltage response for three different current strengths when sweeping the frequency across, always normalising to the highest voltage response for a given drive strength, similar to a VNA type of measurement. In a certain range of frequencies, we find very similar behaviour as in the experiment, Fig. 7.54, with the Kerr being positive in a certain range of powers, before becoming negative again for increasing powers. This behaviour is happening in a region, where the third harmonic of the cavity frequency is very similar to the plasma frequency of the junction. A junction is a nonlinear element with the ability to transfer energy between different modes. As the current-phase relation of the junction is described by a sinusoidal, we expect that, next to the fundamental mode, the third harmonic has most influence, in this case the third harmonic of the cavity mode. Therefore, we believe that the plasma frequency of the junction is the reason for this Kerr anomaly.

This complex behaviour prevents us from comparing full cooling traces to the theory, as this would require a quantitative modelling of the power dependent Kerr. Developing such a model is highly challenging, as already for a single power, the photon number in the cavity changes with the probe-cavity detuning, which also changes the power dependent Kerr in this region. Additionally, flux noise is clearly present in this range of coupling strengths of around 2 kHz, and not only does it influence the cooling traces, but also the frequency sweeps of the cavity.

7.4.7 Best cooling currently achieved in our system and theoretical limit

To achieve the best cooling currently possible in our system, we use a bias point in the anomalous Kerr region (Chapter 7.4.6). We measured several cooling traces with power up to bistability at a coupling strength of around 2.1 kHz (and a cavity frequency of 7.97 GHz, which is the same as for the power sweep shown in Fig. 7.54b). Additionally, we lowered the temperature of our cryostat, which benefits us in two ways. First, the thermal occupation of the mechanical mode decreases (Eq. 2.15), and second the linewidth of the cantilever decreases with decreasing temperature (see e.g. Fig. 7.29), which reduces the rate at which mechanical mode thermalises to the environment. Together with the Kerr anomaly, which allows for higher drive strength, while we still benefit from the nonlinear cooling and the high coupling strength, we expect strong cooling. Naturally however, at those coupling strengths, the flux noise has a more severe impact, which will be the main limit for achieving best cooling.

Fig. 7.56 shows two cooling traces. The one shown in (a) is taken 2 dB from bistability. Already there we see very strong cooling of the mechanical mode to around 50 phonons. We further see, that far detuned the mechanical mode is in thermal equilibrium at 40 mK. Interestingly, the best cooling happens at around zero detuning compared to the low power measurement of the cavity. This can be explained with the Kerr anomaly (Chapter 7.4.6). In (b) a cooling trace very close to bistability is shown. There we only took data around the detunings with most cooling, and manage to cool the mechanical mode to nearly 10 phonons.

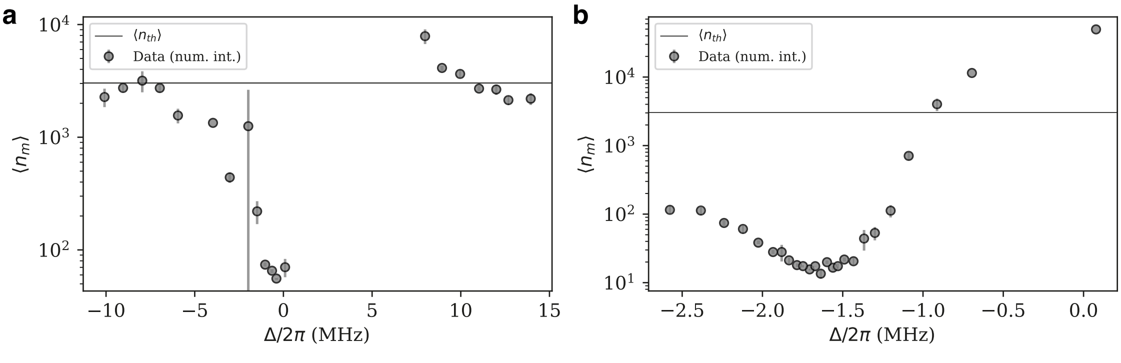

Figure 7.56: Cooling traces at the coupling we obtained the best cooling, at around 2.1 kHz. We also decreased the temperature of our cryostat to 40 mK for those measurements. **a.** Cooling trace around 2 dB from bistability. We observe very strong cooling to around 50 phonons. As fitting the mechanical peak is not reliable anymore due to a distortion from flux noise, we use numeric integration for determining the phonon number. Also the strongest cooling appears around zero detuning, due to the Kerr anomaly, Chapter 7.4.6. **b.** Increasing the power to nearly the bistable one, we cool the mechanical mode to nearly 10 phonons.

To further asses the best cooling in our system, it is illustrative to directly look at the mechanical noise spectrum. Therefore, several of those spectra are shown in Fig. 7.57 ranging from a thermal spectrum to the spectrum with the highest currently achievable cooling. Using the calibration tone (Chapter 7.2.3) we can rescale the data to $S_{xx}/x^2_{\mathrm{zpm}}$, with the following rescaling factor:

$$\frac{S_{xx}}{x_{\mathrm{ZPM}}^2} = \left(\frac{\phi_0\omega_{mod}}{2}\frac{1}{S_{II}(\omega_{mod})\mathrm{ENBW}}\frac{1}{g_0^2}\right)S_{II}(\omega). \tag{7.9}$$

The normalisation with the coupling g_0 arises due to the conversion from $S_{\omega\omega}$ to S_{xx} and $S_{II}(\omega)$ is the measured intensity spectrum. As we operate at higher powers and closer to the cavity resonance, the transduction increases. This leads to a reduction in the noise floor, which might seem counter-intuitive, however arises due to the normalisation to the spectra in terms of x_{ZPM}. It can be seen in the above equation, 7.9, that as the calibration tone increases, the noise floor will decrease. Thus the better transduction allows to resolve increasingly smaller fluctuations of the mechanical mode, resulting in a decreasing noise floor. Another reason for the increase in transduction might be, that our cavity works as a parametric amplifier (Chapter 7.1.5) [3].

Focusing back on the mechanical feature, we observe that the backaction increases due to increased power as well as a different probe-cavity detuning. As expected, the width of the mechanical peak increases and its frequency reduces. To determine the photon number in the

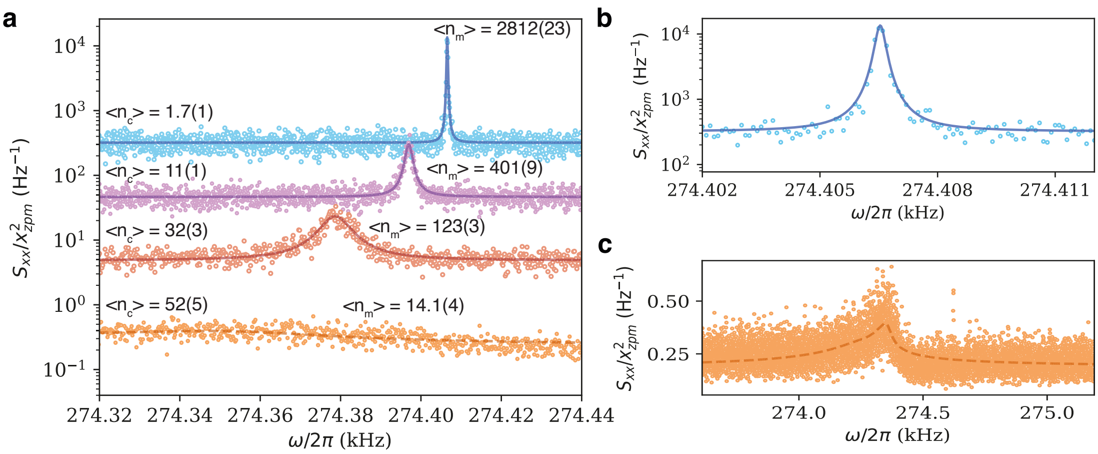

Figure 7.57: Spectra of the mechanical mode for increasing power and optimised probe-cavity detunings. **a.** As the backaction increases, the mechanical peak shifts to lower frequency and its linewidth increases. For traces with most backaction, the signal nearly vanishes in the noise floor (see sub panel (c) for details). The estimated circulating cavity photon number at this detuning as well as the phonon number are also stated. **b.** Magnification and fit of the measurement with low backaction. **c.** Measurement of highest backaction, which is already shown at the bottom of (a). The peak clearly has an asymmetric line shape due to flux noise, thus we use the flux noise model to fit this peak, which reproduces the key features well.

cavity we would usually use the (nonlinear) fit. As the measurements discussed here suffer from flux noise and on top of that we operate in the Kerr anomalous region (Chapter 7.4.6), we are not able to fit the traces. To estimate the photon number, we use a fixed value for the Kerr, which resembles the overall frequency shift well, but underestimates the effective Kerr for most cooling. We then use this this Kerr together with the input photon number known from measurements at lower g_0 and the measured cavity parameters at this coupling.

We see that the spectrum with most cooling, shown in detail in (c), is clearly influenced by flux noise, which imposes therefore also a limit for our cooling strength. Thus, we use a mechanical spectrum generated by our flux noise model (Chapter 7.4.4) for fitting this data. The phonon number we extract is in good agreement with the numerical integration of the peak, giving around 14 phonons. For fitting, we use the offset, the Kerr, the probe-cavity detuning as well as flux noise strength number as fit parameters. We fix the circulating photon number in the cavity given by the known input photon number, calibrated via a measurement at lower coupling. As we just fit a single spectrum and the fit parameters are strongly correlated, we have to be careful with interpreting the values, however they are within an expected range. The shape of the curve is fitted very well, and key features, like the tail towards lower frequencies being much shallower and towards higher frequencies much steeper are reproduced.

As discussed above, it is challenging to determine the cavity photon number, due to the Kerr anomaly. Performing the approach using a fixed Kerr, we get an estimate, given in Fig. 7.57. Here, we will investigate the influence of a different Kerr on the cavity photon number, as due to the Kerr anomalous region, the Kerr increases with drive strength. We know that we are operating close to bistability. Furthermore, we can use the input power known from lower g_0 measurements and use this to estimate the Kerr. Additionally, using the parameters from fitting the spectrum from the model including flux noise, we expect to cool the mechanical mode to below 10 phonons assuming no flux noise. Fig 7.58a shows theoretical cooling traces, using the cavity parameters at this coupling together with different values for the Kerr. Fig 7.58b shows the cavity response and indicate the detunings for best cooling. Depending on the Kerr, we get a photon number of 42 for the highest value of Kerr, where we would operate at 99 % of the bistable Kerr, and up to 49 photons for the lowest Kerr. Those numbers are close to the 52(5) estimated with the method discussed previously, but are slightly lower. This difference can be explained by the Kerr anomaly, where the Kerr is positive for low drive strengths (e.g. see Fig. 7.54b), requiring more photons to reach bistability or simply flux noise leading to an uncertainty in the detuning. Further, we see that the Kerr only has a slight influence on the photon number for optimal detuning for the cooling.

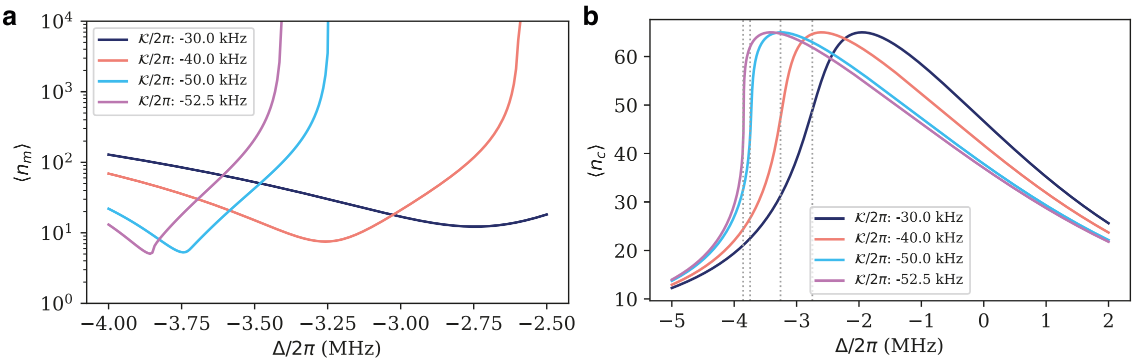

Figure 7.58: Estimation of the cavity photon number for different Kerr values at the optimal detuning for cooling. **a.** Cooling traces for a fixed resonance (input) photon number, but different Kerr values. At the highest Kerr (52.5 kHz), we are at 99% of the bistable photon number. There we would expect to cool (without flux noise) to around 5 phonons. **b.** Cavity photon number against detuning for different Kerr values. Further indicated are (dashed) the detuning for which we achieve best cooling. The photon number at the optimal detuning is similar for all Kerr values, despite the change of the cavity line shape.

Finally, we theoretically investigated the full capabilities of nonlinear cooling without the limiting factors of flux noise and hence the possibilities of increasing g_0 further. For this, we got help from our theory collaborators Nicolas Diaz-Naufal and Anja Metelmann from the Free University Berlin and the Karlsruhe Insitute for Technology, who already developed the theory for the nonlinear cooling, Chapter 4. Fig. 7.59 shows the minimum phonon number achievable working at 99% of the bistability for different g_0. Plotted are the cooling using two different (but fixed) values for the Kerr as well as the linear case, $\mathcal{K}/2\pi = 0$ and the ideal photon number for the linear case. As the Kerr is different for the nonlinear cases, the input power is also different for always working at 99% of the bistability. For the linear $\mathcal{K}/2\pi = 0$ case we use the same photon number as for the $\mathcal{K}/2\pi = -12\,\text{kHz}/\bar{n}_c$ case. Next to the nonlinear cooling being more efficient, we see that it can even beat the standard cooling limit of a linear system in the unresolved sideband regime. The region at which coupling this limit can be outperformed is tuned by the Kerr constant.

With this we have discussed the best cooling currently possible in our system. So far we

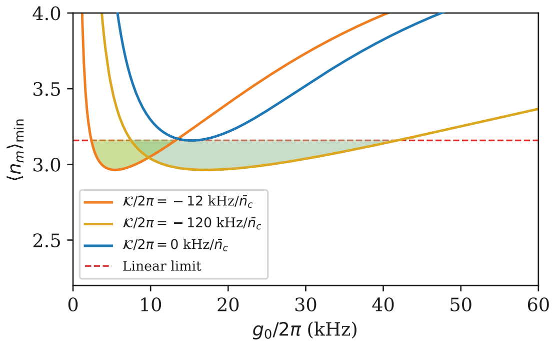

Figure 7.59: Theory prediction for the lowest phonon occupation reachable when increasing g_0 and keeping other parameters constant for two different strengths of the nonlinearity, $\mathcal{K}$. We use an input power of 99% of the bistable power and for the linear prediction, we use the same power as for the $\mathcal{K}/2\pi = -12\,\mathrm{kHz}/\bar{n}_c$ case. In dashed red we show the best cooling achievable with a linear cavity using optimal photon number.

managed to cool the mechanical mode to around 14 phonons, which is not the fundamental limit, but is limited by flux noise. Theoretically we expect that the cooling limit is below 3 phonons, even beating the standard cooling limit of a linear cavity assuming the same linewidth and mechanical frequency for both cases.

7.4.8 Discussion of the nonlinear cooling

The results presented on the nonlinear cooling show several important features, which are summarised here. Further, it will be highlighted what might be possible with such a system in the future. First, the nonlinear cavity response has to be critically taking into account when describing backaction. In Chapter 7.4.2 we have demonstrated a more than ten fold increasing in cooling compared to an otherwise identical linear system at low coupling strengths of around 200 Hz. This shows the efficiency of the nonlinear cooling. As we just discussed in Chapter 7.4.7, theory shows that it even allows to beat the standard linear cooling limit in the unresolved sideband regime. The region where this happens can be tuned by the Kerr constant. In contrast to cooling, amplification/heating of the mechanical mode is reduced due to the nonlinear cavity response. This would be inverted, using a cavity with a positive Kerr.

In the future, we plan to investigate ground state cooling by using squeezed light. It was already shown that externally produced squeezed light can beat the standard cooling limit [98]. Due to the nonlinearity of the cavity, squeezed light can be generated even inside the cavity. This avoids any further losses, which typically occur as the signal has to go through an isolator between the source of squeezed light (typically a parametric amplifier) and the optomechanical system. Thus it will be interesting to see, if the same cooling advantages are possible using internally produced squeezed light.

Efficient cooling in the bad cavity regime is interesting for many experiments operating with low frequency mechanical system. This are typically all systems working with levitation [20], but also generally massive mechanical systems, which are highly interesting for acceleration sensing [18, 17] or answering fundamental questions of quantum physics [9, 11, 12]. With increasing mass, the mechanical frequency typically decreases, which makes cooling more challenging. Nevertheless, cooling is a necessary first step for exploring the quantum regime with low frequency mechanical objects. There, nonlinear cooling might be beneficial, as it allows for new and more efficient ways of cooling. Furthermore, nonlinear cooling increases the variety of optomechanical system, which can be cooled efficiently.

8 | Summary and outlook

My thesis describes the set-up, characterisation and major measurements I did on our optomechanical setup, where a nonlinear microwave cavity is inductively coupled to a mechanical cantilever. The key results are the benefits of using a nonlinear cavity for backaction cooling the mechanical mode. For understanding the necessary underlying theory, we started with explaining linear optomechanics. There, we specifically focused on sideband cooling, as an established way for cooling a mechanical mode using a red detuned probe tone. Next, we addressed nonlinear cavities, where different ways for treating the nonlinearity and to measure gain were shown. Bringing those systems together, we arrived at nonlinear optomechanics, where the theory for our experiment was adapted from earlier works [4, 5] by our theory collaborators. There, we first saw that the nonlinear cavity offers advantages over linear systems, allowing more efficient sideband cooling. This is especially relevant in the unresolved sideband regime, where the frequency of the mechanical mode is below the decay rate of the cavity. While also the nonlinear cooling does not allow to reach the ground state in the unresolved regime, it remarkably allows to slightly outperform the standard cooling limit of a linear system. Further, we discussed microwave cavities. Embedding a SQUID makes them sensitive to magnetic fields, necessary for coupling the mechanical mode, and also nonlinear. In addition, we investigated how losses can be described and the typical loss mechanisms in superconducting cavities.

With the theory introduced, we focused on the experiment. First, we discussed the experimental platform, where we use microstrip microwave cavities, housed in a rectangular waveguide. For characterisation, we used different types of cavities, while we used SQUID based cavities for detecting the signal from the mechanical modes. The mechanical resonator is a cantilever, equipped with a magnet on its tip placed in the vicinity of the SQUID for completing the setup.

In Chapter 7 we discussed all major results and start with the characterisation of different types of cavities before mounting the cantilever. Our first batch of cavities were simple microstrip cavities, produced on a single layer, which showed internal quality factors of up to one million. However, the detection of the cantilever requires a SQUID and thus a multilayer fabrication process. As such processes are less established using niobium compared to the typically used aluminium for superconducting circuits, we already expected significantly lower quality factors, where we found numbers of around 7000. The use of niobium was required due to the strong fields from the magnetic cantilevers. We also investigated the SQUID-based cavities regarding their amplifying capabilities, where we found gain values of 20 dB over a bandwidth of a few 100 kHz.

Afterwards we started the characterisation of the full optomechanical setup. Measuring multiple mechanical cantilevers, we found frequencies of typically around 300 kHz, while a for a high frequency cantilever we even measured above 1.5 MHz. Despite measuring multiple different cantilevers, we almost exclusively focused on one sample, for the in-depth characterisation as well as the backaction measurements. Even for the highest frequency mechanical mode, our setup is in the unresolved sideband regime with a cavity linewidth of around 3.5 MHz. Upon adding the mechanical cantilever, we also saw significant changes of the cavities dynamics, resulting in a higher flux tunability and increased nonlinearity, likely arising due to a lower critical current of the junctions, coming from the presence of the magnet. Our setup also allows to change the coupling strength, but increasing flux sensitivity, also increases the susceptibility to flux noise. We discovered that flux noise is mainly mechanical noise converted to flux noise via the cantilever. Doing several steps to improve the mechanical environment, significantly improved flux stability and only this made several measurements even possible. With those improvements, we could measure the mechanical mode at values of up to $g_0/2\pi \simeq 8\,\mathrm{kHz}$. While flux noise still limits us to those values, the slope of the flux map even predicts couplings of beyond 90 kHz.

In the final part, we focused on (cooling) backaction measurements. For the typical temperatures we operate at, 100 mK, we expect a mechanical occupation of nearly 8000 phonons. First, we did measurements where the cavity is in the linear regime, either operating at low couplings and intermediate powers or high couplings and very low powers (below single photon). This shows the proof of principle for backaction cooling with our setup and even allows to cool with only a single photon in the microwave cavity, owing to the high coupling. There we could suppress the thermal population by around a factor of three. Afterwards, we focused on backaction measurements operating the cavity in the nonlinear regime. Operating close to bistability at a coupling of around 200 Hz, we saw cooling enhancement of an order of magnitude, compared to an otherwise identical linear system, which is the key result of this thesis. This shows that nonlinear cooling is a very efficient way for cooling a mechanical mode. Investigating the cooling limits of our device, we went to a coupling of around 2 kHz. Despite, the cooling performance being limited by flux noise, we managed to cool the mechanical mode to around 14 phonons. While this is not quite the ground state, it is strong cooling of the mechanical mode.

Our result is very interesting for systems in the unresolved sideband regime, as the nonlinearity allows more efficient cooling than a conventional linear system. Still, the scheme is very simple, by only requiring a single coherent pump tone. This is highly applicable for systems operating with macroscopic mechanical resonators, as they are typically low frequency, which inevitable brings the optomechanical system in the unresolved sideband regime.

Nevertheless, the goal is not only to cool efficiently, but to also reach the quantum ground state. Here, several strategies are possible. One could think of using a hybrid approach where sideband cooling brings the mechanical system to a low occupation state and feedback cooling then brings it to the ground state. However for such an approach, it has to be investigated if the direct measurement of the mechanical mode has a high enough efficiency, to benefit from the feedback. Another interesting possibility is squeezing, where it was already shown that the ground state can be reached despite being in the unresolved regime using externally generated squeezing [98]. While it is not entirely clear if squeezing using the internal nonlinearity of our cavity is already sufficient, squeezing might be one possibility for reaching the ground state. Another option - of course - is to improve the internal quality factor of the microwave cavity, to allow operation in the resolved sideband regime.

Bibliography

[1] G. Via, G. Kirchmair, and O. Romero-Isart. Strong Single-Photon Coupling in Superconducting Quantum Magnetomechanics. *Physical Review Letters*, 114(14), April 2015.

[2] T. Luschmann, P. Schmidt, F. Deppe, A. Marx, A. Sanchez, R. Gross, and H. Huebl. Mechanical frequency control in inductively coupled electromechanical systems. *Scientific Reports*, 12(1):1608, January 2022.

[3] D. Bothner, I. C. Rodrigues, and G. A. Steele. Four-wave-cooling to the single phonon level in Kerr optomechanics. *Communications Physics*, 5(1):33, December 2022.

[4] P. D. Nation, M. P. Blencowe, and E. Buks. Quantum analysis of a nonlinear microwave cavity-embedded dc SQUID displacement detector. *Physical Review B*, 78(10):104516, September 2008.

[5] C. Laflamme and A. A. Clerk. Quantum-limited amplification with a nonlinear cavity detector. *Physical Review A*, 83(3):033803, March 2011.

[6] C. Cohen-Tannoudji, B. Diu, and F. Laloë. *Quantenmechanik*, volume 1. de Gruyter, Berlin, 3., durchges. und verb. aufl edition, 2007.

[7] D. J. Griffiths. *Introduction to Quantum Mechanics*. Prentice Hall, Inc., Upper Saddle River, New Jersey 07458, 1995.

[8] W. P. Bowen and G. J. Milburn. Quantum Optomechanics. page 375.

[9] O. Romero-Isart. Quantum superposition of massive objects and collapse models. *Physical Review A*, 84(5):052121, November 2011.

[10] M. Arndt and K. Hornberger. Testing the limits of quantum mechanical superpositions. *Nature Physics*, 10(4):271–277, April 2014.

[11] I. Pikovski, M. R. Vanner, M. Aspelmeyer, M. S. Kim, and C. Brukner. Probing Planck-scale physics with quantum optics. *Nature Physics*, 8(5):393–397, May 2012.

[12] M. F. Gely and G. A. Steele. Superconducting electro-mechanics to test Diósi–Penrose effects of general relativity in massive superpositions. *AVS Quantum Science*, 3(3):035601, September 2021.

[13] N. Lauk, N. Sinclair, S. Barzanjeh, J. P. Covey, M. Saffman, M. Spiropulu, and C. Simon. Perspectives on quantum transduction. *Quantum Science and Technology*, 5(2):020501, March 2020.

[14] G. Arnold, M. Wulf, S. Barzanjeh, E. S. Redchenko, A. Rueda, W. J. Hease, F. Hassani, and J. M. Fink. Converting microwave and telecom photons with a silicon photonic nanomechanical interface. *Nature Communications*, 11(1):4460, December 2020.

[15] A. P. Higginbotham, P. S. Burns, M. D. Urmey, R. W. Peterson, N. S. Kampel, B. M. Brubaker, G. Smith, K. W. Lehnert, and C. A. Regal. Harnessing electro-optic correlations in an efficient mechanical converter. *Nature Physics*, 14(10):1038–1042, October 2018.

[16] A. Vainsencher, K. J. Satzinger, G. A. Peairs, and A. N. Cleland. Bi-directional conversion between microwave and optical frequencies in a piezoelectric optomechanical device. *Applied Physics Letters*, 109(3):033107, July 2016.

[17] C. Whittle, E. D. Hall, S. Dwyer, N. Mavalvala, V. Sudhir, R. Abbott, A. Ananyeva, C. Austin, L. Barsotti, J. Betzwieser, and et al. Approaching the motional ground state of a 10-kg object. *Science*, 372(6548):1333–1336, June 2021.

[18] A. G. Krause, M. Winger, T. D. Blasius, Q. Lin, and O. Painter. A high-resolution microchip optomechanical accelerometer. *Nature Photonics*, 6(11):768–772, November 2012.

[19] C. L. Degen, F. Reinhard, and P. Cappellaro. Quantum sensing. *Reviews of Modern Physics*, 89(3):035002, July 2017.

[20] C. Gonzalez-Ballestero, M. Aspelmeyer, L. Novotny, R. Quidant, and O. Romero-Isart. Levitodynamics: Levitation and control of microscopic objects in vacuum. *Science*, 374(6564):eabg3027, October 2021.

[21] M. Aspelmeyer, T. J. Kippenberg, and F. Marquardt. Cavity optomechanics. *Reviews of Modern Physics*, 86(4):1391–1452, December 2014.

[22] M. Rossi, D. Mason, J. Chen, Y. Tsaturyan, and A. Schliesser. Measurement-based quantum control of mechanical motion. *Nature*, 563(7729):53–58, November 2018.

[23] J. D. Teufel, T. Donner, D. Li, J. W. Harlow, M. S. Allman, K. Cicak, A. J. Sirois, J. D. Whittaker, K. W. Lehnert, and R. W. Simmonds. Sideband cooling of micromechanical motion to the quantum ground state. *Nature*, 475(7356):359–363, July 2011.

[24] J. Chan, T. P. M. Alegre, A. H. Safavi-Naeini, Jeff T. Hill, A. Krause, S. Gröblacher, M. Aspelmeyer, and O. Painter. Laser cooling of a nanomechanical oscillator into its quantum ground state. *Nature*, 478(7367):89–92, October 2011.

[25] M. Aspelmeyer, Tobias J. Kippenberg, and F. Marquardt, editors. *Cavity Optomechanics: Nano- and Micromechanical Resonators Interacting with Light*. Springer Berlin Heidelberg, Berlin, Heidelberg, 2014.

[26] D. M. Stamper-Kurn. Cavity Optomechanics with Cold Atoms. In M. Aspelmeyer, T. J. Kippenberg, and F. Marquardt, editors, *Cavity Optomechanics: Nano- and Micromechanical Resonators Interacting with Light*, Quantum Science and Technology, pages 283–325. Springer, Berlin, Heidelberg, 2014.

[27] P. B. Deotare and M. Loncar. Photonic Crystal Nanobeam Cavities. In B. Bhushan, editor, *Encyclopedia of Nanotechnology*, pages 2060–2069. Springer Netherlands, Dordrecht, 2012.

[28] A. M. Jayich, J. C. Sankey, B. M. Zwickl, C. Yang, J. D. Thompson, S M Girvin, A A Clerk, F Marquardt, and J G E Harris. Dispersive optomechanics: A membrane inside a cavity. *New Journal of Physics*, 10(9):095008, September 2008.

[29] B. P. Abbott, R. Abbott, R. Adhikari, P. Ajith, B. Allen, G. Allen, R. S. Amin, S. B. Anderson, W. G. Anderson, and et al. LIGO: The Laser Interferometer Gravitational-Wave Observatory. *Reports on Progress in Physics*, 72(7):076901, July 2009.

[30] J. D. Teufel, C. A. Regal, and K. W. Lehnert. Prospects for cooling nanomechanical motion by coupling to a superconducting microwave resonator. *New Journal of Physics*, 10(9):095002, September 2008.

[31] A. D. O'Connell, M. Hofheinz, M. Ansmann, R. C. Bialczak, M. Lenander, E. Lucero, M. Neeley, D. Sank, H. Wang, M. Weides, J. Wenner, J. M. Martinis, and A. N. Cleland. Quantum ground state and single-phonon control of a mechanical resonator. *Nature*, 464(7289):697–703, April 2010.

[32] E. E. Wollman, C. U. Lei, A. J. Weinstein, J. Suh, A. Kronwald, F. Marquardt, A. A. Clerk, and K. C. Schwab. Quantum squeezing of motion in a mechanical resonator. *Science*, 349(6251):952–955, 2015.

[33] F. Lecocq, J. B. Clark, R. W. Simmonds, J. Aumentado, and J. D. Teufel. Quantum Nondemolition Measurement of a Nonclassical State of a Massive Object. *Physical Review X*, 5(4), December 2015.

[34] J.-M. Pirkkalainen, E. Damskägg, M. Brandt, F. Massel, and M. A. Sillanpää. Squeezing of Quantum Noise of Motion in a Micromechanical Resonator. *Physical Review Letters*, 115(24):243601, December 2015.

[35] S. Kotler, G. A. Peterson, E. Shojaee, F. Lecocq, K. Cicak, A. Kwiatkowski, S. Geller, S. Glancy, E. Knill, R. W. Simmonds, J. Aumentado, and John D. Teufel. Direct observation of deterministic macroscopic entanglement. *Science*, 372(6542):622–625, May 2021.

[36] T. A. Palomaki, J. D. Teufel, R. W. Simmonds, and K. W. Lehnert. Entangling Mechanical Motion with Microwave Fields. *Science*, 342(6159):710–713, November 2013.

[37] J. J. Viennot, X. Ma, and K. W. Lehnert. Phonon-Number-Sensitive Electromechanics. *Physical Review Letters*, 121(18):183601, October 2018.

[38] J.-M. Pirkkalainen, S. U. Cho, F. Massel, J. Tuorila, T. T. Heikkilä, P. J. Hakonen, and M. A. Sillanpää. Cavity optomechanics mediated by a quantum two-level system. *Nature Communications*, 6(1):1–6, April 2015.

[39] R. Manenti, A. F. Kockum, . Patterson, T. Behrle, J. Rahamim, G. Tancredi, F. Nori, and P. J. Leek. Circuit quantum acoustodynamics with surface acoustic waves. *Nature Communications*, 8(1):975, October 2017.

[40] C. F. Ockeloen-Korppi, E. Damskägg, J.-M. Pirkkalainen, M. Asjad, A. A. Clerk, F. Massel, M. J. Woolley, and M. A. Sillanpää. Stabilized entanglement of massive mechanical oscillators. *Nature*, 556(7702):478–482, April 2018.

[41] Y. Chu, P. Kharel, T. Yoon, L. Frunzio, P. T. Rakich, and R. J. Schoelkopf. Creation and control of multi-phonon Fock states in a bulk acoustic-wave resonator. *Nature*, 563(7733):666–670, November 2018.

[42] U. von Lüpke, Y. Yang, M. Bild, L. Michaud, M. Fadel, and Y. Chu. Parity measurement in the strong dispersive regime of circuit quantum acoustodynamics. *Nature Physics*, 18(7):794–799, July 2022.

[43] T. Bera, S. Majumder, S. K. Sahu, and V. Singh. Large flux-mediated coupling in hybrid electromechanical system with a transmon qubit. *Communications Physics*, 4(1):12, December 2021.

[44] D. Zoepfl, P. R. Muppalla, C. M. F. Schneider, S. Kasemann, S. Partel, and G. Kirchmair. Characterization of low loss microstrip resonators as a building block for circuit QED in a 3D waveguide. *AIP Advances*, 7(8):085118, August 2017.

[45] D. Zoepfl, M. L. Juan, C. M. F. Schneider, and G. Kirchmair. Single-Photon Cooling in Microwave Magnetomechanics. *Physical Review Letters*, 125(2):023601, July 2020.

[46] D. Zoepfl, M. L. Juan, N. Diaz-Naufal, C. M. F. Schneider, L. F. Deeg, A. Sharafiev, A. Metelmann, and G. Kirchmair. Kerr enhanced backaction cooling in magnetomechanics. *arXiv:2202.13228 [quant-ph]*, February 2022.

[47] N. Diaz-Naufal, D. Zoepfl, M. L. Juan, C. M. F. Schneider, L. F. Deeg, G. Kirchmair, and A. Metelmann. *In preparation*.

[48] K. E. Khosla, M. R. Vanner, W. P. Bowen, and G. J. Milburn. Quantum state preparation of a mechanical resonator using an optomechanical geometric phase. *New Journal of Physics*, 15(4):043025, April 2013.

[49] W. Marshall, C. Simon, R. Penrose, and D. Bouwmeester. Towards Quantum Superpositions of a Mirror. *Physical Review Letters*, 91(13):130401, September 2003.

[50] S. Mancini, D. Vitali, and P. Tombesi. Optomechanical Cooling of a Macroscopic Oscillator by Homodyne Feedback. *Physical Review Letters*, 80(4):688–691, January 1998.

[51] P. F. Cohadon, A. Heidmann, and M. Pinard. Cooling of a Mirror by Radiation Pressure. *Physical Review Letters*, 83(16):3174–3177, October 1999.

[52] F. Tebbenjohanns, M. Frimmer, V. Jain, D. Windey, and L. Novotny. Motional Sideband Asymmetry of a Nanoparticle Optically Levitated in Free Space. *Physical Review Letters*, 124(1):013603, January 2020.

[53] I. Wilson-Rae, N. Nooshi, W. Zwerger, and T. J. Kippenberg. Theory of Ground State Cooling of a Mechanical Oscillator Using Dynamical Backaction. *Physical Review Letters*, 99(9), August 2007.

[54] F. Marquardt, J. P. Chen, A. A. Clerk, and S. M. Girvin. Quantum Theory of Cavity-Assisted Sideband Cooling of Mechanical Motion. *Physical Review Letters*, 99(9), August 2007.

[55] C.C. Hohberger and K. Karrai. Self-oscillation of micromechanical resonators. In *4th IEEE Conference on Nanotechnology, 2004.*, pages 419–421, Munich, Germany, 2004. IEEE.

[56] F. Marquardt, J. G. E. Harris, and S. M. Girvin. Dynamical Multistability Induced by Radiation Pressure in High-Finesse Micromechanical Optical Cavities. *Physical Review Letters*, 96(10):103901, March 2006.

[57] F. Marquardt, A. A. Clerk, and S. M. Girvin. Quantum theory of optomechanical cooling. *Journal of Modern Optics*, 55(19-20):3329–3338, November 2008.

[58] A. H. Safavi-Naeini, J. Chan, J. T. Hill, S. Gröblacher, J. Miao, Y. Chen, A. Aspelmeyer, and O. Painter. Laser noise in cavity-optomechanical cooling and thermometry. *New Journal of Physics*, 15(3):035007, March 2013.

[59] I. Wilson-Rae, N. Nooshi, J. Dobrindt, T. J. Kippenberg, and W. Zwerger. Cavity-assisted backaction cooling of mechanical resonators. *New Journal of Physics*, 10(9):095007, September 2008.

[60] S. Weis, R. Rivière, S. Deléglise, E. Gavartin, O. Arcizet, A. Schliesser, and T. J. Kippenberg. Optomechanically Induced Transparency. *Science*, 330(6010):1520–1523, December 2010.

[61] M. A. Castellanos-Beltran. *Development of a Josephson Parametric Amplifier for the Preparation and Detection of Nonclassical States of Microwave Fields*. PhD thesis, Citeseer, 2010.

[62] B. Yurke and E. Buks. Performance of cavity-parametric amplifiers, employing Kerr nonlinearites, in the presence of two-photon loss. *Journal of Lightwave Technology*, 24(12):5054–5066, December 2006.

[63] C. W. Gardiner and M. J. Collett. Input and output in damped quantum systems: Quantum stochastic differential equations and the master equation. *Physical Review A*, 31(6):3761–3774, June 1985.

[64] B. Yurke, L. R. Corruccini, P. G. Kaminsky, L. W. Rupp, A. D. Smith, A. H. Silver, R. W. Simon, and E. A. Whittaker. Observation of parametric amplification and deamplification in a Josephson parametric amplifier. *Physical Review A*, 39(5):2519–2533, March 1989.

[65] A. Kamal, A. Marblestone, and M. Devoret. Signal-to-pump back action and self-oscillation in double-pump Josephson parametric amplifier. *Physical Review B*, 79(18):184301, May 2009.

[66] T. Yamamoto, K. Inomata, M. Watanabe, K. Matsuba, T. Miyazaki, W. D. Oliver, Y. Nakamura, and J. S. Tsai. Flux-driven Josephson parametric amplifier. *Applied Physics Letters*, 93(4):042510, July 2008.

[67] L. Zhong, E. P. Menzel, R. Di Candia, P. Eder, M. Ihmig, A. Baust, M. Haeberlein, E. Hoffmann, K. Inomata, T. Yamamoto, Y. Nakamura, E. Solano, F. Deppe, A. Marx, and R. Gross. Squeezing with a flux-driven Josephson parametric amplifier. *New Journal of Physics*, 15(12):125013, December 2013.

[68] R. Gross and A. Marx. *Festkörperphysik*. De Gruyter Oldenbourg, Berlin, Boston, 2., akt. aufl. edition, 2014.

[69] K. Saito. Temperature Dependence of the Surface Resistance of Niobium at 1300 MHz - Comparison to BCS Theory. 1999.

[70] John M. Martinis and Kevin Osborne. Superconducting Qubits and the Physics of Josephson Junctions. 2004.

[71] J. Clarke and A. I. Braginski. *The SQUID Handbook*. Wiley-VCH, 2004.

[72] M. Tinkham. *Introduction to Superconductivity*. Dover Publications Inc., New York, second edition, 2004.

[73] C. M. F. Schneider. *Magnetic Coupling between Superconducting Circuits and a Cantilever*. PhD thesis, Unversität Innsbruck, 2021.

[74] U. Vool and M. Devoret. Introduction to quantum electromagnetic circuits. *International Journal of Circuit Theory and Applications*, 45(7):897–934, July 2017.

[75] P. Krantz, M. Kjaergaard, F. Yan, T. P. Orlando, S. Gustavsson, and W. D. Oliver. A quantum engineer's guide to superconducting qubits. *Applied Physics Reviews*, 6(2):021318, June 2019.

[76] M. Möttönen. *Quantum Electric Circuits: Basis for Engineered Quantum Technological Devices*. Lecture notes, Quantum Connections in Sweden 6, 2019.

[77] D. M. Pozar. *Microwave Engineering*. Wiley, Hoboken, NJ, 4th ed edition, 2012.

[78] M. J. Reagor. *Superconducting Cavities for Circuit Quantum Electrodynamics*. PhD thesis, Yale University, Yale, December 2015.

[79] D. Zöpfl. Characterisation of stripline resonators in a waveguide. Master's thesis, Innsbruck, April 2017.

[80] C. Müller, J. H. Cole, and J. Lisenfeld. Towards understanding two-level-systems in amorphous solids: Insights from quantum circuits. *Reports on Progress in Physics*, 82(12):124501, December 2019.

[81] J. Wenner, R. Barends, R. C. Bialczak, Yu Chen, J. Kelly, E. Lucero, M. Mariantoni, A. Megrant, P. J. J. O'Malley, D. Sank, A. Vainsencher, H. Wang, T. C. White, Y. Yin, J. Zhao, A. N. Cleland, and J. M. Martinis. Surface loss simulations of superconducting coplanar waveguide resonators. *Applied Physics Letters*, 99(11):113513, September 2011.

[82] H. Wang, M. Hofheinz, J. Wenner, M. Ansmann, R. C. Bialczak, M. Lenander, Erik Lucero, M. Neeley, A. D. O'Connell, D. Sank, M. Weides, A. N. Cleland, and J. M. Martinis. Improving the coherence time of superconducting coplanar resonators. *Applied Physics Letters*, 95(23):233508, December 2009.

[83] P. Heidler, C. M. F. Schneider, K. Kustura, C. Gonzalez-Ballestero, O. Romero-Isart, and G. Kirchmair. Non-Markovian Effects of Two-Level Systems in a Niobium Coaxial Resonator with a Single-Photon Lifetime of 10 milliseconds. *Physical Review Applied*, 16(3):034024, September 2021.

[84] D. P. Pappas, M. R. Vissers, D. S. Wisbey, J. S. Kline, and J. Gao. Two Level System Loss in Superconducting Microwave Resonators. *IEEE Transactions on Applied Superconductivity*, 21(3):871–874, June 2011.

[85] J. Goetz, F. Deppe, M. Haeberlein, F. Wulschner, C. W. Zollitsch, S. Meier, M. Fischer, P. Eder, E. Xie, K. G. Fedorov, E. P. Menzel, A. Marx, and R. Gross. Loss mechanisms in superconducting thin film microwave resonators. *Journal of Applied Physics*, 119(1):015304, January 2016.

[86] J. Gao, J. Zmuidzinas, A. Vayonakis, P. Day, B. Mazin, and H. Leduc. Equivalence of the Effects on the Complex Conductivity of Superconductor due to Temperature Change and External Pair Breaking. *Journal of Low Temperature Physics*, 151(1-2):557–563, April 2008.

[87] D. C. Mattis and J. Bardeen. Theory of the Anomalous Skin Effect in Normal and Superconducting Metals. *Physical Review*, 111(2):412–417, July 1958.

[88] E. M. Levenson-Falk, R. Vijay, N. Antler, and I. Siddiqi. A dispersive nanoSQUID magnetometer for ultra-low noise, high bandwidth flux detection. *Superconductor Science and Technology*, 26(5):055015, May 2013.

[89] J. A. B. Mates, G. C. Hilton, K. D. Irwin, L. R. Vale, and K. W. Lehnert. Demonstration of a multiplexer of dissipationless superconducting quantum interference devices. *Applied Physics Letters*, 92(2):023514, January 2008.

[90] M. Hatridge, R. Vijay, D. H. Slichter, John Clarke, and I. Siddiqi. Dispersive magnetometry with a quantum limited SQUID parametric amplifier. *Physical Review B*, 83(13):134501, April 2011.

[91] M. B. Metcalfe. *A New Microwave Resonator Readout Scheme for Superconducting Qubits*. PhD thesis, Yale University, 2008.

[92] P. Bertet, F. R. Ong, M. Boissonneault, A. Bolduc, F. Mallet, A. C. Doherty, A. Blais, D. Vion, and D. Esteve. Circuit quantum electrodynamics with a nonlinear resonator. *arXiv:1111.0501 [quant-ph]*, November 2011.

[93] S. Probst, F. B. Song, P. A. Bushev, A. V. Ustinov, and M. Weides. Efficient and robust analysis of complex scattering data under noise in microwave resonators. *Review of Scientific Instruments*, 86(2):024706, February 2015.

[94] M. S. Khalil, M. J. A. Stoutimore, F. C. Wellstood, and K. D. Osborn. An analysis method for asymmetric resonator transmission applied to superconducting devices. *Journal of Applied Physics*, 111(5):054510, March 2012.

[95] Ansys HFSS | 3D High Frequency Simulation Software.

[96] M. Gurvitch, M. A. Washington, and H. A. Huggins. High quality refractory Josephson tunnel junctions utilizing thin aluminum layers. *Applied Physics Letters*, 42(5):472–474, March 1983.

[97] S. Etaki, M. Poot, I. Mahboob, K. Onomitsu, H. Yamaguchi, and H. S. J. van der Zant. Motion detection of a micromechanical resonator embedded in a d.c. SQUID. *Nature Physics*, 4(10):785–788, October 2008.

[98] J. B. Clark, F. Lecocq, R. W. Simmonds, J. Aumentado, and J. D. Teufel. Sideband cooling beyond the quantum backaction limit with squeezed light. *Nature*, 541(7636):191–195, January 2017.

[99] G. A. Peterson, S. Kotler, F. Lecocq, K. Cicak, X. Y. Jin, R. W. Simmonds, J. Aumentado, and J. D. Teufel. Ultrastrong Parametric Coupling between a Superconducting Cavity and a Mechanical Resonator. *Physical Review Letters*, 123(24):247701, December 2019.

[100] G. Batey and G. Teleberg. Principles of dilution refrigeration, 2015.

[101] O. Gargiulo. *Towards Analog Quantum Simulation with Superconducting 3D Transmons*. PhD thesis, Unversität Innsbruck, 2021.

[102] R. Gross and A. Marx. Applied Superconductivity: Josephson Effect and Superconducting Electronics. 2005.

[103] M. L. Gorodetksy, A. Schliesser, G. Anetsberger, S. Deleglise, and T. J. Kippenberg. Determination of the vacuum optomechanical coupling rate using frequency noise calibration. *Optics Express*, 18(22):23236–23246, October 2010.

[104] V. K. Kornev and A. V. Arzumanov. Numerical simulation of Josephson-junction system dynamics in the presence of thermal noise. *Inst. Physics Conf. Ser.*, 158:627, January 1997.

[105] S. V. Polonsky, V. K. Semenov, and P. N. Shevchenko. PSCAN: Personal superconductor circuit analyser. *Superconductor Science and Technology*, 4(11):667–670, November 1991.

[106] J. O. Smith. *Spectral Audio Signal Processing*. http://ccrma.stanford.edu/ jos/sasp/, accessed 27.04.2022.

[107] K. P. Burnham and D. R. Anderson, editors. *Model Selection and Multimodel Inference*. Springer New York, New York, NY, 2004.

[108] https://scikit-learn.org/.

[109] V. E. Manucharyan, E. Boaknin, M. Metcalfe, R. Vijay, I. Siddiqi, and M. H. Devoret. RF bifurcation of a Josephson junction: Microwave embedding circuit requirements. *Physical Review B*, 76(1), July 2007.

A | Data treatment and additional considerations for the measurements

Measuring the optomechanical system requires a sophisticated data taking and analysis routine. Among the main reasons for this is that the mechanical linewidth is very narrow (below 1 Hz), which requires long measurement times and thus high stability over this time. Additionally, the signal to noise ratio of a single mechanical spectrum is low, which requires averaging of multiple measurements, putting even more stringent constraints on the stability.

Some key considerations are already given in the main part of the thesis, here additional information and supporting material about the data taking as well as the treatment will be given. While some common procedure remained the same for all data sets, the routines became more sophisticated as the experiment got more complex. Thus, the following will also address how the data taking and analysis procedures changed over time.

A.1 Common procedure

There are some steps, which are in common for (nearly) all the sets we took and those will be explained in this part.

As it was only possible to take data without the pulse tube cooler running, it was always switched off before starting a measurement. To measure the mechanical signal, we used a single microwave probe tone and the spectrum analyser (SA), usually operated at a bandwidth (BW) of 0.1 Hz and a span of 800 Hz yielding 8001 points per spectrum. For some traces, especially for those sensitive to flux noise, we also used the SA at a BW of 0.2 Hz or 0.4 Hz, where we increased the span to keep the number of points fixed. Despite using the same number of points, the measurement time decreases, as it (mainly) depends on the BW and thus halves or quarters when using 0.2 Hz or 0.4 Hz instead of 0.1 Hz.

When acquiring the spectrum, a Fourier transform is performed. Different types of filtering functions (windows) can be chosen, which typically either give advantages in the amplitude or frequency resolution. We performed all measurements, using a uniform window, which means that no special window was chosen. While we did not see significant change in the outcome by using another window, the measurement times per trace significantly increased for other windowing types. Additional information on the different types of windowing functions is found in [106].

While early on in the experiment, i.e. for the data discussed in Chapter 7.3, we took 40 consecutive spectra within a PT off window, we later on halved this to 20 traces (i.e. data discussed in Chapter 7.4). This set of 20 (40) traces then usually lead to a data point considered for the cooling traces (or the temperature ramps, etc). The mechanical traces are fitted with the model for a damped harmonic oscillator [103]

$$S_{\omega\omega}(\omega) \approx g_0^2 \langle n_m \rangle \frac{2\omega_m}{\hbar} \frac{2\Gamma}{(\omega^2 - \omega_m^2)^2 + \Gamma^2\omega^2}, \tag{A.1}$$

already partly discussed in the main part. In contrast to the main, here the amplitude is rewritten and $g_0^2 \langle n_m \rangle$ can be read off. Also the calibration routine, necessary to extract the coupling strength/phonon number, is already discussed in Chapter 7.2.3. Prior to fitting, we always average 4 mechanical spectra on top to improve the signal to noise (in case we measure with 0.2 Hz BW, we usually average 8 etc.). This gives us multiple spectra per data point, which yields sufficient statistics.

With this, the common steps are discussed, now let us focus on the taken steps specific for different measurements, which also changed over time.

A.2 Routines for doing the temperature ramp

When doing a temperature ramp, we typically measured at a point with a low coupling, to avoid significant influence from flux noise. Furthermore this prevents backaction on the sample, also when not measuring with lowest power. Here, we will discuss the routines used for the temperature ramps early in the experiment (e.g. the one shown in Fig. 7.28), while later on we changed to the more sophisticated routines, explained in Chapter A.5.

In a first step, we set the cavity frequency to be on resonance with the probe tone. Before and after starting the measurement set of 40 SA traces, we took a VNA trace, to ensure that the frequency of the cavity did not move (significantly) during the measurement. As the measurement power is low enough, a frequency change should not have an influence and induce no backaction. We even confirmed to not induce backaction for one of the initial temperature ramps, by performing measurements at different powers (Fig. A.1). As $g_0\sqrt{n_m}$ remains constant with power, there is no (measurable) backaction occurring on the mechanical system.

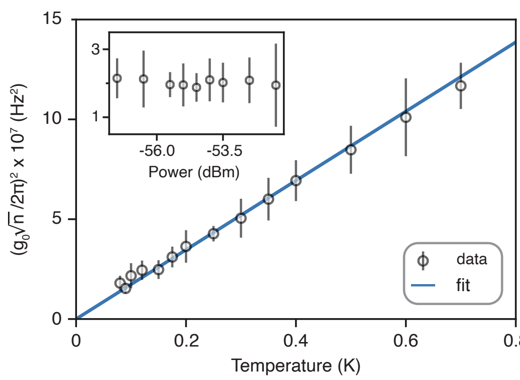

Figure A.1: Temperature ramp, which is already shown in the main manuscript (Fig. 7.28). The additional inset shows the independence of the measurement on the input power, as expected for a temperature ramp. This measurement was taken at 100 mK. We performed the temperature ramp at a fridge input power of 54.5 dBm, so we do not expect any influence of backaction.

As already mentioned in Chapter A.1, before fitting we average the SA traces in groups of four. This gives us 10 of those groups, providing us with sufficient statistics. The fit of the SA traces is performed on a limited span around the mechanical peak.

A minor issue we correct for, is that the maximum frequency the cavity reaches, increases with temperature (Fig. A.2). To compensate for this, we always perform the temperature ramp measurements at a given frequency below the top frequency.

For the temperature ramps performed in more advanced stages of the experiment, we used the sophisticated data acquisition routine, developed for measuring the nonlinear backaction

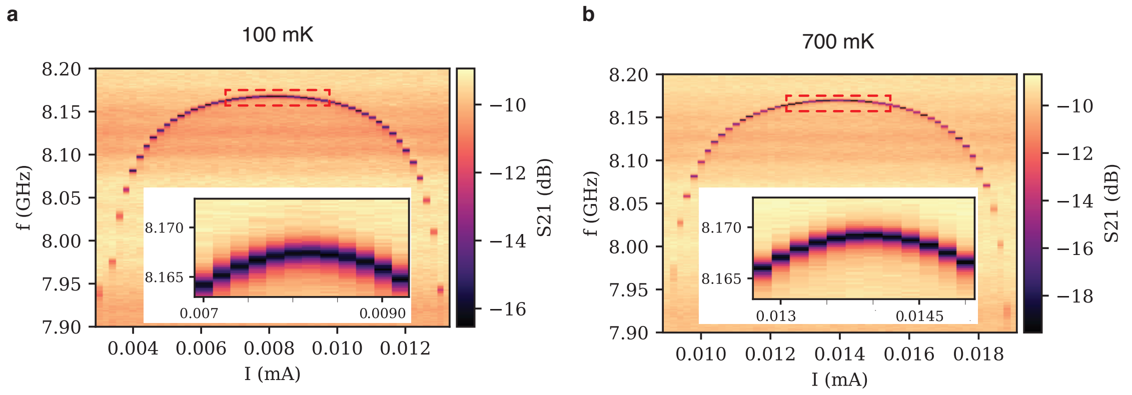

Figure A.2: Flux maps at 100 mK and 700 mK. Especially comparing the insets, it is evident that the top of the flux map increases with temperature. This was taken into account when doing the temperature ramps to keep the coupling constant, by shifting the cavity frequency accordingly. This figure was also shown in [45].

(more details on that in Chapter A.5). A temperature ramp measured with this routine is plotted in Fig. A.3. Despite several differences in the data taking routine, there is, as expected,

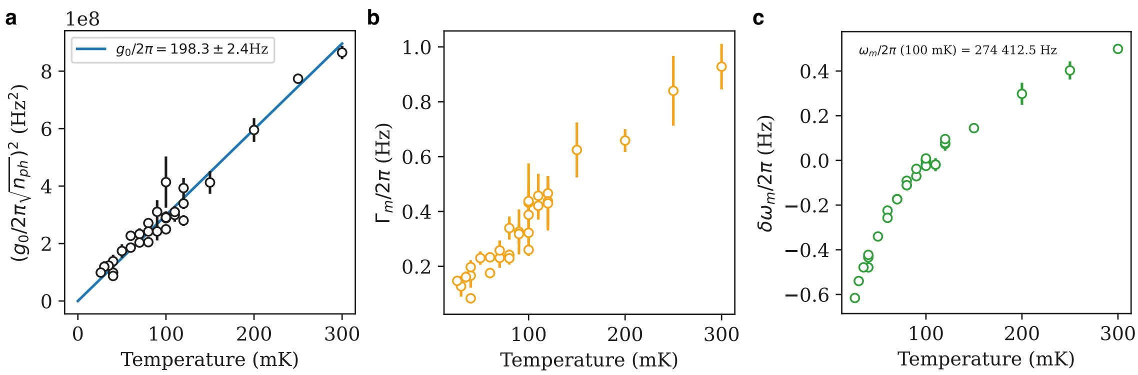

Figure A.3: Temperature ramp taken with the more sophisticated measurement routine, discussed in Chapter A.5. Both measurements and the results are very similar. This measurement here was performed at a high coupling of around 200 Hz. Additionally, we only measured up until 300 mK, but down to base temperature, where we still see that the mechanical mode is thermalised to its environment.

no difference in the results and we can trust all available measurements. Here, we also measured until base temperature, where the mechanical mode is still thermalised to its environment.

A.3 Information on measuring the change of g_0 with flux bias point

As the frequency of the cavity is tuned along the flux map, it becomes increasingly sensitivity to flux signals, which increases the coupling strength, as already discussed in Chapter 7.2.6. We can either measure the coupling directly by extracting $g_0\sqrt{n_m}$ or by extrapolating the slope of the flux map. When measuring it directly, one has to be very careful to not induce backaction, which would falsify the extracted coupling. Another option is to extrapolate the coupling by using the changing slope of the flux map. For setting a g_0 when doing a cooling trace, we took a local flux map (Fig. A.4) and followed exactly that procedure. Also for the tunability of the coupling discussed in Chapter 7.2.6 we implemented this procedure, where we compared those values to a flux map taken over the complete range. To confirm the values once more, we also

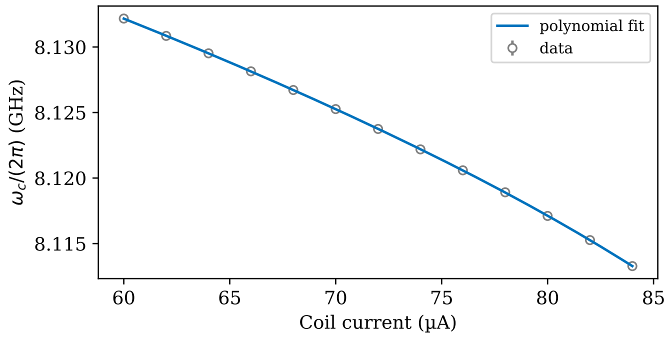

Figure A.4: Local flux map showing the change of cavity frequency with tuning the coil. The fit is a 4-th order polynomial. To find out the best order for the polynomial, we use the Akaike criterion [107]. This figure was also shown in [46].

took the values from the cooling traces towards the tail, where the backaction is not significant anymore.

In the early measurements, we also measured $g_0\sqrt{n_m}$ directly and reduced the input power with increasing coupling, to avoid backaction. However this measurement is very challenging, as for higher couplings, the signal significantly decreases. The results of this measurement is shown in Fig. A.5, which are very similar to the ones shown in Fig. 7.30. The slight difference

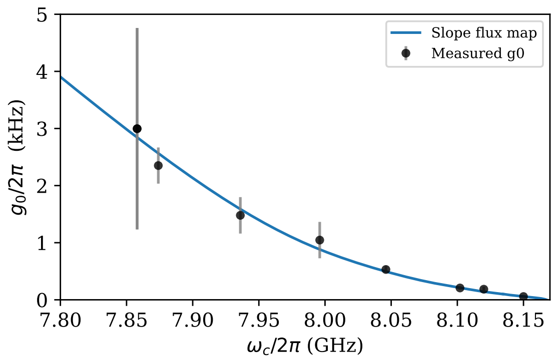

Figure A.5: Direct measurement of the optomechanical coupling strength at different cavity frequencies (sensitivities). To avoid backaction we had to lower the power accordingly, which leads to a large uncertainty for high couplings and the inability for measuring at even higher couplings due to a vanishing signal. The values extracted here are slightly below the ones shown in Fig. 7.30. This figure was also shown in [46].

can be explained with a different top frequency of the flux map for this cooldown.

A.4 Additional information on the measurements in the linear backaction regime

A.4.1 Measurements at low coupling

In this part, the measurement protocol for the backaction measurements in the linear regime at low couplings, presented in Chapter 7.3.1, is discussed. For this measurement we measure the mechanical cantilever with a probe tone sweeping the cavity resonance. This is the only backaction measurement, where we sweep the probe and not the cavity. As flux noise is only a minor concern compared to the high g_0 and high power measurements, we assume a stable operation over the measurement time. To ensure that we are operating at the intended flux bias point, (compensating drifts over the full day) we tune the cavity frequency using the VNA before each measurement with the probe tone switched on (always at the same frequency). For the measurements itself we detune the probe tone to the intended frequency. We fit the data on a limited span around the mechanical peak and apply some *goodness of fit* and data criteria, which have to be passed. Those are, that the maximum of the data and the maximum of the fit are not allowed to be more than 4 dB apart and the maximum of the fit has to be at least 4 dB above the noise floor. Those values were empirically found, and helped to avoid outliers, while the vast majority of traces passed those criteria. We additionally check the average height of the calibration tone, which has to be above −130 dBm. This is about 10 dB above the noise floor, which is especially relevant working far off resonance. The error shown in the main body is the propagated fit error. Using the standard deviation instead gives qualitative very similar errors. We also used the SA with 0.2 Hz BW, which reduced the measurement time for one data point to around 5 minutes. In contrast to later datasets, we stuck with averaging four traces, despite increasing the BW for this dataset.

A.4.2 Measurements at high coupling

Below, the measurement protocol for the data measured at high coupling, presented in Chapter 7.3.2, is discussed. For the measurement at large g_0, flux noise has a significant influence. At that time, we usually took 40 traces within a pulse tube off slot, leading to a measurement time of about 10 minutes. A first modification was to only take 10 traces within a pulse tube off slot. In addition, a low power VNA trace was acquired in parallel to the spectrum, to determine the probe-cavity detuning. For fitting this trace (Fig. A.6), we cut out a 2 MHz window around the pump and an additional small window 6 MHz from the pump, as the VNA shows a spurious pump component there.

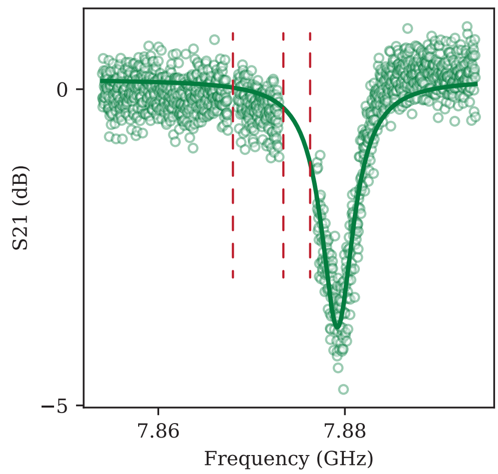

Figure A.6: Lorentzian fit to the VNA trace measured at very low power in parallel to the mechanical spectrum. We cut out a 2 MHz region around the pump, as well as a narrow region 6 MHz below the pump where a spurious peak occurs. Despite the cutouts, the fit worked reasonably well to determine the detuning for each trace. The circles are the measured data, the line is the fit. This figure was also shown in [45].

As the signal to noise ratio is low, especially in the regions with larger detunings, additional averaging is required. We do this by grouping the data with similar detuning in bins and again averaging the data in groups of 4. We decided for bin sizes of 1 MHz. The size of each bin against the detuning is plotted in Fig. A.7. To obtain the frequency detuning of each bin, we take the average of the detunings in each bin, known from the Lorentzian fit. Changing the sizes of the bins does not give any qualitative difference on the data. The standard deviation of the detunings to the mean value is used as a x-error for each bin. Similar to the data measured

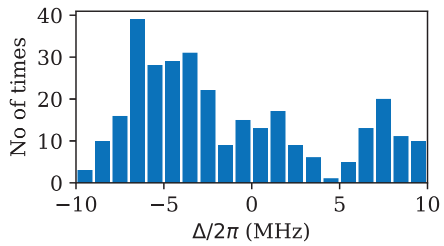

Figure A.7: Grouping of the data traces in the case of high coupling. Each bin gives one data point for the back action measurement. To fit the data, at least four traces are averaged on top of each other. Here plotted is a histogram of the bin sizes against the detuning to the cavity resonance. This figure was also shown in [45].

at low coupling, Chapter A.4.1, we perform several checks, which we apply to all the data. If the data fails one of the checks, we reject it in the analysis. We check the calibration tone, the goodness of the fit and require a bin to contain at least four data traces. Concerning the calibration tone, we additionally check the leakage to be below −130 dBm and disregard the data otherwise. For checking the leakage we set the development of the frequency modulation to 500 kHz, which is roughly double the modulation frequency. During this measurement, we used 200 kHz for the development due to the weak signal, but for most other measurements we used values between 10 kHz and 50 kHz. For the goodness of fit, we require that the highest data point is not more than 4 dB away from the highest point of the fit. Furthermore, we require that the maximum of the fit has to be at least 4 dB above noise floor. Only if a data point (consisting of at least four traces) passes all of these tests, we consider it in the analysis. As in the weak coupling we use the propagated fit error as the error for the y-axis.

A.5 Additional information on the measurements in the nonlinear cooling regime

For taking data in the nonlinear regime, we developed a more sophisticated process for both measuring and analysing the data. This was necessary, as due to the nonlinearity of the cavity, small variations in probe cavity detunings (e.g. due to a shift of the cavity because of flux noise) can lead to a large change in the cavity response and thus in the backaction. We took all data for low and high g_0 using this routine.

A.5.1 Data taking routine

Before doing the measurement itself, we took a local flux map over the range which we are measuring, Fig. A.4. To measure a data point (see diagram Fig. A.8), we start by checking the frequency of the cavity and retune it according to the flux map until it is within a certain threshold (i.e. 20 kHz for the measurement at $g_0/2\pi = 201$ Hz). We always take a pair of traces, where we first measure the frequency of the cavity with a low power VNA trace. Then we switch on the microwave generator and measure the cantilever using the spectrum analyser. We usually take five of those pairs before taking another VNA trace for re-checking the detuning as explained above. In total we do four of those sets, giving us 20 measurements of the mechanical mode per data point. Afterwards we switch the pulse tube on, detune the sample to measure the leakage of the calibration tone and a background VNA trace. Ideally we would measure no calibration tone as the cavity is detuned, but sometimes we measure a measure a small leakage, which is however small enough to not have a (significant) influence on the actual calibration. In contrast to earlier, we only took 20 traces within a pulse tube off window. One of the reasons was, that we allocated hourly slots for the vibration sensitive measurements, and this

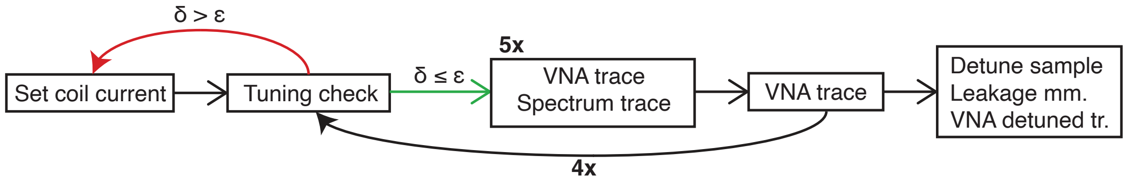

Figure A.8: Diagram of the measurement process. Here, δ is the measured detuning, while ϵ is the detuning threshold we require to start the measurement. In the last box, *Leakage mm.* stands for measurement of the leakage and *VNA detuned tr.* for a VNA trace with the cavity detuned. See text for details. This figure was also shown in [46].

time could be used better doing multiple shorter measurements. Also here we use the third different method to set and measure the detuning between the cavity and the pump. While the pump power was low (Chapter 7.3.2), the nonlinearity did not significantly influence the cavity response, and measuring the cavity in parallel to the spectrum or tuning the cavity with the pump tone turned on worked well for those measurements. Here, this is different as the cavity response gets distorted due to the nonlinearity of the cavity. Additionally, as for those measurements the nonlinear response of the cavity is well included in our model and the low power detuning is necessary for the data analysis.

A.5.2 Data analysis

Here, details on how data taken for the nonlinear cooling is treated. The routines remained the same for all data sets, only some goodness of fit criteria changed, explained in Chapter A.5.3. As we shift the frequency of the cavity, instead of changing the frequency of the pump, g_0 is slightly different depending on the exact detuning. To compensate for this, we took a flux map of the cavity and evaluate g_0 via the slope of the flux map. In Fig. A.4 we show such a flux map with the corresponding polynomial fit. To find out the best order for the polynomial, we use the Akaike criterion [107].

In Fig. A.9 we compare using a fixed $g_0/2\pi$ at 201 Hz (black) to a changing g_0 (blue) as estimated from Fig. A.4 and thus show the importance for correcting this.

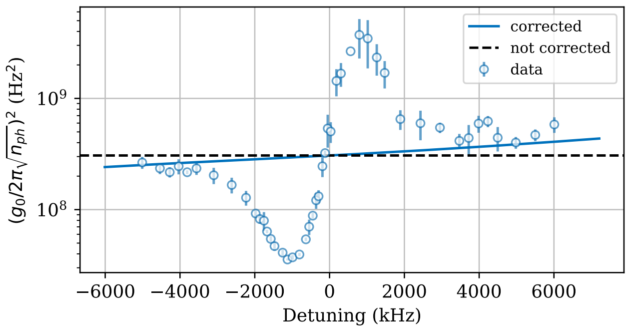

Figure A.9: Here plotted is $(g_0/2\pi \times \sqrt{n_{\text{phonon}}})^2$ to demonstrate the necessity for correcting for the change of g_0 over the measurement range. In the not corrected version a constant g_0 is assumed, while in the corrected version, the slightly changing slope of the flux map for different detunings (Fig. A.4) is corrected. This data is taken from the high power set at $g_0/2\pi = 201$ Hz presented in Chapter 7.4.2. This figure was also shown in [46].

This was already a problem, which occurred when measuring backaction in the low power, but high coupling regime (Chapter 7.3.2). Doing those measurements, this was however not anticipated, and only a minor correction, as the overall signal to noise was not as good as for the later measurements discussed here. Reasons are the improvements of the vibrations coupling into the system, Chapter 7.2.7, but also the more sophisticated data processing.

As discussed in the beginning of this chapter, due to the small mechanical linewidth, we typically operate our spectrum analyser at the lowest bandwidth it allows of 0.1 Hz, which leads to a measurement time of 10 s. The cavity frequency can change during a measurement due to flux noise, which changes the detuning between the probe tone and the cavity frequency and as a consequence the backaction. Especially operating close to bistability and in the region with highest cooling we are very sensitive to such changes. While we cannot compensate for flux noise happening on shorter time scales than our typically 10 s spectrum analyser traces, we can partly compensate for slower flux drifts, by using the measurements of the cavity directly before each measurement. To do this, we bin our data together by applying a k-means binning [108], which groups the traces having most similar cavity frequencies. Doing this, we regroup the data, but do not change the total number of bins for the cooling trace. This means that the number of traces per bin is determined by the binning routine, but as we do not change the number of total bins, on average there are 20 traces within a bin. In the next step we fit the mechanical traces using the damped harmonic oscillator model, Eq. A.1. First, we average all data within a bin and fit it on a limited span, where we expect the mechanical frequency. This helps to get good initial parameters for the subsequent fits, but is also required, as we remove residual peaks away from the mechanical resonance. As usual, we then average the data in groups of four. Afterwards we remove the residual peaks, which we identify by being 6 standard deviations above the noise, where we exclude an area of 100 Hz to 200 Hz around the mechanical frequency depending on the mechanical linewidth (Fig. A.10a). This is required, as the fit of the mechanical trace is performed over the whole measurement range. We also numerically integrate the area under the curve as an additional check (Fig. A.10(b-d)). We usually estimate the error as the standard error between the groups within a bin, which is the error shown for all backaction data of the nonlinear cooling in the main part. We also compared this to the propagated fit error and obtain very similar results.

In Fig. A.11 we show the complete cooling trace, of which we already show a few spectra in Fig. A.10. We clearly see that the numerical integration and the fit agree very well. Typically we show the phonon number obtained from the fit to the data.

A.5.3 Goodness of fit criteria

We also updated the goodness of fit criteria compared to what we did for the backaction in the linear regime. For instance, some mechanical traces were heavily influenced by flux noise, which lead to some spurious, narrow peaks within the mechanical peak or the mechanical peak itself being distorted due to flux noise (for more details, see Chapter 7.2.7). This made comparing the highest point of the data and the fit a not ideal criterion and pushed us into updating those checks. Below are all automated criteria applied to the data, which have to be passed chronologically in order to accept a data point. Even though there are multiple criteria, the majority of data points is accepted.

1. Check the leakage of the calibration tone. This checks the credibility of the calibration tone. If we measure a significant calibration tone, even though the cavity is detuned we cannot trust the data point, and therefore ignore the data. As we usually check the calibration before starting the measurement, this is a rare occurrence.

2. We obtain the detuning for each data trace by fitting the cavity response directly measured before the measurement with the spectrum analyser. In case this fit fails, we have to neglect this trace. This only happens for the highest couplings we measured and usually happens due to a distorted cavity response due to excessive flux noise.

3. We check if the cavity frequency moved too much between subsequent data traces. In case it did, we assume that there was excessive flux noise during the measurement of the mechanical mode and neglect the data. On top of that, we also check if the standard

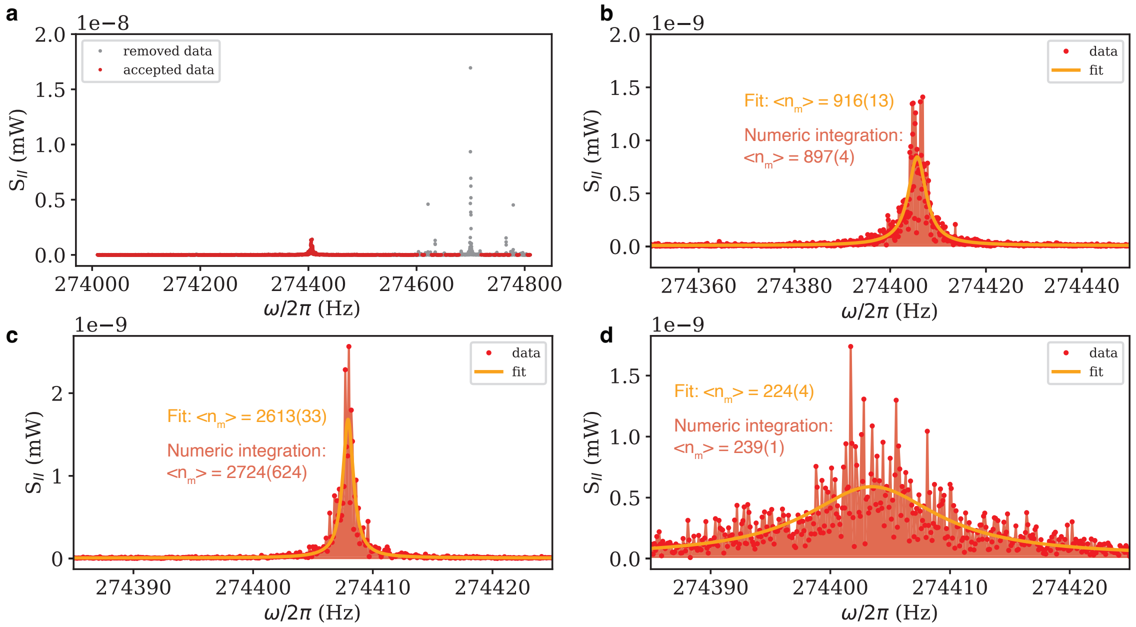

Figure A.10: Some aspects of the analysis on data from one of the cooling traces taken at $g_0/2\pi =$ 201 Hz close to bistability. **a,** Outlier removal. As described in the text, we remove outlying peaks far from the mechanical ones, which is shown here (grey). Those peaks often appear around the calibration peak, where we believe that those peaks are upmixed flux noise. **b-d,** Comparison of fit and numeric integration for traces with medium cooling (b), weak cooling (c) and strong cooling (d). Coloured is the area below the mechanical peak, which we integrate over. The two methods show good agreement. For the fit, we give the propagated fitting error. For the numerical integration, we propagate the standard error of the noise floor. All traces shown here, are averages of four traces measured with the spectrum analyser. This figure was also shown in [46].

deviation of the cavity frequencies within a subgroup of four averaged mechanical traces is below a threshold.

4. When the data passed the above criteria, we fit the mechanical spectrum. Afterwards we compare the phonon number from the fit to the one obtained from numerical integration, and neglect the data if the phonon number does not agree within a factor 1.5. Also we neglect the data if the fit is not more than 3 dB above the noise.

5. In a final step, we neglect data, if the obtained linewidth is above 300 Hz or below 5 μHz, which points to an issue within the fitting routine.

The first criterion aims at checking the credibility of our calibration tone, which is crucial for trusting the phonon number. Criteria two and three aim at assuring that we can trust the frequency of the cavity we extract and that no excessive flux noise occurred during the measurement. With criteria four and five we want to make sure that the fit gives an accurate description of the data, also requiring that we have enough signal to get faithful information doing the fit.

We keep most parameters the same for all the data sets treated (i.e. sets at different g_0). The only parameter we systematically change according to the change of coupling, is how far the cavity can move in frequency between subsequent data traces (criterion no. 3), as flux noise increases with increasing g_0. Also, for the data of highest cooling, we relax criterion no. 4 comparing the phonon number obtained by numerical integration and the fit, as the spectra are heavily influenced by flux noise and we cannot trust the fit anymore (see Chapter 7.4.7). While there are several checks done on the data, especially for low g_0, only a small fraction of the data is removed, as the system is very well behaved. For instance, for the high power set at

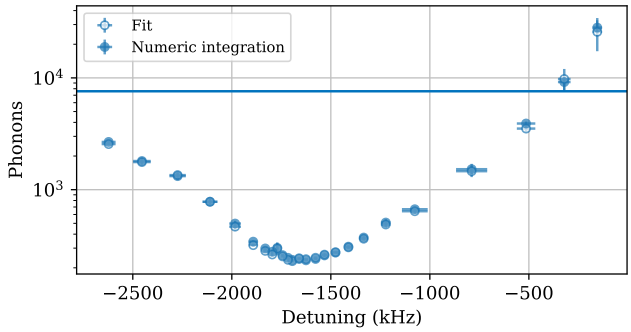

Figure A.11: Cooling trace, comparing phonon numbers extracted via numerical integration and fitting. Fig. A.10 already showed some spectra corresponding to data points here. We see very good agreement between the fit and numeric integration. The plotted error is the standard error of multiple data points for each detuning (see main text). This figure was also shown in [46].

$g_0/2\pi = 201\,\text{Hz}$ presented in Chapter 7.4.2 more than 85% of the data is accepted. For other data this acceptance is also far above 90%. For data at higher g_0 this naturally changes, while we still have typical acceptance rates of 60%.

B | Duffing model for fitting the cavity response

B.1 Model used for the fit of the Duffing model

We developed a routine in mathematica to fit the Duffing model (Chapter 3.2) to the response of our nonlinear cavity. The results are discussed in Chapter 7.1.3 and 7.1.4. The Duffing model we use to do the fit slightly differs from the equation given in the main, Eq. 3.34, and reads [109]

$$F^2 = \left(\frac{\Omega^2+1}{Q^2} + \frac{3\Omega}{2Q}A^2 + \frac{9}{16}A^4\right)A^2, \tag{B.1}$$

where

$$\Omega = 2Q\frac{\omega_p - \omega_c}{\omega_c}.$$

The solutions can be made identical by replacing A with $A\omega_0$ and setting $\eta = 1$ in Eq. 3.34, which are just re-normalisations. However with setting the nonlinear parameter $\eta = 1$, the nonlinearity cannot be read off directly. In Chapter B.2, we discuss how we calculated a Kerr value from fitting this model.

Now, let us review the further modifications we had to do for fitting the cavity, which is measured in notch configuration. An ideal resonator in notch configuration is described by

$$S_{21}(\omega) = 1 - Q_l/|Q_c|e^{i\phi_0}x(\omega), \tag{B.2}$$

where $x(\omega)$ is the response of resonator. This can be made identical to Eq. 6.6 describing a linear resonator, by inserting the Lorentzian response x

$$x^{\mathrm{Lin}}(\omega) = \frac{1}{1 - 2iQ_l\frac{\omega-\omega_c}{\omega_c}}. \tag{B.3}$$

In case of the notch configuration, the response of the Duffing model (Eq. 3.34/ B.1) is used for x.

B.2 Evaluating the Kerr constant using the Duffing model

For estimating the Kerr we had to do a detour, as in the reduced parameter model introduced before in Chapter B.1, the nonlinearity parameter is set to 1. From the fit parameters we know the drive amplitude and can calculate the critical drive (Eq. 3.38). At the same time, we also know the frequency shift at the critical drive. With this, we can estimate the frequency shift at the given drive strength. Now we have to convert this into frequency shift per photon. To do so, we convert the fitted drive strength to the photon number using the estimated attenuation.

With this, we can estimate the Kerr in frequency shift per cavity photon. Fig. B.1 shows the different Kerr values extracted for the dataset, where four fits are shown in Fig. 7.7. To estimate the Kerr, we used the five lower powers, as the others are beyond bistability, where the fit starts to deviate from the data. The reasons for this might either be higher order effects playing a role, or that the current through the junction is already close to the critical current.

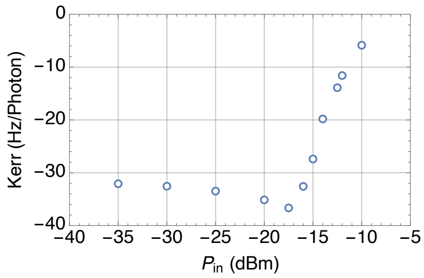

Figure B.1: Different Kerr values extracted for the dataset shown in Fig. 7.7. To extract the Kerr, we used the first five points. Higher powers are above bistability, where the data starts to deviate from the model, as probably higher order effects start to influence the response.

Acknowledgement

Foremost I want to thank you, Prof. Gerhard Kirchmair, for giving me the opportunity of doing a PhD in your research group. I want to thank you for the great support throughout the whole time I spent in your group. Even though there are many things on your agenda, you are always very supportive and always take the time for discussing and improving the project. I am still amazed by your never ending passion for science as well as your knowledge in general. For me, it was a great experience working together.

I also want to thank Mathieu Juan, for all the support. Especially before you moved on to Sherbrooke, we worked together very closely, which was great and also real fun. I could learn a lot of things from you and you were the main driving force behind setting up the experiment, and getting it to work. You always had an open ear for me, and I really enjoyed our discussions together. I also want to thank you for the ongoing support, even though you moved to Sherbrooke and wish you all the best for your own research group.

With this, I want to thank other people involved in the optomechanical subgroup, Christian Schneider and Lukas Deeg. Next to all the frutiful discussions and your advice, I especially want to thank you, Christian, for developing all the programming code, we use for running the experiment. I am well aware, that this is a lot of work, which is not necessarily seen and usually, we approach you - somehow unhappy - when something works differently or we discover I bug. With this, I also want to say thank you for all this work in the background, and immediately working on a bug fix, whenever a problem occurs. Also Lukas, who joined us in the beginning of 2021, it was a pleasure working together and introducing you to our experiment. I want to thank you for all the discussions, and also for proof-reading my thesis. I admire your passion and I am more than convinced the experiment is in excellent hands.

I also want to thank you, Aleksei Sharafiev, for all the interesting conversations we had in general, and especially for the discussions about Josephson junctions, where I could really benefit from your knowledge. I also want to thank you, Desi Atanasova and Vasilisa Usova (and Lukas of course!), for regularly joining me on my late outside lunch break, and making those really fun. Also I want to thank Oscar Gargiulo, not only for supporting me when I started in the Kirchmair group. With this, I generally want to thank all the others currently in Gerhard's group, Romain, Julian, Teresa, Stefan, Christian (Schlager), Markus, Ian and Max. I really believe Gerhard formed a terrific team, there is a great team spirit, great passion and whenever somebody is in need we help each other. I truly enjoyed working with all of you and I wish the group all the best.

I also want to thank our theory collaborators. Prof. Anja Metelmann and Nicolas Diaz-Naufal, whom we collaborated with for our nonlinear cooling theory. I think we got (and still do whenever we talk) a much more sophisticated understanding of the theory behind the nonlinear cooling. Especially I also want to thank Nico, for all the discussions and also supporting me whenever I had a question about theory, be it more general or in particular for our device. Also I want to thank you, for your daily food deliveries and caring about me during the Gordon conference, when I was isolated in the hotel room, due to Covid-reasons.

Furthermore, I am thanking our collaborators from the MaQSens consortium. We always had nice scientific discussions whenever we met. Especially I want to thank Prof. Hans Hübl from the WMI, who was also part of MaQSens. You really helped us in improving our setup, especially pointing out the possibilities of nonlinear cooling during one of our early discussions or introducing us to the calibration routine for extracting the coupling strength.

Of course a huge thank you also goes to the administrative staff at IQOQI, with whom it is a pleasure to work with. This is also a reason, why we can focus so much on science, as the all the administrative tasks run extremely smooth. This concerns Elisabeth Huck and Klaus Falschlunger, who help us with ordering or organising our travels. I am still sometimes amazed how quick orders are placed or followed up. Of course this also concerns David Jordan for all the IT support, and also Markus Knabl, as the head of the administration. Also those two usually helped for taking some of those amazing pictures I presented in the thesis, which includes the title picture of the thesis, taken by David Jordan. Another key part of IQOQI is also the mechanical workshop, run by Andreas Strasser, Bernhard Öttl and David Arnold. Especially I want to point out Andreas, who fabricated all the waveguides and required parts for mounting the samples. Working together with the workshop is always very smooth and they are highly professional. Even though we sometimes approached them last minute before a cooldown, they always supported us with all they could.

A big thank you also goes to my parents. Without their support throughout all my studies nothing of this would have been possible and I want to thank you for all the encouragement. Of course, I am also thanking my girlfriend Verena, for all the support and your understanding. Especially you were extremely patient with me whenever I was staying long at the lab and let you wait.

I also want to thank the funding agencies, where I was funded by the Union's Horizon 2020 research and innovation program under grant agreement No. 736943. Without this grant, my PhD in Gerhard's group probably would not have been possible in the first place.